

REPORT DOCUMENTATION PAGE

AFRL-SR-BL-TR-98

88

Public reporting burden for this collection of information is estimated to average 1 hour per response, including the time for reviewing the collection of information, sending the collection of information, including suggestions for reducing this burden, to Washington Headquarters Services, Directorate for Information Operations and Reports, 1204, Arlington, VA 22202-4302, and to the Office of Management and Budget, Paperwork Reduction Project (0379), Suite 1204, Arlington, VA 22202-4302.

0379

urces, gathering
his collection of
Highway, Suite

1. AGENCY USE ONLY (Leave Blank)

2. REPORT DATE
November 19963.1
Final

4. TITLE AND SUBTITLE

A Frequency Domain Analysis of Surface Heat Transfer/Free-Stream
Turbulence Interactions in a Transonic Turbine Cascade

5. FUNDING NUMBERS

6. AUTHORS

David G. Holmberg

7. PERFORMING ORGANIZATION NAME(S) AND ADDRESS(ES)

Virginia Polytechnic Institute and State University

8. PERFORMING ORGANIZATION
REPORT NUMBER

9. SPONSORING/MONITORING AGENCY NAME(S) AND ADDRESS(ES)

AFOSR/NI

110 Duncan Avenue, Room B-115

Bolling Air Force Base, DC 20332-8080

10. SPONSORING/MONITORING
AGENCY REPORT NUMBER

11. SUPPLEMENTARY NOTES

12a. DISTRIBUTION AVAILABILITY STATEMENT

Approved for Public Release

12b. DISTRIBUTION CODE

13. ABSTRACT (Maximum 200 words)

See attached.

14. SUBJECT TERMS

15. NUMBER OF PAGES

16. PRICE CODE

17. SECURITY CLASSIFICATION
OF REPORT

Unclassified

18. SECURITY CLASSIFICATION
OF THIS PAGE

Unclassified

19. SECURITY CLASSIFICATION
OF ABSTRACT

Unclassified

20. LIMITATION OF ABSTRACT

UL

DTIC QUALITY INSPECTED 3

Standard Form 298 (Rev. 2-89)

Prescribed by ANSI Std. Z39.18

Designed using WordPerfect 6.1, AFOSR/XPP, Oct 96

A Frequency Domain Analysis of Surface Heat Transfer/
Free-Stream Turbulence Interactions in a Transonic Turbine Cascade

by
David G. Holmberg

Dissertation submitted to the Faculty of the
Virginia Polytechnic Institute and State University
in partial fulfillment of the requirements for the degree of

DOCTOR OF PHILOSOPHY
IN
MECHANICAL ENGINEERING

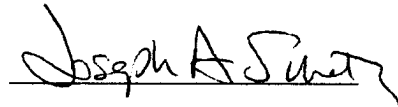
APPROVED:



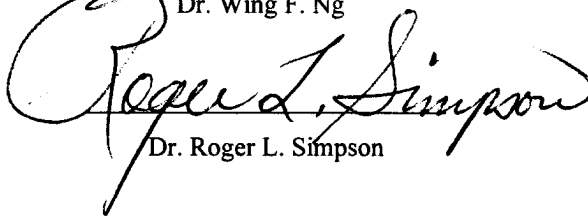
Dr. Thomas E. Diller, Chairman



Dr. Wing F. Ng



Dr. Joseph A. Schetz



Dr. Roger L. Simpson



Dr. Charles D. MacArthur

November 12, 1996
Blacksburg, Virginia

19980430 042

Keywords: turbine, heat transfer, free stream turbulence, frequency domain, coherence

DTIC QUALITY INSPECTED 3

A FREQUENCY DOMAIN ANALYSIS OF SURFACE HEAT TRANSFER/
FREE-STREAM TURBULENCE INTERACTIONS IN A TRANSONIC TURBINE CASCADE

by

David G. Holmberg

Thomas E. Diller, Chairman

Mechanical Engineering

(ABSTRACT)

The relationship of time-resolved surface heat flux to the turbulent free-stream flow over a turbine blade is investigated. Measurements are made in a transonic linear cascade with a modern high pressure turbine blade profile. Time-resolved direct heat transfer measurements are made with Heat Flux Microsensor (HFM) inserts along the pressure side, and with one HFM directly deposited on the suction surface near the leading edge. Simultaneous velocity measurements are made above the heat flux sensors using miniature hot-wire probes. Grids are used to produce two turbulence fields of constant inlet turbulence intensity, $Tu = 5\%$, but significantly different integral length scales (Λ_x). Results are compared with a low free-stream turbulence baseline condition. Special emphasis is given to frequency domain analysis of the data via coherence function magnitude and phase, energy spectra, and time auto- and cross-correlations.

Results are presented for both mean and fluctuating velocity and heat flux. Mean heat transfer is highest for the smaller length scale grid, but inlet integral length scale appears of limited use in predicting surface heat flux interactions with the observed complex passage flow. While free-stream rms velocity, u' , and surface rms heat flux, q' , show some correlation with mean heat transfer in the laminar region near the leading edge, no such correlation is seen on the pressure side. Instead, u' decreases along the pressure side while low frequency transitional

activity causes q' to increase. Application of laminar heat transfer correlations to the near leading edge region shows some success. However, application of laminar and turbulent heat transfer correlations along the pressure side gives poor results which are likely due to the transitional state of the boundary layer and complex flow.

Frequency domain analysis allowed estimation of scales, frequency, and time lag across the boundary layer of passing flow structures. Coherence between free-stream velocity and surface heat flux was found useful for determining the scale and frequency range of free-stream turbulent structures interacting with the surface heat flux, but did not correlate with mean heat transfer. Suction side coherence was low relative to the pressure side and isolated to a narrow frequency band. Pressure side coherence was broadband with significant low frequency energy near the leading edge. This low frequency energy (larger structures) decayed along the pressure side while higher frequency coherent structures were seen to grow.

Acknowledgments

The support of the U.S. Air Force via the Laboratory Graduate Fellowship program administered through the Southeast Center for Electrical Engineering Education is gratefully acknowledged, as well as the support of AFOSR under grant F49620-93-1-0047 monitored by Dr. Jim McMichael. The support of the Aeropropulsion Directorate at Wright-Patterson AFB in the persons of Dr. Richard Rivir and Dr. Charlie MacArthur is appreciated. The guidance of my committee, and especially the help, direction, and friendship of Dr. Tom Diller have been encouraging and necessary in bringing me to the successful conclusion of this degree.

I also acknowledge the support of my family and the loving patience and support of my new wife. Finally, I want to thank the Lord Jesus for making this effort successful, and for granting rest. "Unless the Lord builds the house, its builders labor in vain...In vain you rise up early and stay up late, toiling for food to eat, for he grants sleep to those he loves." Psalm 127:1,2.

Table of Contents

ACKNOWLEDGMENTS	iv
TABLE OF CONTENTS	v
LIST OF FIGURES	x
LIST OF TABLES	xii
NOMENCLATURE	xiii
1. INTRODUCTION	1
1.1 TURBINE BLADE HEAT TRANSFER	1
1.2 LITERATURE REVIEW	2
1.2.1 HEAT TRANSFER AND TURBULENCE	2
1.2.2 TIME-RESOLVED HEAT TRANSFER	3
1.2.3 HEAT TRANSFER CORRELATIONS	4
1.3 FUNDAMENTAL ISSUES	5
1.4 THIS WORK	7
1.4.1 ANOTHER PERSPECTIVE	7
1.4.2 MOTIVATION	7
1.4.3 POINTS OF CONTRAST	8
1.4.3.1 Heat transfer measurement	8
1.4.3.2 Inlet turbulence	8
1.4.4 OVERVIEW	9
2. EXPERIMENTAL DESIGN	11
2.1 OVERVIEW	11
2.2 FACILITY	11
2.2.1 WIND TUNNEL	11
2.2.1.1 System overview	11
2.2.1.2 Tunnel control and heating	12
2.2.2 SUPPORTING HARDWARE	12
2.2.2.1 Data Acquisition	12
2.2.2.2 Instrumentation: Anemometer, HFM amplifiers, filters	13
2.2.2.3 Traverse and pressure instrumentation	13
2.2.3 TEST SECTION AND LINEAR CASCADE DESIGN	14
2.2.3.1 Test section and cascade	14
2.2.3.2 Design parameters	14

2.2.4 INSTRUMENTED BLADES	14
2.2.5 HFM INSTRUMENTING METHOD	15
2.2.5.1 Insert sensors	15
2.2.5.2 Direct sputtered sensor	15
2.2.6 TURBULENCE GRIDS	16
2.3 TURBULENCE	17
2.3.1 DEFINITION	17
2.3.2 SPECTRUM AND INTEGRAL PARAMETERS	17
2.3.2.1 Intensity	17
2.3.2.2 Auto-correlation and scales	18
2.3.3 ISOTURBULENCE	20
2.3.4 GRID TURBULENCE	21
2.4 TEST CONDITIONS AND PROCEDURES	22
2.4.1 UPSTREAM TURBULENCE	22
2.4.2 HEAT TRANSFER COEFFICIENTS	23
2.4.3 PASSAGE MEASUREMENTS	23
3. HIGH FREQUENCY INSTRUMENTATION	31
3.1 HFM	31
3.1.1 DESIGN AND OPERATION OF HFM-6 SENSORS	31
3.1.2 SURFACE DIRECT-SPUTTERED GAGE	32
3.1.3 CALIBRATION	32
3.1.3.1 Manufacturer calibration of HFM	32
3.1.3.2 In-situ HFS calibration (convection/ conduction)	33
3.1.4 FREQUENCY RESPONSE/ SPATIAL AVERAGING ISSUES	35
3.1.4.1 Frequency (time) response	35
3.1.4.2 Spatial averaging limitations and the Corcos correction	35
3.1.5 LIMITATIONS/ ERROR ANALYSIS	36
3.1.5.1 Flats, reasons for choice of these gages	36
3.1.5.2 Comparison of DS1 with insert	37
3.1.5.3 Effect of insert installation on PS HTC	37
3.1.5.4 Use of HFM sensors	38
3.2 HW PROBES	39
3.2.1 DESIGN AND OPERATION	39
3.2.1.1 Dimensions	39
3.2.1.2 IFA-100 Anemometer and frequency response	40
3.2.2 CALIBRATION	41
3.2.2.1 Hot-wire calibration theory	41
3.2.2.2 One point calibration methodology	42
3.2.2.3 Changing tunnel pressure calibration	44
3.2.2.4 PHW passage calibration	46
3.2.2.5 Issue of u' vs. $(\rho\sqrt{u^2+v^2})'$	47
3.2.2.6 Calibration uncertainty	48
3.2.3 LIMITATIONS/ ERROR ANALYSIS	49
3.2.3.1 Effect of spectral noise on Tu , Λ_x	49
3.2.3.2 Spatial resolution	50

3.2.3.3 PHW probe disturbance	50
3.3 DATA REDUCTION	51
3.3.1 HIGH-FREQUENCY DATA	51
3.3.2 TU , Λ_x CALCULATION METHOD FOR NOISY SPECTRA	52
4. INLET CONDITIONS	58
4.1 BASELINE, NO GRID (INLET VELOCITY SURVEY)	58
4.1.1 INLET TRAVERSE, TU , Λ_x	58
4.1.2 TIME SERIES AND SPECTRA	58
4.2 GRIDS	59
4.2.1 TU AND Λ_x	59
4.2.1.1 Data and correlations	59
4.2.1.2 Uncertainties	59
4.2.1.3 Comparison to normal grid theory	60
4.2.2 INLET ONE DIMENSIONAL POWER SPECTRA	61
4.2.2.1 G_2 , G_4 @ $Tu=5\%$	61
4.2.2.2 G_2 psd series at different Tu	61
4.2.2.3 Comparisons to Isoturbulence	61
4.2.3 CORRECTION FOR HIGH-FREQUENCY ATTENUATION	61
4.2.3.1 Correction based on isoturbulence	61
4.2.3.2 Comparison to Wyngaard's correction	63
4.2.4 GRID EFFECT ON BLADE POTENTIAL FLOW FIELD	64
5. MEAN DATA AND INTEGRAL PARAMETERS	73
5.1 BLADE SURFACE HEAT TRANSFER	73
5.1.1 HEAT TRANSFER COEFFICIENTS	73
5.1.1.1 HTC calculation method	73
5.1.1.2 Grid affected potential field: BL2D code results	75
5.1.2 INTEGRAL SCALES: Q' , TUQ , T_0	76
5.1.3 COMPARISON OF MEASURED DATA TO CODE PREDICTIONS	78
5.1.3.1 KEP	78
5.1.3.2 Laminar Stability Theory	79
5.2 FLOW IN PASSAGE	79
5.2.1 PHW MEASUREMENT MATRIX	79
5.2.2 MEAN VELOCITY ABOVE SURFACE	80
5.2.3 INTEGRAL SCALES: U' , TU , T_x , Λ_x	81
5.3 TRANSITION INFORMATION	82
5.3.1 SHADOWGRAPHS	82
5.3.2 STATE OF THE BOUNDARY LAYER	83
5.4 CONCLUSIONS	84
6. FREQUENCY DOMAIN AND TIME-CORRELATION	99
6.1 TURBULENCE SPECTRA IN PASSAGE	99
6.1.1 DS1: G_0 , G_2 , G_4	99

6.1.2 PS: G0, G2, G4	100
6.2 HEAT FLUX SPECTRA	101
6.2.1 DS1: G0, G2, G4	101
6.2.2 PS: G0, G2, G4	102
6.3 COHERENCE	103
6.3.1 DS1: G0, G2, G4	104
6.3.2 PS: G0, G2, G4	105
6.4 PHASE	106
6.4.1 DS1: G0, G2, G4	107
6.4.2 PS: G0, G2, G4	107
6.5 TIME-CORRELATION	107
6.5.1 BACKGROUND	107
6.5.2 PHW MOVEMENT STREAMWISE RELATIVE TO HFM	108
6.5.3 RESULTS AT DS1 AND PS	109
6.6 COMPARISON DATA FROM WPAFB	109
6.7 CONCLUSIONS	111
<hr/> 7. ANALYSIS AND DISCUSSION	<hr/> 152
7.1 INTRODUCTION	152
7.2 APPLICATION OF EXISTING CORRELATIONS	152
7.2.1 LAMINAR BOUNDARY LAYERS	153
7.2.1.1 Dullenkopf and Mayle's effective turbulence	153
7.2.1.2 Van Fossen's Frossling number correlation	154
7.2.2 TURBULENT BOUNDARY LAYERS	155
7.2.2.1 Moss and Oldfield's X_{tr}	155
7.2.2.2 Ames' TLR	156
7.2.2.3 Maciejewski and Anderson's general correlation	157
7.3 AN INTERPRETATION OF THE FLOW-FIELD/ SURFACE INTERACTIONS	159
7.3.1 MECHANISMS OF FLOW/ SURFACE INTERACTIONS	160
7.3.1.1 The leading edge vortex	160
7.3.1.2 Swirling flow	161
7.3.1.3 Streamwise vorticity due to curvature	161
7.3.2 ANALYSIS OF PRESENT DATA	163
7.3.3 CONCLUSIONS	166
7.4 PRESSURE SIDE Q' INCREASE AND THE SIGNIFICANCE OF Q'	167
7.5 LENGTH SCALE EFFECTS IN THE PRESENT DATA	168
7.6 THE SIGNIFICANCE OF COHERENCE	169
7.7 PRACTICAL APPLICATION TO TURBINE DESIGN	170
7.8 CONCLUSIONS AND RECOMMENDATIONS	171
<hr/> REFERENCES	<hr/> 179
 <hr/> APPENDICES	 <hr/> 184
APPENDIX A AUTHOR'S PUBLISHED RESEARCH	184

A-1 HOLMBERG AND PESTIAN, 1996	185
A-2 HOLMBERG AND DILLER, 1995	195
APPENDIX B COMPUTER PROGRAMS	201
CALIBRATION (HFS, UHW, PHW)	201
QT.FOR	201
HFM2qt.FOR	207
HWcal.FOR	208
HIGH SPEED DATA PROCESSING	209
dghspec.m	209
hfmphw2.m	211
PSD3Lx.FOR	212
APPENDIX C HOT-WIRE FREQUENCY RESPONSE TESTS	214
PHW	214
UHW	216
APPENDIX D KEP OVERVIEW	217
<u>VITA</u>	<u>219</u>

List of Figures

Figure 2.1.1 Virginia Tech transonic cascade wind tunnel facility	25
Figure 2.1.2 View of test section showing instrumentation cables, amplifiers, and grids (Grid 4 in front and Grid 2 in back).....	26
Figure 2.1.3 Side-view cut-away of test section showing blade cascade and angle of grid parallel to blade row inlet.....	27
Figure 2.1.4 Detail of blade dimensions and locations of heat flux sensors and hot-wire measurement stations.....	28
Figure 2.1.5 The HFM-6 Heat Flux Microsensor mounted in an aluminum housing and equivalent to the insert gages used on the pressure side (dimensions in inches).....	29
Figure 2.1.6 A streamwise view looking downstream toward the leading edge of the blade showing the direct sputtered sensor (DS1) on the suction side with the custom Passage Hot-Wire (PHW) probe extended from the end-wall.	29
Figure 2.2.1 Examples of the auto-correlation function calculated from the energy spectrum for the five grid conditions measured above DS1.	30
Figure 2.2.2 Example of the measured auto-correlation and the exponential fit used to find the integral time scale.....	30
Figure 3.1.1 Heat Flux Microsensor resistance layer cross section.	54
Figure 3.1.2 Sputtering pattern of HFM thermopile.	54
Figure 3.1.3 Output from the conduction calibration of DS1 using the code QT.FOR to convert heat flux to temperature.	55
Figure 3.1.4 The Corcos correction comparing a rectangular sensor to a line sensor of equal area.	55
Figure 3.1.5 Heat Flux gage disturbance, comparison of two insert gage installations on pressure side, and insert vs. direct sputtered gage on suction side.....	56
Figure 3.2.1 Hot-wire probes.....	57
Figure 4.1.1 Baseline G0 upstream inlet flow traverse intensity (Tu).	66
Figure 4.1.2 Time series showing nature of inlet flow at different distances below test section top wall boundary layer.	66
Figure 4.2.1 Grid turbulence: Tu decay behind G2 and G4, $U = 120$ m/s.	67
Figure 4.2.2 Grid turbulence: Λ_x growth (integral length scale) behind G2 and G4.....	68
Figure 4.2.3 Comparison of Grid 2 and Grid 4 at $Tu = 5\%$ locations.....	69
Figure 4.2.4 Decay of energy spectrum behind Grid 2.	69
Figure 4.2.5 Comparison of grid turbulence to the isotropic spectrum fit, $Tu = 5\%$	70
Figure 4.2.6 The Wyngaard correction compared to correction of the present data by using the isotropic spectrum at higher frequencies.	71
Figure 4.2.7 Measured Mach number distribution on blade at different grid conditions with the KEP prediction.....	72
Figure 4.2.8 Measured blade P_{static} and fits to the data.	72
Figure 5.1.1 Heat Transfer Coefficient measurements with DS1 (suction side) and insert HFM sensors (pressure side), including KEP and BL2D code predictions.	89
Figure 5.1.2 Example of tunnel data and HTC calculation result for one tunnel run.....	90
Figure 5.1.3 BL2D predicted suction side (SS) heat transfer coefficient for G0 vs. G2 using measured G0 and G2 blade surface static pressures as input.....	91
Figure 5.1.4 BL2D predicted pressure side (PS) heat transfer coefficient for G0 vs. G2 using measured G0 and G2 blade surface static pressures as input.....	91
Figure 5.1.5 BL2D suction side (SS) strain ($a=dU/dx$) prediction for G0 and G2 based on measured blade surface pressure distributions.....	92
Figure 5.1.6 BL2D pressure side (PS) strain ($a=dU/dx$) prediction for G0 and G2 based on measured blade surface pressure distributions.....	92
Figure 5.1.7 Heat flux intensity (Tu_q) along pressure side (PS) for different grids.....	93

Figure 5.1.8 Heat flux integral time scale (T_q) along PS for different grids.	93
Figure 5.2.1 DS1 turbulence intensity (Tu), grid vs. wire position.....	94
Figure 5.2.2 DS1 integral length scale (Λ_x), grid vs. wire position.	94
Figure 5.2.3 Fluctuating velocity (u') upstream and into passage (1 mm wire position above PS), Grid 4 vs. Grid 2.....	95
Figure 5.2.4 Turbulence intensity (Tu) upstream and into passage (1 mm wire position above PS), Grid 4 vs. Grid 2.	95
Figure 5.2.5 Integral time scale (T_x) upstream and into passage (1 mm wire position above PS), Grid 4 vs. Grid 2.....	96
Figure 5.2.6 Integral length scale (Λ_x) upstream and into passage (1 mm wire position above PS), Grid 4 vs. Grid 2.....	96
Figure 5.2.7 PS u' grid comparison at different y_{wire}	97
Figure 5.2.8 PS Tu grid comparison at different y_{wire}	97
Figure 5.2.9 PS Λ_x grid comparison at different y_{wire}	98
Figure 6.1.1 Hot-wire Energy spectra over DS1 at $y = 0.2$ mm.....	113
Figure 6.1.2 Hot-wire Energy spectra over DS1 at $y = 0.4$ mm.....	114
Figure 6.1.4 Hot-wire Energy spectra at DS1 for G2u and G2b vs. y_{wire}	116
Figure 6.1.5 Hot-wire energy spectra for DS1 for G4u and G4b vs. y_{wire}	117
Figure 6.1.6 Hot-wire energy spectra for PS1 at 1.0 mm comparing grids.....	118
Figure 6.1.7 Hot-wire energy spectra for PS2 at 1.0 mm comparing grids.....	119
Figure 6.1.8 Hot-wire energy spectra for PS3 at 1.0 mm comparing grids.....	120
Figure 6.1.9 Hot-wire spectra for PS1, G2 and G4 comparison at different y_{wire}	121
Figure 6.1.10 Hot-wire spectra for PS2, G2 and G4 comparison at different y_{wire}	122
Figure 6.1.11 Hot-wire spectra for PS3, G2 and G4 comparison at different y_{wire}	123
Figure 6.2.1 Heat flux spectrum at DS1.	124
Figure 6.2.2 DS1 heat flux comparing “up” and “back” cases.	125
Figure 6.2.4 Heat flux spectra at PS1 comparing grids.	127
Figure 6.2.5 Heat flux spectra at PS2 comparing grids.	127
Figure 6.2.6 Heat flux spectra at PS3 comparing grids.	128
Figure 6.2.7 Pressure side heat flux spectra, G0 comparison.	128
Figure 6.2.8 Pressure side heat flux spectra, G2 comparison.	129
Figure 6.2.9 Pressure side heat flux spectra, G4 comparison.	129
Figure 6.3.1 DS1 Coherence, G4u and G4b.	130
Figure 6.3.2 DS1 Coherence, G2u and G2b.	131
Figure 6.3.3 DS1 Coherence, all data.	132
Figure 6.3.4 PS1 Coherence, G2 and G4.	133
Figure 6.3.5 PS2 Coherence, G2 and G4.	134
Figure 6.3.6 Coherence at PS1, 0.2 mm and 0.4 mm comparing grids.....	135
Figure 6.3.7 Coherence at PS2, 0.2 mm and 0.4 mm comparing grids.....	136
Figure 6.3.8 Coherence at 1.0 mm, PS1 and PS2, comparing grids.	137
Figure 6.3.9 PS3 Coherence comparing grids.	138
Figure 6.3.10 G2 Coherence along pressure side, 0.2 mm vs. 1.0 mm.	139
Figure 6.4.1 DS1 phase, G2u and G2b.	140
Figure 6.4.2 DS1 phase, G4u and G4b.	141
Figure 6.4.3 PS1 phase, G2 and G4.....	142
Figure 6.4.4 PS2 phase, G2 and G4.....	143
Figure 6.4.5 PS3 phase, G2 and G4.....	144
Figure 6.5.1 DS1 cross-correlation vs. y_{wire} for G0, G2u, and G4u.	145
Figure 6.5.2 PS1 HF/PHW cross-correlation vs. y_{wire} for G0, G2, and G4.....	146
Figure 6.5.3 PS2 HF/PHW cross-correlation vs. y_{wire} for G0, G2, and G4.....	147
Figure 6.5.4 PS3 HF/PHW cross-correlation vs. y_{wire} for G0, G2, and G4.....	148

Figure 6.6.1 Mean and fluctuating velocity across WPAFB wall-jet boundary layer.....	149
Figure 6.6.2 Coherence vs. y^+ in wall-jet boundary layer.	150
Figure 6.6.3 Phase vs. y^+ in wall-jet boundary layer.....	150
Figure 6.6.4 Cross-correlation time shift vs. y^+ in wall-jet boundary layer.....	151
Figure 6.6.5 Time lag vs. y in wall-jet boundary layer	151
Figure 7.1 Dullenkopf and Mayle's correlation based on strain and length scale effective turbulence intensity.	174
Figure 7.2 Heat transfer coefficient vs. u'	174
Figure 7.3 Van Fossen's heat transfer augmentation for FST above a low-FST baseline for laminar region downstream of the stagnation point.	175
Figure 7.4 Moss and Oldfield's turbulent boundary layer heat transfer augmentation for FST above a low FST baseline against their X_{ir} parameter.	175
Figure 7.5 Ames' correlation of mean heat transfer increase and $TuLu^{-1/3}$	176
Figure 7.6 Maciejewski and Anderson's general turbulent heat transfer correlation.....	176
Figure 7.7 Comparison of PS3 heat flux time series, G0, G2, G4.	177
Figure 7.8 Heat transfer coefficient vs. q'	178
Figure 7.9 u' vs. q'	178

List of Tables

Table 2.1 HFM sensor locations relative to leading edge.....	14
Table 3.1 DS1 HFS experimental vs. manufacturer calibration.	34
Table 3.2 Example of passage hot-wire (PHW) calibration at $y = 0.2$ mm above PS1.	47
Table 5.1 Summary of No-PHW heat flux data.....	86
Table 5.2 Summary of heat flux data for With-PHW runs.	87
Table 5.3 Summary of hot-wire data, corresponding to Table 5.2.....	88

Nomenclature

a	Strain rate = dU_e/dx
c	Specific heat (J/kgK), blade chord (cm)
$E(f)$	Energy spectrum = power spectral density (m^2/s)
Fr	Frossling number, $Fr = Nu_d/\sqrt{Re_d}$
h, HTC	Heat Transfer Coefficient = $q''/(T_{aw}-T_s)$
k	Thermal conductivity (W/mK)
k_1	Wavenumber = $2\pi f/U$ (1/m)
L	Length scale or wire length (mm)
M	Mach number
Nu	Nusselt number, $Nu = hL/k$
Pr	Prandtl number = $\mu c/k$
Q, q'	Surface heat flux, and rms fluctuating component, q' (W/cm^2)
r	Recovery factor, $(T_{aw}-T_s)/(T_t-T_s) = (T_{aw}-T_s)/(U^2/2c_p)$
R	Resistance (Ω)
Re	Reynolds number based on blade chord = $\rho Uc/\mu$
S	Sensitivity of Heat Flux Microsensor, ($\mu V/(W/cm^2)$)
St	Stanton number, $St = h/\rho Uc = Nu/RePr$
T, t'	Temperature and rms fluctuating component ($^{\circ}C$)
T_m	Property reference temperature = $(T_{\infty}+T_w)/2$ for hot-wire calculations ($^{\circ}C$)
Tu	Turbulence intensity, u'/U , or $\sqrt{(u'^2+v'^2)}/U$ for present single wire measurements.
Tuq	Heat flux turbulence intensity, q'/Q
U, u'	Streamwise velocity, and rms fluctuating component (m/s)
v'	Velocity normal to surface rms fluctuating component (m/s)
y^+	Near-wall dimensionless distance $(yu_{max}/\nu) / (c/2)^2$

Greek symbols

δ_{995}	Boundary layer thickness (mm)
ε	Dissipation (m^2/s^3)
η	Kolmogorov microscale = $[\nu^3/\varepsilon]^{1/4}$
γ	Ratio of specific heats
μ	Viscosity (kg/ms)

ν	Kinematic viscosity (m^2/s)
ρ	Density (kg/m^3)
f	Frequency ($1/\text{s}$)
Λ	Integral length scale (mm)
T	Integral time scale (ms)
ΔT	$T_{\text{aw}} - T_s$ ($^{\circ}\text{C}$)

subscript

aw	Adiabatic wall
calc	Calculated from code
cor	Corrected value
d	Wire diameter, leading edge diameter
e	At the edge of the boundary layer
exp	Experimental measured value
iso	Related to isotropic turbulence
m	Measured value, or mean value
norm	Normalized, q' by ΔT
max	Maximum value in the boundary layer
op	At hot-wire operating condition
q	Of the heat transfer
s	Surface, or static conditions
t	Total (stagnation) conditions
u	Of the x velocity component
w	At the wall, or a property of the wire
x	In the flow direction
y	In direction normal to the surface
z	Spanwise direction

1. Introduction

1.1 Turbine blade heat transfer

Gas turbine engine design continues to improve, with ever higher demands on engine performance. The military's demand for higher thrust-to-weight ratios with higher efficiencies is driving fundamental redesign of engine components with development of new materials, structures, airfoils, cooling, seals, etc. Considering the turbine section, better performance requires increasing both thermal and aerodynamic efficiencies.

From a heat transfer perspective, the issues are finding higher temperature materials as well as minimizing heat transfer to the blades. Heat transfer can be reduced through more intelligent cooling schemes and better airfoil design. However, aero design has largely reached its limits based on steady-flow analyses. In order to design better cooling schemes and airfoils, a better understanding of the flow's unsteady interaction with the blade surface is required.

The present work falls under the domain of external heat transfer, focused on basic understanding of the unsteady mechanisms of heat transfer. We can perhaps control the flow itself through design so as to minimize or direct the heat transfer. With better understanding of how the energy from the flow is reaching the surface will come better strategies for controlling heat transfer to the turbine.

The nature of the flow within a turbine has been a matter of debate for years due to the great difficulty of actually measuring the flow within an operating engine. It is generally accepted that the flow passing through a turbine stage is 3-D due to the influences of rotation, acceleration, and curvature that cause dominant secondary flows. The flow is also highly unsteady due to the chopping of wakes and shocks coming off the upstream rotor on to the next stator row and *vice versa*. This is known to cause large fluctuations in velocity, length scale, transition location, angle of attack, and resulting fluctuations in heat transfer (e.g. Mayle, 1991).

The study of this complicated flow has generally been simplified by focusing on individual components of interest, e.g. transition inducers and indicators, wake and shock effects, free-stream turbulence effects, leading-edge heat transfer, boundary layer flow turbulent structure, computational modeling.

The particular facility in use will determine the focus and simplification possible in a given research effort. The simple low-speed flat plate has allowed careful control of variables and led to repeatable heat transfer results, but the results are not always applicable to real gas-turbines. Full rotating rig experiments allow near operating conditions, but are both costly and give results where concurrent phenomena are not easily separable. The cascade facility and instrumentation used in this work fall somewhere in the middle ground.

The focus of the present work is the unsteady time resolved interactions of free stream turbulence with surface heat transfer. Removing upstream blades and rotation eliminates shocks and wakes. The facility is, however, closer to a real engine than the flat plate typically used for this kind of study. Using a transonic, high-turning blade allows a more realistic look at turbulence effects, and the high-frequency heat flux instrumentation allows looking at the surface phenomena in new ways.

1.2 Literature Review

1.2.1 Heat Transfer and turbulence

Free stream turbulence (FST) is seen as the turbulence that is present above the boundary layer and from a source external to the boundary layer's own turbulence production. It is typically set apart from wake turbulence by defining it as what turbulence is present when the wake is not. It is also seen as the turbulence of larger scale exiting the combustor and entering the first row of nozzle guide vanes.

The study of the effects of turbulence on heat transfer has included flat-plate studies with sources of turbulence including grids of bars (e.g. Zhou and Wang, 1993, Keller and Wang, 1994) or air jets (Thole et al., 1991, Ames and Moffat, 1990), as well as that produced by a wall jet or round jet (Rivir et al., 1992, Kim et. al., 1992), cylinder stagnation point studies at NASA (Van Fossen and Ching, 1994) and Stanford (Ames and Moffat, 1990), low speed turbine cascades (Ames, 1994), transonic turbine cascades (Arts, 1992, Wittig, 1988a, b), and full rotating rigs at Oxford (Ashworth, 1989, Garside, 1994), at MIT (Guenette, 1989), and CALSPAN (Dunn, 1989).

In the early 1980s, Hancock and Bradshaw published their work on FST (with maximum turbulence intensity, $Tu_{max} = 6\%$) effects on heat transfer for a flat plate turbulent boundary layer giving a length scale, Tu correlation for heat transfer, and claiming no Reynolds number effect. Abu-Ghannam and Shaw (1980) established that while acceleration effects were significant, they were dominated by FST effects (this has since been well established, e.g. the work of T. Wang in Zhou and Wang, 1993, and Mayle's 1991 review paper). Blair (1982) looked at FST in the presence of pressure gradient effects on a flat plate, noting that FST moves up transition, and increases the transition length in the presence of acceleration. In 1983, Blair published data for flat plate FST ($Tu_{max} = 7\%$), reporting length scale growth and Tu decay correlations behind grids, as well as his low-Re correction to the Hancock and Bradshaw correlation. He also noted that the Reynold's analogy factor increased linearly with FST. Castro (1984) gathered more low-Re data and corrected Blair's work. The work of Oxford (Moss and Oldfield, 1992) reviews and collects the correlations from these works.

Ames and Moffat (1990) examined higher FST effects (also Maciejewski and Moffat, 1992, Thole et. al., 1991, Rivir et. al., 1992) on flat plate turbulent boundary layer heat transfer. These data sets include hot-wire measurements in the boundary layer, but with no time-resolved heat flux. Ames (1994) extended this flat plate work with data from a low speed turbine, giving data similar in nature to that presented here, except that he was able to probe the relatively large boundary layer, but he does not have time-resolved heat flux.

1.2.2 Time-resolved heat transfer

Presently, there is limited time-resolved heat transfer data on turbine blades. Direct heat transfer measurements have been made at MIT in a rotating rig (Guennette, 1989), here at VPI with Heat Flux Microsensors on 2-D turbine blades (Johnson, 1995) and thin film gages have been used at CALSPAN (Dunn, 1989) and Oxford (Ashworth, 1989) in rotating rigs, and also at VKI in a transonic cascade (Arts, 1992).

Throughout the 80's, Dunn et al. (1986, 1989) at CALSPAN published time-resolved heat-transfer data on a full rotating stage short duration facility. Guenette et al. (1989) at MIT also published rotating stage data. In the late 80's, Ashworth et. al. (1989) at Oxford published data from Oxford's Light Isentropic Piston Tunnel with data similar to MIT's, but focusing on shocks. They identified five mechanisms for heat transfer fluctuations: Unsteady turbulent spot production (including the FST effect--see Mayle 1991 review), NGV wake tripping of the boundary layer, NGV shock causing boundary layer separation and turbulent strip caused by separation bubble collapse, shock compressive heating, and shock induced pressure change flattening of the boundary layer increasing the temperature gradient. In these data sets, all engine effects (shocks, wakes, background FST, rotation, secondary flows, etc.) are included in the data such that effects of individual components cannot be easily separated, and no time-resolved velocity information is available to correlate flow and surface phenomena. More recently, Garside et al. (1994) at Oxford published data from this facility with upstream wakes removed allowing comparison to cascade data.

Of the work done with time-resolved heat flux, very few measurements include simultaneous velocity information. The work at Oxford is one notable exception (Moss and Oldfield, 1992, 1996). Moss and Oldfield used a single wire probe traversed above thin-film gages on a flat plate in a short duration flow to deduce heat flux (q) and velocity (u) correlations, as well as spatial correlations between heat flux gages. They conclude that eddies in the boundary layer mimicked those in the free-stream, convecting at the free-stream velocity rather than at the characteristic boundary layer velocity $\approx 0.8U_\infty$ (turbulent spot propagation velocity of a transitional boundary layer, Ashworth et al., 1989), and that free-stream eddies reach into the boundary layer rather than enhancing existing boundary layer turbulence. Similar work by this author (Holmberg

and Pestian, 1996, attached in Appendix A-1) was conducted in a wall-jet facility with time-resolved u' and v' velocity components plus fluctuating temperature, t' , along with surface q' measured with an HFM. The heat flux was seen to be controlled by the u' fluctuating velocity field, and primarily by large free stream eddies reaching deep into the boundary layer. This agrees with the conclusions of Moss and Oldfield (1996).

1.2.3 Heat transfer correlations

Several correlations have been developed that account for free-stream turbulence (FST) and Reynolds number (Re) effects for relating heat transfer to a baseline turbulent boundary layer flow. Ames and Moffat developed their TLR ($T = Tu$, $L = Lu$, a dissipation based length scale, $R = Re$) correlation based on a theoretical derivation, giving the Tu , Lu , Re correlation for heat transfer for a turbulent boundary layer in the presence of high FST. Thole (1991) gives data in support of TLR, but uses an integral length scale (Λ_x) rather than Ames' Lu . Other correlations include that of Moss and Oldfield (1992) at Oxford who present one similar to that originally proposed by Hancock and Bradshaw and modified by Blair for flat-plate heat transfer. These two correlations indicate heat transfer increasing with turbulence intensity (Tu) and with decreasing length scale, but with no minimum length scale for optimum heat transfer.

For the laminar region of the turbine blade downstream of the stagnation point, several studies are helpful. Ames (1994) presents low speed turbine data with boundary layer and heat flux measurements along the laminar pressure side of the blade. He found that the data supported using the TLR parameter in this laminar region. He discusses the influence of length scale, but much is left open for future work and verification. Van Fossen and Ching (1994) made measurements on a cylinder leading edge and Van Fossen and Simoneau (1994) in the stagnation region of elliptical models with grid generated turbulence. They give a correlation for stagnation heat transfer with Frossling number given as a function of a parameter that includes Tu , Re_d , and Λ_x . They claim that Ames' correlation (TLR) was unsatisfactory in predicting mean heat transfer for their data. They note the sensitivity of various correlations to particular data sets. Dullenkopf and Mayle (1994) present a correlation of cylinder and airfoil data that describes a linear relation between laminar heat transfer and an effective turbulence parameter. Their analysis presents an optimum length scale for exciting a laminar boundary layer based on cylinder stagnation point work, and they state that their correlation should be valid in other regions of constant strain such as exist on the pressure side of many airfoils.

In contrast to these correlations built on normalized variables, Maciejewski (1995) gives reason to dismiss Re and St based correlations entirely for high FST. Maciejewski and Anderson (1996) give surface heat flux beneath a turbulent boundary layer as a function of the fluctuating velocity component (u'_{max}), fluid properties, and the adiabatic to surface wall temperature

difference. There is hope that such a formulation will help bring together the varying geometry-specific correlations.

The above correlations, as they apply to the present data, will be reviewed in more detail in chapter 7.

1.3 Fundamental Issues

Based on this body of work, the effects of FST on heat transfer must be discussed in conjunction with several factors. First, the *state of the boundary layer* significantly changes the unsteady relationships between the flow field structures and surface heat transfer. Dullenkopf and Mayle (1994a) state that "heat transfer from FST is solely an unsteady effect within a completely, albeit highly disturbed, laminar boundary layer." Nonetheless, increases in mean heat transfer due to FST are often greater for laminar boundary layers than for turbulent boundary layers (Dullenkopf, 1994a, Ames, 1996). Dullenkopf notes that it is not uncommon to see heat transfer increases of 60%. Mayle and Schulz (1996) note that free-stream fluctuations produce proportional fluctuations in the boundary layer. Work by Zhou and Wang (1993) gives detailed boundary layer u' , v' , t' measurements through transition. With FST they note a steadily increasing u' fluctuation in a laminar boundary layer rising to $u'/U_e = 18\%$ prior to the start of transition. This high level of fluctuating u velocity continues through the first half of transition before dropping to the peak level of a turbulent boundary layer, which is a few percent lower. The v' fluctuating velocity is very low prior to transition, v'/U_e near 2%. This low value relative to that seen in transition and in a turbulent boundary layer reflects the laminar state where turbulent eddies are not the mechanism for transferring momentum or heat. Interestingly, even low levels of FST seem to be enough to overwhelm the normal low-FST turbulent boundary layer bursting process so that the near wall v' peak in a low-FST boundary layer is completely absent when FST is present (Zhou and Wang, 1993). This supposition is supported by the references above (e.g. Moss and Oldfield, 1992) where the large eddies reach deep into the boundary layer and control heat transfer.

Secondly, a study of FST effects on heat transfer must include the effects of *acceleration*. Whereas FST is known to destabilize the boundary layer leading to earlier transition, acceleration has the opposite effect of stabilizing the boundary layer, and if strong enough can lead to re-laminarization (Mayle, 1991). Mayle gives the value of the acceleration parameter $K = (v/U_e^2) * (dU_e/dx) = 3 \text{ E-6}$ above which a boundary layer cannot transist and a value, $K = -0.513 \text{ E-6}$, below which a laminar boundary layer is likely to separate. Zhou and Wang's study of a transitional boundary layer included results with acceleration up to $K = 1 \text{ E-6}$. They showed very little effect on the actual distributions of fluctuating parameters throughout the boundary layer and transition, but

noted that the transition start location was moved back and transition length was increased. Both Mayle (1991) and the more recent work of Zhou and Wang (1993) show that acceleration also causes thermal boundary layer transition to lag momentum boundary layer transition so that heat transfer data does not directly imply momentum boundary layer transition.

Thirdly, a study of FST, especially on a turbine blade, must be discussed in terms of *curvature*. The present data shows significant differences in the unsteady velocity/ heat flux relationships on the suction side (SS) vs. the pressure side (PS). Kim and Simon and Russ (1992) and Kestoras and Simon (1994) present their work and give a good review of that of others showing that Görtler vortices can form on a concave surface increasing heat transfer. At high FST these are not seen, but the forces that produce them are still active. Kestoras and Simon note that while convex curvature attenuates turbulent eddies, concave curvature amplifies large-scale motions, the most important source of the Reynolds normal and shear stresses. Concave curvature causes a structural change to the boundary layer, first by driving higher momentum (larger) eddies to the surface, and secondly through the growth of these eddies, a process completed after about 20 boundary layer thicknesses of the start of curvature. They also show heat transfer rising significantly above flat-plate values after the initial region of curvature, with a strong increase in v' fluctuations. Boundary layer codes often under-predict pressure side heat transfer (Dring, 1988). The present study examines the unsteady effects on the pressure side of this turbine blade.

Fourthly, *length scale* effects must be considered. One can argue that very large eddies will only appear as mean flow unsteadiness to a boundary layer, whereas small eddies have no energy to disturb, leading to the conclusion that there must be some optimum size of turbulence for disturbing a laminar or turbulent boundary layer. This has been known theoretically for years in terms of laminar boundary sensitivity to frequency and the growth of Tollmien-Schlichting waves leading to transition. Hydrodynamic stability theory predicts that a laminar boundary layer will be most sensitive to frequencies corresponding to length scales of 7δ , where δ is the boundary layer thickness (Schetz, 1993, p.180). Dullenkopf and Mayle (1994b) review stagnation flow data showing optimum heat transfer for $4 < L/\delta < 12$, while their own theoretical development predicts an optimum length scale of roughly 25δ .

Van Fossen and Ching (1994) note that a large number of studies have been performed looking at flat plate and cylinder FST length scale effects producing a large number of facility dependent correlations. Oxford (Moss, 1992) notes the strong effect of the low-wavenumber end of the velocity spectrum on determining heat transfer, i.e. the anisotropy characteristic of different facilities. Mayle (1991) notes the dearth of length scale information and recommends any

experiments that would add data that looks at transition with appropriate FST, length scale, and acceleration.

It is the writer's opinion as a result of this present work and a review of the literature that the concept of length scale is at best of limited use, and at worst misleading, as are arguments over which length scale is "best" for correlations. Length scale is a weak concept in that it takes a complicated 3-dimensional turbulent flow and reduces it to a single number (or two if the similarly weak concept of intensity is included). If we use an integral scale, we lump together all the facility dependent anisotropy. The dissipation scale seeks to avoid the anisotropy, but is typically calculated based on measurements that include it. Finally, the energy scale of Ames (1990) is based on dissipation calculated from the high frequency end of the energy spectrum, and thus avoids low frequency anisotropy, however the low frequency anisotropy has been shown to control heat transfer. This study seeks to gain a better understanding of these issues by looking at the non-integrated spectra of heat flux and velocity.

1.4 This work

1.4.1 Another perspective

In the work reviewed above, an underlying assumption is often made that the complex turbulent flow-field and its later interactions with a blade surface can be characterized by a few simple parameters. These scales are then correlated to mean heat transfer measurements, often with facility dependent results.

The present work focuses on the analysis of the whole spectrum of data and the picture it communicates of how the energy of the free-stream is interacting with the surface. Rather than integrating the spectrum into a measure of intensity and scale and relating this to measured mean heat transfer in limited regions of the blade surface, this work attempts to understand the flow developing along the blade surface. Rather than trying to draw more information out of weak integral measures, it seeks to determine the value of frequency domain analysis, and specifically of coherence. Not being limited to mean heat transfer measurement, it seeks the value of the fluctuating heat transfer in relation to the free-stream fluctuations above.

1.4.2 Motivation

The main goal of this work is to better understand how a turbulent fluid stream interacts with the boundary layer on a turbine blade, transferring energy from the hot turbulent flow to the surface. This is accomplished through a frequency domain examination of both heat flux and hot-wire signals, with data taken using new instrumentation in a linear turbine blade cascade and grids

upstream to give turbulence with constant inlet turbulence intensity but with varied integral length scale. Specific goals are to:

- Obtain mean and time-resolved simultaneous heat flux and velocity data at several points on a modern blade profile to allow comparison of mean data with code predictions and available correlations.
- Examine this data in both time and frequency domains to give a new perspective on the issue of turbine blade heat transfer and an understanding of the value of a frequency domain (energy spectra, coherence and phase) analysis.
- Provide some data with turbulence spectra information in a high speed turbine flow. Help clarify the uses and import of the fluctuating component of heat flux.
- Help clarify other important issues here: the measurement and value of length scales, pressure side heat transfer, and instrumentation issues (e.g. flow disturbance, spatial averaging).

1.4.3 Points of contrast

1.4.3.1 Heat transfer measurement

Most published heat transfer data is mean heat transfer calculated based on a variety of measurement techniques (Diller, 1993). Time-resolved measurements have been limited. The present measurements are unique in having time-resolved direct heat flux measurements in a high-speed, steady flow facility with simultaneous velocity information. "Direct" heat transfer means that the value of heat transfer is not converted numerically based on changing surface temperature or an internal conduction model of the blade. Instead, the Heat Flux Microsensor used here gives voltage as a linear function of heat flux with frequency response on the order of 100 kHz. A complete review of these issues is given in chapter 3.

1.4.3.2 Inlet turbulence

Others have noted the influence of low frequency inlet turbulence anisotropy on heat transfer (Moss and Oldfield, 1996), the facility dependence of this anisotropy (Van Fossen and Ching, 1994), and the need to better characterize the actual anisotropy in an engine in order to reproduce it in test facilities (Ames, 1994). The very different scales coming from the combustor versus that in blade wakes are known to react differently with the blade surface (Mayle, 1991). Very high values of measured actual engine intensities have been used to justify high intensity wall-jet and mock combustor experiments, and to create doubt as to the usefulness of lower intensity grid generated turbulence.

The argument for reproducing real-engine-like turbulence is valid. The present work does not pretend to reproduce this, but instead looks for the effect of turbulence of different scales on

the time-resolved interactions of heat flux and velocity. The inferences made as to the actual mechanisms at work should be applicable to real-engine turbulence.

The argument over low grid intensity is weak. The actual level in an engine turbine blade passage between wakes may not be as high as thought. Camp (1995) has shown that $Tu\%$ in a compressor passage is not that high, if unsteadiness of wakes is taken out, with typical values in the 5% range. Walraevens (1995) gives HW and LDV measurements in a turbine, with ensemble averaged rotor data showing Tu in the passages in between wakes of 2% to 8%, with up to 15% in wakes. The highest levels are seen in the passage vortices, and the maximum where these interact with tip flows near the casing wall (see also Moore and Moore, 1994).

Therefore, the high Tu levels often quoted for the turbine passage are primarily due to wake unsteadiness and secondary flows. Wake unsteadiness, however, should not be regarded as turbulence at all. It is more helpful to view the turbulence field inside the wake as separate and different from the turbulence field of between-wake flow with wake turbulence being of higher intensity and shorter length scale. An inlet turbulence intensity of 5% is realistic for the between wake flow. By varying the length scale of this flow, we can gain some measure of the different flow-surface interactions of a smaller length scale wake-like flow as compared to a larger length scale between-wake flow. In addition, removing the effects of wakes and shocks and secondary flows limits the possible sources of measured fluctuations in the energy spectra.

1.4.4 Overview

The purpose of this section is to give an overview of the tests performed and the results to be presented. Preliminary work included inlet velocity field measurements, code preparation, and probe development. Final results include mean heat transfer on the blade under the different flow fields, with transition information and comparisons to theory and codes, and then frequency domain results with interpretation and a discussion of the value of frequency domain analysis.

Three flow conditions were used. A baseline low turbulence no-grid flow (G0), a small mesh screen (G2), and a large mesh screen (G4) where "G" stands for "grid". G2 produced an integral length scale of $\Lambda_x = 0.95$ mm at 2.9 cm downstream of the grid plane where $Tu = 5.0\%$. G4 had $\Lambda_x = 2.7$ mm at 12.2 cm downstream where $Tu = 5.1\%$. The grid was placed so that the inlet plane of the blade row corresponded to these points.

Four heat flux sensor locations were used: one on the suction side and three along the pressure side. Flow measurements were made with custom miniature hot-wire single-wire probes. These passage hot-wire probes (PHW) were placed above each heat flux gage to allow for surface/ flow correlations. Hot-wire data were taken at three y (normal to surface) locations above each heat flux sensor: 0.2 mm, 0.4 mm, and 1.0 mm. The three grid cases (G0, G2, G4) were run sequentially with the wire located at each wire position and the wire position held constant while

grids were exchanged. For the suction side, additional data were taken for two extra grid positions for a total of five grid conditions.

Tests were run at design Mach numbers, with total temperatures near 70°C with typical $T_{aw} - T_s$ flow to wall temperature differences of 34°C for a T_{wall} to T_{gas} temperature ratio of 0.90. Inlet pressure was 2.3 bar with exit pressure equal to atmospheric. The cascade consists of 11 blades and a 5.1 cm (2.0 in.) span with periodicity and two-dimensionality over the mid-span demonstrated with surface flow visualization.

The heat flux measurements were made with a combination temperature/ heat-flux sensor called the Heat Flux Microsensor (HFM). This sensor was sputtered on the end of a cylinder that was inserted into the blade for the pressure side measurements. Suction side measurements were made with an HFM directly deposited on the blade surface.

The blow-down wind tunnel facility, instrumentation, cascade and blade design, grid descriptions, and testing procedures are presented in chapter 2, followed by more details on the Heat Flux Microsensor (HFM) and hot-wire (HW) probes in chapter 3.

A different upstream hot-wire (UHW) was used for measurements of the inlet velocity field. These measurements were made upstream of the cascade inlet but downstream of the grids. The UHW results are presented in chapter 4 documenting the turbulence field downstream of the specially fabricated slanted grids. The grids were mounted to frames that allow the grids to be shifted in the streamwise direction, and also set the grids at the same angle as the inlet plane of the blades (lying 58° from vertical).

Mean heat transfer data is presented in Chapter 5 as well as integral scales of the fluctuating velocity and heat flux (u' , Tu , T_x , and Λ_x). Code results and blade surface pressure measurements are also presented in Ch. 5 along with boundary layer shadowgraph results.

The frequency domain results including velocity and heat flux spectra, coherence, phase and time correlations are presented in chapter 6 along with some discussion. An interpretation of the mechanisms at work in the flow is presented in Chapter 7. In addition, data is compared to existing correlations and the practical significance of a frequency domain analysis is discussed.

2. Experimental Design

2.1 Overview

The Virginia Tech Cascade Wind Tunnel is a long duration blow-down type wind tunnel. The wind tunnel allows heating of the inlet air via a regenerator type heat transfer arrangement, allowing real engine similarity of gas to wall temperature ratios near 1.4. The present cascade uses small chord blades that have engine similar Re and a modern engine profile with high turning. Ongoing work in this facility is focused on understanding the unsteady interactions of passing shocks (injected from external to the test section) and turbulence on blade heat transfer and pressure. The facility allows variation of temperature ratios, Re , shock strength, run duration, and measurement tools. Direct surface heat transfer measurements are supplemented by Kulite surface pressure measurements, low-speed static taps, and optical measurements.

The present work takes advantage of the engine similarity to allow measurement of the effects of turbulence on the unsteady blade heat transfer. Short runs were used to acquire the high frequency heat flux and simultaneous flow data, while long runs were used to measure heat transfer coefficients. The gas to wall temperature ratio was kept at a lower value for this work due to hot-wire limitations, however this should have a relatively minor effect on the flow/ surface interactions compared to proper matching of Re and blade shape.

This chapter gives more detail on the facility and test section as used for the present work. An overview of turbulence is included here with a discussion of the auto-correlation function used to find integral length scales, and a discussion of isoturbulence. The grids used in this study are discussed along with theory for the development of turbulence behind a normal grid. A summary of test conditions and detailed test procedural information is given in section 2.4.

2.2 Facility

2.2.1 Wind Tunnel

2.2.1.1 System overview

The Virginia Tech Cascade Wind Tunnel is a blow-down to atmospheric facility (Fig. 2.1.1). Air from a compressor is dried and sent to outdoor tanks that were pumped up to an initial pressure of 830 kPa (120 psig) for these tests.

Run times of 40 seconds are possible at this tank pressure with the present test section, which has a mass flow of 2.1 kg/s. Heated flow is made possible using a thermal regenerator type bank of copper tubes upstream of the test section. Two valves upstream allow for on/off, and control of air flow. Exhaust is vented to the outdoors through a muffler.

2.2.1.2 Tunnel control and heating

Establishing rapid control of tunnel pressure is necessary for accurate measurements in the early part of the tunnel run when gas to wall temperature ratios are greatest. Tunnel control is effected via a feedback control circuit. A data-acquisition card in a PC computer reads supply tank pressure, flow total temperature, and total pressure upstream of the test section. Flow temperature is monitored just downstream of the copper tubing using a thermocouple total temperature probe with its bead near the center of the pipe. Flow total pressure is measured by a dedicated pressure sensor connected to a pitot tap upstream of the test section. Another pressure sensor monitors the supply tank pressure. These signals are input to a C-language code used to control the valve open angle throughout the tunnel run. The code works through feed-forward and feed-back control.

The code reads temperatures and pressures and then based on a thermodynamic model of the system decides what, ideally, the open angle of the valve should be in order to maintain constant test section total pressure throughout the run. Feedback PID control on tunnel P_{tot} is used to correct this theoretical valve angle due to the many assumptions in the model. The combination of feedback control on top of the theoretical model provides acceptable control, with stable operation at design pressure typically established within 5 seconds.

The details of the heating loop are shown in Fig. 2.1.1. Between runs the downstream flapper valve is rotated to close off the test section, and the upstream butterfly valve is opened to allow flow to circulate through the heater below and copper tubing above. A fan circulates air transferring thermal energy from the 36 kW electric heater to the copper tubing. The tubing consists of two 1 m bundles of 350 tubes, each bundle with a mass of 136 kg. For the short runs used to collect data in this work, only a few minutes of heating were required between tunnel runs to bring tube temperature back up. Thirty second runs to measure heat transfer coefficients required approximately 10 minutes of heating between runs.

2.2.2 Supporting Hardware

2.2.2.1 Data Acquisition

High-speed data were collected using LeCroy model 8610 four channel modules with 12 bit digitization and capable of acquiring 1 Megabyte of data each at 1 MHz. Data collection can be triggered manually, externally, or from a signal pulse. Signals from the amplifiers are carried via co-axial cables, with captured data sent from the LeCroy via IEEE-488 cables to a PC for storage. On board this PC is also a National Instruments AT-MIO-16 software configurable 12-bit DAQ card that allows 8 channels of low-speed data acquisition via a LabVIEW interface.

All of the high-speed data was collected on the LeCroy units. Some low-speed data were collected in LabVIEW if more channels were required. A trigger out from the LeCroy was used to synchronize timing between the different data acquisition units.

2.2.2.2 Instrumentation: Anemometer, HFM amplifiers, filters

Hot-wire probes were controlled using an IFA-100 2 channel anemometer (further discussed in Ch. 3). Each channel has a signal conditioner allowing low-pass filtering up to a cut-off frequency of 200kHz. These filters were used to filter the hot-wire signal as well as the heat flux signal for high-speed tests. The filters were set with a cut-off frequency of 100kHz, allowing significant attenuation of the signal below the Nyquist frequency of 250kHz (one half the sampling frequency). The frequency response of the sensors themselves was less than 100kHz due to spatial resolution limitations. Low frequency signals (50Hz used for mean heat transfer measurements and T_t , P_t) were not filtered as their spectra were not an issue.

Vatell manufactured amplifiers were used for the signals from the Vatell HFM sensors, one amplifier for each sensor. The amplifier drives the resistance temperature sensor, and amplifies both the heat flux and temperature signals at gains set at 500X for temperature and 1000X for heat flux. Signals out from these amplifiers were routed via bnc cables through the IFA-100 filter (high-speed heat flux) to the data acquisition units.

2.2.2.3 Traverse and pressure instrumentation

The traversing mechanism was run in tandem with the multiple pressure data acquisition system (Pressure Systems Inc. model PSI 780B 32 channel unit).

The traverse allows linear motion with a stepper motor controlled via a PC. The PC runs BASIC code that controls both the traverse movement and pressure acquisition using the PSI system. The PC communicates with the traverse controller card via a serial port, while GPIB is used for the PSI system. The traverse was programmed to take discrete steps, as well as move continuously, with adjustable velocity. The traverse was used for grid turbulence field measurements allowing a traverse of the hot-wire probe vertically behind the grids to be completed in a single tunnel run. More traverse procedure and details are given in section 2.4.

The PSI system was used both to establish exit mach numbers via a row of downstream wall static pressure taps, as well as for measuring blade surface pressures to see the effects of the upstream grids on the mean flow over the blades (Ch. 4).

2.2.3 Test section and linear cascade design

2.2.3.1 Test section and cascade

The test section and cascade are shown in Figs. 2.1.2 and 2.1.3. The test section is 20.3 cm (8.00 in.) high by 5.08 cm (2.000 in.) in span. The exit flow is vented to atmosphere. The flow enters at $P_{\text{tot}} = 220$ kPa (32. psia) and $M = 0.36$, and is accelerated through the blade row, exiting at an isentropic Mach number of 1.25. The cascade consists of 11 blades mounted between Plexiglas endwalls resulting in 10 flow passages. The instrumented blade passage was the fifth from the bottom for these tests.

2.2.3.2 Design parameters

The turbine blades (profile shown in Fig. 2.1.4) have a span of 5.08 cm (2.000 in.) constant through the cascade, and an aero chord, $c = 4.5$ cm. As noted on Fig. 2.1.4, the passage throat = 11.46 mm (0.451 in.), with a throat aspect ratio = 4.43, and inlet blade-to-blade pitch = 38.1 mm (1.500 in.). The cascade lies at a 58° inlet angle. The exit angle is 39° for a total turning of 129° .

2.2.4 Instrumented blades

Several different instrumented blades were used to collect data. Heat flux data presented here were collected using 2 blades, one with 3 HFM insert sensors on the pressure side (PS), and one with an HFM directly sputtered on the suction side (SS) near the leading edge. The locations of these gages are shown in Fig. 2.1.4. The 3 PS locations are labeled PS1, PS2, and PS3. Table 2.1 gives the axial location (x_{le}) from the leading edge to the center of each sensor. In addition, a third blade was used with 4 insert gages on the SS. One of these insert locations is nearly the same as for sensor DS1 and data from this insert will be referred to in reference to discussion of insert gage disturbance.

Table 2.1 HFM sensor locations relative to leading edge

Location	PS1	PS2	PS3	DS1
sensor type	insert	insert	insert	directly sputtered HFM
x_{le} (cm)	-0.43	-1.47	-2.46	0.86

At each location, a 1.3 cm (1/2 in.) port in the endwall Plexiglass allowed the insertion of the passage hot-wire (PHW) probes. The probe itself (see Ch. 3 for description) was held by a pressure fitting that mounted into the port plug. This plug in turn could be rotated, as could the probe body itself, to allow adjusting the location of the hot-wire relative to the HFM surface both in the x (streamwise direction) and in y (normal to surface).

Two additional blades were instrumented with static pressure holes, along the pressure side and suction side respectively, allowing blade surface static pressure measurements to measure any flow disturbance created by the grids.

2.2.5 HFM Instrumenting method

2.2.5.1 Insert sensors

The HFM-6 sensors (Ch. 3 details) were inserted into the blade surface. The intention was to have the sensor surface cause as small a surface flow disturbance as possible. The HFM itself is sputtered on the surface of a ceramic cylinder and this is mounted in an aluminum cylinder with an outer diameter of 0.633 cm (0.249 in.), Fig. 2.1.5.

Holes were drilled into the surface of the blade at the locations noted above. The side of each sensor aluminum housing was coated with silicone sealant and the sensor inserted into the hole. A set screw was used to lock the sensor in place. The silicone was used to prevent leakage from around the sensor. Although silicone has a low thermal conductivity, the thermal distribution in the blades was judged to not be significantly disrupted based on good mechanical contact created by the set-screw between the aluminum sensor housing and the aluminum blade on at least one side. The sensor holes were typically a few thousandths of an inch larger in diameter than the HFM inserts.

2.2.5.2 Direct sputtered sensor

The sensor called DS1, or "direct-sputtered" at location 1 on the SS was deposited by Vatel Corp. engineers on to the surface of one of the aluminum turbine blades, Fig. 2.1.6. The hot-wire probe is also shown in place over the sensor. The surface was prepared by polishing and then anodization for electrical isolation. The blade was then put in the sputtering chamber mounted in a fixture that held the various sputtering masks tight against the curved surface.

The sputtered leads from the sensor were connected via silver paint traces to small countersunk holes in the surface of the blade near the edge of the blade, Fig. 2.1.6. The four holes (one for each lead wire) lead into a single hole drilled in from the side of the blade. Teflon coated 0.075 mm (3 mil) copper wires from outside the blade came in through these four small holes to the surface where the coiled end of each wire lay in the countersink of each hole in contact with the silver paint. Isolation in the countersink was created using polyurethane. Polyurethane was in turn painted over the silver paint leads and holes for protection from the flow.

External to the cascade, the Teflon coated copper leads, both for the DS1 sensor and for the insert sensors, were taken to the back pins of panel Lemo connectors which connected to 1 m shielded cables to the amplifiers. These Lemo connectors were mounted on a special fixture

attached to the cascade endwall and insulated to avoid temperature disturbances to the wires. At the amplifier the temperature and heat flux signals were amplified and taken out via bnc co-axial cables to the data acquisition units.

2.2.6 Turbulence Grids

The turbulence generating grids (shown in Fig. 2.1.2 photo) used in this work are made of standard round wire square-mesh screens mounted to box frames. The frames were made of stainless steel sheet metal folded to fit within the dimensions of the test section, and have a triangular shape. The triangle allows the screen to lie at the same angle as the blade row inlet so that each blade sees the same turbulence field, Fig. 2.1.3. Internal frames allow the grids to move in the streamwise direction within the test section upstream of the cascade as well as to support a screen at an angle. The box shape gives the frame the maximum strength, needed to carry the heavy loads in the tunnel. In addition, two airfoil shaped cross-supports are soldered across the upstream opening of the frame to keep the frame from buckling.

The frames were constructed of two 1.0 mm (0.040 in.) thick stainless steel triangular sections that were folded and joined by spot welding. Joining the two sides of the frame in this manner allowed tight control on the width of the completed box frame such that frames fit into the test section with a minimum amount of sidewall blockage. Tolerances were kept within a few thousandths of an inch so that the blockage of the frame in the test section was approximately 1.1 mm (0.045 in.) per side, or 2.2 mm (0.090 in.) out of a 50.8 mm (2.00 in.) test section width. Blockage on the top and bottom of the frame is estimated at close to 6.4 mm (0.25 in.) total. As a result, the frame itself blocks approximately 7% of the flow area of the test section.

Two screen mesh sizes were used in these tests. In total 5 different screens were tested, which resulted in the notation: G0 for Grid zero = no grid, G2 for Grid 2 = smaller mesh, 0.89 mm (0.035 in.) wire diameter at 6 wires per inch spacing, and G4 for Grid 4 = 3.05 mm (0.120 in.) diameter, at 19.0 mm (0.75 in.) spacing. G2 has an open area of 60% and G4 an open area of 70% including frame blockage.

The grid frames were mounted in the test section using a single bolt through the top of the frame into the test section top wall near the point of the triangle. In the final positions, G4 was bolted into the test section upstream of the cascade, followed by placing the cascade into the test section, and then closing the doors. G2 needed to be closer to the blade row and required placement inside the cascade Plexiglass endwalls. For G2 the grid frame was loosely placed upstream, the cascade was then set in place, and then the grid frame was slid into place between the Plexiglas endwalls where a preset bolt acted as a stop for the grid to keep it at the correct location with respect to the blade row inlet.

2.3 Turbulence

2.3.1 Definition

Hinze (1975) describes turbulence as follows, "Turbulent fluid motion is an irregular condition of flow in which the various quantities show a random variation with time and space coordinates, so that statistically distinct average values can be discerned." Tennekes and Lumley (1972) discuss its irregular, diffusive, three-dimensional, dissipative nature. Turbulent flow consists of all different scales of vorticity co-existing and interacting. These "eddies" are described by Townsend (1976) as, "flow patterns with spatially limited distributions of vorticity and comparatively simple forms." The work presented here will be a combination of looking at the details of a turbulent flow's interactions with a surface, and of statistical analysis of this flow. Following are some of the statistical tools which will be used.

2.3.2 Spectrum and integral parameters

2.3.2.1 Intensity

The flow over the turbine blade is instantaneously varying at all points with time. A hot-wire in the flow over a heat flux sensor sees only one dimension (time) at one point in space, and even this information is averaged over the space occupied by the finite length of the hot-wire. The heat flux sensor similarly sees phenomena at one point, except that it is averaging over a finite area. The output from these sensors is a time-varying voltage that can be described in the traditional way as a mean and a fluctuating component. The intensity is given as the fluctuating component over the mean:

$$Tu = \frac{\sqrt{u'^2}}{\bar{U}} = \frac{\text{rms}}{\text{mean}} \quad (2.1)$$

where for the present data u' is the fluctuating component of total velocity (see section 3.2.2.5). This data can also be viewed in the frequency domain as a spectrum of the energy containing eddies in the flow (or of the fluctuating energy in the heat flux). The fluctuating energy is the integral of this spectrum, and thus intensity can be viewed as the sum of this spectrum over the mean where

$$\overline{u'^2} = \int_0^{\infty} E(f) df \quad (2.2)$$
$$E(f) = \text{PSD} = \text{Power Spectral Density} = \frac{S_{xx}}{\Delta f}$$

where S_{xx} is the auto-power spectrum, and Δf is the frequency resolution equal to sampling frequency divided by the length of the processed data block (500 kHz / 1024 = 488.3 Hz). For the

present data, S_{xx} was calculated using Matlab software which uses the Welch method of power spectrum estimation. The computer codes used for these calculations are presented in Appendix B. The auto-spectrum (and cross-spectrum substituting y in) is defined as

$$S_{xx}(f) = \frac{1}{n^2} \mathbf{X}(f) \mathbf{X}^*(f), \quad \text{where } \mathbf{X}(f) = FFT\{x(t)\} \quad (2.3)$$

Integral length scale (Λ_x) is a measure of where the energy is in this spectrum and is generally based on the auto-correlation, R_{uu} , of the velocity signal.

2.3.2.2 Auto-correlation and scales

2.3.2.2.1 Definition

The auto-correlation function is a time-domain measure of correlation between points of a time series with its own past, present, and future values. For a known function $x(t)$ the auto-correlation is:

$$R_{xx}(\tau) = \int_{-\infty}^{\infty} x(t)x(t+\tau)dt \quad (2.4)$$

where τ is the separation in time between two points in the function $x(t)$. In terms of a discrete time series such as the velocity signal from a hot-wire, $u(t)$, the integral over infinity becomes a sum over the data series, and τ takes on the discrete value of the sample period (inverse of the sampling frequency). Thus:

$$R_{uu}(n) = \sum_{t=0}^{N\Delta t} u(t)u(t+n\Delta t)\Delta t$$

This calculation will produce a vector equal in length to $2N-1$ where the original time series is of length N . The time series is first offset so that the last point is multiplied by the first, $R_{xx}(-N)$, and then stepped through time until $n=0$ and then continuing until the first point is multiplied by the last, $R_{xx}(N)$. Several points can be made of R_{xx} (Stearns, 1990):

- 1) R_{xx} is an even function, symmetric about $R_{xx}(0)$
- 2) $|R_{xx}(n)| \leq R_{xx}(0)$; that is, the product is maximum when $x(t)$ is multiplied by itself without shifting. $R_{xx}(0)$ is also referred to as the auto-correlation at zero lag, and this value is often used to normalize the whole series such that $R_{xx}(n)$ is maximum at zero lag and equal to one.
- 3) For the case of a random non-periodic signal, such as that which is assumed for turbulence, the auto-correlation will decay to zero as $|n|$ increases.
- 4) $R_{xx}(n)$ carries no phase information about $x(t)$.
- 5) $R_{xx}(0)$ can also be viewed as the power in $x(t)$ equal to the sum of the squares of $x(t)$.

An alternative to calculating the auto-correlation directly from the time series according to Eq. 2.2 above is to calculate it based on the power spectrum. The auto-correlation is a cosine transform of the spectrum (Hinze, p132).

$$R_{xx}(t) = \frac{1}{U_{\infty}^2} \int_0^{\infty} E(f) \cos(2\pi f t) df \quad (2.5)$$

where $E(f)$ is defined in Eqn 2.2. The benefit of using this equation relative to calculating directly from the time series is that if the averaged power spectrum has already been calculated then it is computationally more efficient to calculate the auto-correlation using this, rather than re-processing the entire data block. This approach was used with the present data, and is discussed further in Ch. 3.

2.3.2.2.2 Application

The utility of R_{xx} for the study of turbulence can be seen in the rate at which $R_{xx}(n)$ decays to zero as n increases, see example in Fig. 2.2.1. A slower decay implies that correlation exists within the flow for greater time delays, and thus flow structures (e.g. turbulent eddies) are relatively larger. This helps describe time scales (and length scales) present in the flow. The most common parameter for quantifying this time scale is called the integral time scale, T_x , and is defined as the integral of R_{xx} , and is typically taken out to the first zero crossing, thus:

$$T_x = \sum_{n=0}^{n|R(n)=0} R_{xx}(n) \Delta t \quad (2.6)$$

where R_{xx} is normalized by $R_{xx}(0)$ such that $R_{xx}(n)$ is unitless. In addition, $x(t)$ must be a mean zero time series in order to avoid R_{xx} being dominated by DC level correlation. In practice, with $x(t)$ being a velocity signal, the mean velocity must be subtracted from the time series before calculating R_{uu} . Because R_{xx} is an even function, the integral is only taken from $n = 0$ using the truncated autocorrelation.

A length scale can be based on the integral time scale by multiplying by the mean velocity, and this is called the integral length scale.

$$\Lambda_x = \bar{U} T_x$$

The integral of $R_{uu}(n)$ is typically only taken out to the first zero crossing due to noise that may be present in the auto-correlation. This noise is an effect of dominant peaks in the frequency spectrum (characteristic of non-isotropic turbulence), and integrating to the first zero crossing is often not sufficient to give a time scale indicative of the size of turbulent eddies in the flow. This is because the auto-correlation is a measure of the largest eddies in the flow, so that low-frequency energy can strongly affect its integral. Lower frequency energy in the flow that originates from a source other than turbulent eddies (e.g. mean flow unsteadiness) can inflate the value of T_x and

produce a value that is not representative of the turbulence time scale. In order to minimize this, a decaying exponential function can be fit to the points of R_{uu} at small n , typically for values of $R > 0.2$, and this was the procedure followed for the present measurements. Some examples of this are shown in Fig. 2.2.2. The integral under this exponential will eliminate the low frequency noise producing a time scale representative of the turbulent energy.

$$T_x = \int_{t=0}^{N\Delta t} e^{-t/\tau} dt = \sum_{n=0}^N e^{-n\Delta t/\tau} \Delta t \quad (2.7)$$

The time correlation is affected by hot-wire frequency response. If energy exists at frequencies greater than the hot-wire can see, this will result in that energy being lost in the higher end of the frequency spectrum, and thus lost in the auto-correlation and will result in an inflated value of T_x . This in turn will produce estimates of Λ_x that are greater than actually present. Correction for this effect is discussed in chapter 3.

2.3.3 Isoturbulence

Isoturbulence has been a useful concept that has simplified turbulence analysis, as well as being representative of some turbulent flows to an acceptable degree. In the absence of outside forces, an already developed turbulent flow will tend toward isotropy. That is, it is the balanced posture turbulence will assume if left to its own decay. It is therefore representative of the flow downstream of a grid, or far enough downstream of a wall-jet, but not a valid representative for any turbulent field near the source of turbulence, or near a wall.

Isoturbulence is maintained by the energy cascade where larger eddies break up into smaller eddies and so on until the smallest eddies are viscously dissipated. This cascade remains similar even as the overall energy (Tu) decays. The formula most often used to fit the isoturbulent spectrum is known as Von Karman's interpolation formula (Ames and Moffat, 1994):

$$\frac{E(f)U}{u'^2 \Lambda_x} = \frac{4}{\left[1 + \left(\frac{8\pi f \Lambda_x}{3U}\right)^2\right]^{3/2}}$$

Alternatively,

$$E(f) = \frac{4UTu^2 \Lambda_x}{\left[1 + \left(\frac{8\pi f \Lambda_x}{3U}\right)^2\right]^{3/2}} \quad (2.8)$$

This formula accurately fits experimental data across the low frequency end of the spectrum and for higher frequencies where the turbulence is seen to decay according to a -5/3 power law. The second form gives the energy spectrum, $E(f)$, normalized by Tu and Λ_x . When plotted versus $f\Lambda_x/U$, this spectrum will remain unchanged even as the turbulence field decays.

In addition to the construct of the isoturbulence spectrum presented above is the more limited concept of local isotropy. In the words of Hinze (1975), "Certain theoretical considerations concerning the energy transfer through the eddy-size spectrum from the bigger to the smaller eddies lead to the conclusion that the fine structure of non-isotropic turbulent flows is almost isotropic (local isotropy)." In terms of the power spectrum, non-isotropy is primarily a large scale, low frequency phenomena. At higher frequencies, where the spectrum decays according to the $-5/3$ power law (the inertial sub-range), turbulence exists independently of the surrounding larger scale eddies.

The concept of local isotropy at higher frequencies has useful application with the present data. For measurements behind the grids, and especially close behind the smaller grid, the hot-wire is limited by spatial resolution and cannot resolve the smaller scales. In this case the assumption of local isotropy can be used to help correct for hot-wire length attenuation of the higher frequency end of the energy spectrum.

2.3.4 Grid turbulence

According to theory for a normal grid of round wire square-mesh screen (Roach, 1987), turbulence intensity and integral length scale (for square-mesh round wire) are given as

$$\begin{aligned} Tu &= 0.80 \left(\frac{x}{d} \right)^{-\frac{5}{7}} \\ \Lambda_x &= 0.20 d \left(\frac{x}{d} \right)^{\frac{1}{2}} \end{aligned} \tag{2.9}$$

There are many restrictions given by Roach for the application of the above equations. Among the more important are that the inlet flow be low turbulence, and that the test section be significantly large relative to the grid mesh dimension to avoid side-wall boundary layer distortion. Of the two grids used in these tests, Grid 2 (G2) has 12 mesh widths across the test section, which is marginal, while Grid 4 (G4) has only 2.6 mesh widths and therefore should not be expected to follow this theory. In addition, the above equations are limited to the "homogenous" region approximately beyond 10 mesh widths downstream of the screen. In the final tests, G2 is only 6.9 mesh widths downstream, and G4 only 6.4. Finally, these correlations are for grids normal to the flow, whereas in these tests the grids lie at 58° to the flow due to the test section arrangement.

Interestingly, the turbulence field behind a grid (as described by the above two equations) is not dependent on the porosity of the screen. This was born out in preliminary tests where G2 and another grid (G3) of similar wire diameter, but with different porosity, produced results showing little difference in Tu and Λ_x .

2.4 Test conditions and Procedures

Tests were run at design Mach numbers ($M_{in} = 0.36$, $M_{isent,exit} = 1.25$), with total temperatures near 70°C with typical $T_{aw} - T_s$ flow to wall temperature differences of 34°C for a T_{wall} to T_{gas} temperature ratio of 0.90. Inlet pressure was 2.3 bar with exit pressure equal to atmospheric (typically $P_{atm} = 94.3 \text{ kPa} = 13.7 \text{ psia}$). Three flow conditions were used: a baseline low turbulence ($Tu = 0.25\%$) no-grid flow (G0), a small mesh screen (G2), and a large mesh screen (G4). G2 produced an integral length scale of $\Lambda_x = 0.95 \text{ mm}$ at 2.9 cm downstream of the grid plane where $Tu = 5.0\%$. G4 had $\Lambda_x = 2.7 \text{ mm}$ at 12.2 cm downstream where $Tu = 5.1\%$. The grid was placed so that the inlet plane of the blade row corresponded to these points. For the suction side, additional data were taken for two extra grid positions where G2 and G4 were moved upstream so that inlet $Tu = 3.6\%$.

There were several different run procedures for the present data, variations of a standard procedure. Standard procedure included loading the compressor to set the upstream tanks to an initial pressure of 830 kPa (120 psi), and setting up the tunnel control program to set the control valve ready for tunnel start. For baseline (no grid) operation the tunnel control object pressure $P_{obj} = 19 \text{ (psig)}$ gave a Mach number at design. With grids in place P_{obj} needed to be raised to 20.5 due to a 10 kPa (1.5 psi) drop across the grids since P_{tot} is measured upstream of the grid location. Inlet turbulence surveys and heat transfer coefficient measurements required long tunnel runs while passage measurement runs were only long enough to get a short burst of data after stabilizing tunnel control.

2.4.1 Upstream turbulence

For grid upstream turbulence measurements, the traverse mechanism was mounted on top of the test section, with the UHW (see Fig. 3.2.1) probe held in a 0.64 cm (0.25 in.) steel tube that extended from the traverse down through an aluminum plug into the test section. The traverse controller card is linked via the serial port to the PC that is used to run the PSI system. Two programs were used for operating the traverse: Travstep.BAS allows setting the traverse to take steps and pause, Travmove.BAS gives one continuous movement with return. The traverse has an LVDT transducer connected to it that gives a voltage proportional to velocity or distance, depending on polarity of input 5V. The LVDT needs careful calibration and is sensitive to input voltage. The entire traverse and plug could be rotated 180° to allow moving the streamwise traverse location the width of the plug. This gave some flexibility in locating the hot-wire.

The grid frames were pushed upstream as far as possible (to the point where the upstream edge of the box entered the contraction section) so that turbulence measurements could be made downstream of the grids but upstream of blade potential flow effects. The UHW probe was traversed downward vertically behind the grids such that the distance of the hot-wire

behind the grid increased during the traverse due to the slant of the grid. The two UHW probe shapes gave added flexibility in locating the initial wire position relative to the grid with UHW2 having a 90° bend in the shaft (see Fig. 3.2.1). UHW2 allowed placing the wire close to the grid but away from the top wall boundary layer.

Individual wire voltages were used to calculate proper operating resistance (for OHR = 1.9). Cable resistance was measured with a voltmeter and entered into the IFA-100. The hot-wire was turned on and the frequency response at no-flow adjusted (using the anemometer square wave test signal viewed on an oscilloscope) to give the properly shaped response. The relationship of the no-flow frequency response to that with-flow was known based on testing with these probes (see Appendix C). The traverse program (Travmove.bas) was set-up ready for a start trigger. The tunnel was started and allowed to stabilize before starting the traverse motion. The hot-wire data was taken on the LeCroy, with a trigger out to the LabVIEW TUNDAQ.VI. Individual data samples were manually triggered at regular intervals (CATLST software can be set to take up to 4 MB of data in "sections" which are then converted using the "channel" switch option of CATTEXT) timed so that the traverse would reach the bottom of its traverse at the point of the last DAQ event. The LVDT signal was then used to find average hot-wire location over the time of the high-speed acquisitions (LeCroy trigger "high").

2.4.2 Heat Transfer Coefficients

For heat transfer coefficient measurement, the instrumented blades were set up with HFM amplifiers connected to the LeCroy and/ or LabVIEW depending on number of channels required. The LeCroy allows for easier timing of the signals with up to 12 channels with the present set-up. T_t and voltage out from each HFM temperature and heat flux sensor are required for HTC calculation. The tunnel was heated to 93 °C (200 °F) and the fan and heater turned off at the same time as unloading the compressor. The tunnel was run for approximately 40 seconds during which time the blades heated up to the flow temperature and heat flux decreased to zero. The method for calculating heat transfer coefficients is given in section 5.1.

2.4.3 Passage Measurements

The unsteady hot-wire HFM measurements required opening the test section between every run and extra care with adjusting the hot-wire close to the blade surface. Run time was typically less than 10 seconds where the tunnel P_t was allowed to peak and drop back to object pressure at which point the HFM and PHW data were triggered (0.5 sec of data at 500 kHz). All data were collected on the LeCroy units. Only PHW and HFS data were saved, while T_t , P_t , and $Trts$ (T_s) were recorded as mean values over the DAQ period and used for later data reduction.

The PHW probe was held in a specially machined pressure fitting that screwed into the port plug. For each gage position, the PHW was inserted into the port plug and then this plug carefully screwed into the endwall ports corresponding to each HFM. The probe was then extended out over the blade and the plug and probe position adjusted so that the wire was centered over the HFM center at the proper distance above the surface, y_{wire} . A finely graduated scale was used to gauge y_{wire} ; at the near wall (0.2 mm) wire position the probe was located with the prongs approximately one prong thickness above the heat flux sensor surface. The probe body and prong angles were customized for each HFM position to set the wire parallel to the surface and to minimize probe blockage.

Once the wire position was set, the grid and cascade were set in the tunnel, doors secured, hot-wire leads and HFMs connected and set for operation, and heating and cooling systems shut off and set for run. Between runs, different grids were alternated while the wire was left in position, although all instrumentation needed to be disconnected after each run in order to remove the cascade.

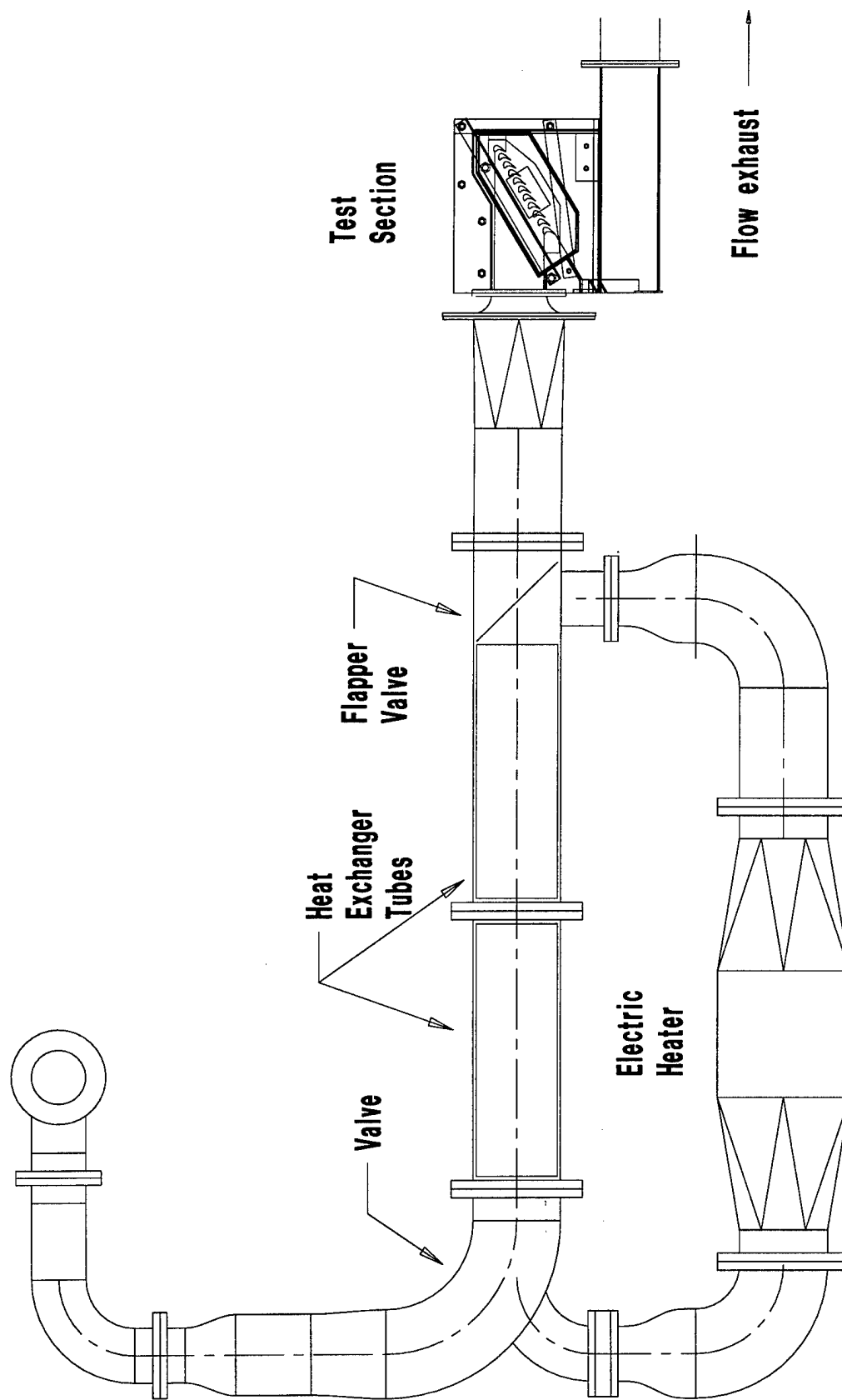


Figure 2.1.1 Virginia Tech transonic cascade wind tunnel facility

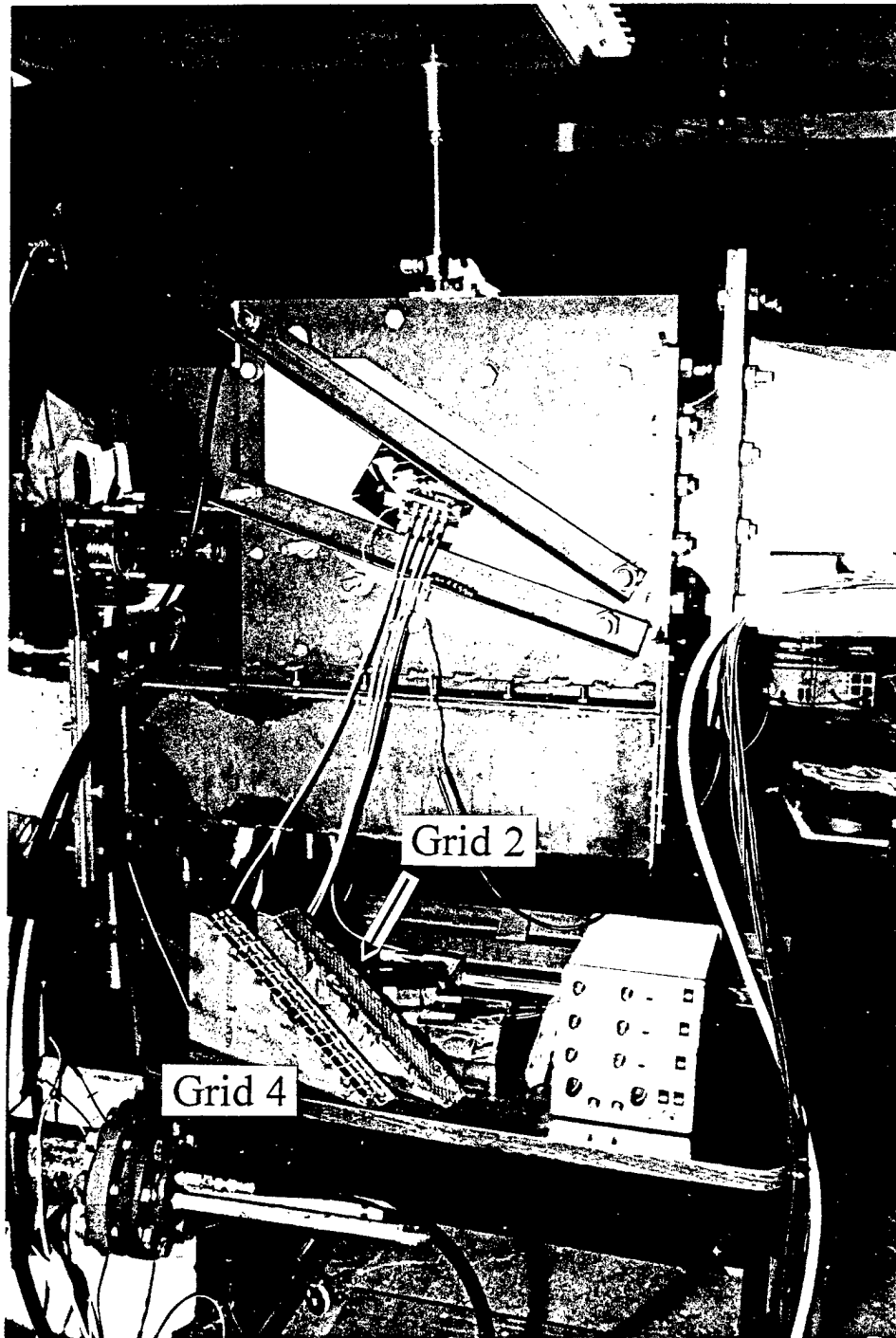


Figure 2.1.2 View of test section showing instrumentation cables, amplifiers, and grids (Grid 4 in front and Grid 2 in back).

Test Section Turbulence grid position

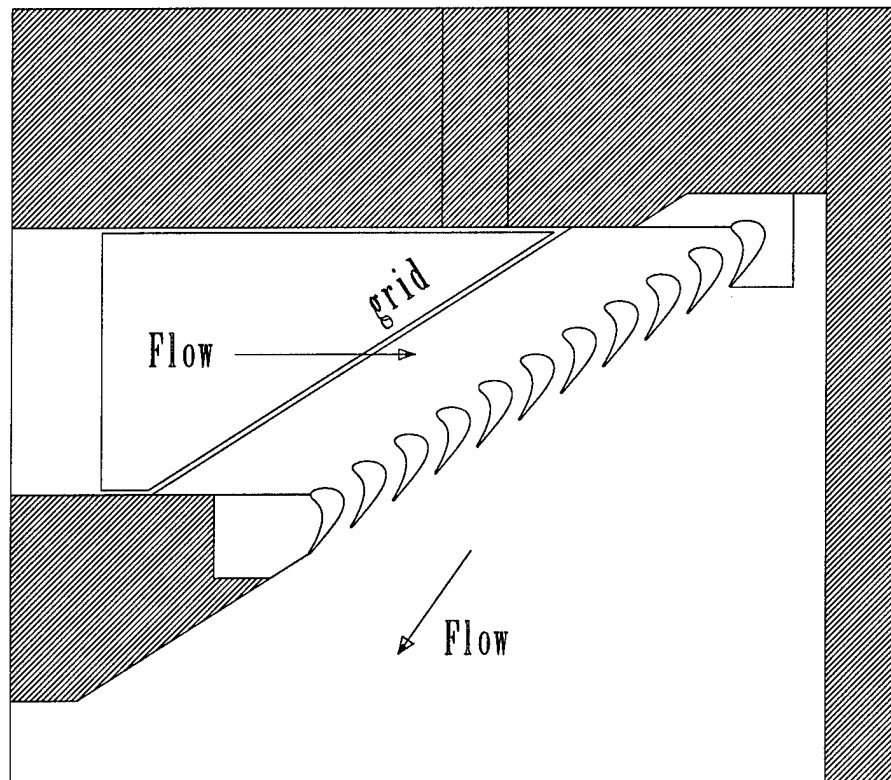


Figure 2.1.3 Side-view cut-away of test section showing blade cascade and angle of grid parallel to blade row inlet.

Dimensions in mm

**Hot-wire measurement
locations indicated
by + location.**

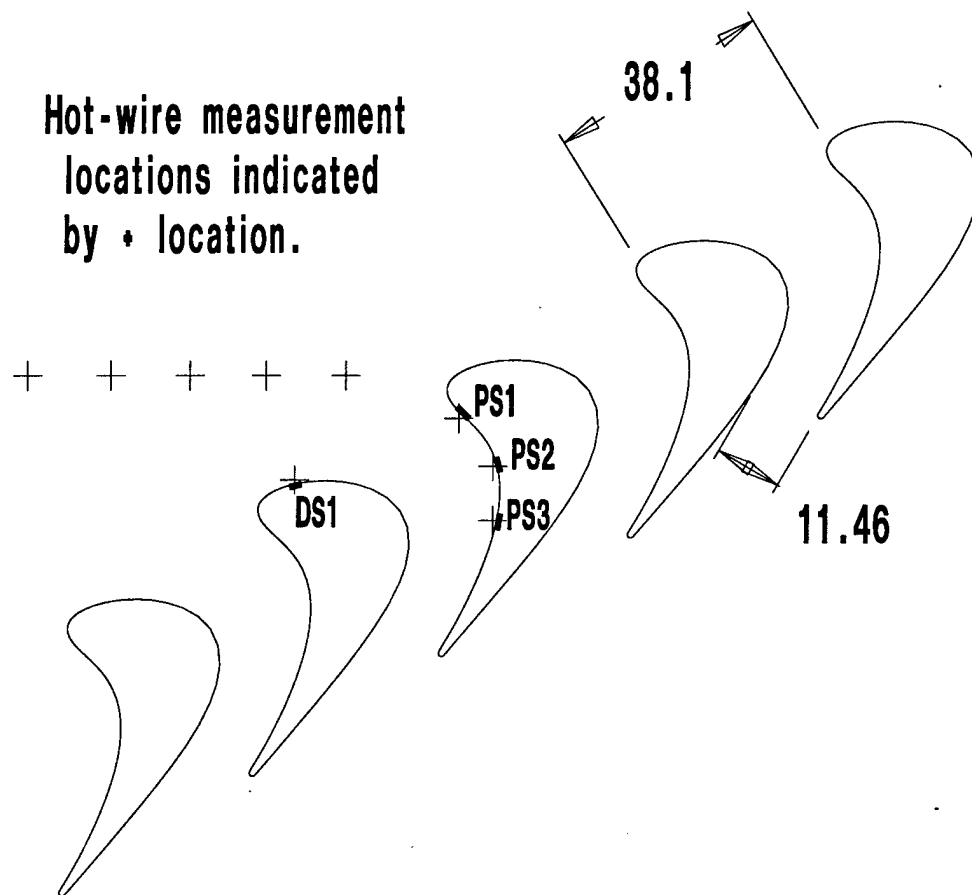


Figure 2.1.4 Detail of blade dimensions and locations of heat flux sensors and hot-wire measurement stations.

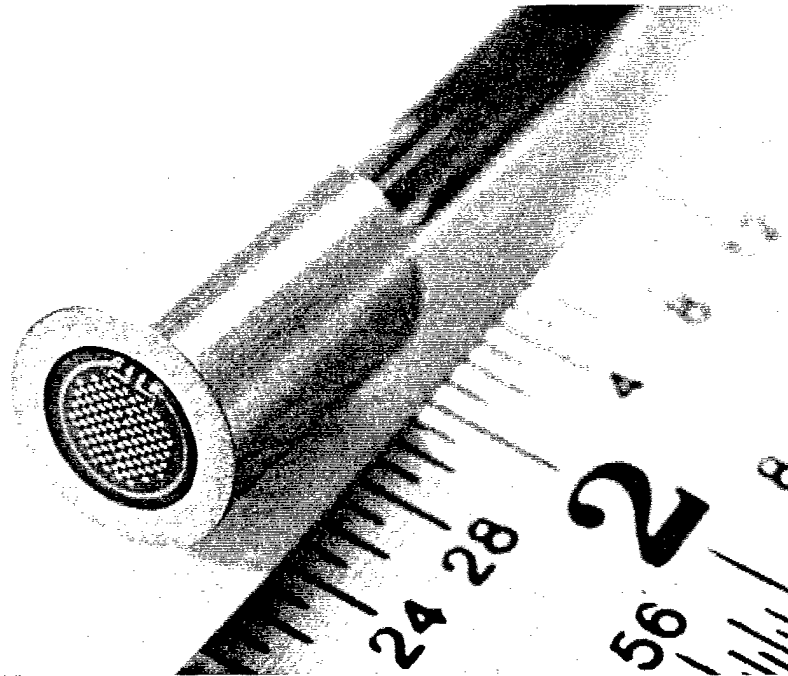


Figure 2.1.5 The HFM-6 Heat Flux Microsensor mounted in an aluminum housing and equivalent to the insert gages used on the pressure side (dimensions in inches).

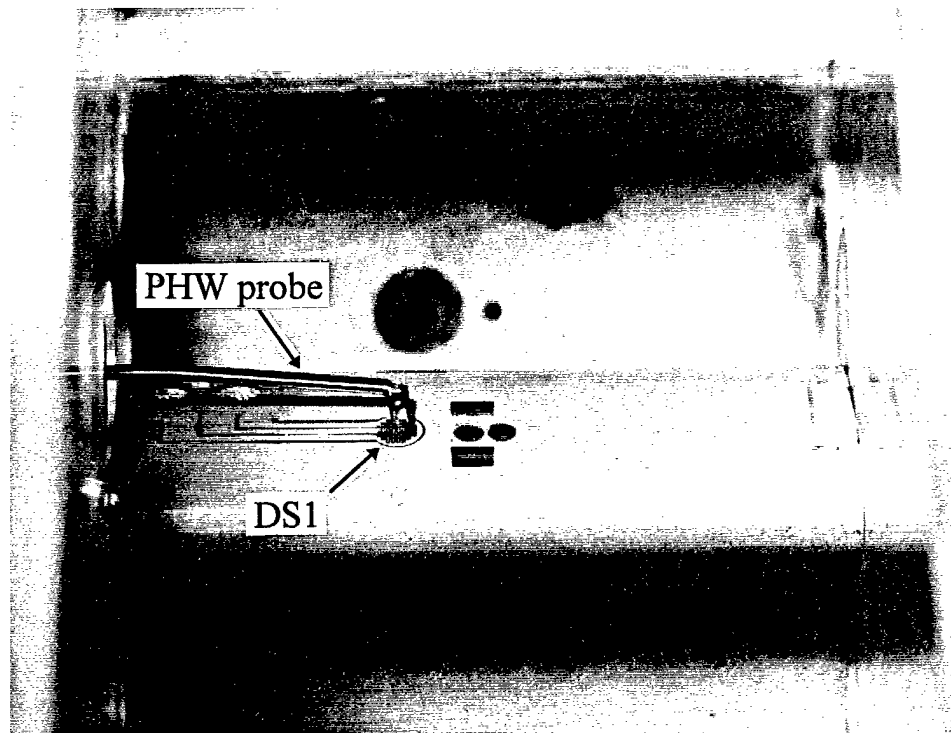


Figure 2.1.6 A streamwise view looking downstream toward the leading edge of the blade showing the direct sputtered sensor (DS1) on the suction side with the custom Passage Hot-Wire (PHW) probe extended from the end-wall.

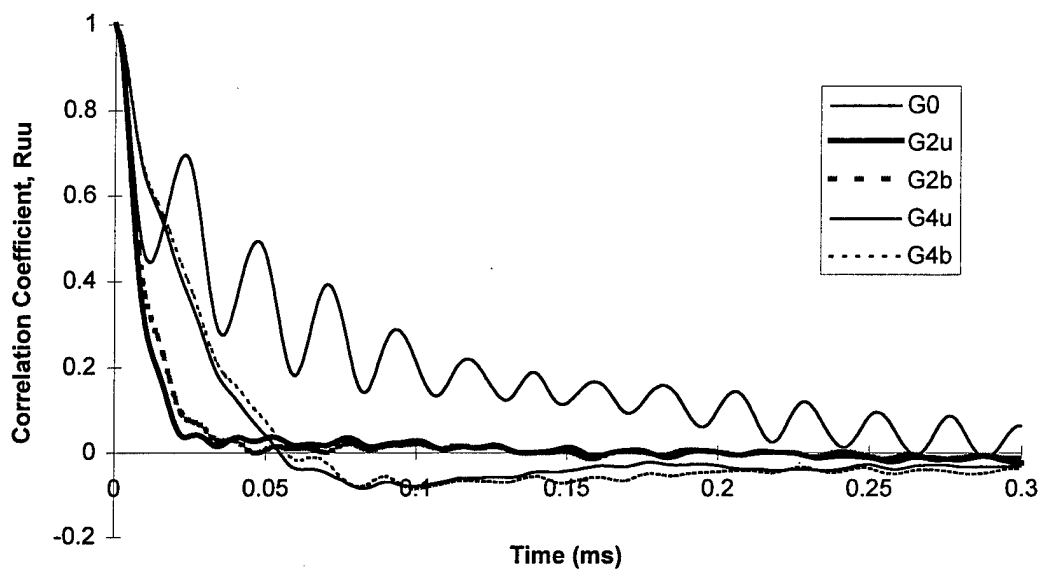


Figure 2.2.1 Examples of the auto-correlation function calculated from the energy spectrum for the five grid conditions measured above DS1.

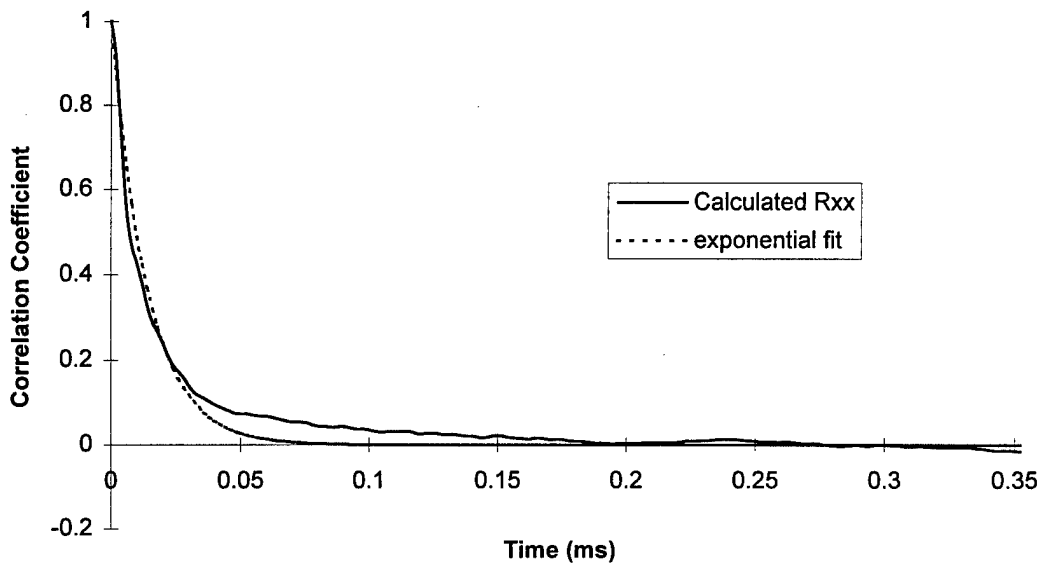


Figure 2.2.2 Example of the measured auto-correlation and the exponential fit used to find the integral time scale.

3. High Frequency Instrumentation

3.1 HFM

3.1.1 Design and operation of HFM-6 sensors

A review of advances in heat transfer measurements is given by Diller (1993). Doorly and Oldfield (1986, 1987) proposed techniques to create new thin-film gages on metal turbine blades that measured surface heat flux. These gages were dependent on the idea of placing a thermal resistance layer on a substrate to measure transient surface temperatures. If the properties of the thermal resistance layer and the substrate were known along with a proper analytical model, then the surface heat flux could be determined.

Hager, et al. (1991) discussed the design of a new heat flux gage made from microfabrication techniques. These sensors have fast time response and can measure high heat flux levels. The gage presently is known as the Heat Flux Microsensor (HFM) and consists of two independent sensors, sputtered on the face of a ceramic cylinder in the case of the HFM-6 shown in Fig. 2.1.5 which is the "insert" sensor referred to in these experiments. The first sensor is a passive Heat Flux Sensor (HFS), which measures the temperature difference across a thin thermal resistance layer, Fig. 3.1.1 and the second an active resistance temperature sensor (RTS) driven by the amplifier with a 0.1 mA current. The HFS consists of a thermopile -- a series of many thermocouple pairs which boost the heat flux signal to a measurable level and allow an output signal directly proportional to the heat flux, Fig. 3.1.2. The total thickness of the sputtered gage is less than 2 μm . The HFM has a fast response time (see section 3.1.4) and gives a continuous (not transient) signal.

The HFS works according to simple theory by measuring temperature above and below the sputtered resistance layer, Fig. 3.1.1. According to Fourier's Law, the heat flux across this resistance layer is proportional to the temperature difference across the layer:

$$q = \frac{k}{\delta} \Delta T \quad (3.1)$$

where k is the thermal conductivity, δ the layer thickness, and q is the heat flux.

The heat flux sensor must be calibrated since material properties of all the sputtered layers are not known exactly. The operation and calibration of these sensors have been discussed in detail in previous publications (e.g. Holmberg and Diller, 1995, attached in Appendix A-2) which discusses a conduction calibration and details of the sputtered layers and numerical modeling of the gage time response. In addition, Lewis (1996) measured the time-resolved unsteady heat flux in a junction vortex flow. Other uses of the HFM are mentioned by Hager, et. al. (1991).

3.1.2 Surface direct-sputtered gage

The direct sputtered gage (DS1) was introduced in section 2.2.5.2 and is identical in sputtering detail to the HFM-6 discussed in the preceding section. The difference is that DS1 was deposited directly on the aluminum blade surface (on an electrically isolating anodization layer) rather than on a ceramic insert. The 2 μm thickness of the HFM sensor is less than the roughness of the blade itself and thus presents no flow disturbance. This is in contrast to the inserted gages that due to the flat face cannot match the surface curvature perfectly and present some disturbance to the flow.

The purpose of using the DS1 sensor was to obtain more accurate measurements at the location nearest the leading edge of the suction surface (SS). This serves several purposes. Because this is a curved portion of the blade with a thin boundary layer, it is believed that the flow disruption due to the insert gage is greatest at this point. DS1 serves to judge the effects of this flow disturbance. In addition, hot-wire/ heat-flux measurements made with this sensor can be used as a reference for hot-wire/ heat-flux measurements made above the insert. This allows separating hot-wire flow disturbances from HFM insert gage flow disruptions. Finally DS1 serves as a test bed for future use of directly deposited sensors. The blade was not fully instrumented with direct deposited sensors due to the difficulty in manufacture and cost. Future blades may be instrumented in this way as an outcome of this work.

3.1.3 Calibration

3.1.3.1 Manufacturer calibration of HFM

The HFS is calibrated by the manufacturer using radiation. The HFM is painted with a known emissivity black paint (later removed) and placed with its face normal to an aperture from which an intense radiation is shuttered. The level of radiation from this lamp is calibrated using a reference Gardon gage with its calibration traceable to AEDC. The resulting transient signals give HFS direct heat flux measurement in the constant heat flux radiation field, as well as the rising surface temperature recorded by the RTS. A typical HFM-6 HFS calibration including temperature sensitivity would appear as

$$Q = V * 1E6 / (G*S), \text{ where } S = 0.033 * T + 10.84 \text{ } (\mu\text{V per W/cm}^2)$$

where Q is the heat flux, V is the voltage out from the amplifier, G is the gain, S is the sensitivity, and T is the RTS temperature in $^{\circ}\text{C}$.

The RTS is calibrated separately in an oven referenced to a thermocouple.

3.1.3.2 In-situ HFS calibration (convection/ conduction)

3.1.3.2.1 The method

A method has been developed that allows checking the HFS calibration based on data acquired during a normal tunnel run. This allows a calibration for each tunnel run, and over a series of runs gives a value with some statistical confidence, typically better than $\pm 10\%$.

The method has been codified into a FORTRAN program called QT.FOR and this is given in Appendix B. The program converts an HFM heat flux signal to the corresponding surface temperature according to a one dimensional semi-infinite model of heat conduction into a substrate of known thermal properties and initially constant temperature. This model is valid for short times where the 1-D, semi-infinite assumptions are valid. This program utilizes Green's function method to integrate the heat flux with respect to time to yield a calculated temperature, T_{calc} . T_{calc} is based on a guessed value of sensitivity, S , and is compared to the measured wall temperature from the RTS temperature sensor. The program iterates S to find the best value of gage sensitivity for each data set. Additional results using this code are presented in Holmberg and Diller (1995, attached in Appendix A-2).

3.1.3.2.2 Use with DS1

The above code was used to check the calibration of the direct sputtered sensor, DS1. Because of the differences in the mounting of the sensor (on the blade rather than a flat insert) and the differences of mounting in the radiation field, there was doubt about the accuracy of the manufacturer calibration.

A total of 6 tunnel runs allowed for use with this code, and a sensitivity value was calculated for each of the six runs. Table 3.1 (next page) shows the results from the six runs. Blade aluminum thermal properties necessary for the calculations are given in the code (QT.FOR, Appendix B) and are documented in L. Johnson's masters thesis (1995). The data was taken at 50 Hz of which the two seconds preceding the start of flow were used for zeroing purposes, while 0.6 seconds following the start of flow (30 data points) were used as the basis of the sensitivity calculation. The accuracy of the calculated sensitivity is dependent on the change in surface temperature during these 0.6 s, and the accuracy of the initial temperature (the average temperature prior to the heat flux pulse, used to zero the RTS noise level). A sensitivity value of lower certainty, compared to the radiation calibration, results because the heat flux at the start of the tunnel run is much lower than that produced by the manufacturer applied radiation with only a 2 °C change in surface temperature in the 0.6 s. However, 0.6 s represents the maximum accuracy point, in that after 0.6 seconds the 1-D assumption begins to break down and thus produce erroneous sensitivity values.

Table 3.1 DS1 HFS experimental vs. manufacturer calibration.

Run	Average Temperature (°C)	Calculated Sensitivity ($\mu\text{V/W/cm}^2$)	Manufacturer Sensitivity ($\mu\text{V/W/cm}^2$)	Difference ($\mu\text{V/W/cm}^2$)
3, 6/24	19.0	11.78	11.46	0.32
1, 6/25	25.0	11.35	11.66	0.31
2	16.5	11.18	11.38	0.20
3	18.5	11.13	11.45	0.32
7	17.0	11.24	11.40	0.16
9	16.5	11.74	11.38	0.36
mean	18.75	11.40	11.46	0.28

In Table 3.1, the independent conduction calibration sensitivity result for each run is compared to the value that would result from the manufacturer calibration at that temperature, where the manufacturer calibration for HFM-192 sensor DS1 (6/96).

$$\begin{aligned} S(\mu\text{V/W/cm}^2) &= 10.836 + 0.0331T_{SUR}(\text{°C}) \\ T_{SUR}(\text{°C}) &= 3.148 R(\Omega) - 491.2 \end{aligned} \quad (3.2)$$

The average sensitivity for all the runs was $11.40 \pm 0.23 \mu\text{V/W/cm}^2$ (95% confidence). Figure 3.1.3 shows one of the runs comparison of HFM measured temperature versus temperature calculated from heat flux. The average difference between calculated and manufacturer sensitivities was 0.28. This is excellent agreement, given that calibrations between radiation and convection often differ considerably, and that heat flux calibrations are in general no better than 5%. Despite this, there was some doubt about the longevity of this calibration throughout the testing (approximately 40 tunnel runs) that led to a re-calibration by the manufacturer after completion of testing (8/96)

$$\begin{aligned} S(\mu\text{V/W/cm}^2) &= 11.332 + 0.0377 T_{SUR}(\text{°C}) \\ T_{SUR}(\text{°C}) &= 2.99 R(\Omega) - 467.6 \end{aligned} \quad (3.3)$$

The measured change in the two calibrations over the course of 40 tunnel runs and two months as seen in equations 3-2 and 3-3 shows a decrease in the RTS temperature slope of 5% and an increase in HFS sensitivity of 5%, independent of temperature over the range used for these tests (10 - 50 °C). This measured shift in the HFM calibration of 5% is on the border of significant, and cannot be taken as strong evidence of a shift in the calibration.

3.1.4 Frequency response/ Spatial averaging issues

3.1.4.1 Frequency (time) response

Based on previous research with the HFM, frequency response is above 100 kHz (Holmberg and Diller, 1995, attached in Appendix A-2). This work was performed by placing a previous model of the HFM in the sidewall of a shock tunnel to measure the response to the shock wave passing over the face of the gage. Recent tests have confirmed this frequency response with a shock wave striking directly and reflecting from the face of one of the HFM-6 sensors used in this research. This provides a more instantaneous step in heat transfer than given by a shock passing laterally over the gage face.

In addition to the time response of the sensor itself is that of supporting electronics. The HFM amplifiers are known to have limited frequency response that varies as a function of gain. For the present research, tests were run at a gain of 1000. At this setting, frequency begins to attenuate at approximately 25 kHz. The amplifiers were tested and found to be very stable, with no measurable drift in the zero level or gain over long periods of time including during warm up.

3.1.4.2 Spatial averaging limitations and the Corcos correction

A sensor will be limited to measuring scales (turbulent eddies) no smaller than the size of the measuring element. In the case of the heat flux sensor (HFS), this implies that the HFS cannot see any scales of turbulence smaller than the diameter of the sensor, $D = 3$ mm. Assuming that the HFS can see no frequencies with a wavelength less than twice its diameter implies that for a 3 mm sensor the resolution is a 6 mm wave, which with a convected velocity, $U_c = 120$ m/s, implies a frequency of $U_c / 2D = 120 / 0.006 = 20$ kHz above which the frequency resolution is zero. The data support this simple analysis. Specifically, turbulent energy in the heat flux spectrum beyond 20 kHz is significantly attenuated (including all small scale boundary layer activity) and there is no coherence between hot-wire and surface heat-flux signals beyond 20 kHz. However, the hot-wire with its smaller active length does not see much energy past 20 kHz implying that not much information is lost by this limitation of the HFM.

Can this lost energy be accounted for? It may be possible to correct the energy spectrum of the heat flux, even though coherence cannot be reconstructed. Reconstructing the energy spectrum would allow calculating more accurate heat flux turbulence intensities and time scales.

Earlier work performed by Corcos (1963, 1967) addresses the complicated response of round and rectangular sensors to the fluctuating pressure field beneath a turbulent boundary layer from a theoretical perspective and using pressure data to form corrective correlations. In his first paper he gives tabulated values for the attenuation of the frequency-spectral density (PSD) for a round sensor in terms of $\omega r / U_c$ vs. ϕ_m / ϕ , where ω is the frequency ($2\pi f$) of interest, r is the sensor

radius, U_c is the convection velocity (here taken as U_∞), and ϕ is the energy spectrum, and the subscript m is for the measured value.

Corcos' second paper gives a re-thought analysis and adds more recent data, but states that "from the standpoint of transducer resolution, it would appear that while the estimates published in (the 1963 paper) are not necessarily numerically very accurate, they should lead to no gross errors..." The issues responsible for the error are complicated and situation dependent and no better estimates are given.

D. Lewis' dissertation (1996) discusses using Corcos' correction for heat-flux measurements in a turbulent boundary separating flow. His data does not give strong support to the Corcos correction. The correction has also been applied to the present data with similarly poor results as will be seen in chapter 6.

Although Corcos' correction appears of limited use, a by-product of his work is useful. D. Lewis wrote a numerical code to apply Corcos' correction to rectangular sensors of different aspect ratio. For a line gage (as was used in the work at Wright-Patterson AFB, Holmberg and Pestian, 1996, attached in Appendix A-1), results showed that the HFS attenuated more rapidly initially, but that some significant frequency response remained at higher frequencies. Figure 3.1.4 shows the numerical output of attenuation for a square sensor versus a rectangle of 10 to 1 aspect ratio. For the present sputtered HFM-6 pattern, the entire sensor covers an area of 3 mm diameter, however, this sensor is composed of over 100 individual sputtered square pads that see much smaller scales. Even though the voltages of these individual pads are summed together, which smears the high frequency information, some frequency response can be expected to remain similar to the line gage. This is demonstrated in the measured heat flux spectra given in chapter 6.

In conclusion of this matter, it appears that the actual heat flux energy spectrum is not well represented with the Corcos correction, and that there is no clear way to correct the spectrum. The spectra are presented "as measured." The influence of this attenuation will be discussed as applicable.

3.1.5 Limitations/ error analysis

3.1.5.1 Flats, reasons for choice of these gages

These gages were chosen because they offer a first-look at some phenomena that heretofore have been unexamined. Their high frequency response and small size have allowed them to be used on the surface of a realistically sized turbine blade in a high speed flow. They are presently the only sensor available of this size and durability and accuracy in measuring direct heat flux with fast time-response.

It was known at the outset that the flat face of the gage would likely cause disturbance to the heat flux measurements, although the degree of this was unknown. The present research was deemed worthwhile in the faith that this limitation would not be too severe and useful results would be found. Beyond this, the scope of gage disturbance could be found also. The following sections give two means of checking the disturbance.

3.1.5.2 Comparison of DS1 with insert

The suction side (SS) of the blade will have the most disturbance due to the presence of the HFM insert. This is due to the convex curvature where corners and flats are fully exposed. On the concave pressure side (PS) the curvature allows the corners of the HFM to be set just below the surface and silicone to fill in the resulting depressions, with little change to the profile. The HFM sensors near the SS leading edge of the blade see more curvature than the two sensors toward the trailing edge and the leading edge of the SS also has a thin boundary layer. Therefore, the largest disturbance to heat flux measurement will be at the two SS forward sensor locations.

The Direct Sputtered HFM at SS location 1 (sensor DS1) allowed undisturbed measurements at this location, and by comparison allows inference of the disturbance caused by the insert gage at the same location.

There appears to be a reduction in the differences between the heat transfer levels measured by the insert as compared to those measured by DS1, Fig. 3.1.5. That is, the baseline heat transfer measured by the insert is significantly above that measured by DS1, and the large variation in heat transfer seen by DS1 between G2 and G4 is not seen by the insert. In fact, the insert sees less heat transfer due to G2 than G4, while DS1 sees more.

One explanation for this converging of the data (where G0, G2, and G4 appear to produce relatively close heat transfer coefficients) is that the insert has some disturbance that influences the heat transfer level. This self induced disturbance acts to disrupt the laminar boundary layer present in G0 and thus to raise heat transfer. The flat of the insert and the abrupt change in curvature at the edge of the sensor flat also causes a thickening of the boundary layer that may be reducing the influence of FST on the heat transfer. This added thickness could react differently with the different scales of the turbulence and change the dynamics of the interactions with the scale of the turbulent fluctuations. Thus, G2 may increase heat transfer relative to G4 when measured by DS1, but decrease heat transfer for the insert.

3.1.5.3 Effect of insert installation on PS HTC

In addition to the direct comparison of the insert vs. DS1 on the SS, some inferences can be made from PS data using the inserts alone. Mean heat transfer coefficient (HTC) data were taken at the three PS locations. The sensors were then removed and reinserted. The second

installation was performed with more care taken to achieve the best possible match of HFM surface to blade surface. This is largely an art requiring careful application of silicone in the small gaps in order to minimize surface roughness. The final roughness achieved in the second installation is estimated to be 0.1 mm or less, or of the order of the very thin boundary layer thickness at DS1 and PS1 and less than the boundary layer thickness at PS2 and PS3. However, this is significantly better than the roughness observed for the first installation. The mean heat transfer results bear out this observation with an average 17% drop in HTC. Figure 3.1.5 shows the average HTC for the two installations at the 3 gage locations. Most significantly, the HTC for the baseline G0 case at the location nearest the leading edge dropped by 25% indicating a much less disturbed laminar boundary layer. The 17% drop in HTC values is greater than the 10% uncertainty typically allowed for heat transfer measurements due to calibration and other factors.

This significant drop in HTC between the two installations confirms that gage installation has a significant effect on measured heat transfer, disturbing the boundary layer and raising heat transfer. It is not clear whether the HTC values measured in the second installation have reached the actual heat transfer that would be there in the absence of the gages (the undisturbed value). Certainly it is approaching it. These results highlight a widespread difficulty in the heat flux community in that heat flux data are often taken with some variety of inserts, and casts doubt on uncertainty levels quoted with said mean heat transfer measurements.

All high-speed frequency data for the present work were taken with the second installation of HFM sensors on the PS, while all SS reported results are from measurements using DS1. Because of the lack of a direct-sputtered sensor on the PS there is no way of demonstrating that the influence of the PS insert disturbance on the frequency-domain data presented here is as small as believed.

3.1.5.4 Use of HFM sensors

All heat flux measurements are subject to a variety of uncertainties. These include differing gage responses to radiative vs. convective vs. conductive fluxes, calibration difficulties, frequency response, disturbance of heat flux due to a resistance layer, and installation effects as just mentioned. The HFM has been shown to respond uniformly to different modes of heat flux (Holmberg and Diller, 1995, attached in Appendix A-2) and to have excellent frequency response, and no significant disturbance due to its very thin resistance layer. However, in addition to the installation effects for the flat insert gages on this curved surface, there are other potential sources of uncertainty.

Sensor calibrations are generally only trusted to $\pm 5\%$, and are also subject to drift over time, as seen in the section on calibration, requiring regular re-calibration. In addition, the signals from the two HFM sensors (RTS and HFS) are low-voltage, and are susceptible to noise (with rms

fluctuations typically $0.2\text{ }^{\circ}\text{C}$ on temperature, and 0.2 W/cm^2 on heat flux). The heat flux signal is only microvolts, and the tiny wires from the sensors must be guarded from temperature fluctuations that can cause thermocouple effects. Twisting pairs of wires and shielded cables are necessary to avoid picking up radiated noise. Finally, it is difficult to quantify these primarily bias type errors, and to identify others that are installation dependent.

However, for the present measurements the largest uncertainty on the PS is believed to be installation effects as discussed in the previous section (3.1.5.3) that may bias the mean heat transfer measurements. The disturbance to the boundary layer is assumed small enough to allow rapid recovery and that comparisons of how different free stream turbulence length scales transfers energy to the surface are still valid. That is to say, while PS mean heat transfer may be high, conclusions based on fluctuating values are still valid. DS1 heat transfer measurements are not compromised in any way by installation effects.

3.2 HW Probes

3.2.1 Design and operation

3.2.1.1 Dimensions

Two different custom probe types were ordered from Auspex Corporation (Broad Street Business Center, Suite 115, 44 E. Broad St., Bethlehem, PA, 18018, Tel (610) 866-5064, owner: KC Muck). Two larger probes were ordered, dubbed the Upstream Hot-Wire (UHW), and also four miniature sensors, named the Passage Hot-Wire (PHW), see Fig 3.2.1. The UHW were used for measurements upstream of the cascade within the test section behind the grids. The PHW were primarily used within the passage, and were made as small as possible.

The UHW is a HW probe similar to the standard TSI U-wire, but custom made by Auspex. The wire is oriented with the prongs at 90° to the body (3.2 mm stainless tubing). The probe was traversed vertically behind the grids.

The Passage Hot-Wire (PHW) is a custom probe with 3 mm long stainless steel prongs on a very small body. The probe is mounted in the cascade endwall extending out into the blade passage so that the wire is positioned above the heat flux sensor. The section of the body extending from the endwall to the wire prongs is flattened 1.1 mm diameter stainless tubing with a final frontal height of 0.9 mm. The wire is parallel to the probe body and is approximately the same length as the UHW wire (1 mm).

Wires used are $5\mu\text{m}$ ($0.005\text{ mm} = 0.0002\text{ in.}$) annealed Tungsten attached using facilities at Virginia Tech. Frequency response and anemometer control settings for these two wires were

significantly different, and are discussed in the following section, with frequency response testing details given in Appendix C.

3.2.1.2 IFA-100 Anemometer and frequency response

The hot-wires were controlled by a TSI Corp. IFA-100 anemometer. In terms of frequency response, two controls are given on the front panel of the IFA-100 unit. The first is called "cable" and the second "bridge compensation" which will be called "BC". In general, there is a window of stable operation in the setting of "cable." Too far CW or CCW will lead to electronic instability of the anemometer. Proper setting of this knob involves adjustment until the proper test signal is seen on an oscilloscope, as documented in hot-wire literature (e.g. Freymuth and Fingerson, 1980). This adjustment must be performed in a flow similar to the test conditions, i.e. same Reynolds number. The BC knob must be set properly as well. Standard TSI probes come with recommended BC values while the custom probes used in this work required testing. In general, frequency response increases with BC, but too high a value leads to system instability. The proper value of BC is also sensitive to Re , with higher Re causing greater instability and requiring a lower BC value.

Initial data taken 12/95 showed oscillation (OSC) problems with the PHW. Further use of the PHW showed noise in the frequency spectrum, with very strong disturbances present when the wire was placed into the higher velocity (SS) passage flow. In order to better understand this, a series of tests was performed, with results of these presented in Appendix C. These tests showed that the disturbances in the PHW spectrum are not completely controllable by use of the controls available on the front panel of the IFA-100. "Best settings" were found for the different flow conditions and these were used for later data acquisition. Later testing also seemed to show a history effect where a new wire on the PHW probe produced a noisy spectrum at higher frequencies, whereas after some aging in the tunnel the same wire changed character and a clean spectrum resulted. This wire specific and installation specific behavior is not understood.

Frequency response of the hot-wire/ anemometer system was velocity dependent. For the grid measurements the frequency response was near 70 kHz, judged by the square-wave test signal attenuation (appendix C) and by a corresponding 70 kHz peak in the hot-wire spectrum followed by attenuation of the hot-wire signal. For the higher velocity suction side measurements the same peak seemed to occur near 100 kHz, while near the leading edge of the pressure side this peak was near 60 kHz. In addition to the frequency response of the system, there is the issue of spatial resolution of the finite length hot-wire (discussed in section 3.2.3) which results in an attenuation of turbulent flow energy content at similar frequencies (i.e. attenuation above 60 kHz). In all cases the analog LP filter was set with a cut-off frequency at 100 kHz.

3.2.2 Calibration

3.2.2.1 Hot-wire calibration theory

The usual approach to calibrating a hot-wire is to place a hot-wire in a known velocity laminar jet and to record voltage out for a given flow velocity and temperature. The data is then used in an equation of this form:

$$Nu = A + B Re^x$$

The actual values for A, B, and x will vary some, but both Bradshaw (p. 115) and Hinze (2nd ed. p.89) give these numbers as applicable to the different Re_d regimes:

$$Nu \left(\frac{T_m}{T_s} \right)^{-0.17} = 0.24 + 0.56 Re^{0.45} \quad \text{for } Re_d < 44 \quad (3.4)$$

$$Nu \left(\frac{T_m}{T_s} \right)^{-0.17} = 0.48 Re^{0.51} \quad \text{for } Re_d > 44 \quad (3.5)$$

where the term T_m/T_s is a temperature correction factor, and the value of $Re_d = 44$ is where laminar to turbulent transition of flow over the wire occurs.

At wire transition the calibration curve shifts, as seen by the changed Reynolds number exponent (Re exponent), and the calibration curve also goes through the origin for higher Re. For typical cold conditions in the cascade tunnel (grid tests were done in unheated flow):

$$\begin{aligned} M_{\text{inlet}} &= 0.36 \\ P_t &= 31.7 \text{ psia} = 219 \text{ kPa} \\ T_t &= 290 \text{ K} \\ \gamma &= 1.4 \\ T_{\text{wire}} &= 500 \text{ K} \\ d_{\text{wire}} &= 5 \mu\text{m} \\ R_{\text{air}} &= 287 \text{ m}^2/\text{s}^2\text{K} \end{aligned}$$

$$\frac{P_t}{P_s} = \left(1 + \frac{\gamma - 1}{2} M^2 \right)^{\frac{\gamma}{\gamma - 1}} = \left(\frac{T_t}{T_s} \right)^{\frac{\gamma}{\gamma - 1}}$$

which gives:

$$\begin{aligned} P_s / P_t &= 0.914 \\ T_s / T_t &= 0.975 \\ T_s &= 280 \text{ K} \\ P_s &= 29.0 \text{ psia} = 200. \text{ kPa} \end{aligned}$$

then:

$$T_m = (T_s + T_w) / 2 = 390 \text{ (K)}$$

$$\rho_m = \frac{P_s}{RT_m} = 1.79 \text{ (kg/m}^3\text{)}$$

$$\mu_m = 1.716 \times 10^{-5} * \left(\frac{T_m}{273.16} \right)^{15} * \left(\frac{383.716}{T_m + 110.556} \right) = 22.6 \times 10^{-6} \text{ (Ns/m}^2\text{)}$$

$$U = M \sqrt{\gamma R_{air} T_s} = 121 \text{ (m/s)}$$

$$Re_d = \frac{\rho_m U d_{wire}}{\mu_m} = 48$$

Therefore, the wire is actually operating near its transition point, but presumably in the turbulent regime. Two assumptions were made initially:

- 1) Re exponent = 0.51 can be applied to the grid turbulence measurements.
- 2) The calibration will be a straight line through the origin if plotted as:

$$Nu = \text{const} * Re^{0.51}$$

The above assumptions were tested experimentally and were found to be valid within the uncertainty of measurements. A discussion of the validity of these assumptions is included in the next section.

The result of the above two assumptions is that a calibration of a given wire can be obtained with data at only one point (where the origin becomes the second point). Calibration of the UHW used for performing grid turbulence field measurements was done *in-situ* with a calibration performed for each tunnel run using this method. This allowed a calibration without the uncertainty of a varying tunnel total temperature and pressure and changes in the wire itself from run to run. The specifics of this method follow.

3.2.2.2 One point calibration methodology

As discussed above, the conditions in the tunnel for measurements behind the grids upstream of the cascade allow for the use of this equation:

$$Nu \left(\frac{T_m}{T_s} \right)^{-0.17} = 0.48 Re^{0.51} \quad (3.5)$$

Now, each piece of this equation needs to be put into known measured quantities, and put into a form that can lead to a useful calibration.

$$Nu = \frac{hd}{k_m}, \text{ where } h = \frac{(\text{power})}{(\text{area})(\Delta T)} = \frac{\left(\frac{V^2 R_w}{(R_w + R_1)^2} \right)}{(\pi d_w L_w)(T_w - T_s)}$$

where the above equation for the heat transfer coefficient is taken from Freymuth and Fingerson (1980). In this equation, HW voltage V and the tunnel static temperature T_s are the only variables. All wire properties are considered constant given a constant temperature anemometer that in theory maintains wire temperature and thus resistances constant. Therefore the equation for Nu reduces to:

$$Nu \propto \frac{V^2}{(T_w - T_s)k_m} \propto \frac{V^2}{(T_m - T_s)k_m} \quad \text{since } (T_w - T_s) = 2(T_m - T_s)$$

Then, taking the constant wire diameter out of Re , flipping the left and right hand sides of the equation for convenience, and inserting a calibration constant:

$$\left(\frac{\rho_m U}{\mu_m} \right)^{0.51} = C \frac{V^2}{(T_m - T_s)k_m} \left(\frac{T_m}{T_s} \right)^{-0.17} \quad (3.6)$$

simplified to:

$$Re' = C Nu' \quad (3.7)$$

This equation was used in the calibration of the UHW used for grid measurements. The specific step by step procedure of applying these equations follows.

1. Find the average P_t , T_t , and V (HW voltage) over the selected HW sample.
2. Solve for T_s , P_s , and T_m from the above equations using $\gamma = 1.4$ as the initial value.
3. Proceed through the following equations:

$$Cp_{air} = 1037.8 - 0.22371T_s + 2.8556 \times 10^{-4} T_s^2 + 5.2694 \times 10^{-7} T_s^3 - 5.3327 \times 10^{-10} T_s^4 \quad (\text{m}^2/\text{s}^2\text{K})$$

$$\gamma = \left(1 - \frac{R}{Cp_{air}} \right)^{-1}$$

$$P_s = P_t \left(1 + \frac{\gamma - 1}{2} M^2 \right)^{\frac{\gamma}{1-\gamma}} \quad (\text{Pa})$$

$$T_s = T_t - \frac{U^2}{2Cp} \quad (\text{K})$$

$$U = M \sqrt{\gamma R T_s} \quad (\text{m/s})$$

$$T_m = (T_s + T_w) / 2 \quad (\text{K})$$

$$\rho_m = \frac{P_s}{RT_m} \quad (\text{kg/m}^3)$$

$$\mu_m = 1.716 \times 10^{-5} \left(\frac{T_m}{273.16} \right)^{1.5} \left(\frac{383.716}{T_m + 110.556} \right) \quad (\text{Ns/m}^2)$$

$$k_m = 2.414 \times 10^{-2} \left(\frac{T_m}{273.16} \right)^{1.5} \left(\frac{473.16}{T_m + 200} \right) \quad (\text{W/mK})$$

$$\text{Re}' = \left(\frac{\rho_m U}{\mu_m} \right)^{0.51}$$

$$\text{Nu}' = \frac{(\bar{V})^2}{k_m (T_m - T_s)} \left(\frac{T_m}{T_s} \right)^{-0.17}$$

$$C = \text{Re}' / \text{Nu}'$$

This constant then can be used for all the HW data acquired in that run to convert bridge voltage to a velocity series. The value of C is for a given hot-wire, and will be consistent run to run with some small drift over time.

When using this calibration to solve for the velocity, the values of Re' and Nu' must be solved iteratively at each point. The progression is similar to the above calibration equations, but the result is U instead of a calibration constant. The method used was:

- 1) Solve for C_p , T_s , T_m , k_m , μ , γ as above.
- 2) Solve for Mach number, M.
- 3) Then $P_s = f(P_t, \gamma, M)$.
- 4) Solve for Nu' using the instantaneous HW voltage.
- 5) $(\rho U) = \mu(C^* \text{Nu}')^{1/0.51}$, where $\text{Re}' = C^* \text{Nu}'$
- 6) Mean density from the low speed data, $\rho_m = P_{s,m}/RT_s$
- 7) and then instantaneous $U = (\rho U)/\rho_m$ if density fluctuations are assumed negligible.
- 8) Iterate the above sequence until U converges.

3.2.2.3 Changing tunnel pressure calibration

At issue is the validity of the assumed applicable form of King's Law ($\text{Nu} = A + B \text{Re}^x$) as given in Eqn (3.5). Does the calibration for these wires (all wire from one spool) at this flow condition follow a straight line fit through the origin (i.e., $A = 0$) and is Re exponent = 0.51 correct? The validity of this calibration equation can be checked in the tunnel itself.

The method is as follows: with the hot-wire placed in the inlet flow upstream of the cascade, the tunnel is run such that total pressure is not held constant (the air supply is not loaded to as high an initial pressure), but instead peaks and then slowly drops as the upstream compressed air tanks empty. Because of the choked throat of the cascade above a certain

upstream pressure, Mach number is fixed irregardless of total pressure. The result is a changing wire Reynolds number (Re_d) due to the dropping air density as well as total temperature change. For a cold run where temperature changes only slightly, this calibration can be seen as a constant velocity calibration.

The Re_d variation using this method is limited however. For the tests performed, the total variation seen was $30 < Re_d < 54$, where the Re_d depended on overheat ratio ($OHR = R_{wire, To per} / R_{wire, To}$) and tunnel temperature. For any given run the variation was half of this range. Statistical confidence in the calibration constant found from a given run was limited by the small Re_d range relative to the large fluctuations in the data due to flow noise (for HW data taken downstream of the grids). The following conclusions were drawn on the use of this method:

- 1) $Re \text{ exp} = 0.51$ fit the data well with the calibration going through the origin as per theory.
- 2) Using $Re \text{ exp} = 0.51$ and a fit through the origin gives a run to run repeatability of the calibration constant found to be within 2%.
- 3) Certain factors were isolated and can be controlled to allow for more consistent calibrations.

Of the hot-wire data collected, it was found that useful data were taken on four different days (9 runs total), with several different HW's, both PHW and UHW, covering the range of Reynolds numbers from $30 < Re_d < 54$, including the range used for grid measurements. The data shows that the best fit to the data (for a linear fit on a Nu vs. $Re^{0.51}$ plot) should not include the data prior to the initial peak in tunnel pressure. This initial data forms a "tail" that does not lie along the straight line through later data and can be attributed to lag time of some sensors. Looking only at the data after this initial peak and while the cascade throat is choked provides a straight line fit to the data with an approximately $\pm 5\%$ variation on the slope (when line is not fit through origin). This variation seemed largely independent of which wire was used, whether a grid was upstream of the wire, or at what Re_d range the calibration was performed.

The mean Re exponent that best fit the above data was very close to 0.51, allowing the statement that the theory is validated to the accuracy of these measurements. Setting Re exponent equal to 0.51 allows a run to run variation in slope (calibration constant) of $\pm 2\%$ as quoted above. The resulting uncertainty in measured velocity is then something like $\pm 5\%$ based on a one-run calibration using this method. The most significant conclusion, however, is that Eqn (3.6) has been validated for use with the grid measurements. The method discussed here is given in the code Hwcal.FOR in Appendix B.

3.2.2.4 PHW passage calibration

The issue of hot-wire calibrations for velocity measurements above the heat flux sensors is a different matter than for grid turbulence measurements. The focus of the PHW measurements is the interaction in the time and frequency domains between velocity and heat-flux. Frequency domain comparisons (e.g. coherence, time and phase shift, and the integral time scale) do not require that a hot-wire be calibrated at all. However, in order to measure mean and fluctuating velocities, or length scales based on mean velocity, a calibration must be performed. This can be done by two methods.

The first method is to calibrate the hot-wire in the upstream flow of known Mach number. This method requires a separate tunnel run prior to passage measurements, and the wire to be moved. There also are uncertainties introduced due to different tunnel conditions, drift in calibration with time, and the fact that the Re_d of the wire in the upstream flow is below that of the wire in the higher speed flow on the suction side, and above that of the wire on the pressure side. Nonetheless, the accuracy is still believed to be good.

The second calibration method is based on the known Mach number distribution at the edge of the boundary layer along the blade surface. For the near-wall hot-wire measurement points, it is assumed that the velocity at that point can be taken from previous wall static pressure measurements on the blade at that point. This calibration method was investigated with the PHW probe above DS1 and this calibration compared to an independent upstream calibration with the same wire. The two methods produced values of C that agreed within 1%, and within the uncertainty of wire location with respect to the measured Mach number distribution.

Mean velocity is not required to find turbulence intensities because Tu is a normalized value. Equation (3.6) above can be simplified further to allow simple linearization of the hot-wire voltage signal. For the short period of high-speed data acquisition, flow temperature and pressure are nearly constant. Therefore Eq. (3.6) above reduces to:

$$U = V^{2/0.51} \frac{\mu_m}{\rho_m} \left[\frac{C}{(T_m - T_s)k_m} \left(\frac{T_m}{T_s} \right)^{-0.17} \right]^{1/0.51}$$

simplified to:

$$U = C_{linear} V^{3.92} \quad (3.8)$$

In this equation, C_{linear} is now a new calibration constant that is a function of temperature, pressure, and Mach number. Thus, for a given set of measurements at similar Mach number with the same hot-wire (e.g. above one HFM) this simple linearization allows comparison. For the purposes of calculating Tu , however, C_{linear} does not need to be known. By reworking the equation in this form, a linearization of hot-wire voltage is effected, which allowed data to be processed in Matlab using routines developed for the HFM (which has voltage output linear with respect to heat

flux). For the PHW data presented in this work, the mean hot-wire voltage ($V^{3.92}$) was recorded as a part of data reduction. The resulting spectral data and mean quantities were then calibrated post-processing within Excel, requiring working with much less data.

This calibration was done by method two above, i.e., the Mach number at the nearest wall PHW position of 0.2 mm was assumed to be equal to the Mach number at that surface location based on a fit to previous blade static pressure measurements for a particular grid. The calibration constant is therefore based on an average of three measurement points corresponding to the three grid conditions for a given wire position. An example of the wire calibration at 0.2 mm above sensor PS1 is presented in Table 3.2. The significant difference in estimated velocities for the different grids in Table 3.2 is related to measured differences in the surface pressure distributions, as will be discussed in section 4.2.4. The shift in the measured points and in the fits to these points can be seen in Figs. 4.2.7 and 4.2.8. As seen in these figures, there were no measurement points near $x = -0.43$ cm where PS1 is located and the fitted curves are at an inflection point indicating higher uncertainties for the estimated velocities in Table 3.2. These estimated velocities were used to calculate the value of C in the second to last column of Table 3.2, and the average of these three values of C used as the calibration at all other points. The calibrated velocity using this averaged value of C is given in the last column of Table 3.2 and shows that the estimated velocities are significantly off at this point (PS1). This calibration method also makes the assumptions that the probe itself is not significantly disturbing the velocity field (see section 3.2.3 for discussion). In addition, this method assumes that the wire (at 0.2 mm) is outside of boundary layer, which is a safe assumption at PS1 and DS1, but may not be true at PS2 and PS3 if the boundary layer is turbulent as predicted by the KEP code (section 5.1.3).

Table 3.2 Example of passage hot-wire (PHW) calibration at $y = 0.2$ mm above PS1.

Grid	Estimated Velocity from P_s (m/s)	T_{tot} (°C)	Linearized PHW voltage ($V^{3.92}$)	C_{linear} (m/s / $V^{3.92}$)	C , as in $Re' = C Nu'$	Calibrated Velocity (m/s)
G0	92.	71.3	19.53	4.78	3317	93.4
G2	103.	70.3	18.96	4.82	3543	91.4
G4	81.	71.3	19.03	4.76	3158	90.6
average					3340	

3.2.2.5 Issue of u' vs. $(\rho v u'^2 + v'^2)'$

There are two issues that must be addressed with the present hot-wire data. First, the present hot-wire measurements are made with a single wire probe aligned with the spanwise

direction. Therefore the wire is sensitive to both u' and v' fluctuations, and largely insensitive to w' fluctuations. The data presented will refer to u' for simplicity sake, but u' should be understood as the vector sum of u' and v' , and not simply a streamwise velocity fluctuation.

Secondly, the measurements have been made in mildly compressible flow. The measurements upstream behind the grids are in an inlet flow of $M = 0.36$, while on the pressure side $M \approx 0.3$, and above the suction side DS1, $M = 0.5$. In this low-compressible regime, density fluctuations are not negligible, and the u' at these locations will include the fluctuating density according to Eqns. 3.6 and 3.7 where

$$Re' = \left(\frac{\rho_m U}{\mu_m} \right)^{0.51}$$

No simple method can be used to separate density from velocity fluctuations, although density fluctuations are usually assumed to be much less than velocity fluctuations. This assumption has been made for the present data. However, if this assumption is not made, then the " u " fluctuations in this paper actually represent

$$\left(\rho \sqrt{u^2 + v^2} \right)' \quad (3.9)$$

3.2.2.6 Calibration uncertainty

Calibration uncertainty of resulting velocity is strongly dependent on the slope of the Nu vs. $Re^{0.51}$ fit in that velocity goes approximately as the slope squared ($C^{1.92}$ as seen in Eqn. 3.6). As noted in the discussion of the dropping tunnel pressure calibration (section 3.2.2.3), this uncertainty is approximately $\pm 5\%$. The grid measurement calibrations were done using the one point method where a calibration constant, C , was found for each data sample (at each traverse location) and these were in turn averaged to give a mean C for that run. This averaged value of C should produce an uncertainty lower than $\pm 5\%$. Also, because the conditions at which grid data were taken were consistent in terms of Re_d , T_{tot} , T_{wire} (OHR), and P_{tot} , the uncertainty on C for grid to grid comparisons should be further reduced. That is to say, any error related to these consistent factors would appear as a bias error that does not affect grid to grid comparisons.

The uncertainty on turbulence intensity will be less, however, in that the slope, C , is not an issue because Tu is a ratio of velocities. The value of Tu is most sensitive to the Re exponent parameter. This is what prompted the careful investigation of Re exponent based on dropping tunnel pressure. Again, because Re exponent = 0.51 was used in the calibration of all grid data, any error due to using this value will be seen as bias and will not affect grid to grid comparisons. And because the value of Re exponent = 0.51 was confirmed within a few percent for the present data, the Tu values reported in this work can be compared to the literature with similar confidence.

For the PHW measurements, uncertainty on Tu values is similar to that for upstream grid turbulence measurements. Uncertainties on mean velocity are likely higher however, due to the previously discussed calibration uncertainties (section 3.2.2.4) and due to possible probe disturbance as will be discussed in section 3.2.3.3. The total uncertainty on passage velocity measurements (U , u' , Λ_x) is likely closer to $\pm 10\%$.

3.2.3 Limitations/ Error analysis

3.2.3.1 Effect of spectral noise on Tu , Λ_x

Noise in the hot-wire spectra evidenced itself with both the UHW and PHW. In both cases the noise was irregular. As noted in section (3.2.1), there was typically a peak in the spectrum at the point of maximum system frequency resolution between 60 and 100 kHz (depending on velocity).

While UHW measurements in the baseline inlet flow and behind Grid 2 (G2) were free of noise, measurements behind Grid 4 (G4) evidenced a peak near 70 kHz. It is very unlikely that this peak is real flow phenomena due to its high frequency and location in the inertial sub-range of the turbulence where local isotropy should hold true. Also, the spectra of one incomplete set of measurements behind G4 did not contain this peak, and it is this data that allows comparison and estimation of the error caused by the presence of this 70 kHz peak. This comparison was made and appears to confirm some difference between the two data sets. However, the differences between the two sets (approximately 5% for Tu) is within the overall uncertainty of the comparison based on differences in wire location with respect to the grid and calibration of the hot-wire. Therefore, no conclusions can be made except that the total uncertainty is increased, as discussed relative to inlet velocity measurements in Ch. 4.

Noise on the PHW spectra for data taken in the blade passage was sometimes severe at higher frequencies. As noted earlier (3.2.1), this noise seemed related to the age of the wire as well as Re_d (flow velocity). Fortunately, the noise was always above 20 kHz and thus above the majority of flow energy (approximately 90% of the energy is below 20 kHz), and above the frequency of any correlation seen between heat flux and velocity. The method used to find Tu and Λ_x from data with noise is reviewed in the section on data reduction (3.3).

Initial measurements made over DS1 showed this very strong noise above 20 kHz, and necessitated low-pass digital filtering to remove it in order to get Tu and Λ_x . This data was dismissed and the tests repeated. The new data, with an aged wire, produced relatively clean spectra, but also gave Tu and Λ_x values very similar to the discarded data evidencing the usefulness of the noisy data below 20 kHz. This conclusion is important for validating some of the

noisier spectra from the PHW data sets, especially evident in the baseline G0 (no grid) case where no turbulence is present to overpower noise present at higher frequencies.

3.2.3.2 Spatial resolution

As with the HFM, the hot-wire has sensor resolution limits due to sensor size. The wire length of both the PHW and UHW is 1 mm, allowing resolution of scales on the order of 2 mm. Significant work in the past has been done to estimate and correct for the attenuation due to hot-wire length, and this will be reviewed here. In summary, two methods for correcting the hot-wire spectrum are discussed, both based on theoretical models, and giving results that agree fairly well. These corrections are applied to the energy spectrum, and so effect the calculation of Tu and Λ_x , but cannot be used to correct for the loss of coherence.

The first method for correction was documented by Wyngaard (1968), and involves modeling the interaction of flow eddies with the finite wire length. Smol'yakov (1983, pp.194-197) discusses spatial resolution at length, including a review of Wyngaard's derivation and results. The results of Wyngaard are given in graphical form with corrections to the spectrum for dimensionless wavenumber ($k_1 l$) for a limited number of values of η/l where l is the hot-wire length, $k_1 = 2\pi f/U$, and η is the Kolmogorov microscale, $\eta = [\nu^3/\epsilon]^{1/4}$.

The second method relies on the existence of isotropy for the inertial sub-range of the grid turbulence at higher frequencies (local isotropy) as discussed in section (2.3.3). Making this assumption allows correcting the higher end of the measured spectrum to match the isotropic spectrum at these higher frequencies.

The application of these two methods for the grid data is discussed in section (3.3)

3.2.3.3 PHW probe disturbance

Another effect that influences the hot-wire spectrum is the flow disturbance caused by the presence of the PHW itself. Despite the low blockage of the flow due to the PHW (on the order of 1% based on probe frontal area to passage area ratio at DS1), the probe is actually near the surface (Fig 2.1.6) such that it can be expected to cause local flow acceleration. Also, due to the flattened profile of the probe body strut, the strut can act as a lifting body and may cause more disruption when the strut's oval shaped flattened body (Fig. 3.2.1) is not aligned such that the oval's long axis is along the natural streamline of the flow. This was unavoidable when the probe was rotated in order to place the wire at different y locations above the surface but was kept to a minimum by rotation of the plug (instead of the probe) as well as by bending the prongs toward the surface (i.e. customizing the individual PHW probes) to optimize the probe body strut and wire positions.

In general, it seems that the probe disturbance to the measured velocity field is low -- on the order of a few percent. Except for velocity measurements at PS3 (seen in Table 5.3) where blockage is higher due to the narrower passage, and where some probe movement is suspected, the measured velocities look reasonable and consistent. However, no blade surface static pressure measurements were made with the PHW probe in place. Heat flux data shows more of an effect due to the probe presence as evidenced by comparison of heat flux gage measurements with and without the PHW. While no increase in heat transfer with the probe present is seen at DS1, a small decrease is seen at PS1, and an increase near 10% is seen at PS2 and PS3. Disturbance to the velocity field at the wire should be less than the disturbance seen in the heat flux.

3.3 Data reduction

3.3.1 High-frequency data

Apart from low-speed heat transfer data to be presented in Ch. 5, all data samples were 256 KB at 500 kHz, low-pass filtered at 100 kHz. These data were collected on the LeCroy boxes (section 2.2.2) and saved on the PC in binary form. The data were then converted to ASCII format and transferred to the Mechanical Engr. Computer Analysis lab (MECA) in order to process the high-speed data on workstations using Matlab software. The no-PHW heat flux data was run through a program that calculated the power spectral density (PSD) of the heat flux signal with the frequency and corresponding PSD vector written to file.

All PHW data were taken simultaneously with the HFM heat flux signal, and were processed simultaneously. Using the program "hfmphw2.m" (in Appendix B), the two simultaneous heat flux and hot-wire voltage signals were processed to produce 6 column vectors: frequency, hot-wire PSD, heat-flux PSD, cross-spectrum, coherence magnitude, and coherence phase. In addition, "hfmphw2.m" was also used to measure the cross-correlation (time domain) of the two signals, as well as output values for mean heat flux, $Q(V)$, mean hot-wire voltage (linearized voltage, $V^{3.92}$, as discussed in section 3.2.2), Tu , q' , and u' . For the cross-correlation calculation, 10 KB segments were processed, and the average of 20 segments written to file. For the frequency domain calculations, the 256 KB files were broken into 1 KB segments and processed with 50% overlap for a total of 512 averages to the spectral data, and a resulting frequency resolution of 488.3 Hz. These settings seemed to give the best compromise of needed averaging and useful information.

While the auto-correlations of the two signals (PHW and HFM) were initially done in Matlab, this operation is computationally intensive, and averaging of the entire data set is necessary to obtain a clean value. The final method used relied on transforming the already

averaged PSD to obtain the auto-correlation (as discussed in section 2.3.2.2) rather than obtaining the auto-correlation from the time series. An energy spectrum corrected for noise (discussed in the next section) was used to calculate scales. The FORTRAN program "PSD3Lx.FOR" (using Eqns. 2.5 and 2.7 and listed in Appendix B) was used to process the corrected hot-wire spectra and measured heat-flux spectra to obtain length and time scales. In retrospect, "PSD3Lx.FOR" could also have been used to calculate cross-correlations using the cross-spectra output by "hfmphw2.m", and this procedure is recommended for future work.

3.3.2 Tu , Λ_x calculation method for noisy spectra

Noise in the PHW spectra seen at some hot-wire locations was corrected as follows. First, if noise in the baseline (G0) spectra above 20 kHz was present, this was subtracted from the G2 and G4 spectra of the wire at the same y location over a given HFM. This removed some of the noise present in the measured spectra, $E_m(f)$. In addition to this, remaining noise peaks were individually truncated to produce a spectra that followed the decay seen to the right and left of each peak, thus producing a somewhat artificial but clean spectra believed to be very close to the actual turbulent energy spectrum. Call this corrected spectrum $E_{cor}(f)$.

$E_{cor}(f)$ then was used directly to find Λ_x by calculating the auto-correlation using a cosine transformation of $E_{cor}(f)$ according to equation (2.5). Tu was found indirectly from $E_{cor}(f)$ as a correction to the value of Tu measured from the time series. Comparison of the measured spectrum to corrected spectrum allowed forming a ratio that can be applied directly as a correction to the measured value of Tu based on the time series, where according to theory (Hinze, 1975, eqn 1-91)

$$\begin{aligned} \overline{u'^2} &= \int_0^\infty E(f) df \\ Tu^2 &= \frac{\Delta f}{U^2} \sum E_m(f) \end{aligned} \quad (3.10)$$

Basically, the area under the power spectra, $E(f)$, is proportional to u'^2 so that the ratio of the area under $E_{cor}(f)$ to the area under $E_m(f)$ will give the error in u'^2 due to noise in the spectrum.

$$\frac{\overline{u'^2}_{corrected}}{\overline{u'^2}_{measured}} = \frac{\int_0^\infty E_{cor}(f)}{\int_0^\infty E_m(f)}$$

and

$$\frac{Tu_{corrected}}{Tu_{measured}} = \sqrt{\frac{\sum_0^{250kHz} E_{cor}(f)}{\sum_0^{250kHz} E_m(f)}} \quad (3.11)$$

The resulting spectral information from the high frequency Matlab data processing was input to Excel spreadsheets. Post-processing of the hot-wire spectra to find $E_{cor}(f)$ was done within Excel. Also, the integration presented above to find $Tu_{corrected}$ was done in Excel simply by summing the two columns of data ($E_m(f)$ and $E_{cor}(f)$). The corrected Tu ratio was then the square root of the ratio of these two column sums.

To be accurate and fair, there was no correcting done on the hot-wire spectra measured above PS1 (the location nearest the leading edge on the pressure side), and only minor editing done to the measured spectra at locations PS2 and DS1, with a reduction in measured energy of approximately 6% corresponding to a reduction of Tu of approximately 2.5%. Noise on the PHW spectra at location PS3 was more severe with reductions in Tu around 50%. In addition, the heat-flux spectra was apparently free of any noise and therefore no corrections were made. The heat flux integral time scales were determined from the auto-correlation as calculated directly from the transformed measured heat flux energy spectra, $E_q(f)$.

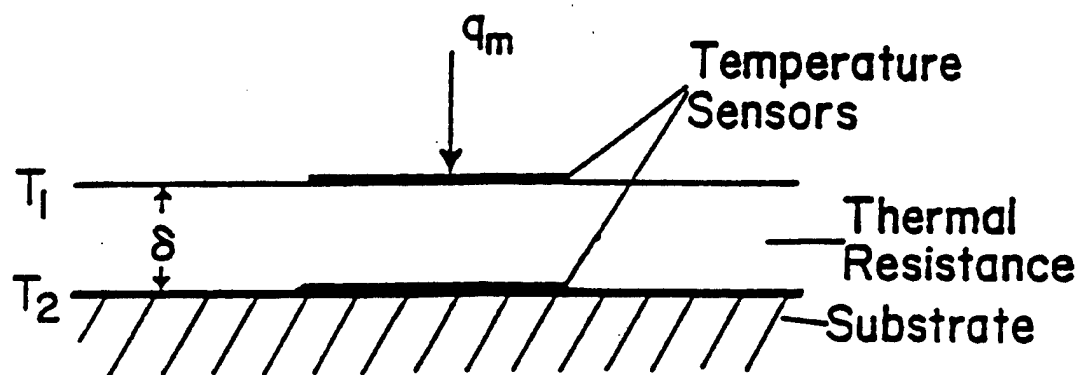


Figure 3.1.1 Heat Flux Microsensor resistance layer cross section.

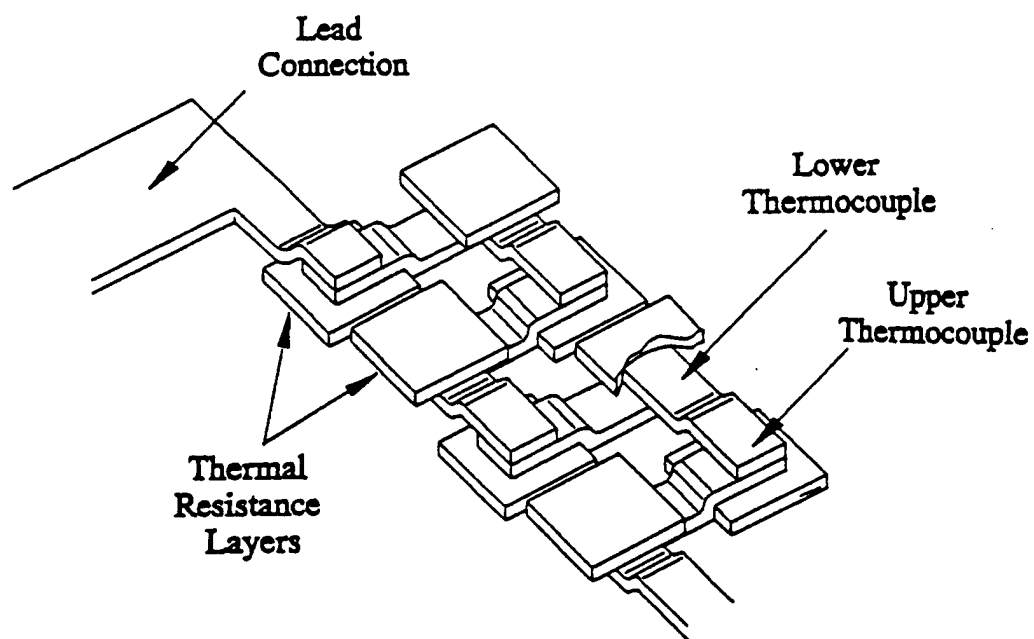


Figure 3.1.2 Sputtering pattern of HFM thermopile.

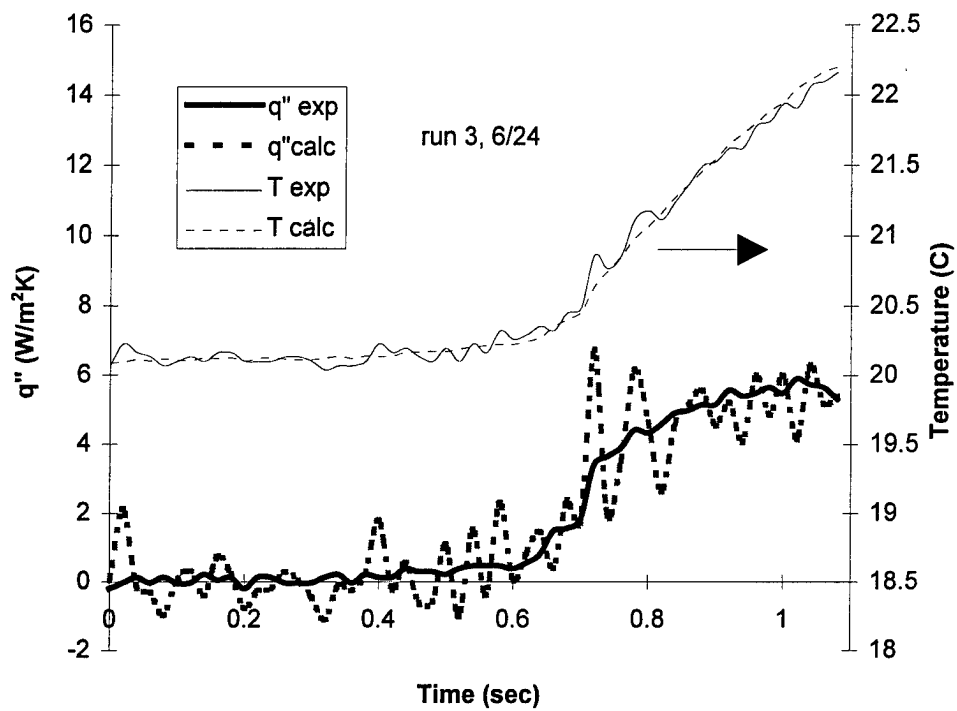


Figure 3.1.3 Output from the conduction calibration of DS1 using the code QT.FOR to convert heat flux to temperature.

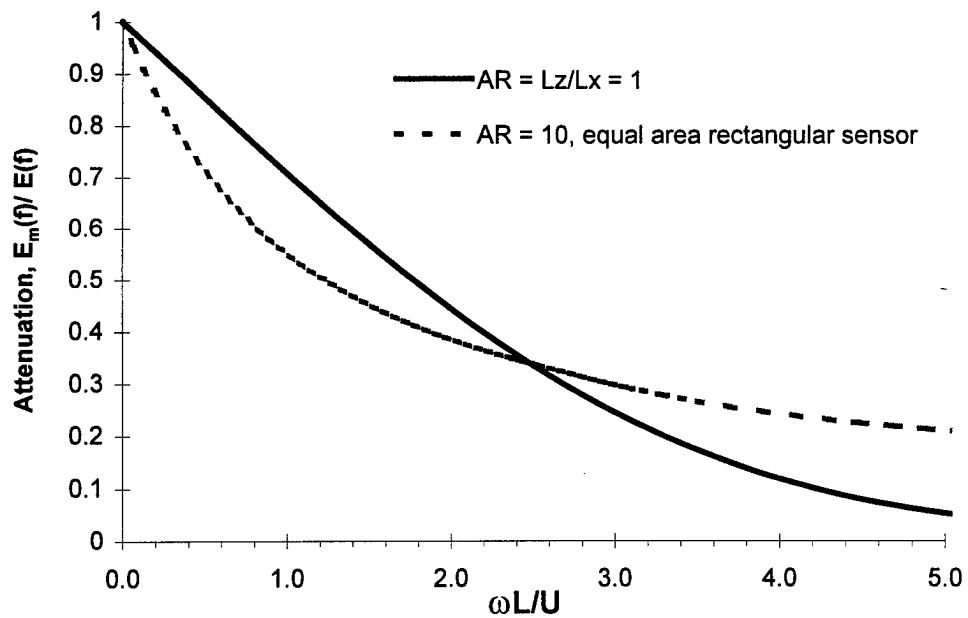


Figure 3.1.4 The Corcos correction comparing a rectangular sensor to a line sensor of equal area.

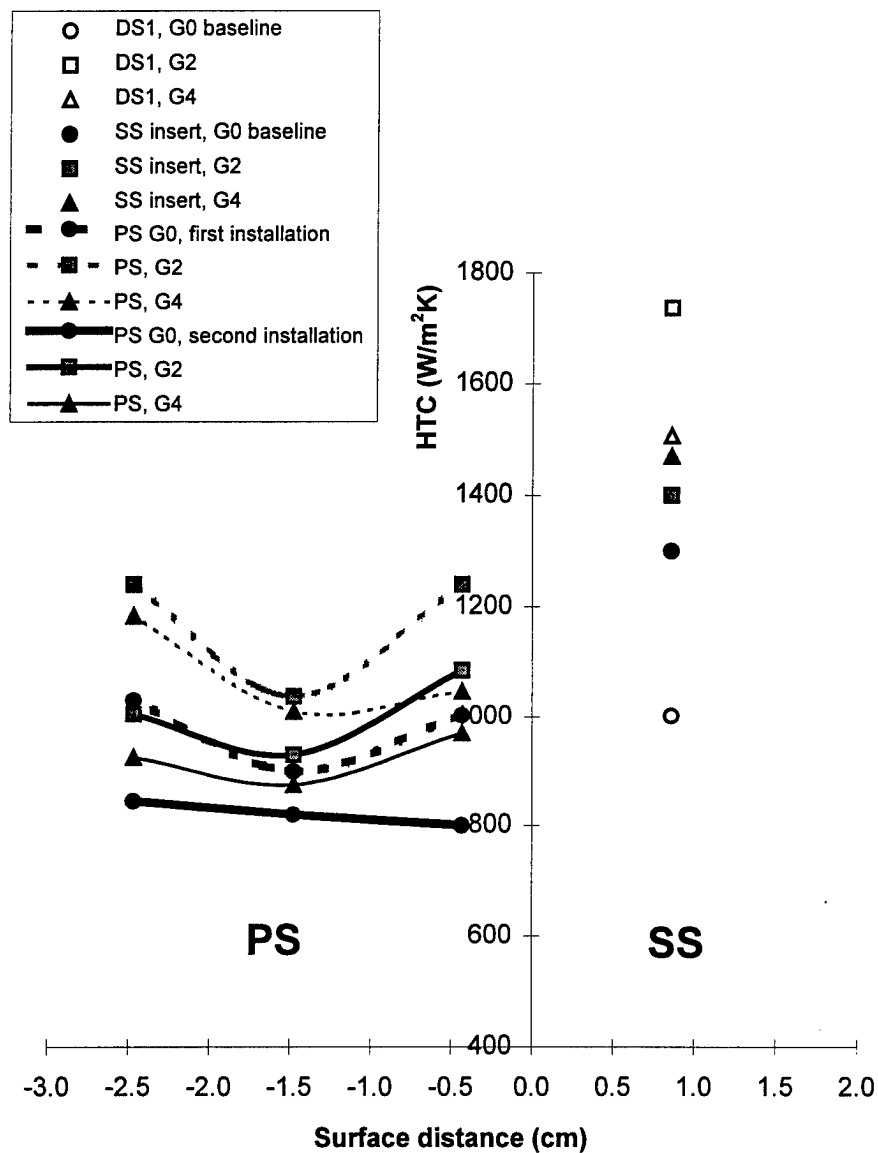
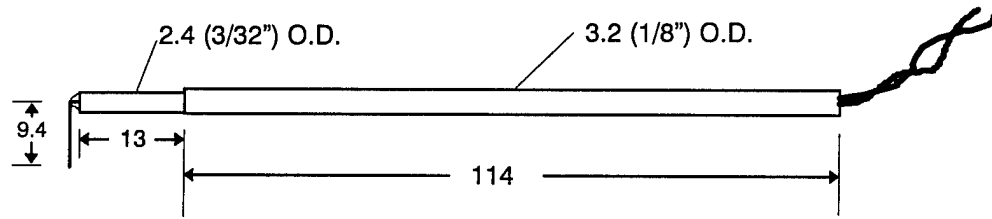


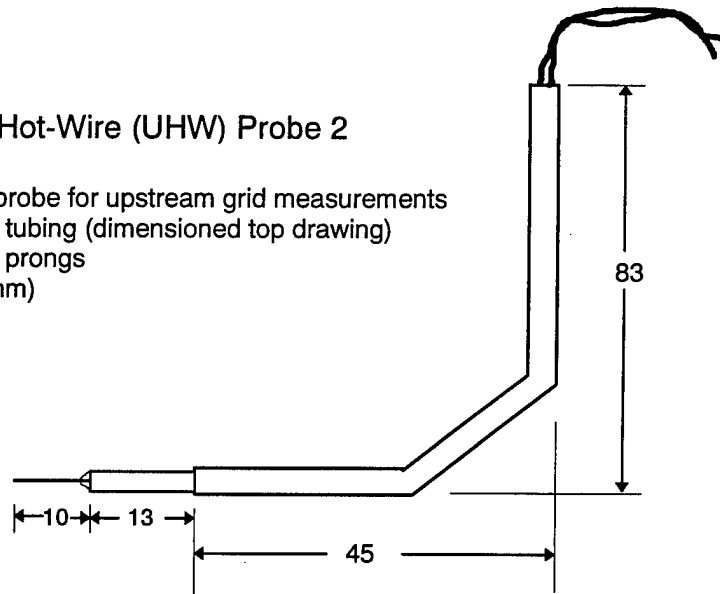
Figure 3.1.5 Heat Flux gage disturbance, comparison of two insert gage installations on pressure side, and insert vs. direct sputtered gage on suction side.

Upstream Hot-Wire (UHW) Probe 1



Upstream Hot-Wire (UHW) Probe 2

Single U-wire probe for upstream grid measurements
Stainless steel tubing (dimensioned top drawing)
Stainless steel prongs
Dimensions (mm)



Passage Hot-Wire (PHW) Probe

Single U-wire probe for passage

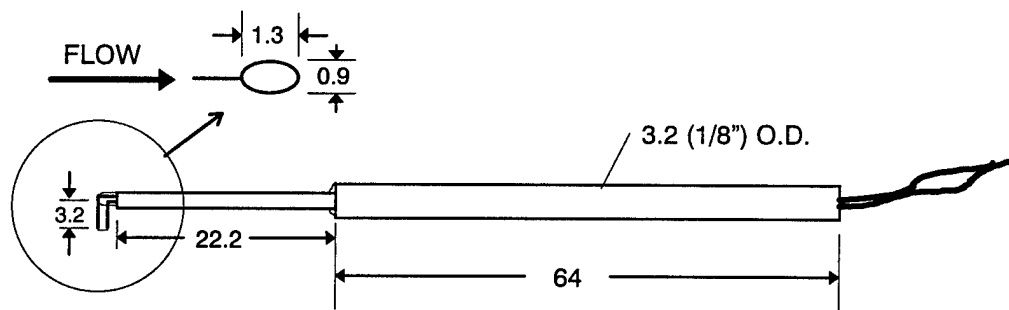


Figure 3.2.1 Hot-wire probes.

4. Inlet Conditions

4.1 *Baseline, No Grid (inlet velocity survey)*

4.1.1 Inlet traverse, Tu , Λ_x

Hot-wire measurements of the inlet flow to the cascade were made using the Upstream Hot-Wire (UHW) probe described in Ch. 3 according to the procedure given in section 2.4. The measurements were made using a traverse mechanism mounted above the test section and which allowed traversing vertically at the mid-span at two locations upstream of the blade row.

The intent of the upstream traverses was primarily to examine the frequency content of the incoming flow to the test section. Secondary to this was looking at flow uniformity. The baseline (no grid, G0) velocity and frequency content across the test section were mapped out at 6.4 mm (0.25 in.) intervals in y .

As mentioned in the facility introduction, immediately upstream of the test section is a contraction from a round pipe, Fig. 2.1.1. Upstream of this, in order, is a settling chamber, a small mesh turbulence reduction screen, a 6.4 mm thick steel plate lying horizontally in the center of the pipe ("flapper valve"), and a bank of copper tubing for thermal storage. The presence of the flapper valve with its wake and turbulence generation was originally a concern. Results of inlet surveys prior to and after installation of the turbulence reduction screen show that the screen effectively reduces the large majority of undesired flow energy.

Mean velocity across the test section was found to be uniform within 2% outside the top boundary layer. A plot of turbulence intensity versus vertical distance below the test section top wall is shown in Fig. 4.1.1, where the intensity at the inlet to the instrumented passage (noted by the dashed line at 4.5 in. below the top wall) is near 0.25%. The majority of the energy which contributes to this intensity is below 2 kHz. Length scales corresponding to this low-frequency range should be regarded as unsteadiness (random passing structures) and not eddies in a uniform turbulence field. For example, a length scale corresponding to 2 kHz in the 120 m/s flow would be $(120\text{m/s}) / (2\text{kHz}) = 6\text{ cm}$, which is larger than the test section width of 5.1 cm. The integral length scales based on this low-frequency energy are similarly larger than the test section. This effect makes the integral length scales for such flows (very low-frequency non-isotropic non-continuous turbulence) unrealistic. Therefore, integral length scales for the baseline G0 case will not be presented.

4.1.2 Time series and spectra

The time series at several measurement locations across the inlet of the test section are shown in Fig. 4.1.2. The high intensity in the top wall boundary layer is seen in the first signal trace

of Fig. 4.1.2, while the edge of the boundary layer with intermittent turbulence can be seen in the second trace (approximately one inch below the test section top wall). Inlet fluctuations representative of the center of the test section are seen in the third trace, where some low frequency energy is seen on top of the small higher frequency energy.

The baseline G0 turbulence spectrum at the center of the test section is primarily low-frequency, with no measurable energy above 20 kHz relative to the noise level. Most of the flow energy is below 2 kHz, as will be seen in chapter 6 for the near blade measurements. As noted in the previous section, this low frequency energy should be regarded as unsteadiness due to upstream structures that are not fully diffused by the small mesh screen upstream of the contraction preceding the entrance to the test section. However, this inlet energy level is well below that produced by the turbulence generating grids by approximately two orders of magnitude.

4.2 Grids

4.2.1 Tu and Λ_x

4.2.1.1 Data and correlations

Measurements behind Grids 2 and 4 will be presented here. Grids were moved upstream as far as possible in the test section for these measurements. The grids were at approximately 20 cm (8 in.) upstream of the blade row inlet plane, allowing measurements only in the 20 cm downstream of the grids. Both UHW probes (Fig. 3.2.1) were used for these measurements.

Turbulence intensity, Tu , and integral length scale, Λ_x , measurements vs. distance downstream of Grids 2 and 4 (G2, G4) are presented in Figs. 4.2.1 and 4.2.2, with fits correlating the data given on the figures. The G2 intensity is seen to drop much more rapidly than for G4, as expected for its smaller grid size with the $Tu = 5\%$ location near 3 cm downstream of G2, but at 12 cm downstream of G4. The corrected values given on the plots are based on the methodology to be presented in section 4.2.3. The normal grid theoretical Tu decay curves are shown as dashed lines on the figures and will be discussed following the next section.

4.2.1.2 Uncertainties

Estimated error in the fits to measured Tu and Λ_x for G2 and G4 in the previous section are shown as error bars. The uncertainties on measured Tu are different from those on Λ_x . Tu is not subject to uncertainties on mean velocity, while Λ_x uncertainty does include this as well as the more difficult issue of accurately measuring the integral time scale (T_x , equal to the area under the

auto-correlation) in the presence of non-isotropic low-frequency disturbances, as discussed in section 2.3.2.2.

For G2, the greatest uncertainty in Tu near the region of interest around $Tu = 5\%$ is due to the rapid decay of intensity in this near-grid region. The correlating fit was chosen with an eye to matching the data at the $Tu = 5\%$ point as well as data farther downstream. Total uncertainty on Tu is judged to be approximately $\pm 6\%$ (e.g. $Tu = 5.0 \pm 0.3\%$). Uncertainty in Λ_x is most influenced by the difficulty mentioned above, i.e. that of accurately measuring T_x in non-isotropic flow. Generally an estimate on integral length scale is not better than $\pm 10\%$, especially in the near grid region.

For Grid 4 (G4), the rapid decay of intensity is not as much an issue simply because of the expanded scale and greater certainty resulting in measuring downstream distance (the same $Tu = 5\%$ point is now 12 cm downstream rather than 3 cm). Equal uncertainty is created by the slight noise seen in the spectrum near 70 kHz. Total uncertainty on Tu can also be judged by comparison of different data sets taken using different hot-wires traversing behind the grid on different days. Based on discrepancies between these data, a total uncertainty of $\pm 5\%$ is estimated.

4.2.1.3 Comparison to normal grid theory

As discussed in section (2.3.4), normal grid theory may apply to the grid turbulence for the region beyond 10 grid dimensions downstream assuming that the test-section side-wall is not interfering significantly and assuming the slant of the grid does not affect the results. As discussed, the ratio of G4 grid dimensions to test-section width of 2.6 indicates that the test section walls will almost certainly interfere with G4 turbulence development. G2 will be more likely to follow this theory.

As seen in Fig. 4.2.1 the decay of Tu for the two grids does follow the $-5/7$ power law indicated by normal grid theory in the far-field beyond 10 grid dimensions downstream. Due to differences in size and interactions with the test section walls, the slant, and other factors as discussed in section 1.3.4, the correlations are seen to differ from one another as well as from normal grid theory. Also, there appears to be some turning of the flow induced by G2 that would alter the near-field behind that grid. This effect will be discussed in section 4.2.4.

Length scale growth compared to theory can be seen in Fig. 4.2.2. Despite the differences in constants for the decay of Tu , G2 length scale is not far from the theory. G4 however shows a slower growth, as should be expected considering that side-wall influence would restrict larger scales in the flow.

4.2.2 Inlet One Dimensional Power Spectra

4.2.2.1 G2, G4 @ $Tu=5\%$

The energy spectra downstream of G2 and G4 at their individual points of $Tu = 5\%$ are presented in Fig. 4.2.3. These are the measured energy spectra for the grids at the streamwise locations downstream of the grids corresponding to the entrance to the blade row (inlet turbulence, “blades removed”). Note the proportion of energy in G4 concentrated at low frequencies which gives it the larger length scale compared to G2.

4.2.2.2 G2 psd series at different Tu

An example of the decay of the energy spectrum behind G2 is shown in Fig. 4.2.4. These spectra correspond to measurement points in the vertical traverse with the UHW probe. Non-isotropy is evident at the lower frequencies and more-so for the spectra nearer the grid (higher Tu) but settles as the intensity drops.

4.2.2.3 Comparisons to Isoturbulence

The isoturbulence spectrum, as discussed in chapter 1, is shown in Fig. 4.2.5 along with the spectra for G2 and G4. According to the theory of local isotropy, higher frequency small scale turbulence exists essentially independently from the more non-isotropic turbulence containing it, and can be considered isotropic. Thus, the measured spectrum should follow the isotropic turbulence fit at higher frequencies, following Von Karman's $-5/3$ power law decay. Clearly the measured G2 spectrum falls below the isoturbulence spectrum which can be attributed to hot-wire length issues, as discussed in 3.2.3. The measured G4 spectrum follows the isotropic fit to higher frequencies and comparisons of the measured spectrum and corrected spectrum (to be discussed) show the difference in energy to be within measurement error.

4.2.3 Correction for high-frequency attenuation

As discussed in Ch. 3, two methods of correcting the energy spectrum are possible. The first involves correcting the higher frequency end of the spectrum to match the isotropic turbulence spectrum at these higher frequencies. This method was used to correct the present G2 measurements resulting in the Tu and Λ_x correlations presented in the previous section. The second method, based on the work of Wyngaard (1968) will be shown to support the validity of correcting the spectrum with the isotropic turbulence spectrum.

4.2.3.1 Correction based on isoturbulence

The true issue at hand is estimating the error in Tu and Λ_x due to spatial averaging. The method used requires matching the measured spectrum to the isotropic spectrum. The validity of

this correction rests on the theory of local isotropy for the higher frequencies. This theory states that smaller scale turbulence exists essentially independently from the more non-isotropic turbulence containing it, and that it can be considered isotropic, and thus will follow the isotropic turbulence fit expressed in Eq. (2.8), following Von Karman's -5/3 power law decay at high frequencies. Equation 2.8, repeated here is

$$\frac{E(f)U}{\overline{u'^2} L_x} = \frac{4}{\left[1 + \left(\frac{8\pi f \Lambda_x}{3U}\right)^2\right]^{5/6}}$$

The measured spectrum $E_m(f)$ is put in place of $E(f)$ in the equation above and both the right and left hand of the above equation are then plotted versus $f\Lambda_x/U$. The values of Tu and Λ_x are then adjusted to get a "best fit", such that the isotropic spectrum goes through $E_m(f)$ in the mid-frequency range. Above some frequency there is significant attenuation of $E_m(f)$ due to spatial resolution of the hot-wire. At lower frequencies there is some non-isotropy due to proximity to the grids as well as attenuation of the lowest frequency due to the narrow test. Therefore the isotropic spectrum (a function of Tu and Λ_x) is fit through the mid-frequency range of the spectrum.

When these "best fit" values of Tu and Λ_x are found, the resulting plot will look like the figure presented earlier in the G2 vs. isoturbulence comparison, Fig. 4.2.3. The approach used to find corrected values of Tu and Λ_x is similar to the method presented in Ch. 3 for correcting the energy spectrum of the hot-wire. In that case, the measured spectrum, $E_m(f)$, was processed to remove noise peaks producing a corrected spectrum, $E_{cor}(f)$. The ratio of the integrals of these two spectra was then used to correct the measured Tu , while Λ_x was calculated from a cosine transformation of $E_{cor}(f)$. For the present case, the isotropic spectrum, $E_{iso}(f)$, is assumed to be correct above the frequency where $E_m(f)$ rolls off and falls below $E_{iso}(f)$. A corrected spectrum is formed by combination of these two spectra. $E_{cor}(f)$ was formed in Excel according to:

$$E_{cor}(f) = \sum_0^{20kHz} E_m(f) + \sum_{20}^{250kHz} E_{iso}(f)$$

As before, the ratio of $E_{cor}(f)$ to $E_m(f)$ is used to correct Tu according to Eqn. 3.11 although in this case the corrected Tu will be higher than that measured, while the noise application reduced the measured Tu . As calculated from $E_{cor}(f)$ using the program "psd3lx.for" (Appendix B), Λ_x will decrease here because energy is effectively being added to the high frequency end of the spectrum.

This produced values of Λ_x and corrected Tu for each individual downstream location for Grid 2. Results show that attenuation at the $Tu = 5\%$ location behind G2 was on the order of 15% (i.e. $Tu_{corrected}/Tu_{measured} = 1.15$), with progressively less attenuation farther downstream as length scale grows (and the high-frequency end of the spectrum is proportionately less of the whole). For

G4 the attenuation was hard to determine due to the uncertainty associated with the apparent electronic noise around 70kHz. No significant difference was found between the isotropic turbulence fit and the measured spectrum, and no correction was used.

4.2.3.2 Comparison to Wyngaard's correction

An alternative to assuming isoturbulence at higher frequencies is to correct for lost energy based on theoretical estimates as a function of wire length. The application of this method agrees well with the preceding isoturbulence correction.

In order to apply the Wyngaard correction (see section 3.2.3), an estimate of η/L_w must be found for the present grid measurements, where η is the Kolmogorov microscale (or dissipation scale) and L_w is the hot-wire length. One method involves a simple approximation given by Smol'yakov (1983) which for turbulence downstream of a grid the dissipation can be estimated as $\varepsilon \approx U^3/L_g$, where U is the flow velocity, and L_g is the grid characteristic length. For the present measurements, $U = 120$ m/s, and a length scale of $L_g = 3$ mm gives $\varepsilon \approx 6 \times 10^8$ (m²/s³).

A second method for estimating dissipation involves fitting Kolmogorov's -5/3 law to the higher frequency end of the energy spectrum. This method is outlined and used by Ames and Moffat (1994) to get dissipation from their data, and this method does not rely on isotropy present behind a grid but instead on the local isotropy present at high frequencies. Using this method at the 1 mm hot-wire locations above the gages near the leading edge gives higher dissipation values on the order of $\varepsilon \approx 10^{11}$ (m²/s³).

Taking the lower dissipation value, Kolmogorov's dissipation scale, η , can then be estimated, where for the conditions at which the grid data were taken

$$\mu = 18.46 \times 10^{-6} \text{ (kg/ms) (air @300K)}$$

$$\rho = 2.38 \text{ (kg/m}^3\text{)}$$

$$\nu = 7.76 \times 10^{-6} \text{ (m}^2\text{/s)}$$

$$\eta = (\nu^3/\varepsilon)^{1/4} = 2.8 \mu\text{m}$$

Then, for a hot wire length of 1mm

$$\eta/L_w = 0.0028$$

Based on the above calculations, a value of $\eta/L_w = 0$ applies to the present grid data and implies that the smallest length scales in the flow are much smaller than the length of the hot-wire. Wyngaard's correction for $\eta/L_w = 0$ is given in graphical form in Fig. 4.2.6, where the correction is given as attenuation (E_m/E = measured energy over true energy), at several discrete values of η/L_w from 0 to 1, versus normalized frequency ($k_1 L_w$, where k_1 is the wavenumber and $L_w = 1$ mm). An exponential fit to Wyngaard's discrete $\eta/L_w = 0$ points is given in the figure. The wavy line in

Fig. 4.2.6 is the E_m/E based on the isotropic turbulence correction used with Grid 2 (where E is taken as $E_{cor}(f)$). The isotropic turbulence correction predicts more rapid attenuation at higher frequencies (above $k_1 L_w = 2$ equivalent to $f = 38$ kHz) and if correct shows that the hot-wire frequency attenuation is rolling off faster than expected based on Wyngaard's correction. Fig. 4.2.6 also indicates that if the Wyngaard correction were used for the present data, Kolmogorov's $-5/3$ power law decay would not be realized at higher frequencies.

4.2.4 Grid effect on blade potential flow field

The presence of the grid themselves is likely to cause some flow distortion coming into the blade row beyond the desired near-isotropic turbulence augmentation. Distortion may be due to increased sidewall boundary thickness, as well as turning of the flow downward due to the inclination of the grid. A turning in the flow is believed to occur by the following mechanism: the grids are lying at 58° to the flow such that, for Grid 2, there is almost no open area visible when the grid is viewed along the straight flow path parallel to the test section top wall. This means that the flow must turn downward to pass through the grid plane before it quickly recovers to its previous straight path. However, for Grid 2, the grid plane is very close to the blade row. The result is an angle of attack on the blade leading edge believed to be present for Grid 2 but not for Grid 4. This effect is unavoidable and is due to the slant of the grid which is required to maintain a constant turbulence intensity at the slanted blade row inlet plane, coupled with the small grid size requiring the grid plane to be located close to the blade leading edge.

Tests performed to investigate these possibilities include sidewall boundary layer hot-wire measurements as well as blade surface static pressure measurements. The grids have a wall thickness of 1.0 mm (0.040 in.) with an effective blockage at the sidewalls in some places greater than this due to the grid wall not being exactly flush with the test section wall, and also due to the presence of welds at the grid screen/ frame junctions. The presence of flow separation behind the step created by the edge of the grid frame was not found in the simple boundary layer probing that was done. No measurements of the baseline inlet sidewall boundary layer are available for comparison.

Blade surface static pressure measurements were made with two blades instrumented with a total of 17 taps read by the PSI system. Surface pressures along the pressure and suction sides of the blade were measured for the baseline, G0, and grid cases, G2 and G4. The results for the averaged pressure distributions over several runs are shown in terms of Mach number in Fig. 4.2.7 where the actual data points are shown as symbols. The same data near the leading edge in terms of static pressure is shown in Fig. 4.2.8. Fits to the measured data, drawn by hand, are also plotted with reference to a numerical code predicted pressure variation also shown on the figure. The Grid 4 pressures nearly agree with the baseline G0 pressures and these close to the

numerical code prediction. Grid 2, however, appears to have a significantly distorted pressure distribution, evidencing what seems to be a shift in the stagnation point toward the suction side.

The fits to the data points in Fig. 4.2.8 were used to calculate near-surface free-stream velocity above the heat flux sensors for the different grids in order to calibrate the hot-wires as well as to obtain length scales. The effect of the distorted G2 pressure distribution on heat transfer will be discussed in the next chapter.

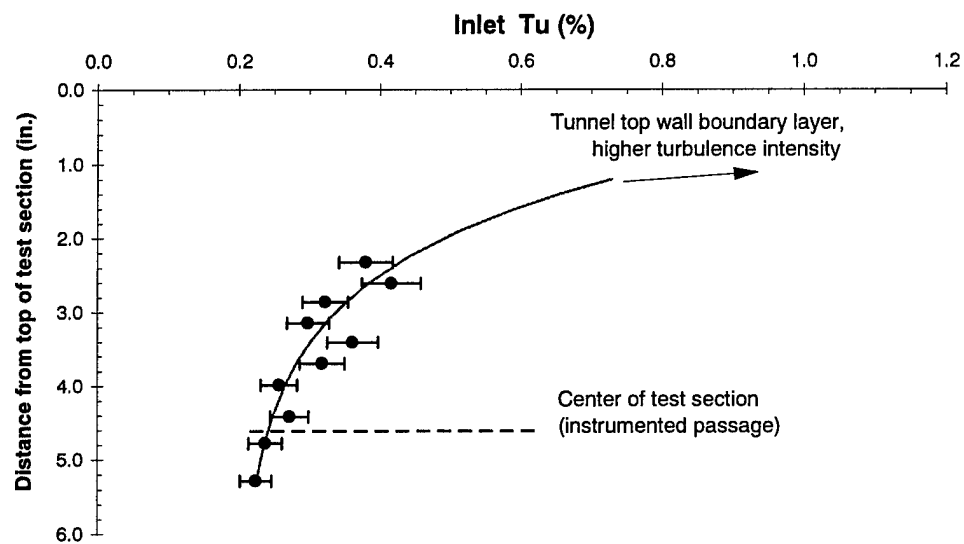


Figure 4.1.1 Baseline G0 upstream inlet flow traverse intensity (Tu).

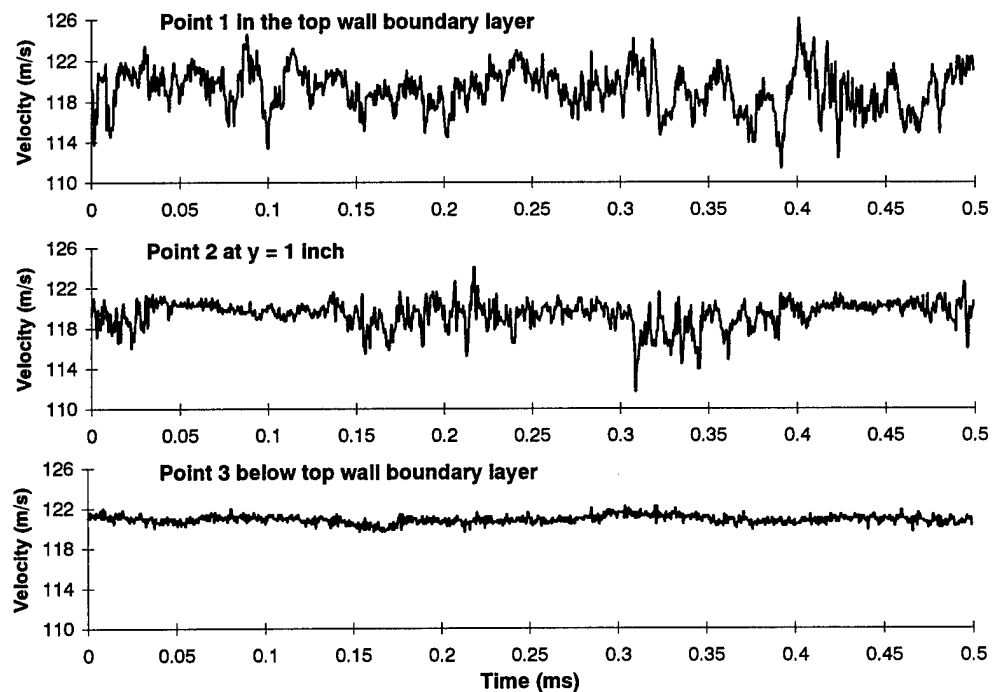


Figure 4.1.2 Time series showing nature of inlet flow at different distances below test section top wall boundary layer.

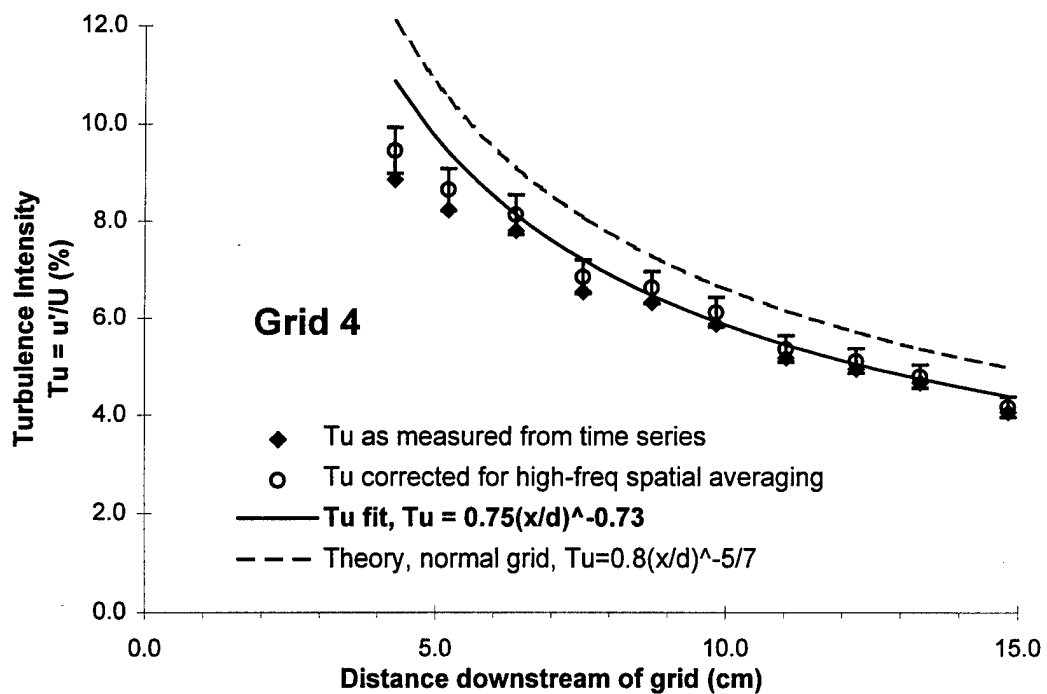
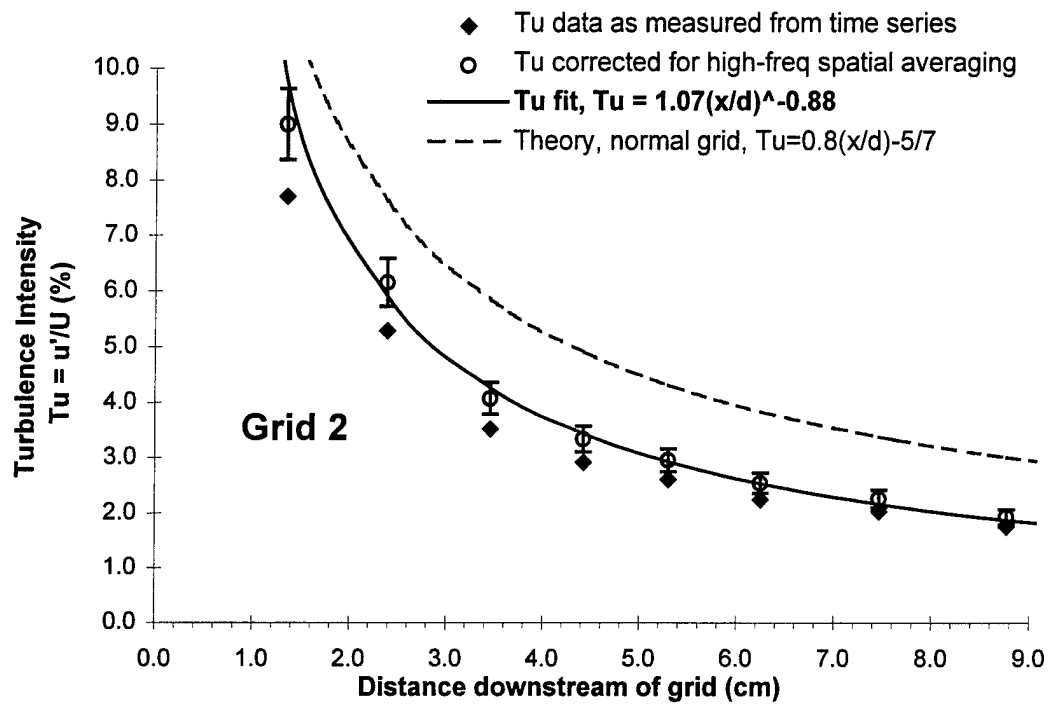


Figure 4.2.1 Grid turbulence: Tu decay behind G2 and G4, $U = 120$ m/s.

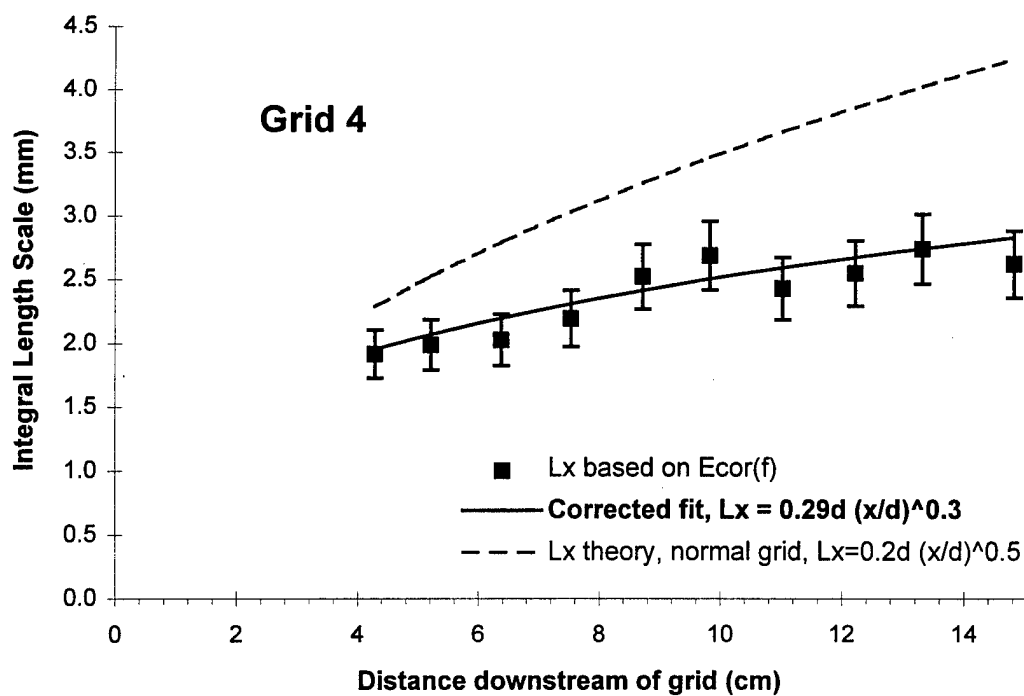
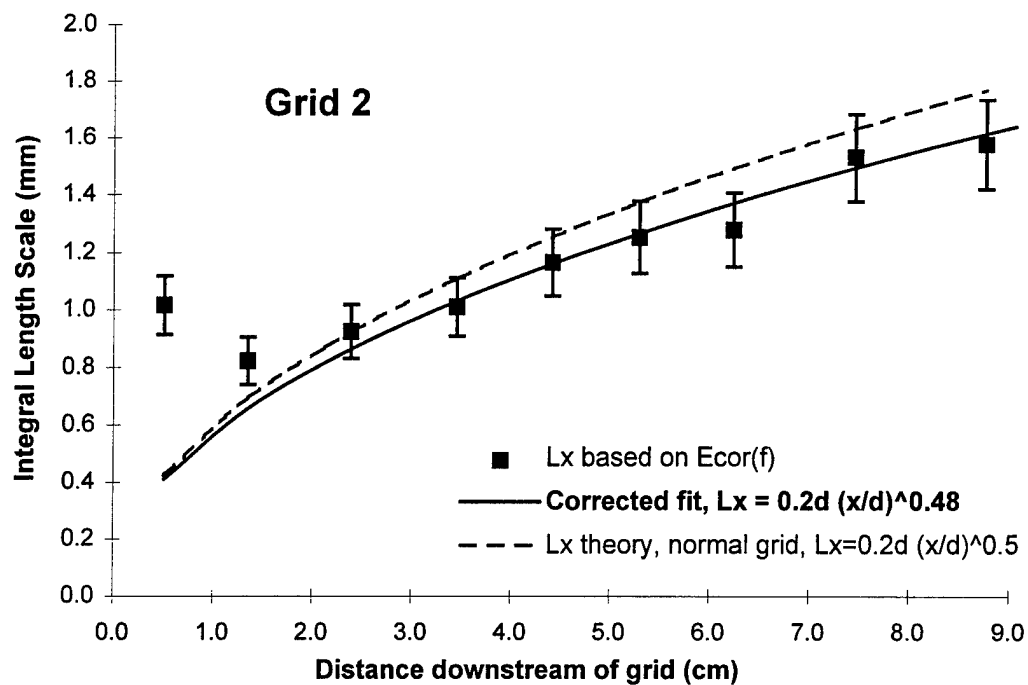


Figure 4.2.2 Grid turbulence: Λ_x growth (integral length scale) behind G2 and G4.

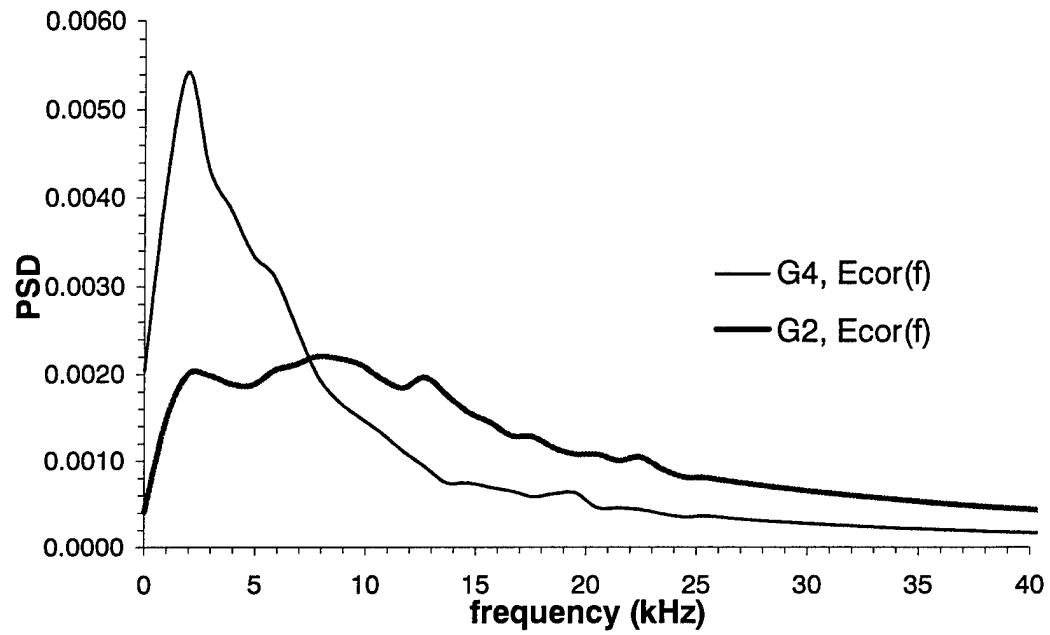


Figure 4.2.3 Comparison of Grid 2 and Grid 4 at $Tu = 5\%$ locations.

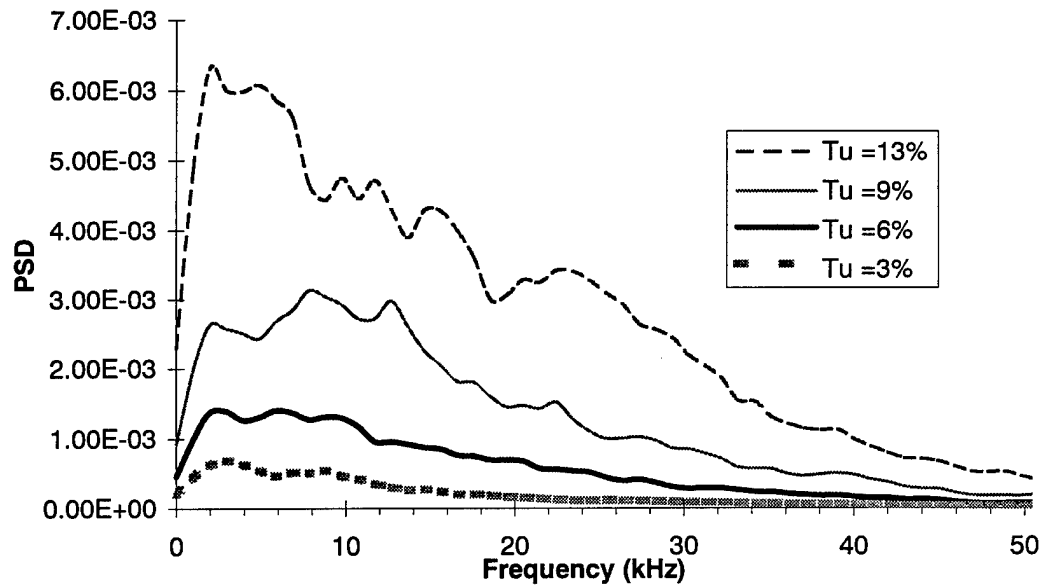


Figure 4.2.4 Decay of energy spectrum behind Grid 2.

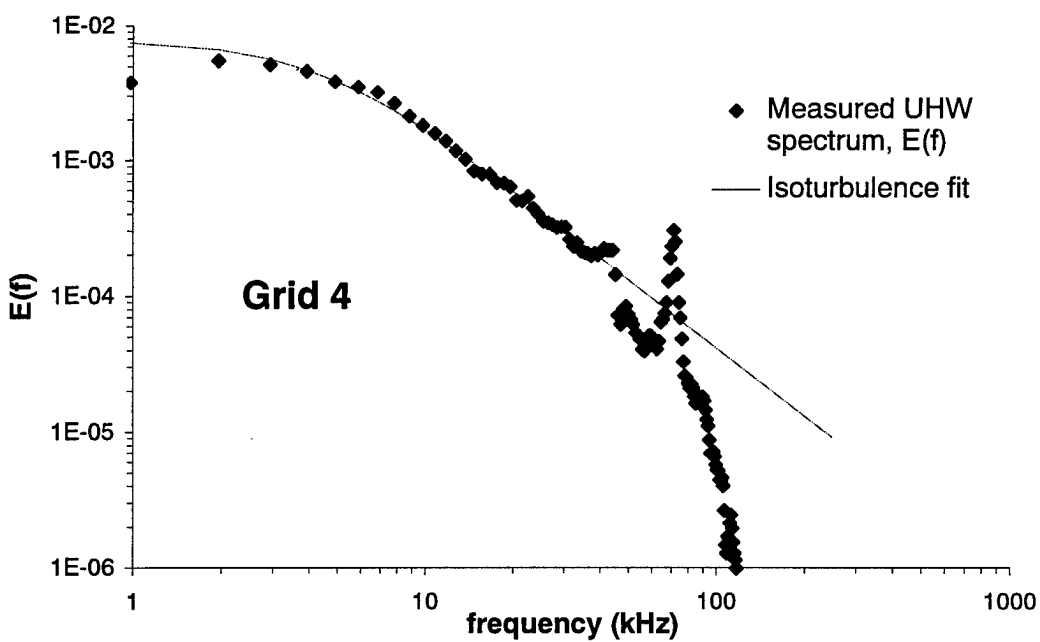
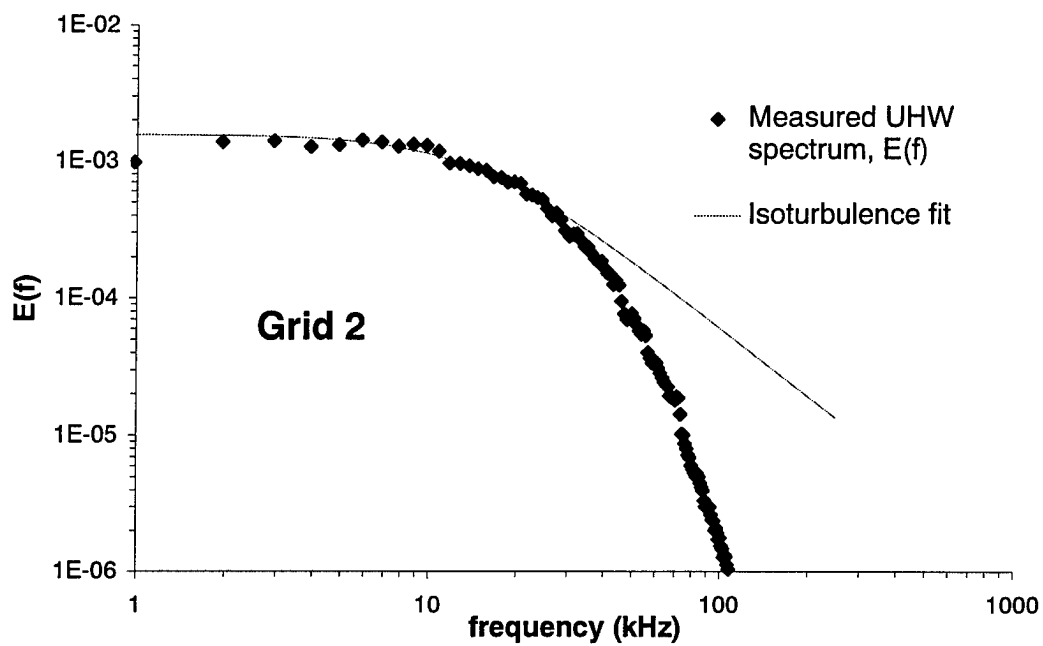


Figure 4.2.5 Comparison of grid turbulence to the isotropic spectrum fit, $Tu = 5\%$.

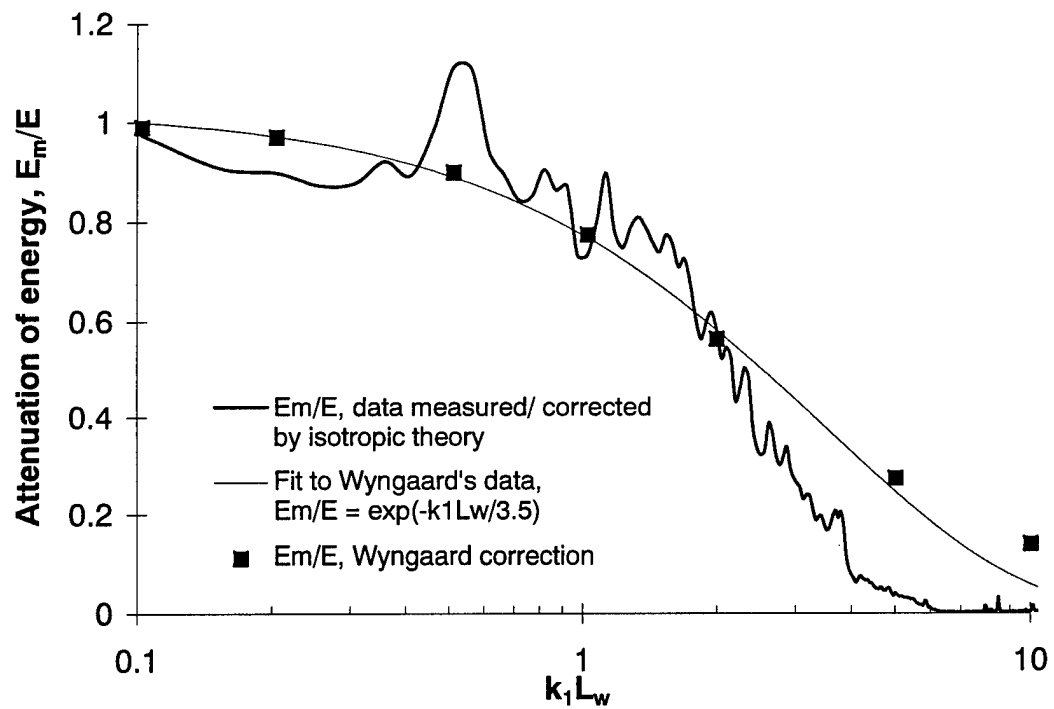


Figure 4.2.6 The Wyngaard correction compared to correction of the present data by using the isotropic spectrum at higher frequencies.

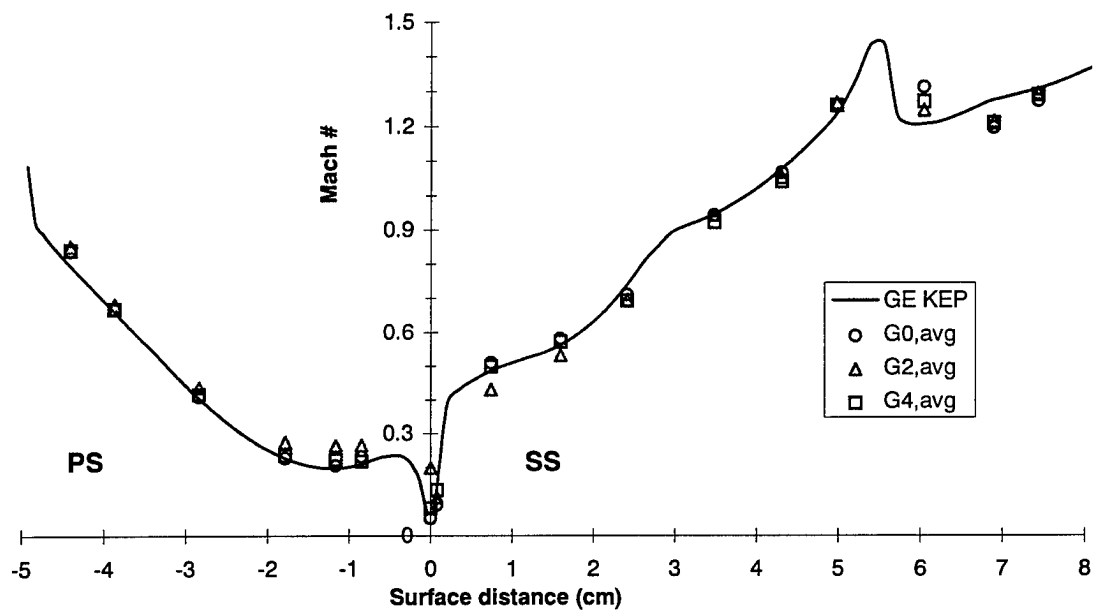


Figure 4.2.7 Measured Mach number distribution on blade at different grid conditions with the KEP prediction.

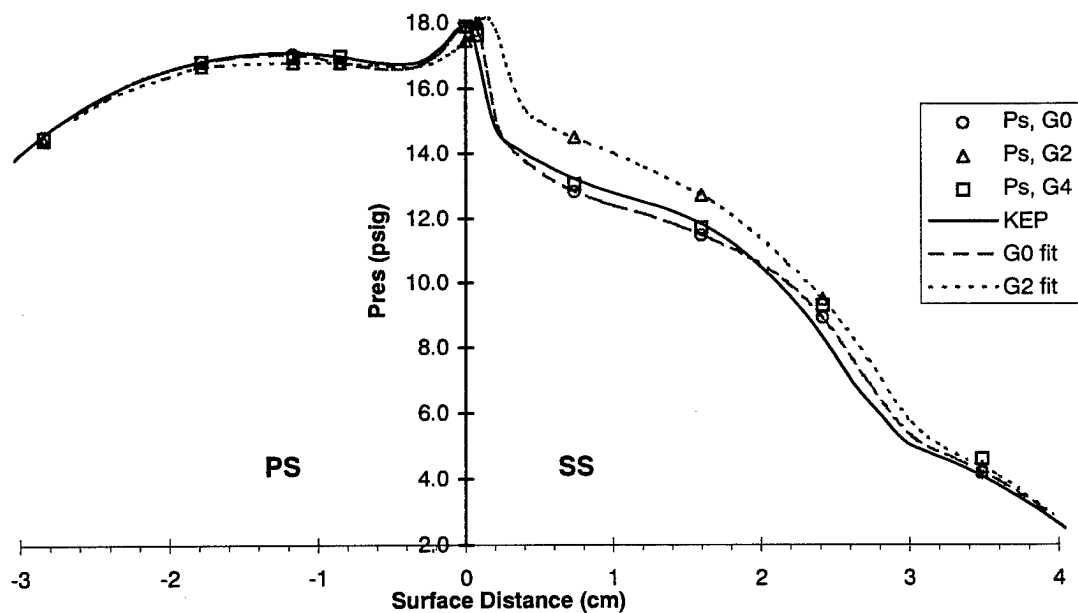


Figure 4.2.8 Measured blade Pstatic and fits to the data.

5. Mean data and Integral parameters

5.1 Blade surface heat transfer

5.1.1 Heat Transfer Coefficients

The heat transfer coefficient (HTC) data presented in Fig. 5.1.1 include the 4 Heat Flux Microsensor (HFM) locations used in this study: one suction side (SS) near-leading-edge point with measurements made by the direct-sputtered sensor (DS1), and three pressure side (PS) locations with measurements made by the insert HFMs (Fig. 2.1.4). DS1 results are given with two separate sets of data for each grid condition (run information given in legend) showing the repeatability of the measurements. Earlier measurements from two other direct sputtered sensors (Johnson and Diller, 1995) are shown as well: one near the SS leading edge and one near the trailing edge of the blade (downstream of the cross-passage shock). Code predictions are also shown and these will be discussed in section 5.1.3. Uncertainties are shown as error bars. In general, uncertainties at a given sensor with respect to grid-to-grid comparisons is small (a few percent). Total uncertainty is higher and includes uncertainty due to calibration (section 3.1.3), calculation method, and insert disturbance (section 3.1.5) on the pressure side, all of which are bias type errors on the set.

5.1.1.1 HTC calculation method

Total temperature was taken from an upstream probe, blade surface temperature from the HFM's resistance temperature sensor (RTS), and surface heat flux from the HFM's heat flux sensor (HFS) sampled low-speed (50 Hz). These data were read into a FORTRAN program where they were processed with known calibration, gain, and offset information to output the signals in proper units ($^{\circ}\text{C}$ and W/cm^2). These three columns of data were read into Excel where the heat transfer coefficient, h , was calculated at each point

$$h = \frac{Q}{(T_w - T_{aw})}$$

where T_{aw} is the adiabatic wall temperature which by definition is the wall temperature that will exist when heat flux is zero, or alternatively the wall temperature required to achieve zero heat flux for a given T_{tot} . The difference $(T_w - T_{aw})$ is then the proper temperature for referencing HTC in high speed flows. Any other temperature, for example $(T_w - T_{tot})$, can result in negative heat transfer coefficients. T_{aw} is defined with respect to T_{tot} and flow static temperature, T_s , as

$$T_{aw} = T_s + r(T_{tot} - T_s) = T_s + r \frac{V^2}{2c_p}$$

where r is the recovery factor. Recovery factor is a function of the Prandtl number and accounts for the effect of viscous dissipation across the high-speed boundary layer. According to theory (Schlichting, 1968), a turbulent boundary layer has a recovery factor, $r = \sqrt{\text{Pr}} \approx 0.89$ for air, while for a laminar boundary layer $r = \sqrt{\text{Pr}} \approx 0.84$. Measurements vary roughly between these values depending on the state of the boundary layer (Schlichting), with a value in the range of 0.84 to 0.89 usually assumed.

For the present data, recovery factor is used to define a temperature difference between the total temperature and the adiabatic wall temperature, $\Delta T = T_{\text{tot}} - T_{\text{aw}}$, then

$$h = \frac{q''}{T_w - T_{\text{tot}} + \Delta T}$$

$$\Delta T = (1 - r)(T_{\text{tot}} - T_s)$$

and ΔT can be estimated using a recovery factor near 0.84 or 0.89 depending on the character of the boundary layer and a known velocity to calculate $T_{\text{tot}} - T_s$. The above equations show that given steady flow over the blade, where a constant Mach number distribution gives a nearly constant flow to static temperature difference, ΔT will be constant if recovery factor remains constant. Because of experimental uncertainties related to drift of the RTS temperature sensor calibration, a more accurate estimate of ΔT was made based on the assumption that HTC would be nearly constant through the point where heat flux goes through zero (later in the tunnel run). ΔT was taken as the temperature difference between the wall and T_{tot} of the flow at the point where heat flux was zero. Values of ΔT based on this method were within the uncertainty of the RTS calibration drift, typically a few degrees Celsius (this drift was at a steady rate over time, and comparison of the two values of ΔT allows the drift in the sensor to be accounted for).

A plot of typical run temperatures and heat flux is given in Fig. 5.1.2. At the point where $T_w = T_{\text{aw}}$, at approximately 30 seconds into the run, T_{tot} has dropped due to heat loss from the upstream bank of copper tubing while the blades have heated up due to the hot flow. Experience shows that using a constant ΔT produces a nearly constant value of HTC (Fig. 5.1.2) even through the point where $Q = 0$, although the apparent noise at this point (from the numerics of calculating 0/0) is very high. HTC is then taken as the value where a flat line fit through this data intersects the ordinate (Fig. 5.1.2). This fit was made more accurate through a moving average of the data. The run-to-run value of HTC found in this way was generally repeatable within $\pm 5\%$ and the average within $\pm 5\%$ from day to day. This value is sensitive to level and stability of P_{tot} , and to heat flux gage sensitivity where lower sensitivity raises the noise level in the HTC plot.

The uncertainty on this method of $\pm 5\%$ does not include the uncertainties of calibration (section 3.1.3) and insert gage disturbance effects (section 3.1.5). With calibration uncertainty

included, the absolute uncertainty for the DS1 sensor is close to $\pm 10\%$. For the pressure side measurements, insert gage disturbance will tend to raise the measured heat transfer coefficient adding a possible bias, and thus gives higher uncertainties.

5.1.1.2 Grid affected potential field: BL2D code results

As discussed in section 4.2.4, there is a shift in the flow-field due to the presence of Grid 2 close to the blade row inlet, with a measured shift in the stagnation point toward the suction side. As seen in Fig. 4.2.7, differences in Mach numbers near the leading edge for the different grid conditions are on the order of 10%. The effect of this on HTC could be significant enough to change conclusions made about the effect of length scales on heat transfer.

In order to give more information to judge the effect of this shift in stagnation point a numerical code was run to predict laminar heat transfer given a known pressure distribution. The same BL2D code used as part of the laminar stability work of A. Wesner (presented in section 5.1.3) was used for these calculations. A curve was faired by hand through the measured surface static pressure measurements, Fig. 4.2.8, with reference to the GE predicted baseline pressure distribution shown on the same figure. A polynomial curve was then fit to this data and the resulting equation was used to give static pressure at the known (x,y) coordinates of the blade profile. Four cases were run: the measured baseline pressure distributions on the SS and on the PS, and the measured Grid 2 distributions on the SS and PS. The G0 and G2 cases were chosen because the largest difference in the measured pressure distribution was seen between these two cases, as well as to allow comparison of these results to KEP predictions for the baseline case. The code does not account for any FST effects so that predicted differences in heat transfer should be due solely to the effect of the change in the pressure distribution.

5.1.1.2.1 Effect on HTC

The code predicted heat transfer results on the suction side (SS) and pressure side (PS) are presented in figures 5.1.3 and 5.1.4. The small fluctuations in the heat transfer results are an artifact of the curve fit to the static pressure data and should not be considered real. The direct sputtered HFM, gage DS1, is located at 0.86 cm, in the region just after the heat transfer coefficients of the two grid cases have stabilized. At this point, Grid 2 has a predicted HTC 10% above the G0 curve (average near that location). This casts serious doubt on the cause of the measured heat transfer difference between G2 and G4 for DS1 in that the pressure distribution for G4 at DS1 is nearly identical to G0 (Fig 4.2.8). In summary, the increase in mean heat transfer due to G2 over G4 cannot be attributed solely to length scale, and may be entirely due to the shifted stagnation point due to the close proximity of G2 to the leading edge of the blade.

The PS BL2D code results (Fig. 5.1.4) show an initially higher heat transfer for the G0 case followed by laminar separation. The code predicts transition rather than laminar separation for the G2 pressure distribution case so that the mean heat transfer rises above G0. In actual tests there is no separation of the baseline flow based on HTC measurements (Fig. 5.1.1), shadowgraph pictures, or the surface static pressure measurements. G2 may transition earlier, however HTC measurements on the blade show the same trend for all 3 grid cases. However, these PS code results should at least give some indication of the heat transfer in the leading edge region prior to predicted separation/ transition. HFM sensor PS1 is located at 0.43 cm in this leading-edge laminar region where predicted heat transfer for the G2 pressure distribution is below the predicted heat transfer for G0 (and G4) pressure distribution. Therefore, the measured heat transfer for G2 above that measured for G4 at location PS1 should not be attributed to the shift in the pressure distribution.

It is important to remember that this code does not allow for any free-stream turbulence. The low values of HTC seen here (referenced to measurements on Fig. 5.1.1) can be attributed partially to a truly laminar free-stream (versus actual baseline conditions, Fig. 4.1.2). Whether the code absolute values are reasonable is not clear, but the comparison of the predictions is believed to be reliable.

5.1.1.2.2 Effect on Strain

For the purpose of later discussions, the results of BL2D predicted strain (dimensional acceleration) are presented in Figs. 5.1.5 and 5.1.6 for the SS and PS. The prediction for the baseline case based on the KEP code (section 5.1.3) are also shown, where the KEP solution is based on the blade profile data, while BL2D results are based on measured grid specific blade surface P_s data as input. The dip in BL2D predicted strain on the suction side should be regarded as an effect of the sensitivity of acceleration calculation (a differential measure) to the fit to the measured pressure distribution. The strain can be seen to follow the trends in heat transfer in terms of a shifted peak due to Grid 2. Also note that the predicted strain on the PS for G2 is less negative at the minimum point, increasing stability. This corresponds to the non-separating boundary layer as seen in the heat transfer predictions.

5.1.2 Integral Scales: q' , Tu_q , T_q

Measured values of q' (rms value), Tu_q (q'/Q_{mean}), and T_q (the integral time scale of the heat flux energy spectrum) can be seen in Table 5.1 for the no-PHW runs. Another measure of the fluctuating heat flux level is given as q'_{norm} in Table 5.1 and is equal to q' divided by the temperature difference at the time of data acquisition (and thus equal to the rms of the heat transfer coefficient over the time of high-speed data acquisition, h'). The necessity for a

normalized rms value, $q'_{\text{norm}} = q' / (T_{\text{aw}} - T_s)$, can be seen from the variation in q' due strictly to the temperature difference at the time of data acquisition that is not a function of the flow.

The measured integral time scale in Table 5.1, T_q , is based on the higher end of the energy spectrum. In the present heat flux data, there is a great deal of low-frequency energy that makes the heat flux spectrum very “non-isotropic”. The effect of this on integral scale calculations is two very different regions in the autocorrelation, similar to that seen in Fig. 2.2.2, with a rapid initial drop followed by a long raised tail. The effect is often much more pronounced than in Fig. 2.2.2. As discussed in section 2.2.2, integral time scales were calculated by fitting a decaying exponential to the upper part of this curve corresponding to the scales at higher frequencies and thus effectively filtering strong low-frequency information. If the auto-correlations had been simply integrated to the first zero crossing (thus including this low frequency information), the resulting T_q values would be much more erratic, and typically an order of magnitude larger. This problem underscores the limited value of using an integral time scale to characterize anisotropic energy spectra.

For measurements above the suction side sensor DS1, the behavior of q'_{norm} , Tu_q , and T_q bears a close look. The “back” cases (G2b and G4b), with larger length scale but lower free-stream turbulence intensity ($Tu = 3.6\%$), have higher Tu_q values than the “up” cases ($Tu = 5\%$). However, at the same time, the back cases have lower mean heat transfer, as evidenced by h . This means that q' is not scaling on mean heat transfer, as can be seen from the q'_{norm} column where values are nearly constant. While mean heat transfer seems roughly dependent on flow turbulence intensity (back less than up), Tu_q seems to scale on length scale (Λ_x), where length scale is larger for the back cases than up cases. The effect of the free-stream length scale (Λ_x) can also be seen in higher heat flux time scales (T_q) for the back cases than the up cases. The relationship of Tu_q and Λ_x is of limited use, however, and says only that the larger scales cause higher measured fluctuating heat flux levels without corresponding raised mean heat transfer. This would seem to indicate that the smaller flow length scales are more effective for heat transfer, but the significant differences in flow intensity above DS1 don't allow such a conclusion.

The measured values of q' along the pressure side are presented in terms of Tu_q (q' / Q) in Fig. 5.1.7. Tabulated data can also be seen in Table 5.1. The fluctuating component of heat transfer is seen to increase along the pressure side, even as the flow u' (Tu) is decreasing. Also, while the fluctuating energy is least for the baseline case, G0, at PS1, this situation changes as q' grows significantly for G0 and G4 compared to G2. This seems indicative of transitional activity, supporting the increased stability of the G2 boundary layer predicted by BL2D (see last section, 5.1.1.2). The integral time scale of heat flux is presented in Fig. 5.1.8. The large increase in scale

along the PS indicates that most of the increase seen in q' is due to very low frequency activity. This will be seen in the spectral data in Ch. 6.

5.1.3 Comparison of measured data to code predictions

At present the only code results that can be used to compare mean heat transfer measurements with FST were generated by engineers at General Electric for this GE blade design using a k-epsilon code called KEP. In addition, a laminar stability analysis of a $Tu_{inlet} = 0\%$ (no FST) case was done for the SS and this will be presented here as well.

5.1.3.1 KEP

Prior to the start of this test program, calculations were performed by GE on the turbine blades using the KEP K-eps code modified from STAN-5. Details of this code are given in Appendix D and in the paper by Zerkle (1988). It is important to note that heat transfer predictions with this code were tailored to match experience from full-rig tests (e.g. transition locations) while measurements here are made in a 2-D cascade.

A comparison of KEP predictions to measured data can be seen in Fig 5.1.1. The KEP results are shown as a solid line for the $Tu_{inlet} = 5\%$ case corresponding to G2 and G4 where the initial transition on the SS, indicated by the first rise, is forced based on real engine data. This transition is not seen in shadowgraphs, however (see section 5.3). Clearly the heat transfer measured by DS1 is significantly above the prediction, although the sensor is near the stagnation point in a region where heat transfer is rapidly changing. The measured HTC near the trailing edge agrees with the KEP prediction within the uncertainty of those measurements.

Results of the boundary layer code BL2D are presented as well for the SS showing the laminar prediction for comparison to the baseline case. No similar KEP predictions were made for a $Tu = 0\%$ inlet FST. Shadowgraph pictures indicate a laminar boundary layer may exist on the front SS even for the grid-in cases. However, the presence of a laminar boundary layer does not mean that it is not a disturbed laminar boundary layer, even for the baseline case where some low frequency energy exists in the inlet flow. BL2D results are based on a truly zero FST inlet flow.

On the PS, the measured HTC is above the predicted values, although the trends in terms of transition are predicted well. Uncertainty on the PS measurements are higher than for sensor DS1 due to the increased roughness inherent in the insert method of the PS gages. This would most effect the baseline case where FST turbulence would not overwhelm near wall disturbances and the boundary layer is believed to be laminar without gage disturbances. The result of such disturbance would be a bias upward on the mean measurements. These issues are discussed in section 3.1.5.

5.1.3.2 Laminar Stability Theory

The results presented earlier for heat transfer coefficient based on pressure gradient for a $Tu = 0\%$ inlet free-stream were generated using the program BL2D (Iyer, 1995). The BL2D code is a fourth-order accurate two-dimensional or axi-symmetric boundary layer code for speed regimes from low subsonic to hypersonic. The code is written in Fortran77, and full documentation is given in the NASA contractor report cited above. This program was used by A. Wesner at Virginia Tech (Wesner, 1996 dissertation) as the first part of a stability analysis performed for the suction side boundary layer of the present blade. BL2D was used to calculate blade surface parameters (e.g. heat transfer), as well as to generate the very smooth fourth-order accurate boundary layer profiles required as input to the stability code analysis.

The intent of the stability analysis was to look at the natural transition process in the absence of FST using laminar stability theory to predict the onset of laminar to turbulent transition. The laminar stability theory is presented in detail by A. Wesner (1996) with assumptions, background theory and pertinent equations. Fundamental to the theory is the growth of boundary layer instabilities (present in any flow) at the natural frequencies of the boundary layer. The issues addressed by this study included determining at which frequencies of disturbance the blade boundary layer responds, and whether these disturbances grow or are damped out. The stability analysis was performed by A. Wesner in conjunction with M. Malik of NASA Langley, using a code named e^{Malik} . Details of the code are presented in A. Wesner's dissertation as well as in a publication by Malik (Malik, 1990).

The results of the stability analysis showed that in the absence of FST the present suction side boundary layer shows very little inclination to transition, in agreement with the laminar boundary layer observed in shadowgraphs taken in the present facility for the baseline case. For all frequencies of instability used as input to the code (0 -100 kHz) no growth of instabilities was found. Secondly, the code results showed that the boundary layer is most sensitive to frequencies of disturbance in the range of 40 kHz. This applies to the present work in that a free-stream spectrum with greater turbulent energy in this frequency range may be expected to disturb the boundary layer most, leading to earlier transition.

5.2 Flow in passage

5.2.1 PHW measurement matrix

Passage hot-wire measurements were taken at 4 locations on the blade surface and at three y locations, Fig. 2.1.4, above each HFM, except for the HFM at location PS3 (farthest from the leading edge) where only two positions were used. These three locations are at 0.2 mm, 0.4

mm, and 1.0 mm, where uncertainty in location is ± 0.1 mm. The three grid cases (G0, G2, G4) were run sequentially with the wire located at each wire position and the wire position held constant while grids were exchanged. This produced a total of nine data sets for each HFM position. For PS3, data were taken only at 0.2 mm and 1.0 mm. For DS1, additional data were taken for two extra grid positions for a total of five grid conditions: G0 (no grid baseline), G2b (G2 in a “back” position where $Tu_{inlet} = 3.6\%$), G2u (in an “up” position equivalent to the G2 position used on the PS, $Tu_{inlet} = 5\%$), G4b ($Tu_{inlet} = 3.6\%$), and G4u ($Tu_{inlet} = 5\%$). Therefore, DS1 has a total of 15 data sets, PS1 and PS2 have 9 sets, and PS3 has 6.

Data were taken with a separate tunnel run for each wire position and each grid condition. The upstream copper tube bank was heated to 200F (93°C) prior to the run as the compressor loaded. The test section was cooled between runs, however not to a repeatable temperature. After the tunnel started, the test section pressure was allowed to peak (slightly over condition typically), and then high-frequency data were acquired as the pressure dropped back to condition. This point was typically 5 s into the run. The initial $T_{tot} - T_w$ varied somewhat depending on blade cooling prior to the run, while the temperature difference at the point of high-speed data acquisition varied to a larger degree due to the several second variation in the time of acquisition relative to tunnel start. Because data were acquired only “at condition” to maintain constant exit Mach number, this time was dependent on tunnel control, with a resulting average temperature difference of approximately 33°C (60F), as seen in Table 5.2.

For each set of data, mean and spectral information were calculated according to the data reduction method given in section 3.3. Mean velocity data will be presented here along with the integral parameters u' , Tu , T_x , and Λ_x , while spectral information will be presented in Ch. 6.

5.2.2 Mean velocity above surface

For the 30 sets of data taken with the PHW above DS1 and on the PS, a total of 3 PHW probes were used, with one broken wire mid-test so that 4 wires were used. These were calibrated according to the method presented in section 3.2.2. Total uncertainties on the mean velocity (affecting U , u' , and Λ_x) are on the order of $\pm 10\%$ (section 3.2.2.6), but less for Tu .

Mean velocity results from the HW velocity measurements are given along with other run data in Table 5.3. For each given grid condition, the Mach number at the three wire positions above DS1 is nearly constant. The Mach number increases uniformly away from the wall above the pressure side locations. These Mach number trends agree with Mach number contours drawn based on surface Mach number distributions. Velocity is seen to drop below the inlet velocity of 120 m/s along the pressure side with a minimum near 90 m/s at PS2, followed by an accelerating flow seen as higher velocities measured at PS3.

5.2.3 Integral Scales: u' , T_u , T_x , Λ_x

Measurements of u' , T_u , T_x , and Λ_x at the suction side (SS) sensor DS1 are given in Table 5.3 at the end of the chapter as well as in Figs. 5.2.1 and 5.2.2. Measurements above the pressure side will be given graphically as well as in Table 5.3. It should be noted that u' as given here is assuming negligible fluctuating density, and the velocity measured is the sum of the u and v velocity vectors because the probe is single-wire (section 3.2.2). The integral time scale (T_x) is calculated as discussed in section 2.3.2.

Table 5.3 u' results show the increase in fluctuating energy comparing each DS1 “back” to “up” case. An increase in length scale is also seen. Progressing from near wall, 0.2 mm to 1.0 mm for the two G2 grid conditions, u' holds approximately constant while Λ_x grows. For the two G4 cases, u' decreases moving away from the wall, while Λ_x remains constant. These relationships will be examined more carefully in Ch. 6 when examining the spectral information.

On the pressure side, u' for the two grids (G2, and G4 at the 1.0 mm wire position) referenced to the upstream hot-wire inlet measurements are presented in Fig. 5.2.3. The UHW measurements are referenced to the blade leading edge (0 cm) where the given points are calculated from the fit to the measured upstream data and the point at the leading edge is given assuming no effect of the blade itself, while the points in the passage correspond to data in Table 5.3. The continuation of the fluctuation energy into the passage on the PS is seen. Based on UHW measurements there is approximately a 15% decrease in u' for G2 due to hot-wire spatial resolution limits (section 4.2) at the $T_u = 5\%$ point, with no significant decrease for G4. The UHW measurements were corrected based on the isoturbulence spectrum, while no such attempt was made for the PHW measurements due to the wall proximity effects on the spectra. However, if the same ratios are assumed at the PS1 location for G2, then the resulting corrected u' would show a comparatively smooth continuation from the extrapolated upstream curve. In contrast, G4 shows an increase in fluctuating energy due to wall effects. A similar plot of T_u upstream and above the PS is given in Fig. 5.2.4. Note that the changes in velocity used to normalize u' causes an abrupt shift in the G4 data, and results in a more pronounced change going through the passage.

Similar plots of integral time scale, T_x , and integral length scale, Λ_x , are presented in Figs. 5.2.5 and 5.2.6. A rapid increase in time scale is seen going from the inlet stream to the wire location above gage PS1. This can be attributed both to lower velocity along the pressure side as well as to boundary layer phenomena along the PS. The length scale follows the same trend. Correcting the G2 length scale for spatial resolution at PS1 would result in a lower value closer to the extrapolated inlet value.

Plots of u' and T_u along the pressure side at different y locations are shown in Figs. 5.2.7, and 5.2.8. Along the PS, T_u is higher nearer the wall, 0.2 mm. This can be attributed partially to a

lower velocity, but primarily to an increase in the measured u' . Notice that the measured Tu at 0.4 mm agrees with the 1.0 mm measurement over PS1 for both G2 and G4 while at PS2 the 0.4 mm measurement agrees with the near-wall 0.2 mm Tu . This could be seen as the influence of curvature amplifying near wall turbulence. Interestingly, Tu actually increases (but due to decrease in U) between PS1 and PS2 for G2. G4 shows a large decrease in u' from PS1 to PS2 due primarily to attenuation of the largest scales at the blade surface and as they enter the constrictive passage. G2 however has less decay than would be expected based on upstream measurements. These results will be discussed more in reference to the spectral data. As the flow moves on toward PS3, a significant drop is seen in both intensity and scale. This is clearly due to the further constriction of the passage as well as the very strong acceleration in the latter part of the pressure side (see Fig 5.1.6 of strain rates). Note, in contrast, that the fluctuating heat transfer (q') is increasing steadily along the pressure side, despite the decreasing u' in the free-stream, as seen in Fig. 5.1.7.

A similar plot of the integral length scale along the blade is shown in Fig. 5.2.9. The length scale is again larger for G4 in general than for G2, indicating the larger proportion of low-frequency energy for G4. There are significant differences between the two grid cases: while G4 shows a lower length scale near the wall as may be expected for attenuation of the larger scales, G2 shows the opposite with an increase in scale near the wall. This corresponds to the growth in u' seen near the wall. Above PS3 there is a very different phenomena; a strong increase in scale indicating large low-frequency energy which corresponds to the large increase in u' seen in the previous figure. Whether this is related to boundary layer transitioning (laminar to turbulent or even an unsteady turbulent to laminar unsteady re-laminarization) or something else is not clear. Clearly there is an increase in scale between PS1 and PS2 while further along the PS at PS3 the scale (at 1 mm) has dropped. This drop follows the drop in u' indicating the attenuation of the low-frequency end of the energy spectrum for both grids. However, at PS3 G2 maintains a larger proportion of high-frequency energy as evidenced by the smaller scale.

5.3 Transition information

5.3.1 Shadowgraphs

Spark shadowgraph pictures (20 ns spark, taken using a Model 437B Nanopulser from Xenon, and using type 57 3000 ISO Polaroid film) were taken for the purpose of gaining a measure of the state of the boundary layer. As discussed earlier, GE engineers believed that the flow over the suction surface (SS) would transition, even for low turbulence levels, near the leading edge, with re-laminarization near the crown of the SS followed by re-transitioning to turbulent on the back SS. However, preliminary photos showed what appeared to be a completely

laminar boundary layer for the baseline flow (G0). As noted in section 5.2.2, laminar stability calculations for this blade predict no transition on the blade. Close-up pictures were planned to investigate this more carefully.

Close-ups of the boundary layer were made using the focused shadowgraph technique. Discussion of this method and interpretation of photos taken by this method are discussed by Holder and North (1956) and in A. Wesner's dissertation (1996). The focused shadowgraph method relies on density gradients in a flow, which are strongest at high speeds, and thus suitable for use in a transonic flow regime. Pictures were taken for flow around the turbine blade with and without the grids in place. Two separate efforts were made to document the boundary layer by this method. In each case, a non-instrumented blade was used.

In the first effort, close-ups on the order of 3X magnification were taken of the blade in the G0 (no grid) baseline flow. As shown in Ch. 4 the flow turbulence intensity for G0 at the blade inlet is low (0.25%). Shadowgraphs appear to confirm that the boundary layer is laminar (photos in A. Wesner's dissertation). These photos show a laminar boundary layer on the suction side up to the cross-passage shock, at which point the boundary layer trips to turbulent. The turbulent nature of the boundary layer is clearly visible downstream of the shock. However, the pictures are not conclusive near the leading edge. This can be attributed both to the lower speed flow that has lesser density variation and also to the very thin boundary layer: laminar stability code calculations (Wesner, 1996, and section 5.1.3) predict a boundary layer thickness of 0.1 mm (.004 in.) along most of the suction side, and less near the leading edge. The lower speed pressure side also appears to be laminar, and clearly so in the high-speed region near the trailing edge. However, due to the very thin boundary layer and low-speed flow at the heat-flux gage locations, the state of the boundary layer cannot be judged conclusively.

In the second effort, 2X magnification images were taken of the blade with G2 and G4 in place. The results are not as clear as for those detailed above. Transition on the back SS upstream of the cross-passage shock impingement seems clear (this was not present for the G0 case), with G2 causing earlier transition than G4. G2 seemed to cause transition near the crown, while G4 transition is closer to the cross-passage shock impingement (2 cm upstream). The state of the boundary layer nearer the leading edge is not clear, however, due to lack of picture clarity and the thinness of the boundary layer. Therefore, the presence of transition followed by re-laminarization cannot be judged from these photos.

5.3.2 State of the boundary layer

Throughout this chapter the evidence has been presented for determining the state of the boundary layer. A summary of that is presented here.

DS1 is located near the leading edge on the SS where the boundary layer is laminar. There are two primary sources of evidence for a laminar boundary layer. The first is the location of the sensor relative to the start of transition based on code predictions. For the KEP code (section 5.2) this transition is forced based on real engine experience, while the present data is taken in a 2-D cascade flow where secondary flows are not a factor. The fact that the KEP code transition begins past the location of DS1 is strong evidence of a laminar boundary layer. Also as seen in section 5.2, laminar stability theory does not predict even a hint of transition for the baseline flow. Secondly, shadowgraphs show a laminar boundary layer on the SS all the way to the cross-passage shock, while transition was earlier with the grids in place but not seen near the leading edge.

The state of the boundary layer on the pressure side (PS) is not clear. Based on mean heat transfer data it appears that the boundary layer progresses from laminar to turbulent, and is most likely transitional along most of the PS. This is in agreement with typical HP turbine data where a strong acceleration stretches the transition zone while FST and curvature encourage transition. In the present case there is also a deceleration near the leading edge with the strain rate becoming negative near the location of PS1 (see Fig. 5.1.6). This would encourage transition, or even laminar separation for a low FST case, as predicted by BL2D. The pressure distribution shift for G2 may be enough to significantly change the state of the boundary layer for G2 as compared to G4. KEP code predictions show a laminar boundary layer at PS1 (as does BL2D) with rapid transition between PS1 and PS2 for the $Tu_{inlet} = 5\%$ case, and showing HTC growing along the PS as measured (Fig. 5.1.1). Because this is a cascade flow it may be that the boundary layer transitions more slowly, or even that it would tend toward re-laminarization near and beyond PS3 at mid-chord due to the growing and very strong favorable pressure gradient. Based on this evidence, the boundary layer will be assumed laminar at PS1 and transitional at PS2 and PS3, pending any further information based on the time-resolved data.

5.4 Conclusions

Mean heat transfer data show higher heat transfer on the suction side (SS) and pressure side (PS) due to the smaller length scale Grid 2 (G2) as compared to Grid 4 (G4). The baseline G0 heat transfer is the lowest as expected. However, code results for the SS indicate that the shift in stagnation point induced by G2 is enough by itself to account for the 10% difference in heat transfer coefficient (HTC) of G2 above G4 seen at gage DS1. On the PS, code results near the leading edge indicate the opposite effect with less heat transfer for G2 based solely on the changed pressure gradient. Therefore, the increase in heat transfer of G2 over G4 at gage PS1 can be attributed to length scale effects, awaiting further analysis based on time resolved data. Grid 2 has more high-frequency energy content so that higher heat transfer due to Grid 2 agrees

with the laminar stability analysis done by A. Wesner which predicts greater boundary layer sensitivity to frequencies around 40 kHz.

Predictions of HTC from KEP with inlet $Tu = 5\%$ agree reasonably well with measurements on the pressure side. A higher HTC is indicated by the DS1 sensor near the leading edge of the SS. Pressure side measurements are in general above predicted values, although this may be partially attributed to disturbances due to the insert gages. The general trend of the PS data points are predicted well. The laminar stability analysis predicts no transition or even persistence of instabilities that would lead to transition for the SS boundary layer upstream of the cross-passage shock with inlet $Tu = 0\%$. This confirms an observed laminar boundary layer seen in the shadowgraph pictures.

Heat flux data show that the fluctuating value, q'_{norm} , is not scaling on the mean heat transfer and that the integral time scale, T_q , generally scales on flow scales. At DS1, very little change is seen in measured q' for the different grid conditions. Along the pressure side, q' is seen to grow strongly even as u' is decreasing.

Distributions of the rms fluctuating velocity above the heat flux gage locations have been presented along with integral scales. Results show a decrease in u' between gages PS1 and PS2 that is less than the upstream decay rate while scale increases more rapidly. The intensity and scales then drop markedly between locations PS2 and PS3. Measurements above DS1 indicate the variation in scale and intensity expected for the five grid conditions.

Table 5.1 Summary of No-PHW heat flux data.

	Grid	Q (W/cm ²)	q' (W/cm ²)	q' _{norm} (W/m ² K)	Tuq	Tq (ms)	h (W/m ² K)	T _{tot} (°C)	T _s (°C)	T _{aw} -T _s (°C)
DS1	G0	3.83	0.194	49.9	5.06	0.09	1000	67.3	26.3	38.8
	G2b	4.70	0.312	98.1	6.64	0.09	1580	69.9	35.9	31.8
	G2u	4.48	0.264	101.0	5.88	0.07	1785	65.6	37.4	26.1
	G4b	3.97	0.228	77.1	5.73	0.10	1360	63.7	32.0	29.5
	G4u	4.96	0.231	62.3	4.65	0.06	1505	68.5	31.0	35.4
PS1	G0	3.75	0.187	46.5	5.00	0.05	800	71.3	30.3	40.3
	G2	4.31	0.257	73.6	5.96	0.04	1085	69.6	34.1	34.9
	G4	3.90	0.331	94.6	8.50	0.04	970	66.7	31.0	35.0
PS2	G0	3.57	0.339	81.6	9.48	0.08	820	71.3	29.3	41.5
	G2	3.82	0.339	91.0	8.88	0.07	930	69.6	31.9	37.3
	G4	3.45	0.380	104.1	11.02	0.08	875	66.7	29.7	36.5
PS3	G0	3.42	0.679	180.1	19.86	0.12	845	71.3	32.6	37.7
	G2	3.77	0.408	118.8	10.80	0.08	1005	69.6	34.2	34.3
	G4	3.57	1.200	355.9	33.56	0.15	925	66.7	31.9	33.7

Table 5.2 Summary of heat flux data for With-PHW runs.

PHW	HFM	Grid	Q (W/cm ²)	q' (W/cm ²)	Tuq	T _{tot} (°C)	T _{rts} (°C)	T _{aw} -T _s (°C)	μ (kg/ms)	ρ (kg/m ³)	k _{air} (W/mK)
0.2mm	DS1	G0	3.69	0.181	4.89	75.5	34.2	39.0	1.95E-05	1.949	0.0280
		G2b	5.57	0.295	5.29	67.9	35.5	30.7	1.94E-05	2.112	0.0279
		G2u	5.69	0.320	5.63	71.1	37.5	31.8	1.95E-05	2.088	0.0281
		G4b	3.43	0.222	6.46	66.7	38.4	26.2	1.94E-05	2.006	0.0279
		G4u	3.95	0.245	6.2	64.0	37.1	24.8	1.93E-05	2.062	0.0278
	PS1	G0	2.62	0.194	7.42	69.6	40.9	28.2	1.97E-05	2.173	0.0284
		G2	3.65	0.220	6.02	70.1	39.3	30.4	1.97E-05	2.178	0.0284
		G4	3.34	0.287	8.59	69.4	38.4	30.5	1.97E-05	2.195	0.0283
	PS2	G0	4.00	0.356	8.91	72.6	32.9	39.5	1.96E-05	2.240	0.0282
		G2	4.04	0.310	7.67	70.8	36.1	34.5	1.96E-05	2.304	0.0283
		G4	3.83	0.405	10.57	70.8	33.7	36.8	1.96E-05	2.278	0.0282
	PS3	G0	3.68	1.520	41.31	73.3	34.2	38.1	1.96E-05	2.079	0.0282
		G2	4.36	0.946	21.68	72.3	34.2	37.2	1.96E-05	2.134	0.0282
		G4	3.70	2.141	57.83	69.9	38.3	30.8	1.96E-05	2.166	0.0283
0.4mm	DS1	G0	3.79	0.148	3.91	68.1	25.4	40.5	1.91E-05	2.013	0.0274
		G2b	5.07	0.302	5.96	70.1	34.2	34.0	1.94E-05	2.065	0.0279
		G2u	5.02	0.245	4.89	63.0	33.0	28.2	1.93E-05	2.115	0.0276
		G4b	4.85	0.255	5.27	69.9	29.3	38.3	1.93E-05	2.041	0.0277
		G4u	4.49	0.256	5.71	69.9	37.3	30.4	1.95E-05	2.029	0.0280
	PS1	G0	3.81	0.240	6.31	75.2	30.5	44.2	1.96E-05	2.201	0.0282
		G2	3.70	0.254	6.87	68.9	37.0	31.4	1.96E-05	2.247	0.0282
		G4	4.56	0.377	8.26	77.2	30.5	46.2	1.96E-05	2.164	0.0283
	PS2	G0	3.72	0.291	7.83	70.8	34.2	36.3	1.96E-05	2.235	0.0282
		G2	4.39	0.343	7.8	72.5	31.6	40.6	1.96E-05	2.196	0.0282
		G4	4.04	0.420	10.38	72.3	31.8	40.2	1.96E-05	2.256	0.0282
1.0mm	DS1	G0	2.93	0.209	7.15	72.1	36.3	33.5	1.95E-05	1.942	0.0280
		G2b	4.42	0.278	6.28	70.6	38.8	30.1	1.96E-05	2.074	0.0281
		G2u	5.84	0.292	4.99	70.8	34.8	34.3	1.95E-05	2.074	0.0280
		G4b	3.78	0.216	5.72	69.1	36.8	30.3	1.94E-05	2.029	0.0279
		G4u	4.90	0.275	5.6	69.1	35.3	31.7	1.94E-05	2.070	0.0279
	PS1	G0	3.54	0.191	5.39	71.3	30.8	40.0	1.95E-05	2.203	0.0281
		G2	4.06	0.244	6.01	70.3	35.9	33.9	1.96E-05	2.175	0.0282
		G4	3.82	0.316	8.26	71.3	33.8	37.0	1.96E-05	2.170	0.0282
	PS2	G0	3.99	0.328	8.24	72.5	33.0	39.2	1.96E-05	2.275	0.0282
		G2	3.64	0.309	8.5	69.9	37.4	32.1	1.97E-05	2.257	0.0283
		G4	3.92	0.409	10.45	71.8	33.2	38.2	1.96E-05	2.240	0.0282
	PS3	G0	3.51	1.414	40.24	70.6	34.6	35.1	1.95E-05	2.153	0.0281
		G2	3.28	1.492	45.43	69.1	41.2	27.0	1.97E-05	2.134	0.0283
		G4	3.67	1.898	51.79	69.9	36.9	32.1	1.96E-05	2.133	0.0282

Table 5.3 Summary of hot-wire data, corresponding to Table 5.2

y_{wire}	HFM	Grid	Mach	Pt (kPa)	Re'	Nu'	U (m/s)	u' (m/s)	T_u (%)	T_x (ms)	Λ_x (mm)
0.2 mm	DS1	G0	0.51	215.2	3978	1.064	187.6	1.32	0.71	0.061	11.45
		G2b	0.45	223.0	3882	1.037	164.5	4.28	2.60	0.012	1.89
		G2u	0.47	224.1	3935	1.054	171.2	5.53	3.23	0.010	1.66
		G4b	0.51	218.9	3999	1.070	182.6	3.48	1.91	0.024	4.44
		G4u	0.49	222.0	3997	1.069	177.5	5.12	2.88	0.020	3.60
	PS1	G0	0.25	212.4	2945	0.882	93.4	2.13	2.28	0.048	4.47
		G2	0.25	212.1	2915	0.872	91.4	5.27	5.77	0.023	2.13
		G4	0.25	213.2	2912	0.871	90.6	7.15	7.89	0.038	3.45
	PS2	G0	0.23	215.7	2836	0.934	85.0	2.65	3.11	0.038	3.23
		G2	0.24	222.7	2913	0.961	86.7	4.70	5.42	0.023	2.00
		G4	0.23	219.2	2872	0.947	85.7	5.54	6.46	0.040	3.38
	PS3	G0	0.35	209.3	3359	1.006	127.2	1.56	1.23	0.059	7.47
		G2	0.34	214.0	3376	1.009	124.8	4.09	3.28	0.010	1.29
		G4	0.31	214.9	3232	0.968	112.7	6.00	5.32	0.036	4.03
0.4mm	DS1	G0	0.50	214.8	3944	1.053	180.0	0.80	0.44	0.069	12.42
		G2b	0.48	221.3	3939	1.051	173.1	4.45	2.57	0.013	2.22
		G2u	0.46	222.0	3909	1.044	166.5	5.03	3.02	0.010	1.60
		G4b	0.52	221.8	4048	1.082	186.3	3.49	1.87	0.023	4.19
		G4u	0.51	222.0	4022	1.076	182.9	5.06	2.77	0.019	3.38
	PS1	G0	0.25	213.3	2931	0.953	93.3	2.62	2.81	0.040	3.72
		G2	0.25	218.0	2979	0.967	92.7	4.52	4.87	0.022	2.01
		G4	0.25	210.0	2879	0.936	91.5	6.17	6.74	0.043	3.94
	PS2	G0	0.24	215.7	2895	0.954	88.4	2.18	2.47	0.033	2.88
		G2	0.25	212.3	2926	0.963	92.1	5.01	5.44	0.028	2.60
		G4	0.24	217.5	2906	0.961	89.3	5.83	6.53	0.043	3.85
1.0mm	DS1	G0	0.51	213.3	3950	1.055	184.6	2.13	1.15	0.053	9.78
		G2b	0.47	222.3	3908	1.046	169.5	4.09	2.41	0.014	2.37
		G2u	0.46	221.0	3893	1.041	169.0	5.33	3.15	0.011	1.79
		G4b	0.51	221.5	4018	1.076	183.3	3.36	1.84	0.024	4.34
		G4u	0.50	224.4	4023	1.077	180.2	4.91	2.72	0.020	3.59
	PS1	G0	0.27	214.0	3062	0.918	101.1	2.19	2.17	0.036	3.66
		G2	0.28	213.2	3101	0.927	103.7	4.74	4.57	0.015	1.52
		G4	0.26	210.9	2981	0.894	97.1	6.94	7.15	0.040	3.92
	PS2	G0	0.24	220.0	2944	0.972	90.3	2.27	2.51	0.039	3.52
		G2	0.25	219.2	2971	0.982	92.1	4.29	4.66	0.029	2.64
		G4	0.25	216.6	2934	0.968	90.9	5.10	5.61	0.041	3.71
	PS3	G0	0.34	215.7	3400	1.018	125.6	1.42	1.13	0.058	7.25
		G2	0.34	215.6	3404	1.020	125.9	2.96	2.35	0.013	1.62
		G4	0.35	214.6	3408	1.021	127.1	3.91	3.07	0.020	2.50

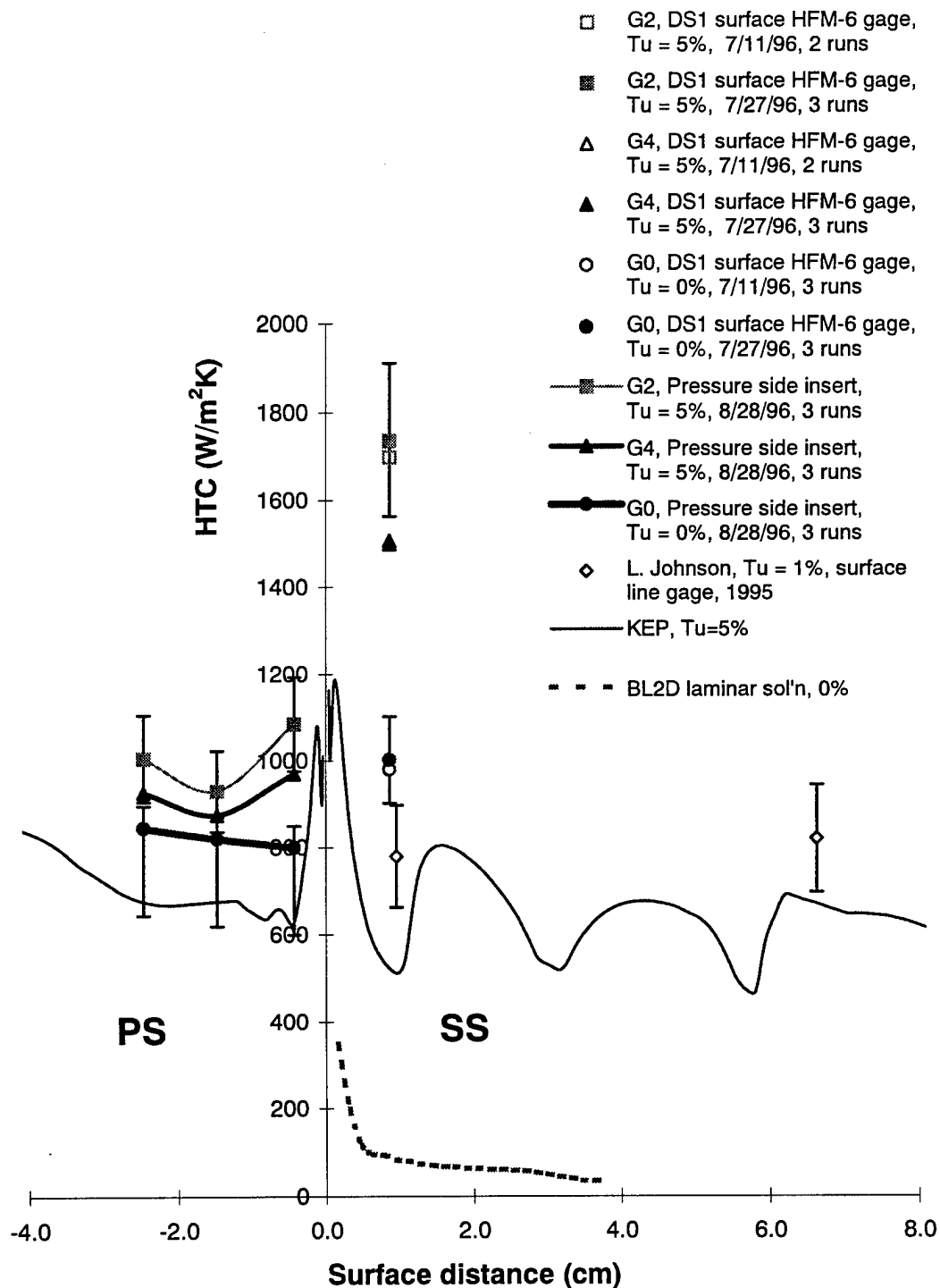


Figure 5.1.1 Heat Transfer Coefficient measurements with DS1 (suction side) and insert HFM sensors (pressure side), including KEP and BL2D code predictions.

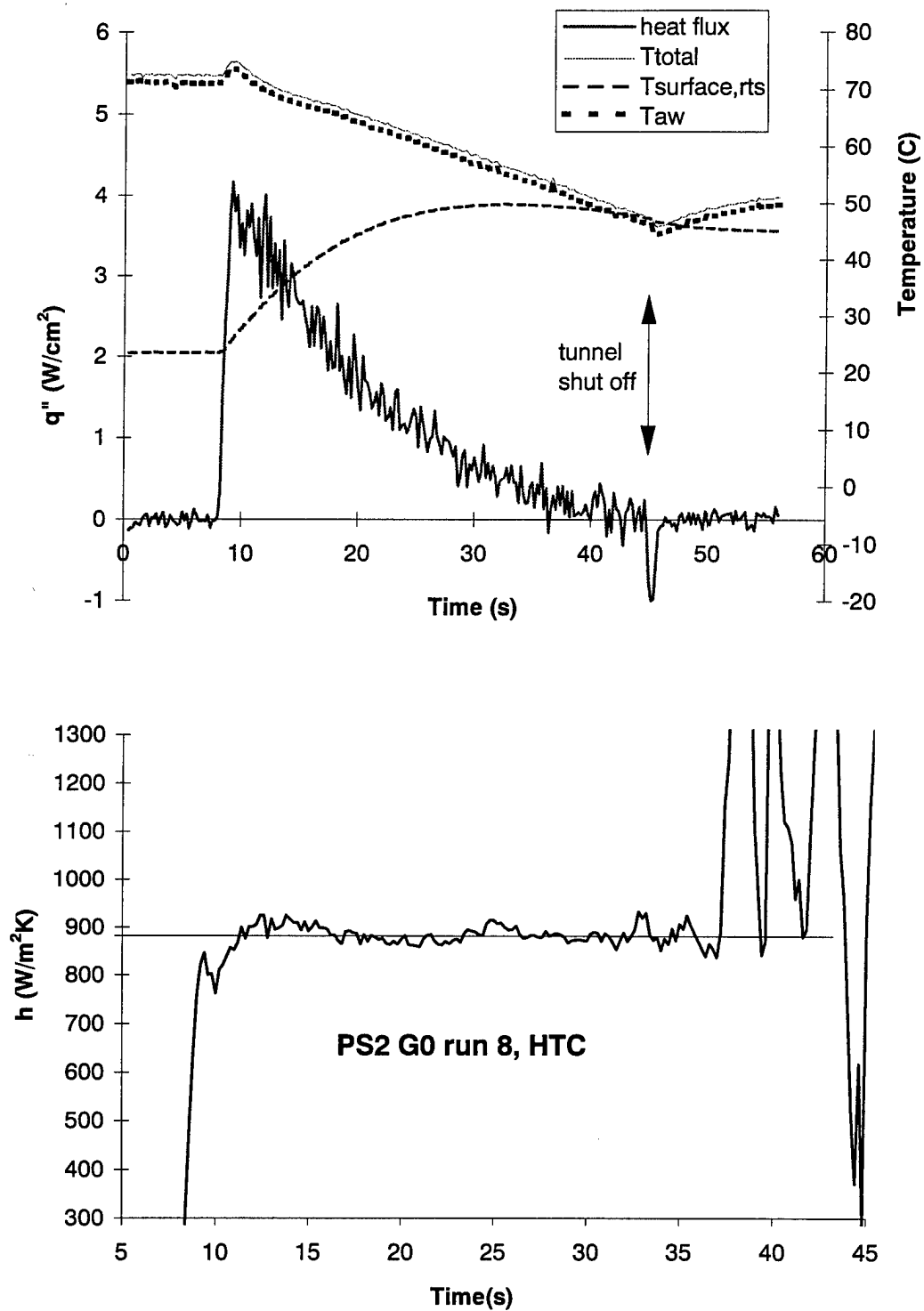


Figure 5.1.2 Example of tunnel data and HTC calculation result for one tunnel run.

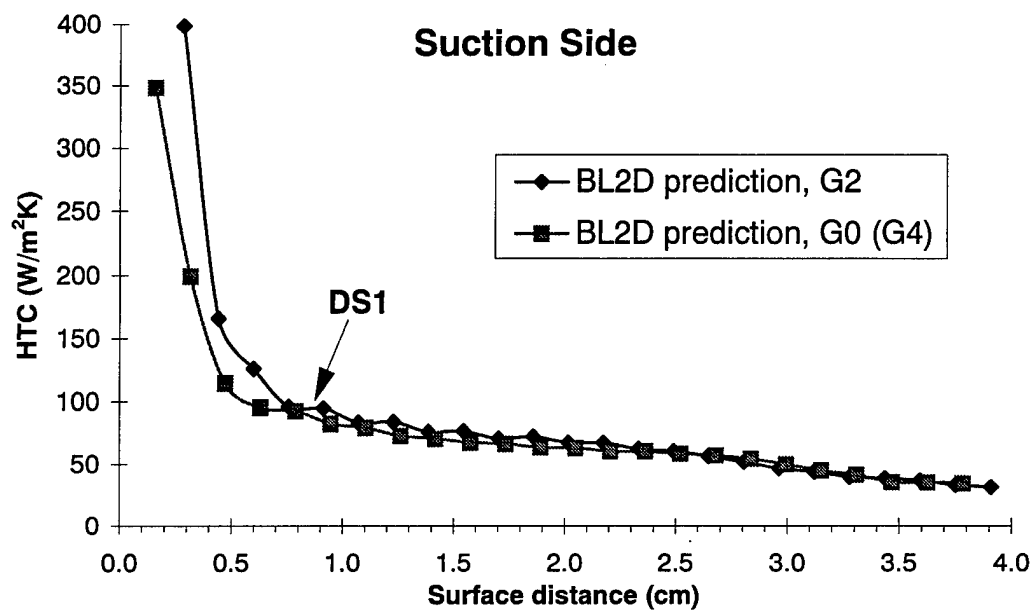


Figure 5.1.3 BL2D predicted suction side (SS) heat transfer coefficient for G0 vs. G2 using measured G0 and G2 blade surface static pressures as input.

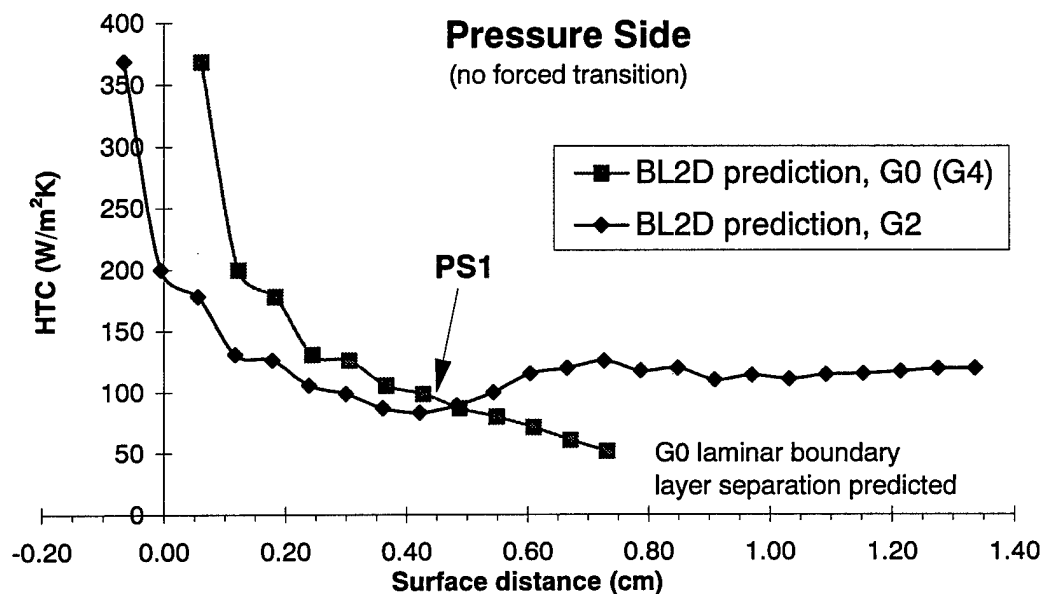


Figure 5.1.4 BL2D predicted pressure side (PS) heat transfer coefficient for G0 vs. G2 using measured G0 and G2 blade surface static pressures as input.

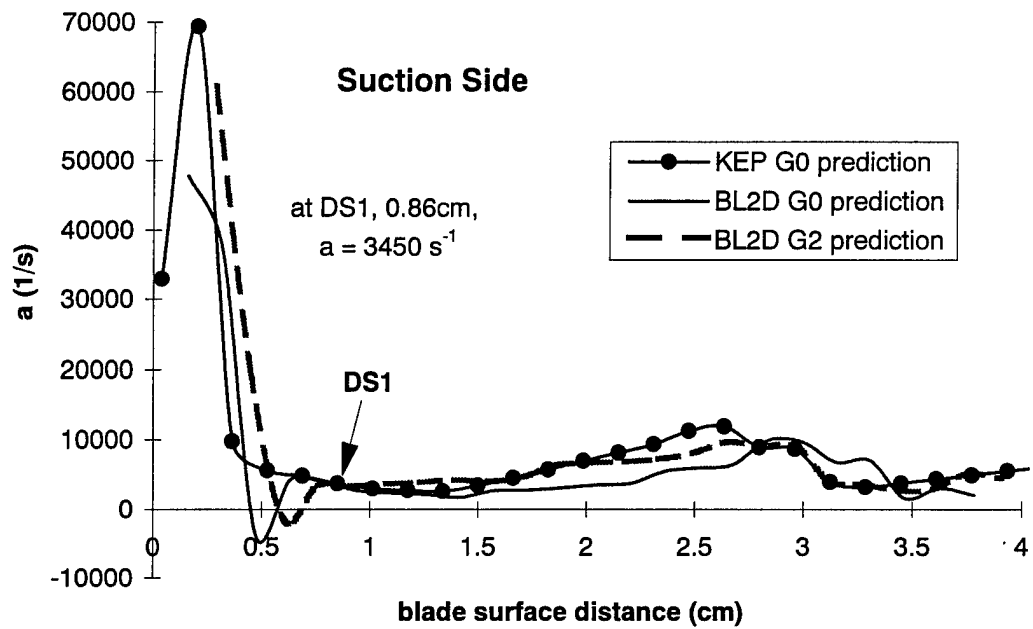


Figure 5.1.5 BL2D suction side (SS) strain ($a=dU/dx$) prediction for G0 and G2 based on measured blade surface pressure distributions.

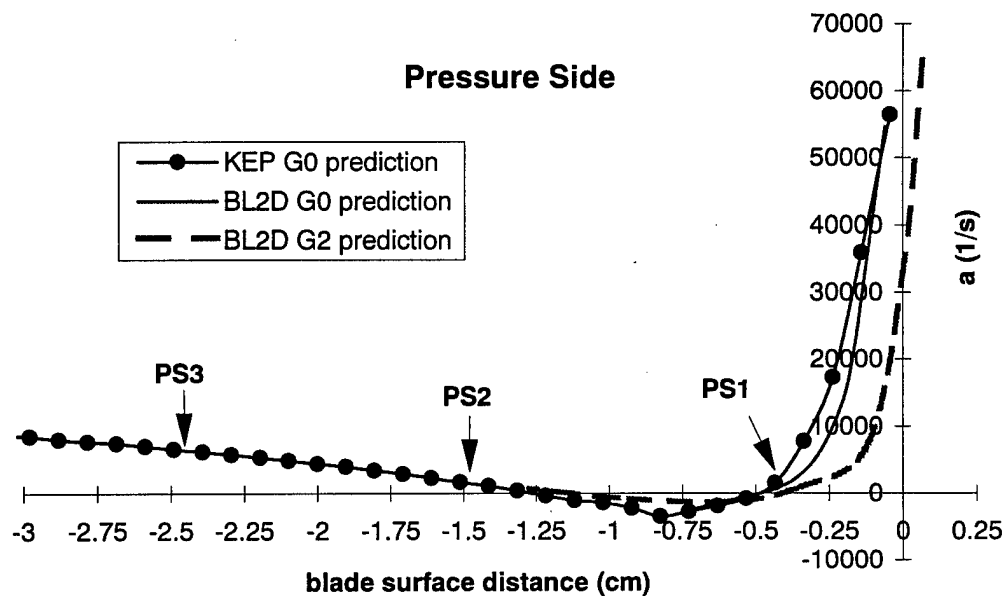


Figure 5.1.6 BL2D pressure side (PS) strain ($a=dU/dx$) prediction for G0 and G2 based on measured blade surface pressure distributions.

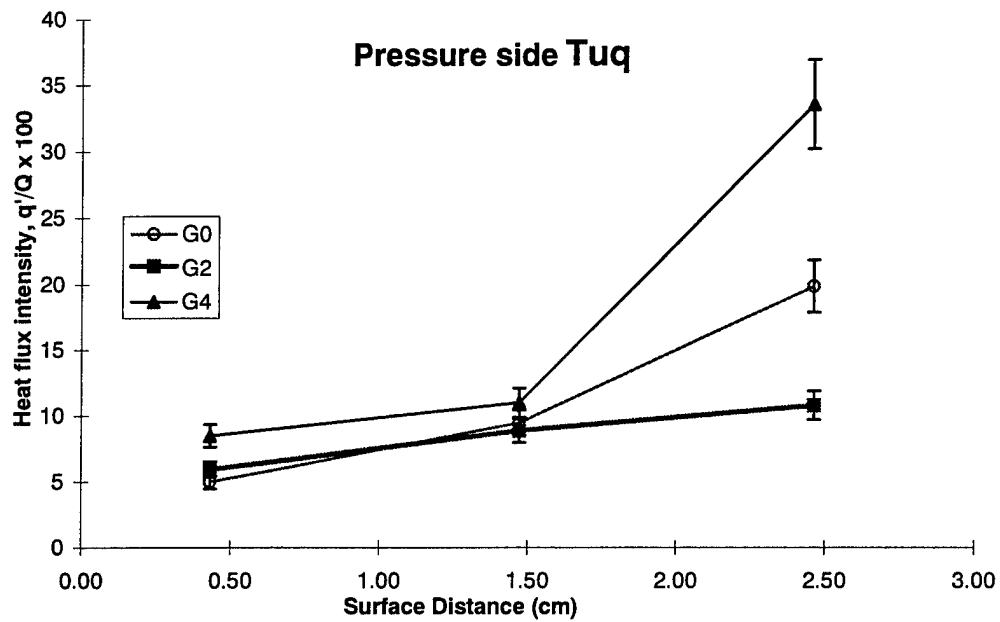


Figure 5.1.7 Heat flux intensity (Tu_q) along pressure side (PS) for different grids.

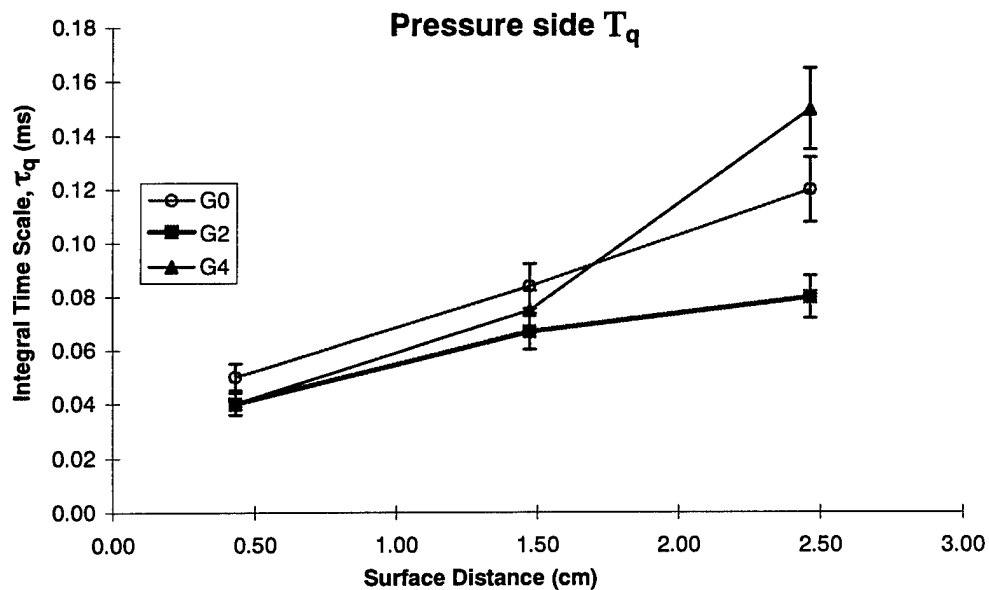


Figure 5.1.8 Heat flux integral time scale (T_q) along PS for different grids.

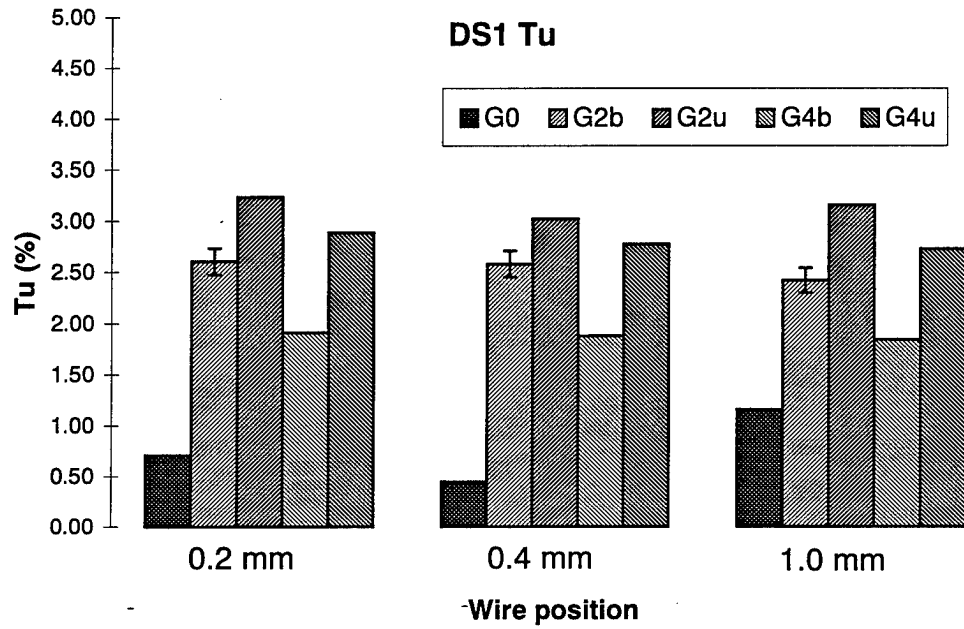


Figure 5.2.1 DS1 turbulence intensity (Tu), grid vs. wire position.

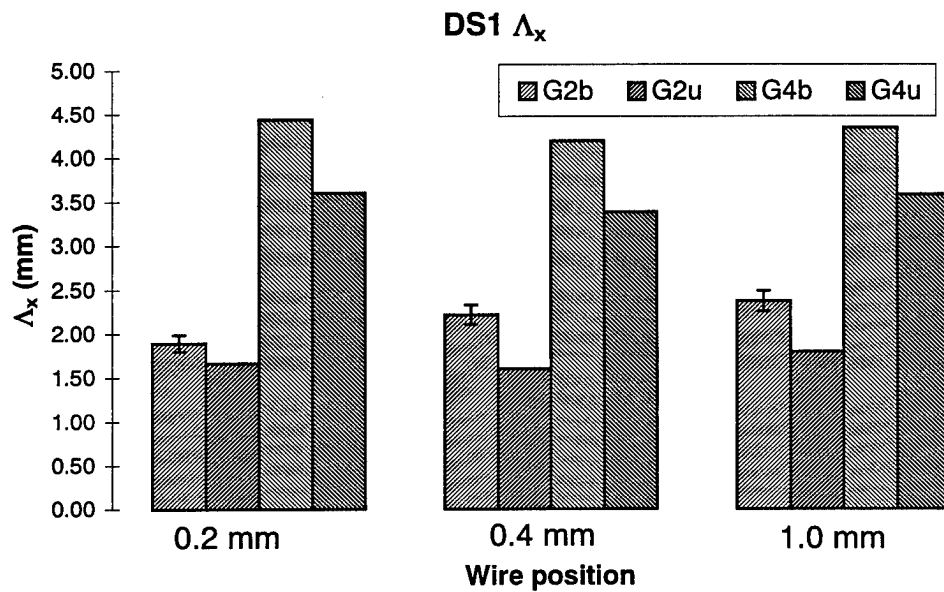


Figure 5.2.2 DS1 integral length scale (Λ_x), grid vs. wire position.

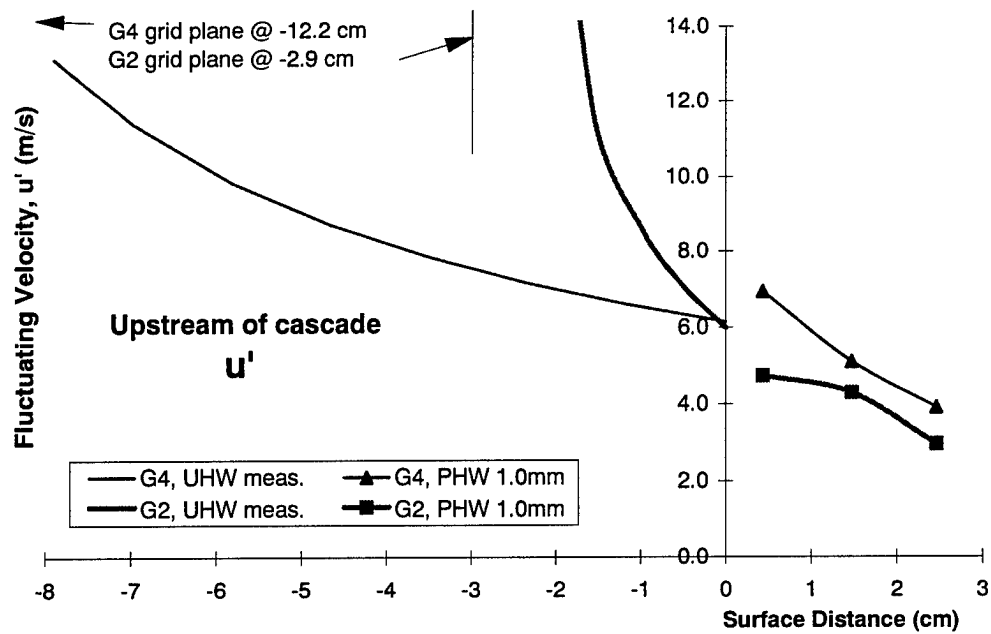


Figure 5.2.3 Fluctuating velocity (u') upstream and into passage (1 mm wire position above PS), Grid 4 vs. Grid 2.

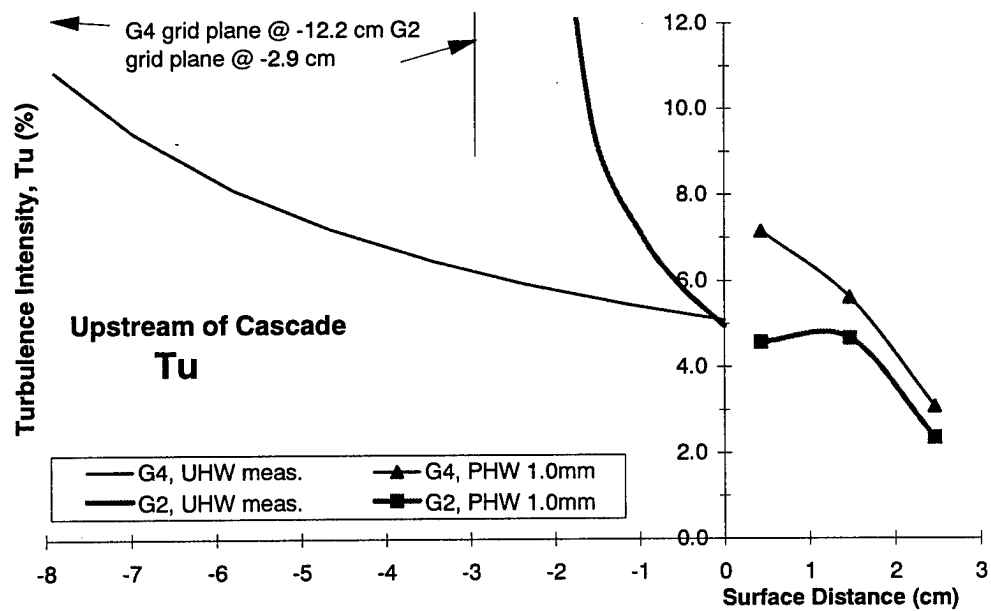


Figure 5.2.4 Turbulence intensity (Tu) upstream and into passage (1 mm wire position above PS), Grid 4 vs. Grid 2.

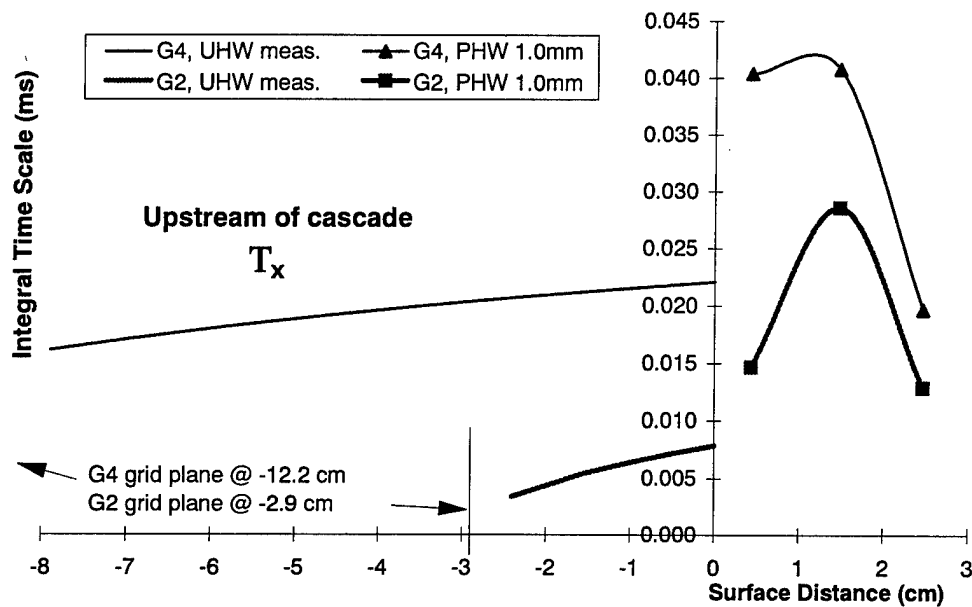


Figure 5.2.5 Integral time scale (T_x) upstream and into passage (1 mm wire position above PS), Grid 4 vs. Grid 2.

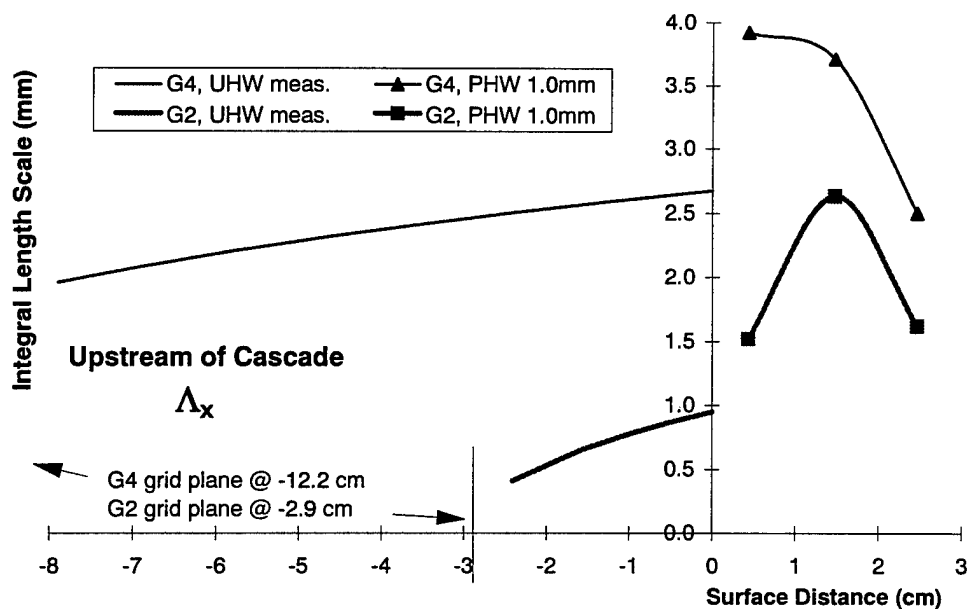


Figure 5.2.6 Integral length scale (Λ_x) upstream and into passage (1 mm wire position above PS), Grid 4 vs. Grid 2.

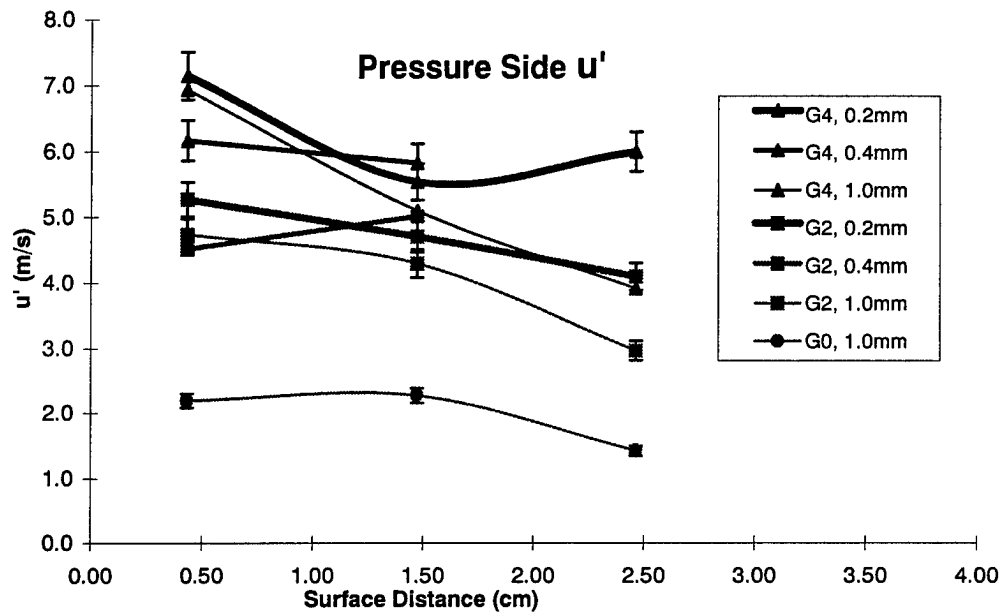


Figure 5.2.7 PS u' grid comparison at different y_{wire} .

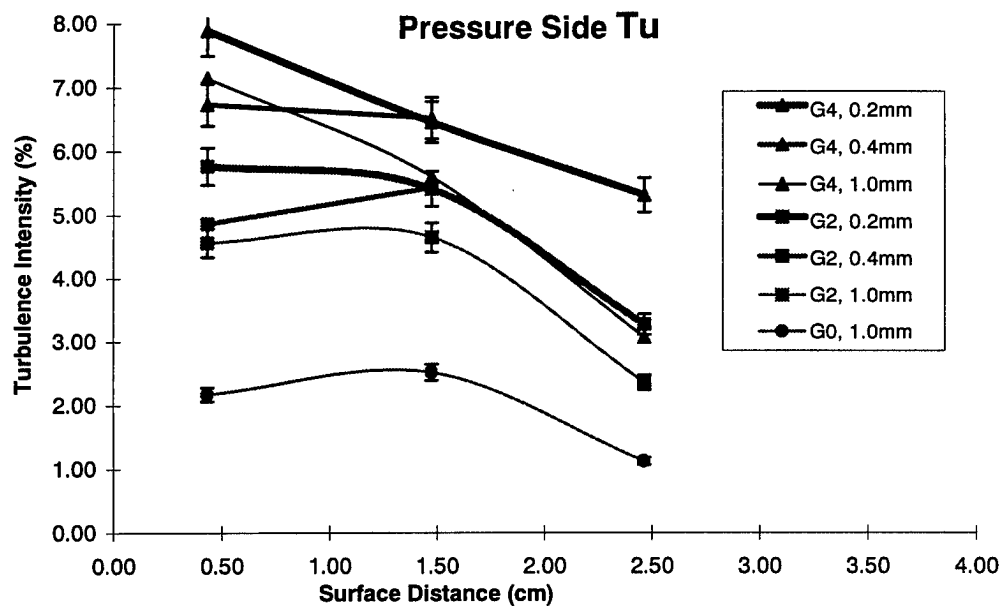


Figure 5.2.8 PS Tu grid comparison at different y_{wire} .

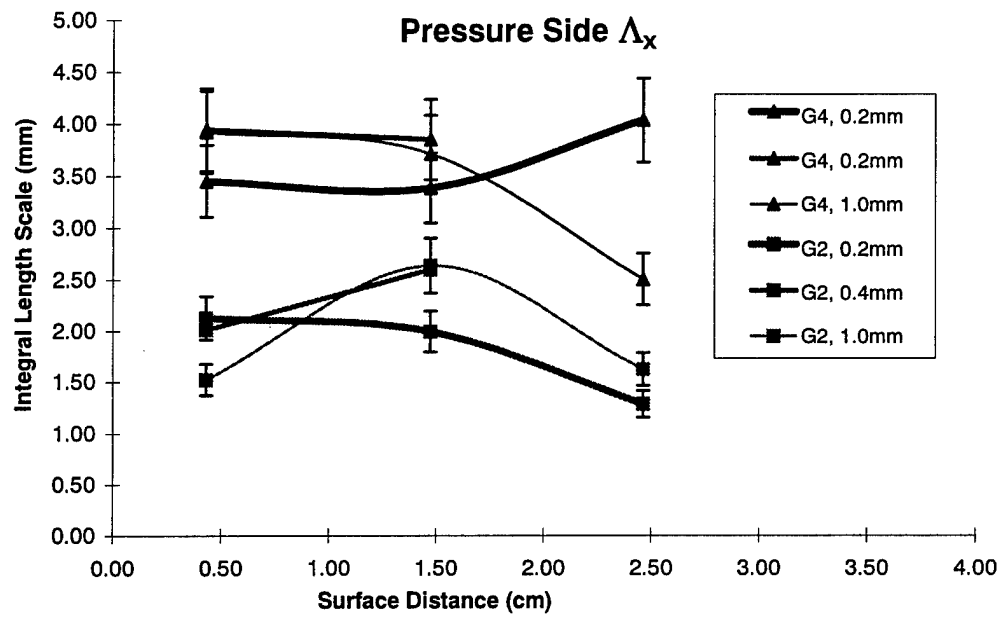


Figure 5.2.9 PS Δ_x grid comparison at different y_{wire}

6. Frequency Domain and Time-correlation

In this chapter, the spectral energy contained within the mean data (Ch. 5) is presented. This includes the energy spectra (PSD) of the velocity above each heat flux gage, the spectra of the heat flux itself for each grid condition, and then the spectra derived quantities of coherence and phase shift. Time correlation is also presented. In each case, the data at sensor DS1 on the suction side (SS) is presented first, followed by the pressure side (PS) data. Discussion is included in each section, but a full interpretation of the mechanisms of flow/ surface interactions is left for chapter 7.

The main thrust of the research is contained here. The goal is to find what is responsible for observed mean heat transfer by studying the unsteady data. The data will be presented along with some discussion of notable points, possible explanations, and resulting conclusions. The influence of acceleration, curvature, length scale, and the state of the boundary layer on the velocity/ heat transfer interactions will be addressed as the data is presented.

The measurement matrix above the HFM sensors was discussed in section 5.2.1 with run procedural information there as well as in section 2.4. Run specific data are presented in Tables 5.1, 5.2 and 5.3 for the heat flux and hot-wire. The measurements above sensor DS1 consisted of 3 PHW y_{wire} positions (0.2 mm, 0.4 mm, 1.0 mm) with 5 grid conditions (G0, G2u, G2b, G4u, G4b; "u" denotes "up" where $Tu_{inlet} = 5\%$, "b" denotes "back" where $Tu_{inlet} = 3.6\%$) at each wire location. On the PS, the forward 2 heat flux gages had the same three wire positions above each heat flux sensor (HFS) with 3 grid conditions at each (G0, G2, G4, with G2 and G4 equivalent to the "up" grid conditions used for DS1). Measurements were made at 0.2 mm and 1 mm y_{wire} above PS3.

6.1 Turbulence Spectra in Passage

6.1.1 DS1: G0, G2, G4

The power spectral density (PSD) of the hot-wire velocity over DS1 at 0.2 mm, 0.4 mm, and 1 mm for the five grid conditions are presented in Figs. 6.1.1, 6.1.2, and 6.1.3. The upper and lower plots are the same PSD, except that the lower non-log plot has the high frequency noise removed from the spectra according to the method outlined in section 3.3. Based on the u' and Δ_x data presented in Figs. 5.2.1 and 5.2.2, the work of the highly strained SS flow field can be seen in reducing the fluctuating energy to the significantly lower levels seen here at DS1. Note that the G4b and G4u spectra are similar in energy distribution with G4b having a lower intensity (proportional to the square-root of the area under $E(f)$, Eqn. 2.2) than G4u. The same relationship holds for G2b and G2u. The energy in the baseline case is an order of magnitude below the grid

turbulence. The progression of the spectra at different y_{wire} values for each grid can be seen in Figs. 6.1.4 and 6.1.5. There appears to be little significant change in the G2 energy spectra approaching the wall, while some growth of the low frequency end of the spectrum can be seen for G4b and G4u. This is seen as a slight increase in u' as the wall is approached, while the distribution, reflected in Δ_x , remains approximately constant, see Fig. 5.2.2.

6.1.2 PS: G0, G2, G4

The energy spectra measured at 1.0 mm above each PS gage for each of the three grid conditions is presented in Figs. 6.1.6, 6.1.7, and 6.1.8. In reference to the noise peak near 70 kHz at sensors PS1 and PS2, a discussion of HW frequency response and electrical noise issues is presented in section 3.2.1. The PS2 spectral noise was removed according to the method of section 3.3. More severe noise is seen in the spectra of PS3 for reasons that are not clear. Large increases in the low-frequency end of the with-PHW heat flux spectra were seen relative to the no-PHW spectra suggesting some significant low-frequency (< 2 kHz) probe disturbance. Therefore, the results will be presented, but should be regarded carefully. Removing the noise in the spectrum was also done according to section 3.3, but required reconstructing much of the high-frequency end of the spectrum. This was done with reference to the isotropic spectrum in order to produce intensity and scale values near actual values, with an estimated uncertainty of twice that for PS1 and PS2. The lower end of the spectrum is reliable based on earlier comparisons of spectra with and without noise.

While the free-stream flow near the wall above DS1 is accelerating, the free-stream flow nearer the pressure side is decelerating, despite the acceleration at the wall seen in Fig. 5.1.6 (PS strain). This deceleration can be seen in the change in Mach number from 0.36 at the inlet to 0.28 at 1.0 mm above PS1. The result of this deceleration, combined with wall effects, is a jump in intensity (Fig. 5.2.4) above the correlation based on decay behind the grid. This effect of increased intensity in the presence of deceleration (where the flow is relaxing) may seem counter-intuitive; Townsend (1976) describes this effect as "inactive swirl," whereby large eddies have superposed velocity at the wall, and he notes this motion is "particularly intense in boundary layers in adverse pressure gradients." The value of u' increases as the wall is approached (Fig. 5.2.7), with amplification at low-frequencies that is more than seen above DS1. G2 increases more significantly in energy in the 1 mm approaching the wall, evidence of its smaller scale. The individual G2 and G4 spectra for PS1 are presented in Figs. 6.1.9. A notable shift of energy from the high frequencies to the low frequencies can be seen in the G2 spectra approaching the wall, another effect of this "swirl." The dominance of the low frequency eddies will be seen in the coherence at PS1.

Fig 6.1.10 presents the G2 and G4 velocity spectra above PS2 at different y_{wire} . The energy in the spectra generally increases toward the wall, but now the maximum is at 0.4 mm, evidence of different structures at work. The boundary layer has entered a region of high curvature and is beginning to accelerate again. Here the effects of curvature, as discussed by Kestoras and Simon (1994), become significant: higher momentum FS fluid is moved toward the surface by the action of streamwise vorticity (Townsend, 1976), while increased mixing occurs causing a growth in near-wall scales and more turbulent transport. The resulting maximum at 0.4 mm in G2 can be attributed to the increased v' motion of this streamwise vorticity, while the increased w' nearer the wall is not seen by the hot-wire. The energy of this vorticity can be seen in the 5 to 20 kHz range, with less near the wall, and more at 0.4 mm. For G4, 0.2 mm energy is equal to the 0.4 mm level, indicating the continued influence of the large frequency energy.

G2 and G4 spectra at PS3 are presented in Fig. 6.1.11. The mechanism responsible for the near-wall increase in fluctuating energy is the same as seen at PS2: that of streamwise vorticity that is grown through the work of curvature, and here amplified and reduced in scale by the acceleration. The smaller scale can be seen in the larger increase (in terms of percentage) in fluctuating energy from 1.0 mm to 0.2 mm. A similar but smaller increase can be seen above 3 kHz for G4, indicating the relatively larger scale of the G4 vorticity. The large spike in the 0.2 mm measurement for G4 is believed to be due to a probe instability that may invalidate measurements at this position, but the data is presented for completeness.

6.2 Heat Flux Spectra

The heat flux spectra is most sensitive to the large scale energy of the flow which dominates near the leading edge. Spatial resolution limits frequency response, but does not prevent *comparison* of spectra, in which case attenuation is relative, nor does it keep one from seeing heat flux interactions with the large majority of the energy containing eddies in the flow. Spatial resolution does prevent observing boundary layer scale turbulence, however. A complete discussion of these issues is given in section 3.1.4. Also note, relative to concerns of probe disturbance, all mean and fluctuating heat flux data presented in this section is without the PHW probe in place.

6.2.1 DS1: G0, G2, G4

Spectra of the heat flux taken with no PHW present are presented in Fig. 6.2.1 for the 5 grid cases used with DS1. The data has been normalized by assuming that the fluctuating heat transfer scales on the temperature difference at the time of data acquisition, $T_{aw} - T_s$, which varies from run to run, Table 5.1. This normalized heat flux is listed as q'_{norm} in Table 5.1. As with the

velocity spectra, the area under the spectral distribution is proportional to the square of the fluctuating component.

$$q'^2 = \int E_q(f)$$

so that proper normalizing of the energy spectrum requires dividing by the square of the temperature difference, $(T_{aw}-T_s)^2$.

The normalized data for G2 and G4 are presented again in Fig 6.2.2. Notice that the strongest energy in the spectra is near 1 kHz, but that distinct peaks are evident at 5 kHz and to a lesser degree at 10, 15, and 20 kHz. This will be discussed in chapter 7 in conjunction with coherent streamwise vorticity shed from the leading edge. The strange character of the G4u spectrum is also worth mention; the G4u data were actually taken on a different day than the other four distributions. This difference may be indicative of the sensitivity of the measurements to very small adjustments in grid location. The heat flux spectra shows very little energy beyond 10 kHz, but with significant differences between the various spectra. The result of the Corcos correction, discussed in section 3.1.4, which gives some estimate of attenuation due to HFS sensor size, is shown in Fig. 6.2.3. Based on this, approximately one third of the spectral energy is lost at 10 kHz, and 75% at 20 kHz. However, this correction is only approximate and is certainly not valid at higher frequencies where it shows energy increasing. In fact, this shows that attenuation is less than predicted so that frequency response is better than predicted.

Also shown in Fig. 6.2.3 is the -5/3 power law slope characteristic of the turbulent velocity spectrum. The uncorrected heat-flux decay seems to follow this. Correction for spatial averaging would raise the energy level at higher frequencies, indicating that heat flux energy rolls off more slowly than the free-stream turbulent velocity spectrum. This result is opposed by Carlson and Reynolds (1991) who made fluctuating heat transfer measurements below a low FST turbulent boundary layer in water. Their sensor also had spatial resolution problems.

The source of the low-frequency (1 kHz) peak is worth discussion. Although the work of Zhou and Wang (1993) indicates very high levels of laminar boundary layer fluctuations as high as 15% of the free-stream velocity, these cannot be at such a low frequency as seen here given the size of the boundary layer. Instead, these fluctuations must be due to similarly scaled flow energy disturbing the boundary layer nearer the stagnation point. These disturbances are then convected along the suction side over DS1 even as the low frequency energy in the free-stream above is attenuated.

6.2.2 PS: G0, G2, G4

Normalized heat flux spectra is shown for each pressure side HFS in Figs. 6.2.4, 6.2.5, and 6.2.6. The no-flow energy level is given as well to show the roll-off and noise level, where the

no-flow has been normalized by a similar $T_{aw} - T_s$ for comparison sake. At PS1, The difference in energy levels at low frequencies is actually very large, in agreement with the large variation in fluctuating energy in the free-stream seen in Fig. 6.1.6. The separation in energy level at low frequencies is much greater than at DS1, with G0 significantly below the grid-in cases. And note that G0 is near the noise level above 20 kHz, while G2 and G4 show energy out to 60 kHz, evidence that the heat flux gage sees this much smaller structure, although attenuated (see section 3.1.4). Also note the strong 5 and 10 kHz peaks as seen in the DS1 heat flux. The heat flux spectra at PS1 with the PHW probe present *does not* have these peaks, however (no plot shown). The reason that these peaks are not present when the probe is in place indicates some probe disturbance and this will be discussed more in section 7.3.2.

In the PS2 spectra (Fig. 6.2.5), less difference is seen between the three grid cases with a significant growth in low frequency energy, especially noticeable in the G0 spectrum. At PS3, continued substantial growth in the low frequency energy is seen, with G4 above the others. The lower HFS gage sensitivity at PS3 is also seen in the higher noise level. The very large increase of the low frequency energy from PS1 to PS3 can be seen in Figs. 6.2.7, 6.2.8, and 6.2.9 showing the individual G0, G2, and G4 spectra along the PS. This low-frequency energy is responsible for the increase in T_{uq} seen in Fig. 5.1.7 and a discussion of its significance is given in chapter 7.

6.3 Coherence

Coherence is a frequency domain representation of the correlation between two simultaneous sampled signals. A significant coherence level at some frequency means that two independent signals, x and y, have energy at the same frequency, and specifically energy that correlates in time at that frequency at some phase that varies independently of the coherence. Coherence is defined as the square of the averaged cross-spectrum divided by the product of each averaged power spectrum.

$$\text{Coherence} = \frac{\overline{S_{xy}(f)}^2}{\overline{S_{xx}} \cdot \overline{S_{yy}}}$$

where the overbar denotes averaging of separate power spectra, S, performed on consecutive blocks of sampled data, and S calculated according to the definition given in Eqn. 2.3. For the case of no averaging, the coherence will always equal 1.0 so that accuracy in measuring coherence depends on a sufficient number of averages to arrive at some asymptotic value. The number of averages required increases with lower values of coherence with 100 or more averages typical.

For the present data, velocity and heat flux were processed with 512 averages at 50% overlap. Calculations of coherence and phase were performed within hfmphw2.m (Appendix B) as

were the power spectra calculations. Phase information will be presented after the coherence data.

6.3.1 DS1: G0, G2, G4

The coherence for the three grid cases at each wire position are given in Figs. 6.3.1 and 6.3.2. The same data with all spectra together for each wire position are shown in Fig. 6.3.3. First notice the significantly higher coherence for G4 vs. G2. Also notice that the G4 “back” case shows less coherence than the G4 “up” case while G2b shows greater coherence than G2u. Tied in with this is the presence of discrete peaks in the coherence, most prominent at 5 kHz in G4, but also at 7, 9, and 11 kHz. These dominant frequencies must be tied to certain turbulent structures preferentially amplifying energy in the inlet flow. These structures can then be seen as the primary large scale sources of $v't'$ in an otherwise low-impact free-stream turbulence above a highly accelerating laminar boundary layer.

The presence of these structures in the G4 measurements and their absence in the G2 measurements can be related to the nature of the inlet turbulence. The larger G4 eddies are significantly distorted in the strong accelerating flow field about the leading edge leading to strong amplification of streamwise vortices. The smaller scales of G2 are perhaps not distorted significantly, so that the flow development (and its effect on heat transfer) is seen to be dependent on length scale. This argument is strengthened by the fact that the G2 intensity is actually significantly higher at DS1 than for G4. However, this effect will be very sensitive to anisotropy of the inlet flows, where mean orientation of low frequency vorticity would be a significant factor not easily seen in inlet hot-wire measurements. The nature of these structures will be discussed more in chapter 7.

The work of T. Wang (e.g., Zhou and Wang, 1993) and others has shown that FST causes proportionately high fluctuations in a laminar boundary layer, and that high acceleration (as here) does not minimize this but instead stabilizes the boundary layer and delays transition. Typical laminar boundary layer unsteadiness with FST is on the order of 15% ($u'/U_e = 0.15$). This unsteadiness is not turbulent eddy motion however, but instead something like U velocity oscillation in the lower half of the boundary layer (Zhou and Wang, 1993). Their measured v' velocity fluctuations, however, are much lower throughout the laminar boundary layer, on the order of $v'/U_e = 0.02$. In the case of the present data, the low coherence of flow and heat flux fluctuations may be due to the indirect way that free-stream eddies interact with the laminar u' fluctuations. The FST presumably does not reach as near to the wall and only induces laminar boundary layer unsteadiness. These laminar fluctuations are not accompanied by v' motion and therefore have little effect on q' relative to turbulent u' , as well as reducing measured coherence.

The issue of the convex curvature also needs to be considered, as previous research has shown the tendency for high momentum eddies to be pushed away from a convex wall, decaying more rapidly (Kestoras and Simon, 1994). Based on the present data, the internal boundary layer fluctuating energy induced by the FST eddies are only indirectly connected to the frequency content of those eddies with the acceleration and curvature significantly limiting their effectiveness at disrupting the boundary layer relative to the pressure side.

6.3.2 PS: G0, G2, G4

The pressure side data shows much higher coherence levels than seen at DS1. Figs. 6.3.4 and 6.3.5 give G2 and G4 coherence for the three wire positions at PS1 and PS2, and Figs. 6.3.6 and 6.3.7 give the combined G0, G2, and G4 coherence at the 0.2 mm and 0.4 mm wire positions for PS1 and PS2. A progression of the coherence along the PS at 1 mm is given in Figs. 6.3.8 and 6.3.9. Measured near-wall coherence for G2 and G4 at PS3 is also shown in Fig 6.3.9. The very low coherence for G4 at 0.2 mm appears to be strong confirmation of the probe instability discussed earlier.

Note that 0.4 mm coherence is generally above that at 0.2 mm. This corresponds to the increased v' energy that should be observed for streamwise vorticity. The lower 1.0 mm coherence (relative to the near wall levels, Fig. 6.3.4) for G2 indicates the difference in scale relative to G4. Also note the higher coherence for G2 above 5 kHz seen at every gage. This is despite the fact that the flow energy at these frequencies is not necessarily higher for G2 -- certainly not at PS1 until beyond 10 kHz (Fig. 6.1.6). However, at PS1 the coherence measured for G2 is significantly greater (Figs. 6.3.6 and 6.3.8), especially considering the attenuation of the heat flux gage. This supports the conclusion of a different state of the boundary layer for G2, as seen earlier in the different fluctuating heat flux levels at PS2 and PS3, section 6.2.2.

The progression of coherence at 1 mm along the PS (Figs. 6.3.8 and 6.3.9) shows that coherence is dropping across the whole spectrum. This drop is seen in the measured drop in length scale (Fig. 5.2.6) and the steep drop in intensity going from PS2 to PS3. Clearly the attenuation of large scales in the free-stream has affected the coherence at these corresponding low frequencies. A clear picture of the decay of large scales, but persistence of mid-scales ($f > 5$ kHz) responsible for cross-stream transport, can be seen in Fig. 6.3.10 where the coherence for G2 at 0.2 mm and 1.0 mm is presented for the three PS locations. The coherence goes to zero at 1.0 mm indicating the full attenuation of larger scales, while the level of the scales corresponding to greater than 5 kHz (and less than 1 mm) persist. The same trend is seen in G4 if the lack of coherence at PS3 for the 0.2 mm wire position is attributed to measurement problems. The presence of baseline G0 coherence is also noteworthy in that strong coherence is seen at PS1

even from this low-intensity free-stream with scales that are apparently effectively amplified. However, these large scales are rapidly attenuated along the PS.

Finally, note that the PS coherence shows no preferential frequencies (peaks as seen at DS1 at 5 kHz). Instead, a broad spectrum of eddies is at work at frequencies above 5 kHz (e.g. Fig. 6.3.10, and 6.2.4 vs. 6.2.5). This indicates that the coherent structures active at the leading edge are replaced continuously by a broader spectrum of turbulent vortices acting along the later pressure side (discussed further in chapter 7).

6.4 Phase

Phase information is the companion of coherence, allowing one to see the amount that a pulse in velocity at the hot-wire leads a corresponding pulse in heat flux. A given phase shift at a given frequency gives the corresponding time shift present between velocity and heat flux events at that frequency.

$$\Delta t = \frac{\phi}{360 f}$$

where ϕ is the phase shift in degrees and f is the frequency. If f is in kHz, the corresponding time shift will be in ms. While phase gives lag at a given frequency, it does not say what frequencies are most influential as seen in the coherence, or where the mean time shift is given by the integrated peak of the cross-correlation. However, a very clean (low noise) region of the phase curve will correspond to strong coherence, and if all y_{wire} positions are in agreement as well, this indicates a structure that spans the 1 mm above the surface interacting strongly with heat flux. Finally, a widely varying slope in the phase at some frequency relative to other frequencies would be evidence of a different flow mechanism at work.

Theory for oscillating flow at a stagnation point (Lighthill, 1954) predicts a phase shift of 90° between the shear at the wall and the free-stream flow. This may be the case at the stagnation point on the blade, but is not seen away from the stagnation point in the present data due to the added convection velocity and effects of flow acceleration.

Phase data seen here show a uniformly increasing lag of heat flux behind velocity fluctuations with frequency. Thus, lower frequency energy (from larger scale structures) are close to being in phase, while phase lag increases for smaller structures. Based on the equation above, it can be seen that a linearly increasing phase lag would correspond to a constant time shift at all frequencies. The shape generally seen here indicates that lower frequencies have a relatively larger time shift. Interestingly, the phase shift at each sensor is largely independent of y_{wire} , indicating most of the shift occurs across the boundary layer, while some grid dependence is seen, indicating the effect of scale on the time shift. Also, phase shift steadily increases along the pressure side and is greatest on the suction side over DS1.

6.4.1 DS1: G0, G2, G4

Phase measurements for the G2 grid conditions at the three wire positions are presented in Fig. 6.4.1, and for the G4 grid conditions in Fig. 6.4.2. G0 showed very little phase information besides noise. Clearly, the regions of grid spectra with high coherence correspond here with cleaner phase, e.g. the region around 5 kHz for G4u. The peak in the phase at 6 kHz in G4u is believed to be significant and will be discussed in the next chapter. As noted, there is no significant difference at different wire positions for the same grid in terms of mean phase shift. Also, the phase shift is approximately 200° at 20 kHz for all grid conditions. This value appears to be dependent on the free-stream flow acceleration such that events in the boundary layer show a large time shift relative to events in the free-stream. In other words, the action of eddies nearer the leading edge are seen in the history of the boundary layer -- a given eddy is accelerating and seen at the hot-wire prior to its influence being seen at the surface.

6.4.2 PS: G0, G2, G4

The phase for PS1 G2 and G4 are shown in Fig. 6.4.3. Here a difference in phase shift can be seen in the nearest 0.2 mm location. This corresponds to a shift in the cross-correlation peak (next section). The phase shift at 15 kHz is different at PS1 with G4 having a larger shift of 120° compared to 100° for G2, evidence of the difference in scale and/ or the shift in pressure gradient for G2, while at PS2, Fig. 6.4.4, there is less difference between G2 and G4. The average increase in phase from PS1 to PS2 is evidence of the work of curvature and of the mean velocity field above the pressure side. Interestingly, even though there was almost no measurable coherence in G4 at PS3, a significant phase is recorded, Fig. 6.4.5. The average shift is similar to that seen at PS2 of approximately 160° .

6.5 Time-correlation

6.5.1 Background

A significant body of literature exists with correlation data, including single-wire auto-correlations as well as spatial correlations between two wires, and in a variety of flows (e.g. work reviewed in Hinze, 1975, or Townsend, 1976). Some studies have been done correlating heat flux spatially, e.g. Ching and LaGraff (1995), in order to watch transition. Much less work has been done correlating surface heat flux to flow velocity.

A study by Brown and Thomas (1977) shows measurements in a low-FST low-speed flat-plate turbulent boundary layer showing wall shear, τ , lagging velocity at increasing time shifts as a hot-wire was moved away from the wall. The peak correlation was measured near the wall at $y/\delta = 0.05$ where $R_{\tau u} = 0.32$. At the edge of their boundary layer, the velocity lagged wall shear by

approximately $t = 30\delta/U$, where δ is the boundary layer thickness. The time shift was also looked at by moving the wire downstream at a given y until the time shift was zeroed. For a point corresponding to the edge of their boundary layer, the shift in streamwise distance was $x/\delta = 2.5$. Comparison of this data with the present blade data will be given in the following section.

The work of Carlson and Reynolds (1991) presents correlation coefficients across a low FST turbulent boundary layer in water. They show uq correlation decreasing uniformly away from the wall with a maximum value of $Ruq = 0.18$ at their nearest wall measurement point at $y^+ = 11$ and going to zero outside the boundary layer similar to the results of Brown and Thomas above, but very different from the results on the present blade as will be seen.

In addition to the above studies, cross-correlation data from Oxford is presented in Moss and Oldfield (1996) for a flat-plate turbulent boundary layer with high FST. They present uq correlation data at one point ($y/\delta \approx 0.14$) showing Ruq peaks near 0.5 for their grid cases. Similar data from this author's work at Wright-Patterson AFB will be presented in section 6.6. The background, mean data, and some of the frequency domain data to be presented were reported in Holmberg and Pestian (1996, attached in Appendix A-1).

6.5.2 PHW movement streamwise relative to HFM

Several tests were performed to examine the effect of moving the PHW streamwise position relative to the surface of the HFS. The tests were performed with G4 and the PHW probe at the PS2 location. The intent was to determine if there was some ideal location for measuring correlating surface/ flow phenomena. The results were inconclusive.

Results for five runs are as follows (data from 4/30/96 and 5/4/96): run 1, wire 1 mm forward of HFS center, $\Delta t = 38\mu s$; run 2, wire 1 mm behind HFS center, $\Delta t = 38\mu s$; run 3, wire at center of a Kulite pressure transducer, $\Delta t = 14\mu s$; run 4, wire at HFS center, $\Delta t = 40\mu s$; run 5, wire at HFS center, $\Delta t = 34\mu s$. These data were all at the same streamwise position (the Kulite being shifted spanwise relative to the HFM). The results show no significant effect of moving the wire on Δt or on coherence data (not shown here).

In retrospect, a shift in Δt should be observed, proportional to the convective velocity. At PS2, the velocity is approximately 90 m/s so that a shift of 2 mm from front to back of the gage should correspond to $\Delta t = x/U = .002/90 \approx 22\mu s$. The fact that this was not observed can be attributed to differences in position of the wire normal to the surface, y_{wire} (where the wire may have been in the boundary layer), and/ or to the few tests performed. However, the observed shifts of $\Delta t \approx 40\mu s$ agree with later results presented in the next section. This also corresponds to the time shift seen across the turbulent boundary layer of Brown and Thomas (above), where they

report $\Delta t = 30\delta/U$ at the edge of their boundary layer, where for the present data, with $\delta \approx 0.3$ mm, $\Delta t = 30\delta/U = 33 \mu\text{s}$.

6.5.3 Results at DS1 and PS

Cross-correlation data at the four sensor locations are presented in Figs. 6.5.1 through 6.5.4. For DS1, Fig. 6.5.1, only the G0, G2u and G4u results are presented. Notice that G0 registers almost no correlation, while G2 is weak compared to G4. For G2, the time shift actually is greatest at the wall, while for G4 the largest time shift is at 0.4 mm. In addition, the correlation shows an asymmetry such that the correlation is higher after the peak. This "post-peak" tail will be discussed in chapter 7.

The results along the pressure side generally show a narrower peak for G2 compared to G4 with a decreasing peak level seen for G2 moving away from the wall, corresponding to the decreasing coherence, while G4 decays less. Also note the very small time shift at PS1 of approximately 0.01 ms for G2 relative to the larger shifts seen at PS2 and PS3. This corresponds to the lower phase lag seen in the phase data (Fig. 6.4.3 vs. 6.4.4). Note that for G2 at PS1 the time shift increases moving away from the wall with almost no time shift measured at 0.2 mm. This indicates that there is very little time shift across the boundary layer, but mostly across the free-stream. As will be discussed later, the very small time shift seen here also shows the strong influence of the lowest frequency eddies, as confirmed in the coherence data.

The magnitude of the peaks in the cross-correlation are similar to the magnitudes reported in Moss and Oldfield (1996) for a turbulent boundary layer with grid generated turbulence. In that case, measurements were in the lower part of the boundary layer. For the present blade, measurements are outside the boundary layer (except perhaps for the near-wall locations at PS2 and PS3) and evidence the large FST scales relative to the thin boundary layer.

6.6 Comparison data from WPAFB

The following work was performed at WPAFB in Dayton, Ohio in the summer of 1994 and has been presented in part in Holmberg and Pestian (1996, attached in Appendix A-1). The test facility is a low-speed wall jet over a heated flat plate. The boundary layer was fully turbulent with an integral length scale of 12 cm due to the large scale vorticity generated at the shear layer. The maximum velocity, $U_{\max} = 21.6$ m/s, was at $y = 51$ mm ($y^+ = 2600$) above the plate. The data included time-resolved u' , v' , and t' across the boundary layer as well as surface q' , allowing comparison of uq correlations similar to those presented in this chapter. Mean and fluctuating velocities are shown in Fig. 6.6.1 as reference showing the much higher turbulence intensity = $u'/U_{\max} = 15\%$ across most of the boundary layer, and the persistence of u' to very close to the wall.

Coherence of wall heat flux and u velocity fluctuations is shown in Fig. 6.6.2. As with the blade data, velocity leads heat flux. The coherence levels are similar to those seen at PS1, except higher near the wall. This should be expected given the very large scales in the WP flow and that the measurements are being made within the boundary layer. Corresponding phase is given in Fig. 6.6.3 at different positions across the boundary layer. Near the wall the two signals are nearly in phase, with increasing lag across the boundary layer. This corresponds to the data reported in Brown and Thomas (1977). As a footnote, the phase presented here in Fig. 6.6.3 is inverted from that given in Holmberg and Pestian (Appendix A-1, Fig. 16), and the magnitude of the phase shift here is twice that reported in Holmberg and Pestian. Fig. 6.6.3 is correct and the data indicates heat flux lagging velocity as seen in the present blade data.

A plot of the normalized cross-correlation peaks at different y^+ is shown in Fig. 6.6.4, where $y_{\max} = 0.051$ m is the y location of the wall-jet's maximum velocity. The peak correlation magnitude at $y^+ = 300$, equal to 0.60, is close to that reported by Moss and Oldfield (1996) in the lower part of their boundary layer. The similar levels measured on the pressure side of the blade, however, are outside the boundary layer. The time-shift of the peak is growing with y^+ indicating increasing lag of the heat flux sensor. This same information is presented as y vs. Δt in Fig. 6.6.5. The time shift of 23 ms seen at $y^+ = 2600$ is small compared to that seen in the zero pressure gradient boundary layer of Brown and Thomas. They reported $\Delta t = 30\delta/U$ at the edge of their boundary layer. For this data, $\Delta t = 10\delta/U$. Also note in Fig. 6.6.5 that most of the time shift is across the outer boundary layer.

In summary, the differences in time shift for these three sets of data shows the large effect that the character of a boundary layer has on the relation of flow and surface heat transfer. For the traditional low-FST flat plate boundary layer of Brown and Thomas, $\Delta t^*U/\delta = 30$ with a corresponding spatial shift of $x/\delta = 2.5$. This corresponds to an inclination in structures, due to the shear layer, of approximately 25° (65° from vertical). However, for the wall-jet data, $\Delta t^*U/\delta = 10$. The smaller time shift reflects the larger length scale active in the wall-jet boundary layer and the dominance of these larger scales in transporting momentum normal to the surface. For the blade data, $\Delta t^*U/\delta \approx 15 \pm 10$ depending on the actual boundary layer thickness, Δt at the boundary layer edge, and gage location. The boundary layer at PS1 appears to have some of the character of that seen in the wall-jet with large scales doing much of the work, while the later PS has the inclination of the low-FST flat-plate turbulent boundary layer. The larger time shift at DS1 shows an even greater shift across the near wall region.

Similarly, the magnitude and location of peak correlation gives information about the influence of the boundary layer or free-stream on heat transfer. In the low FST study of Carlson and Reynolds (1991), the peak correlation of $Ru_q = 0.18$ was at $y^+ = 11$, while for the wall-jet the

peak $Ru_q = 0.60$ is seen away from the wall but in the lower boundary layer evidencing the influence of large scale FST. With the blade data, the peak has moved outside the boundary layer due to larger scale FST relative to the boundary layer thickness.

6.7 Conclusions

Lower coherence was measured at the one suction side location than seen at all three of the pressure side locations. The higher coherence seen on the pressure side is strongest at low frequencies at PS1, but then moves to higher frequencies at PS2 and PS3. In concert with the velocity spectra, this shows that the large scales present near the leading edge are attenuated in the passage, and not interacting with the surface heat flux on the later pressure side. The coherence at frequencies above 5 kHz is actually seen to grow along the pressure side for the smaller scale Grid 2 turbulence, even as the intensity (Tu) of the free-stream is dropping (reflecting the attenuation of the lower frequency energy). The shift of flow/ surface interactions from low frequencies to high frequencies along the pressure side agrees with the drop in free-stream length scales (Λ_x) from PS2 to PS3.

Strong low frequency energy in the heat flux and velocity spectra is seen at DS1 but without corresponding coherence. On the pressure side, low-frequency flow energy is attenuated significantly along the pressure side with a corresponding drop in coherence at these low frequencies. However, low-frequency heat flux energy grows along the pressure side. This low frequency heat flux energy appears to be related to boundary layer transition and will be discussed in chapter 7. The magnitude of the phase shift and low-frequency coherence correlate with the acceleration as well, where at PS1 a small time shift was recorded in a region of free-stream deceleration. Increasing acceleration along the pressure side coincides with decreasing low frequency coherence and increasing phase shift while the largest phase shift and least coherence is seen at DS1 where the acceleration is strongest.

Some strong peaks at 5 and 10 kHz are seen both in the DS1 and PS1 heat flux spectra, and more strongly for Grid 4 (larger scales). Also, the coherence is strongest at DS1 at these frequencies. These peaks appear to be from streamwise vortices originating at the leading edge and will be discussed in chapter 7. The peaks at these frequencies are not present farther along the pressure side, however, indicating different mechanisms at work in the flow/ surface interactions beyond the near leading edge region. Instead, the dominant energy (seen in the coherence) is broadband at the higher frequencies noted above.

The cross-correlation and coherence data at PS1 give an estimate of the scales at work there. For G2, coherence and the magnitude of the correlation drop off at 1.0 mm indicating that the scales responsible for normal momentum transfer are 1 mm or less. For G4 the data indicate scales larger than 1 mm at work, in agreement with Λ_x measurements. The scale of the grid

turbulence is seen clearly on the suction side as well. The coherence for the smaller Grid 2 goes to zero at the 1.0 mm wire position indicating that the scales are less than a millimeter, while for Grid 4 the larger scales are evident in the nearly constant coherence at all wire positions. This is also evident in the velocity spectra where the influence of the wall is seen on the larger scale Grid 4 turbulence, but not on the smaller scale Grid 2 turbulence.

The frequency domain information presented here, when fit together as a whole, allows an interpretation of the interactions responsible for moving thermal energy across the boundary layer at different regions of the blade. Using this data to form a picture of the flow/ surface interactions is the focus of chapter 7.

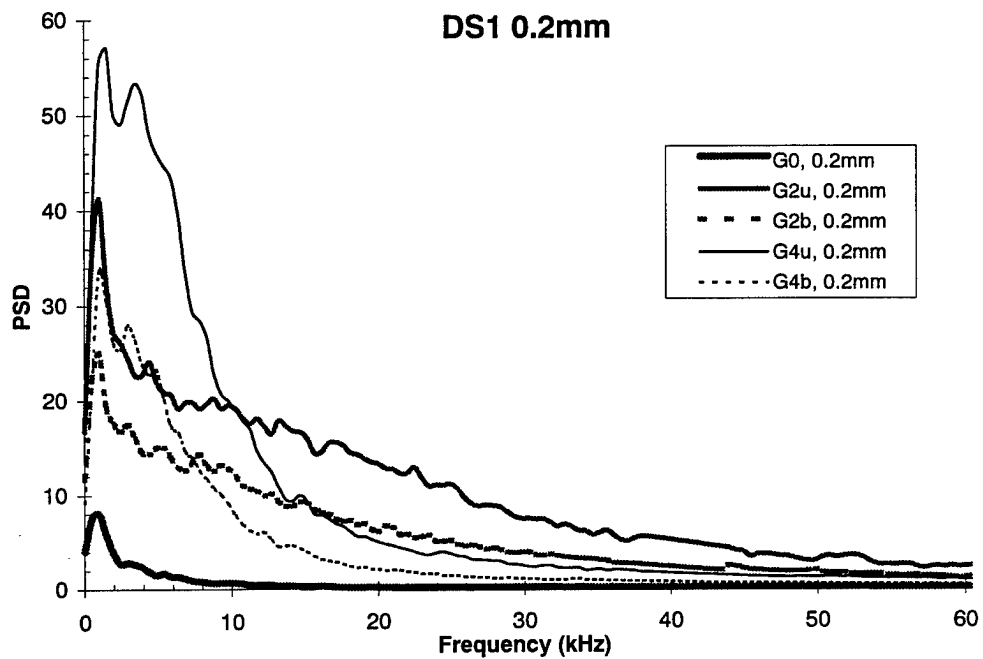
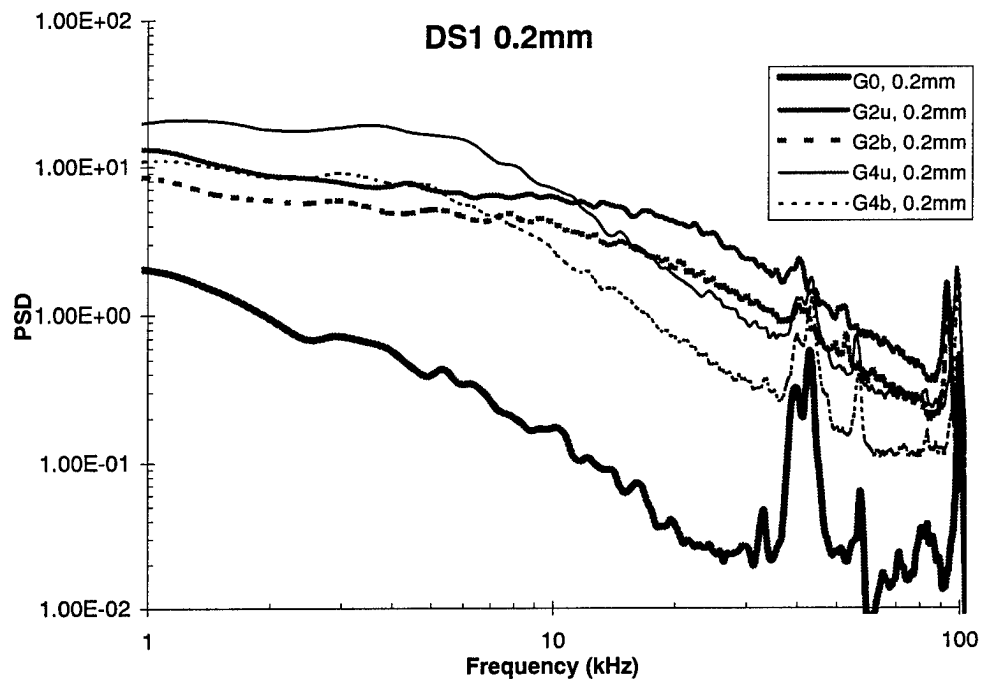


Figure 6.1.1 Hot-wire Energy spectra over DS1 at $y = 0.2$ mm

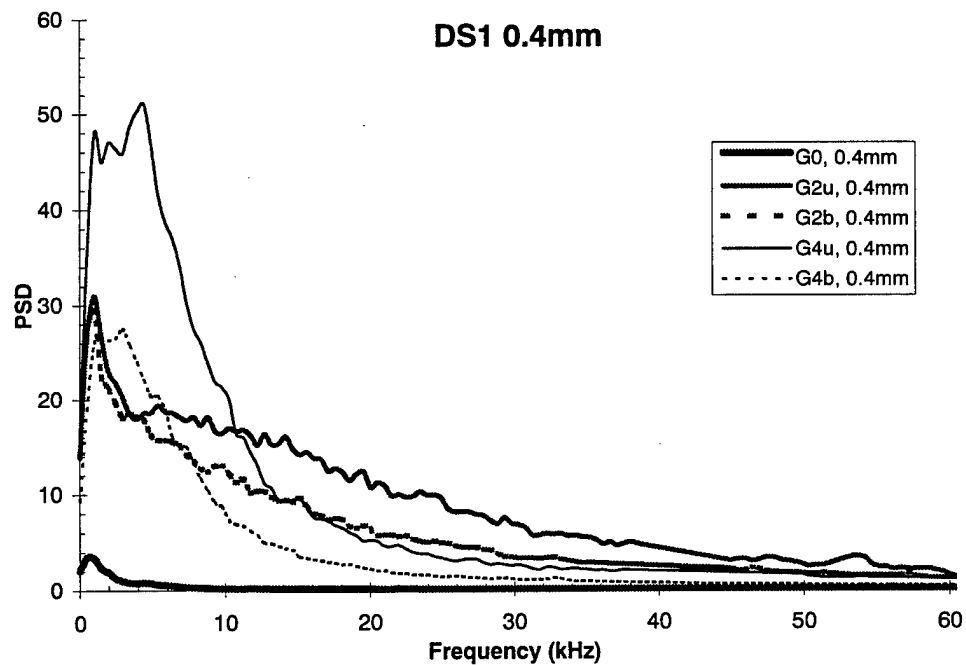
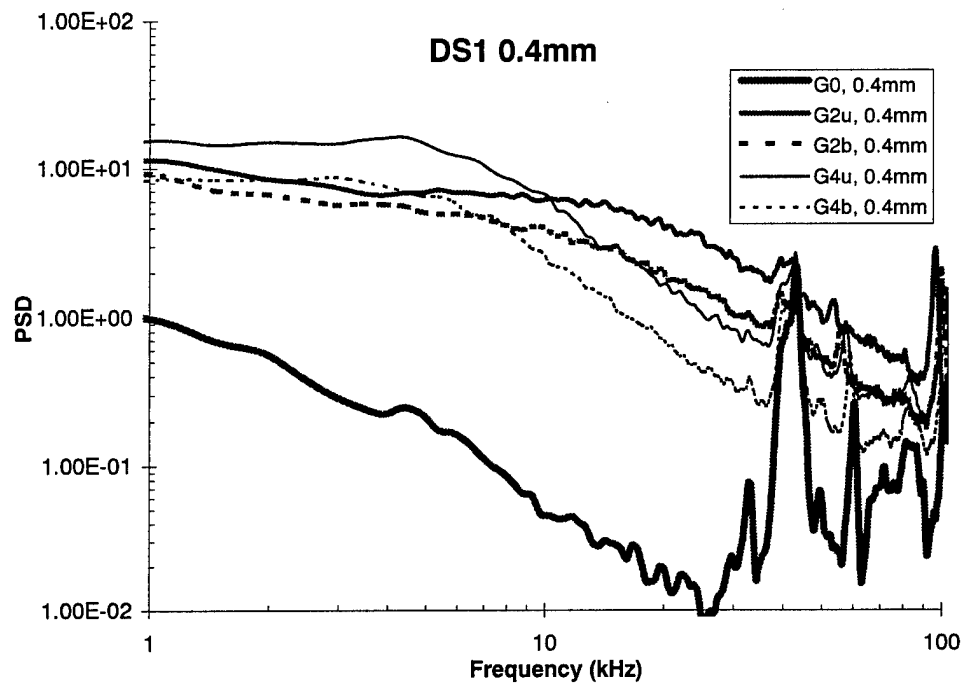


Figure 6.1.2 Hot-wire Energy spectra over DS1 at $y = 0.4$ mm

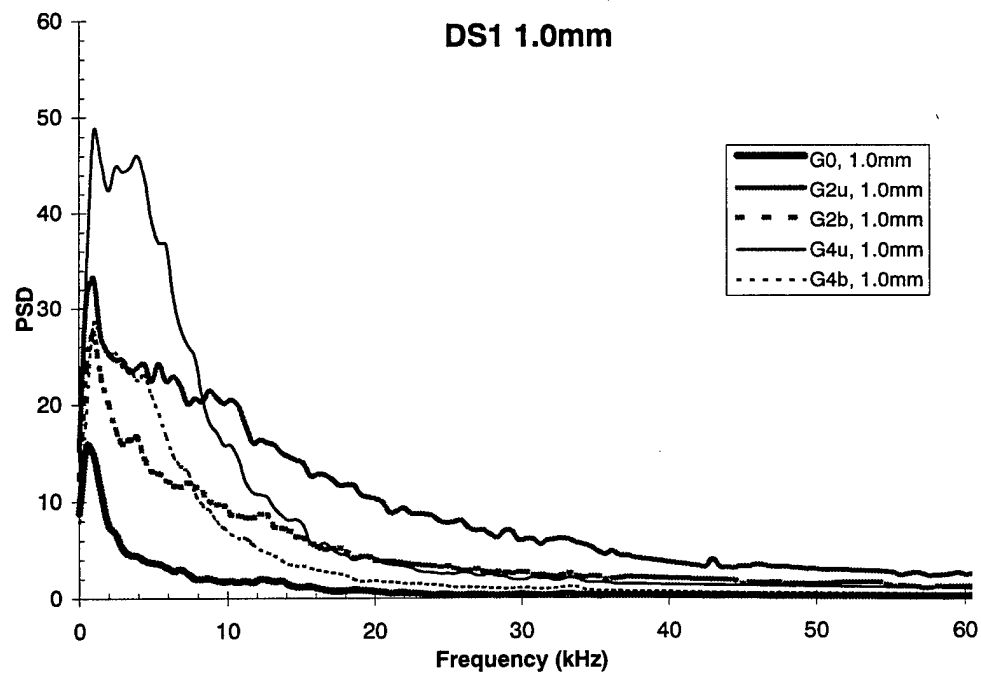
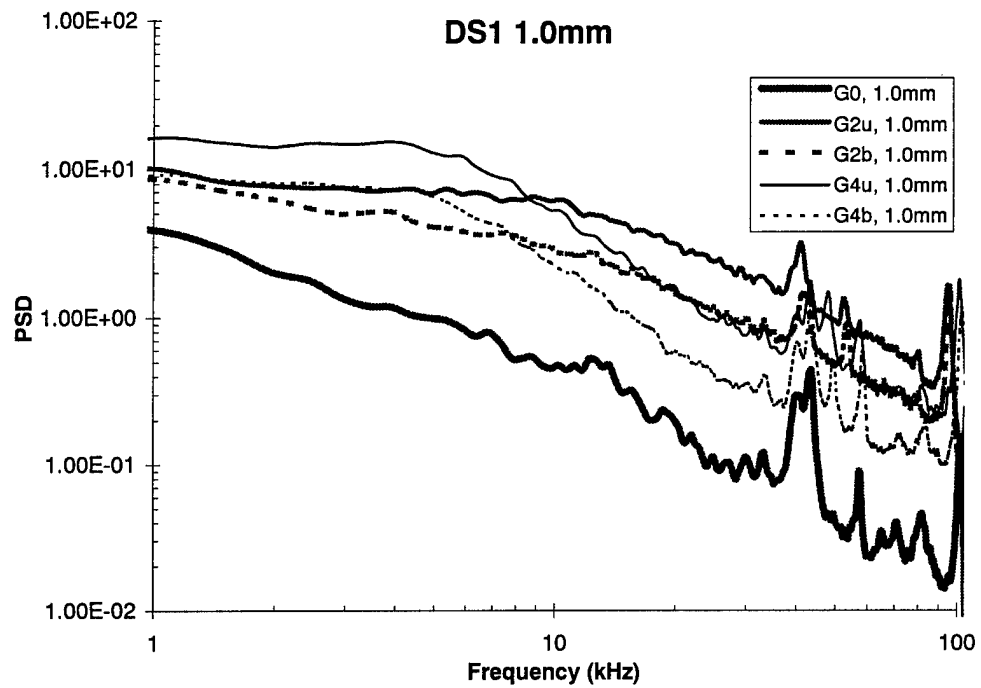


Figure 6.1.3 Hot-wire Energy spectra over DS1 at $y = 1.0$ mm

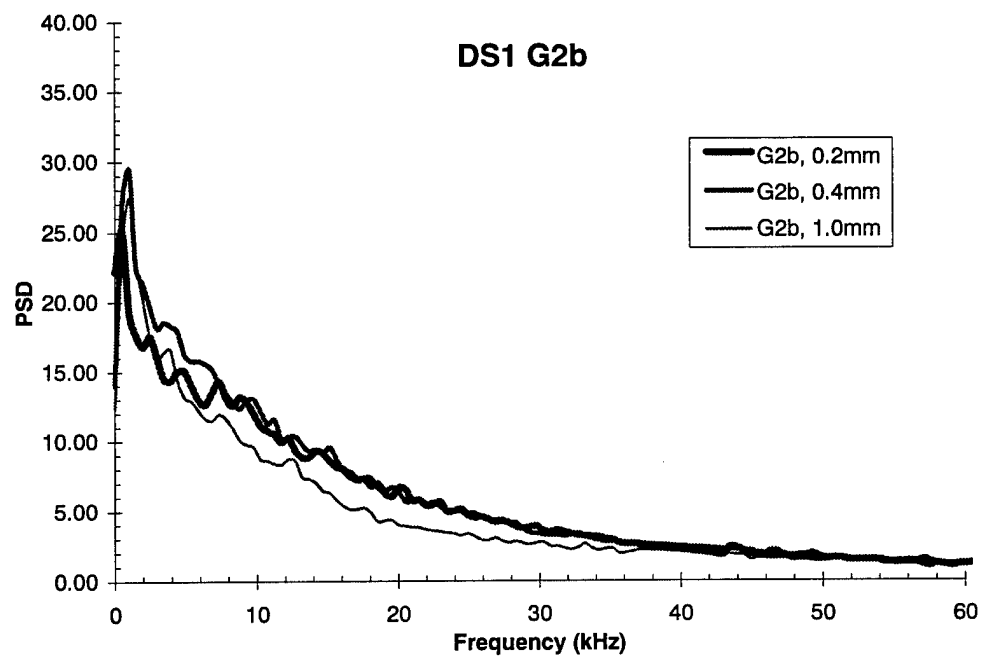
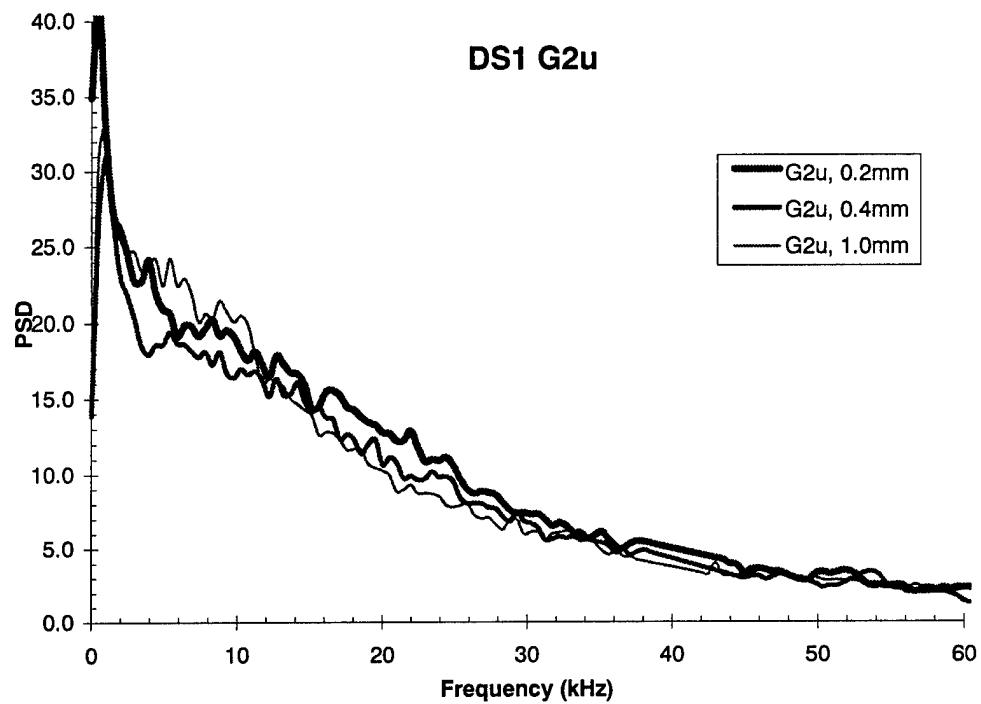


Figure 6.1.4 Hot-wire Energy spectra at DS1 for G2u and G2b vs. y_{wire}

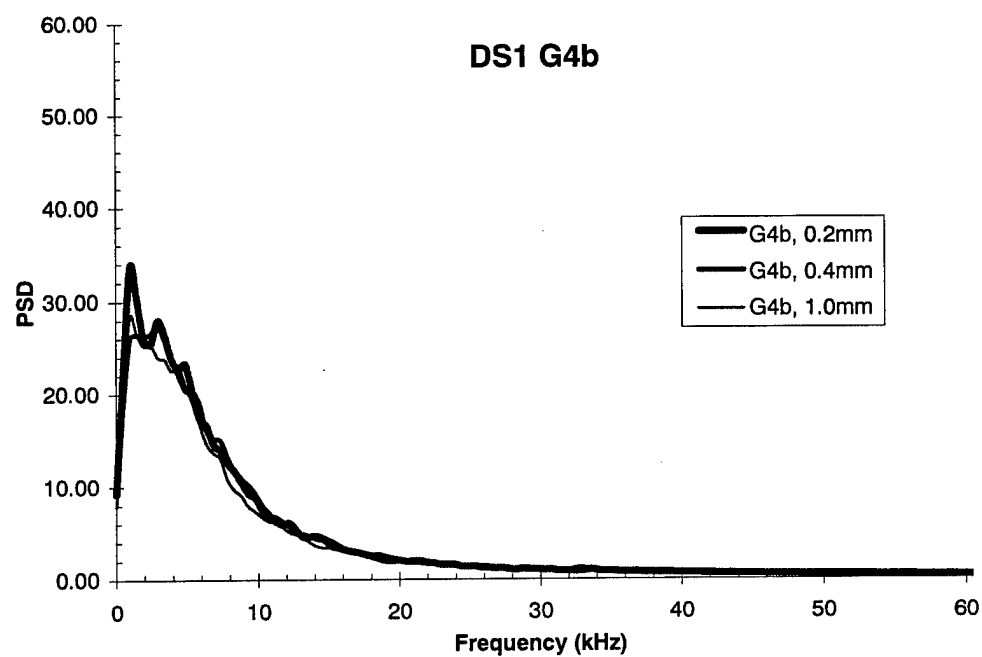
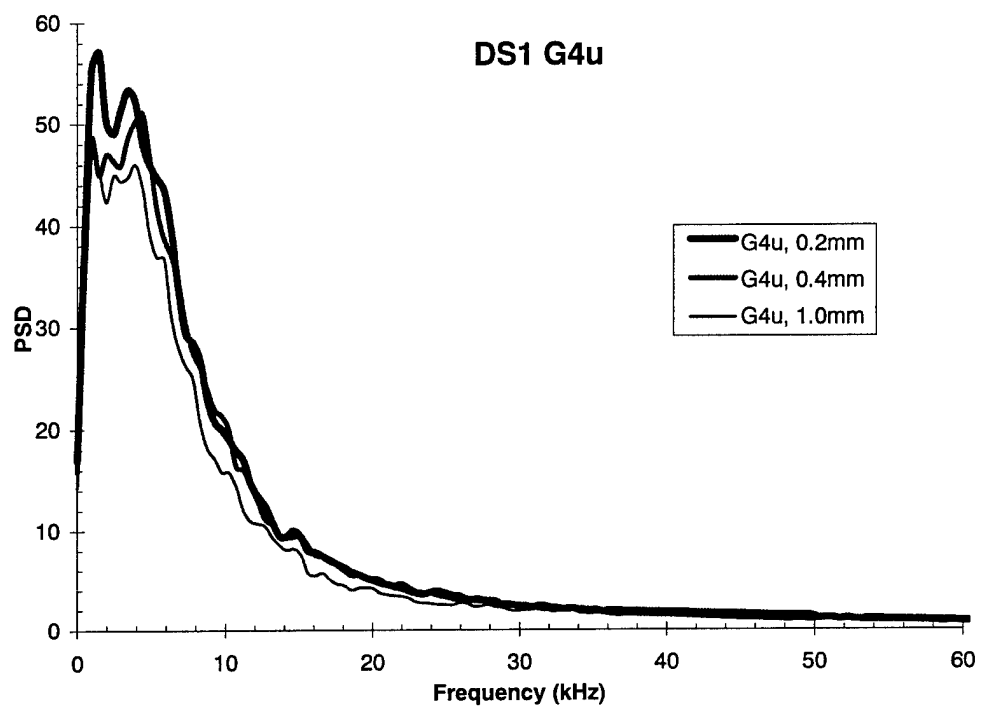


Figure 6.1.5 Hot-wire energy spectra for DS1 for G4u and G4b vs. y_{wire} .

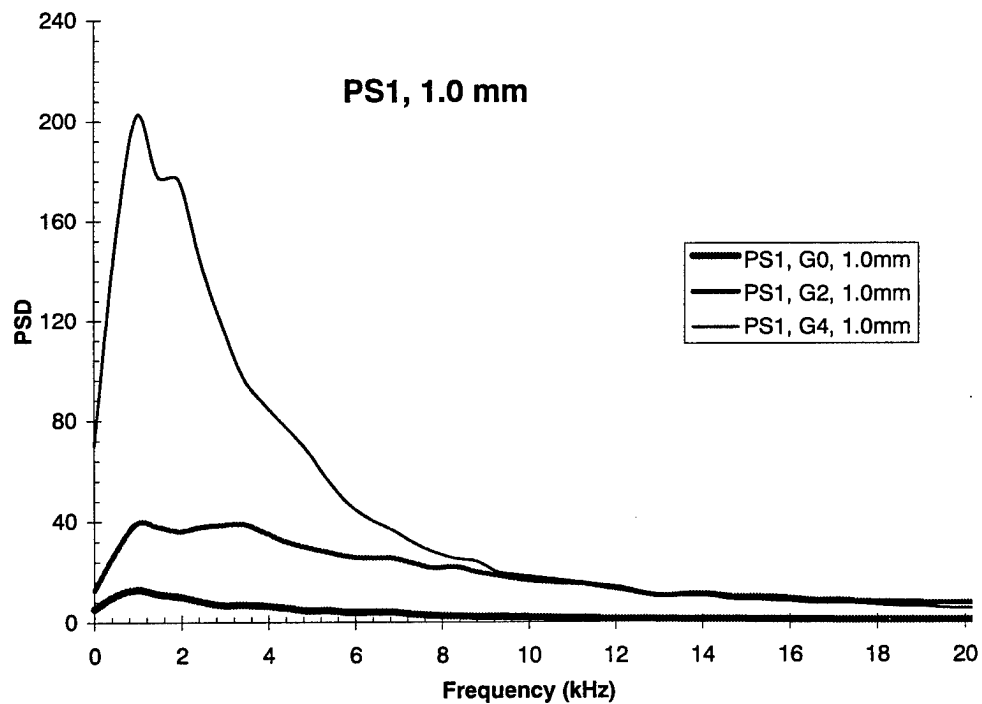
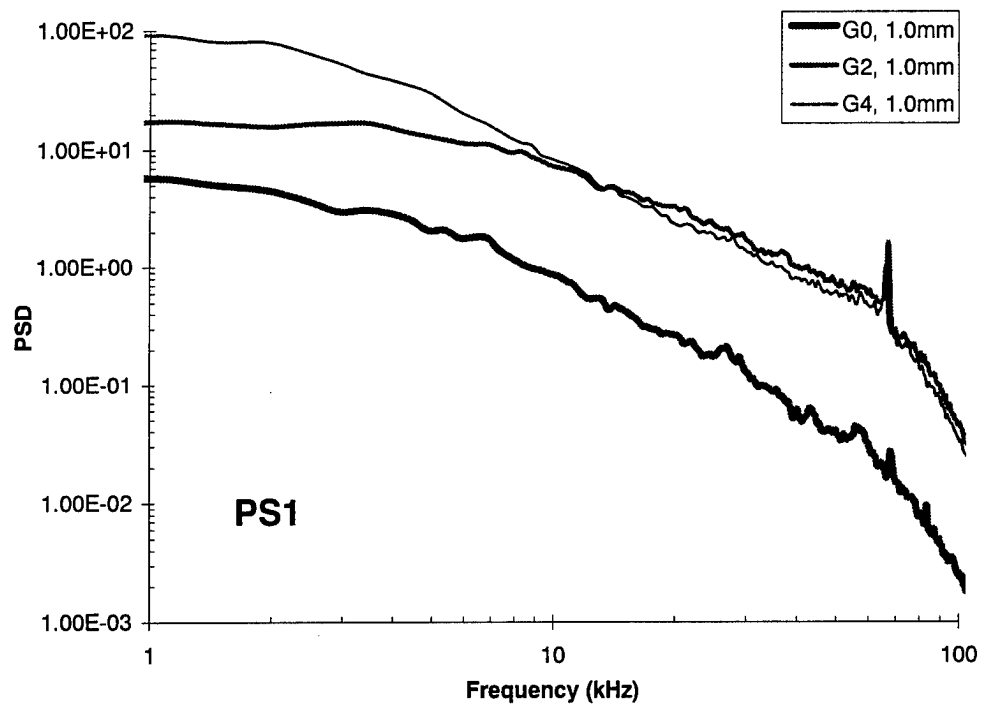


Figure 6.1.6 Hot-wire energy spectra for PS1 at 1.0 mm comparing grids.

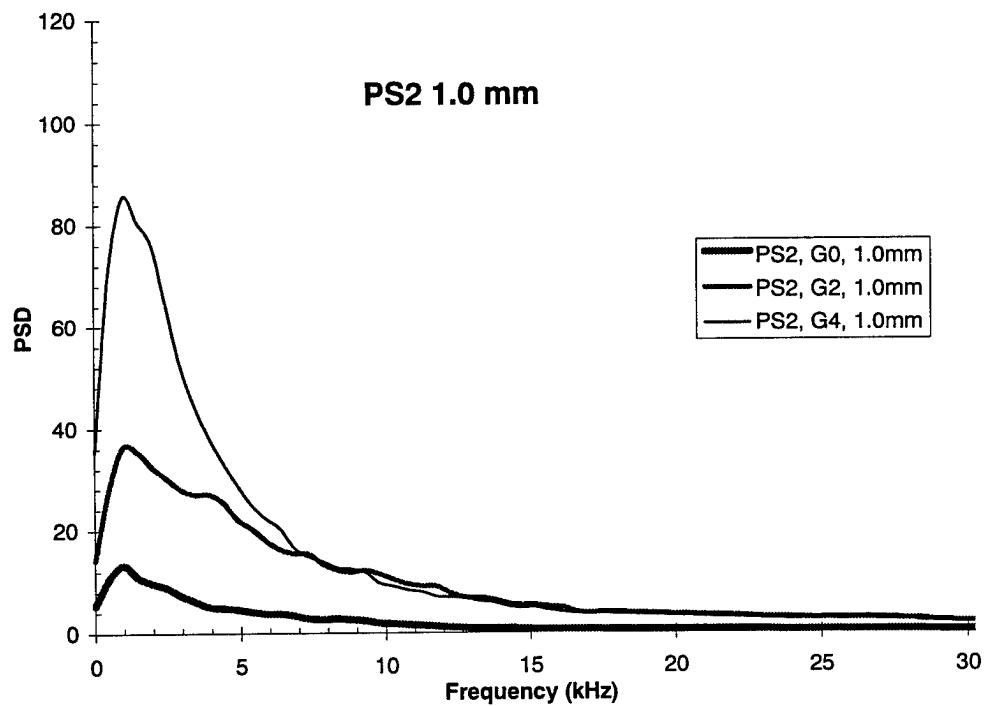
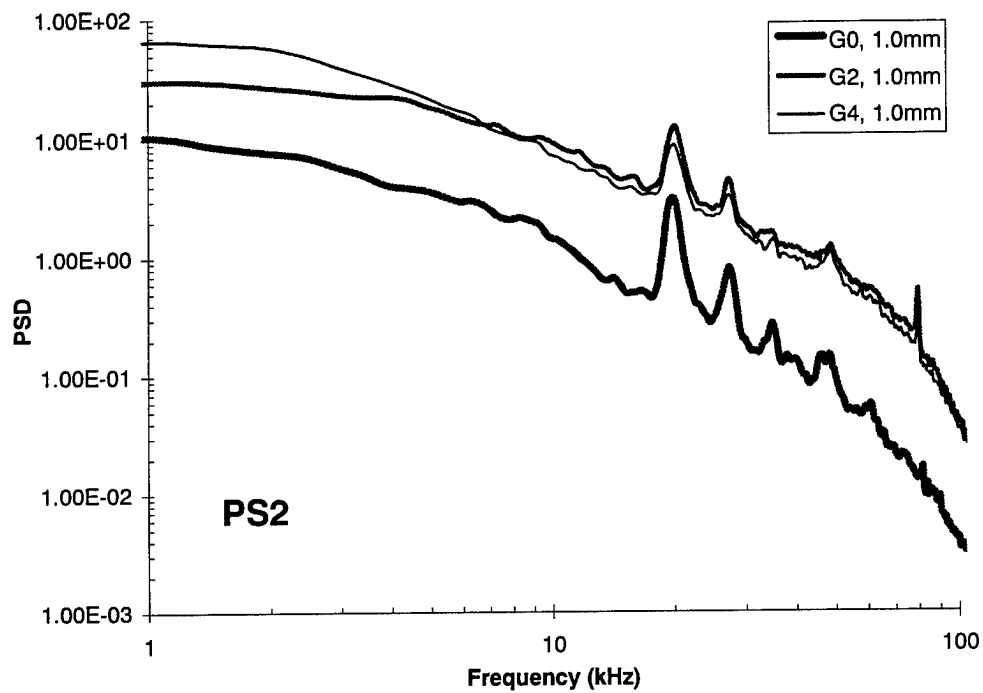


Figure 6.1.7 Hot-wire energy spectra for PS2 at 1.0 mm comparing grids.

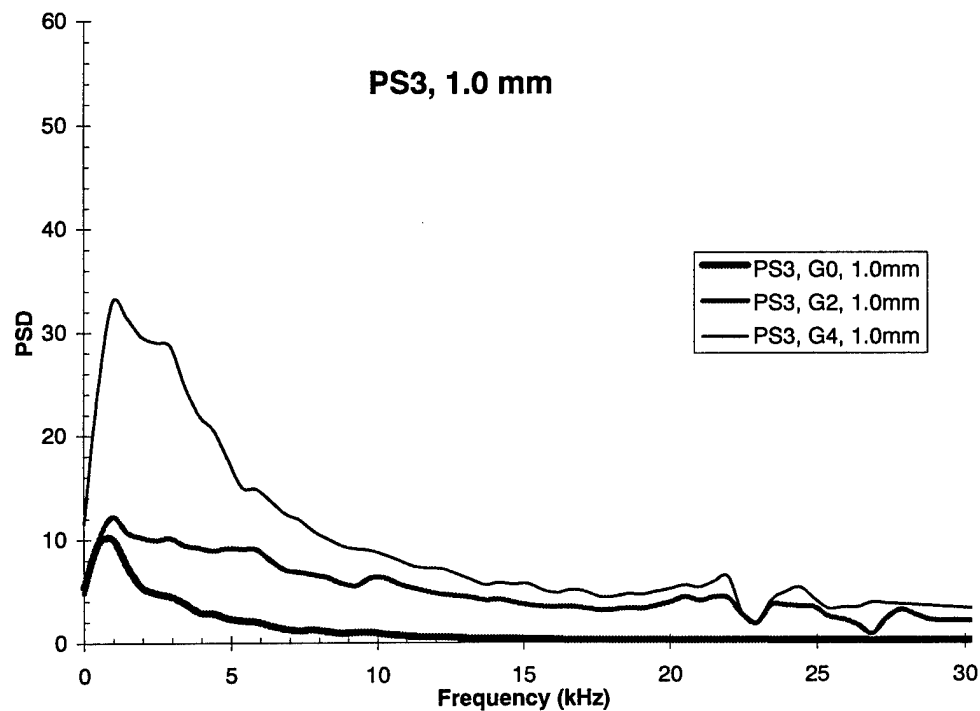
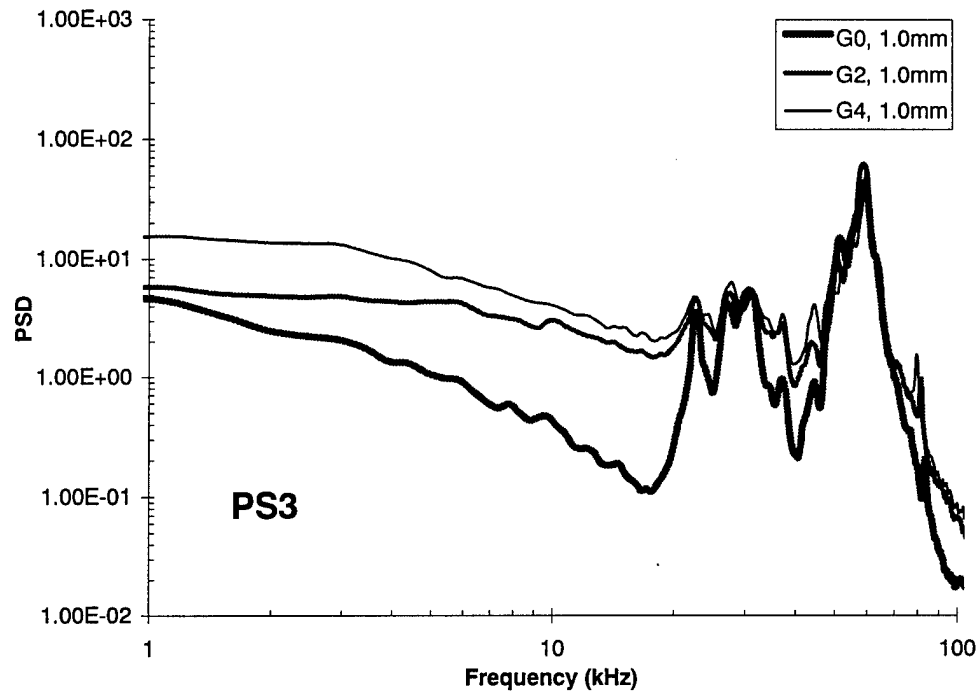


Figure 6.1.8 Hot-wire energy spectra for PS3 at 1.0 mm comparing grids.

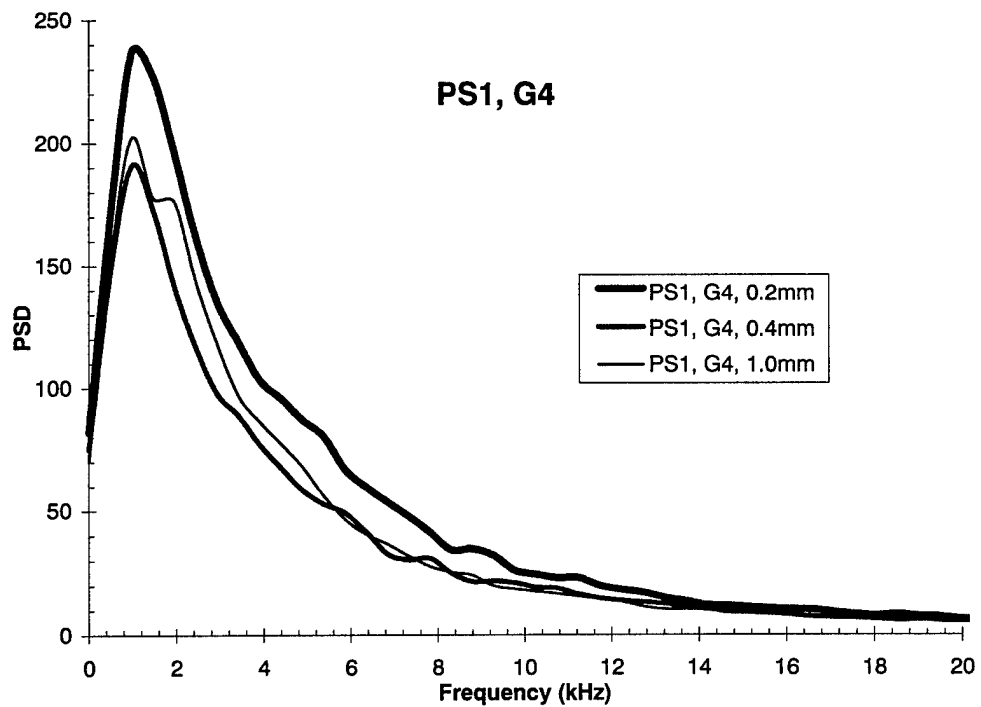
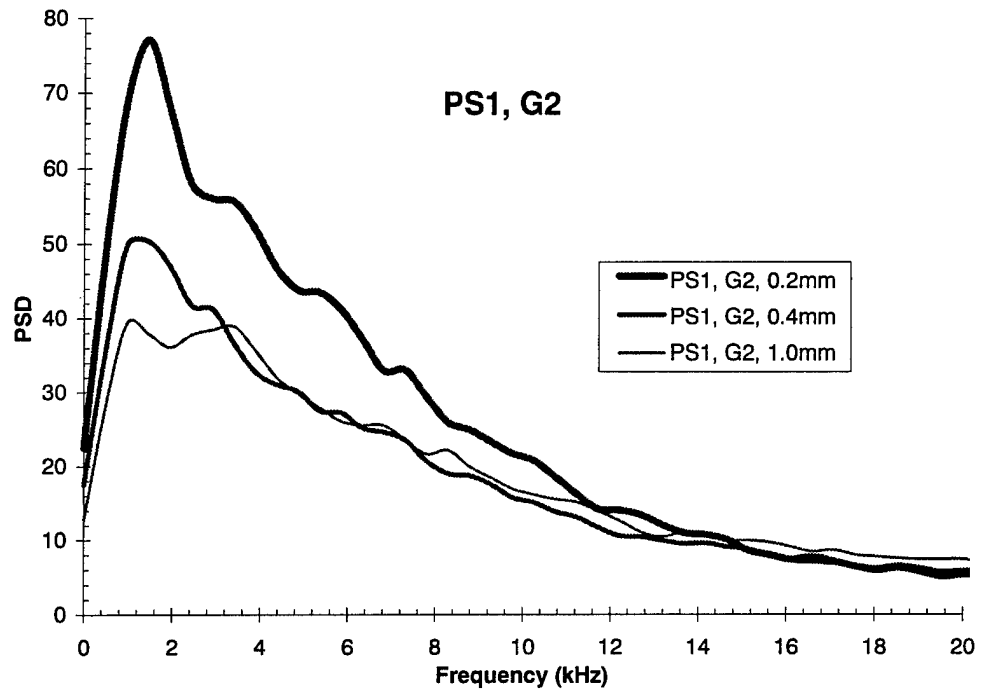


Figure 6.1.9 Hot-wire spectra for PS1, G2 and G4 comparison at different y_{wire} .

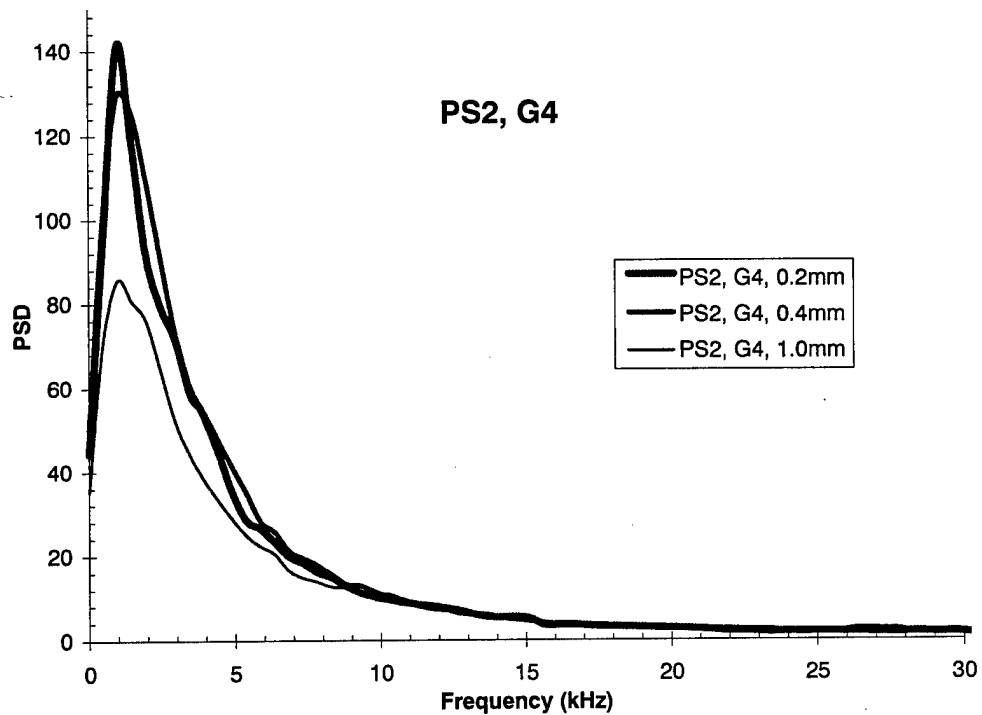
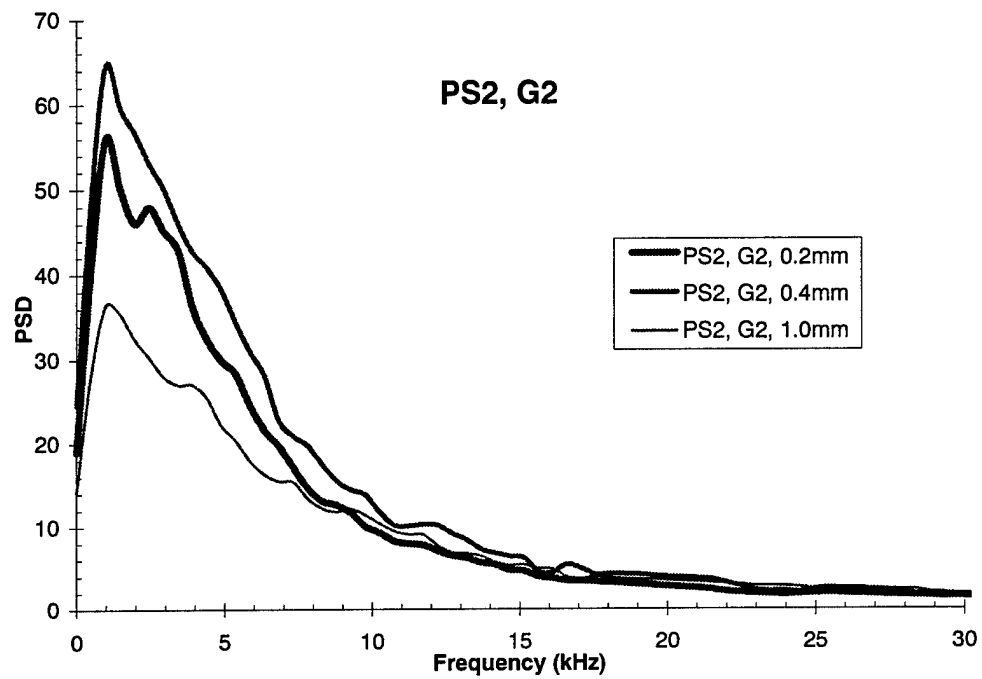


Figure 6.1.10 Hot-wire spectra for PS2, G2 and G4 comparison at different y_{wire} .

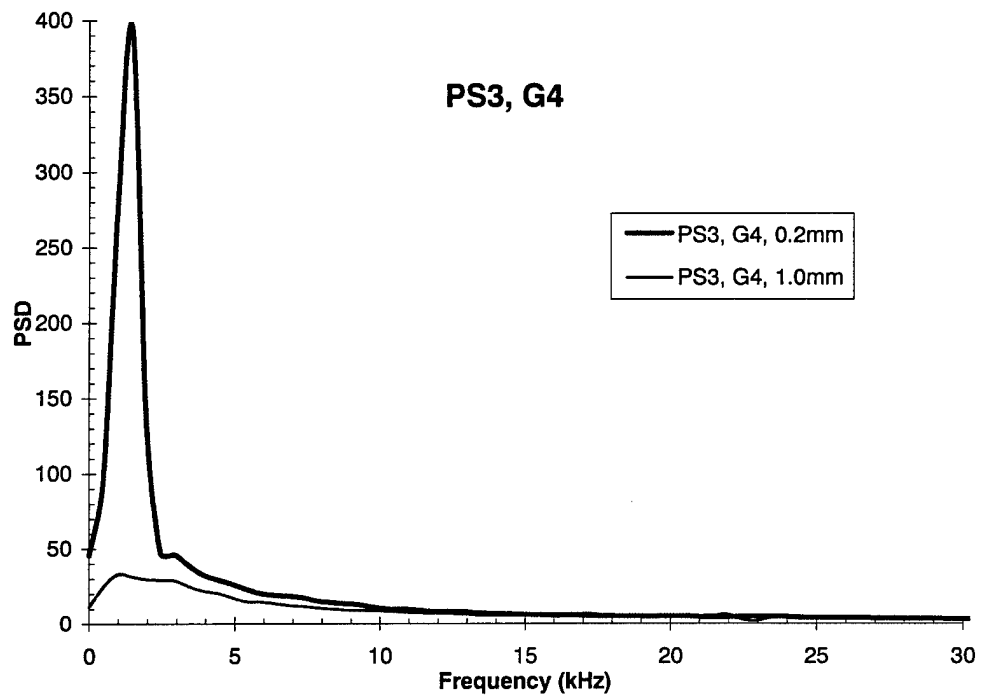
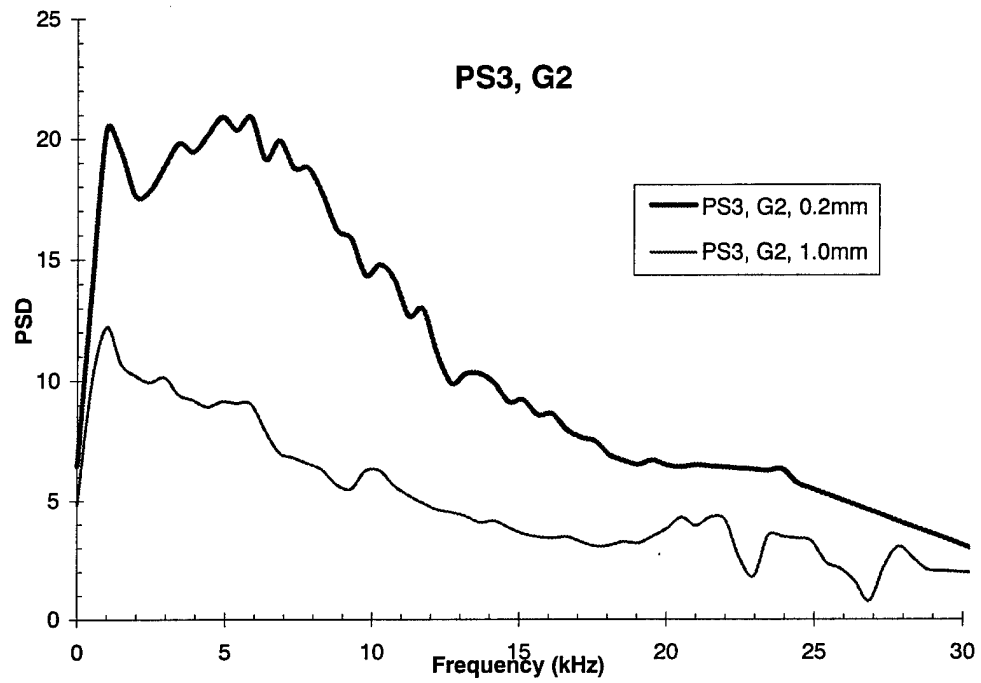


Figure 6.1.11 Hot-wire spectra for PS3, G2 and G4 comparison at different y_{wire} .

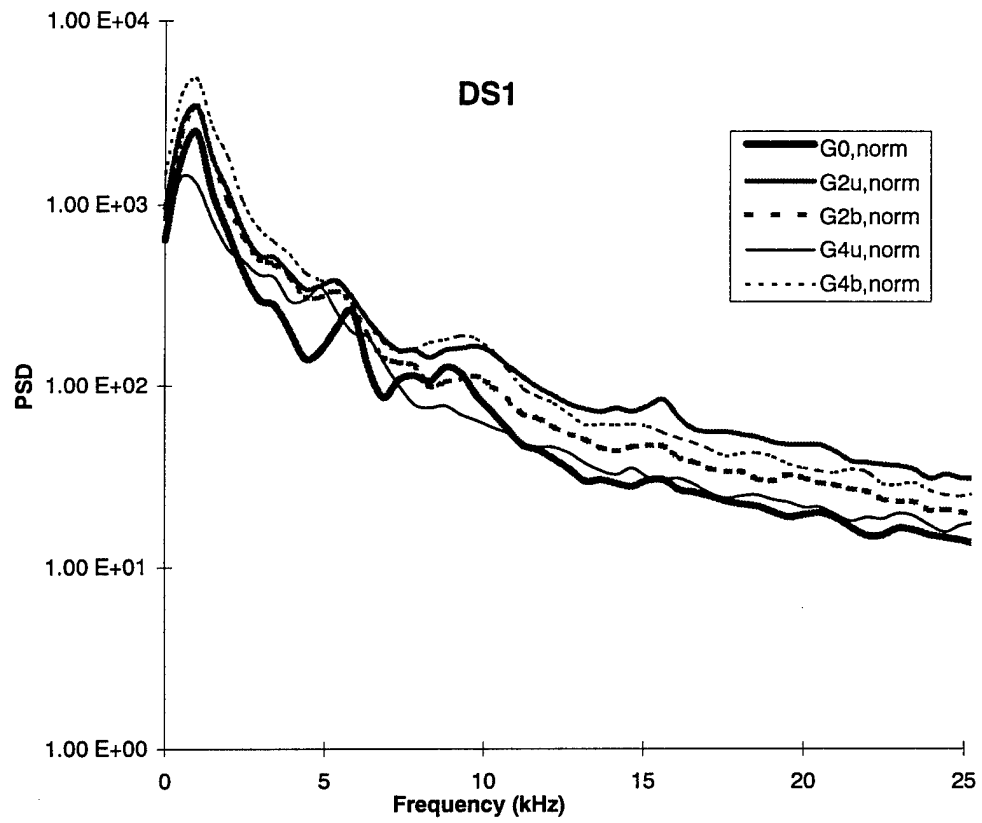


Figure 6.2.1 Heat flux spectrum at DS1.

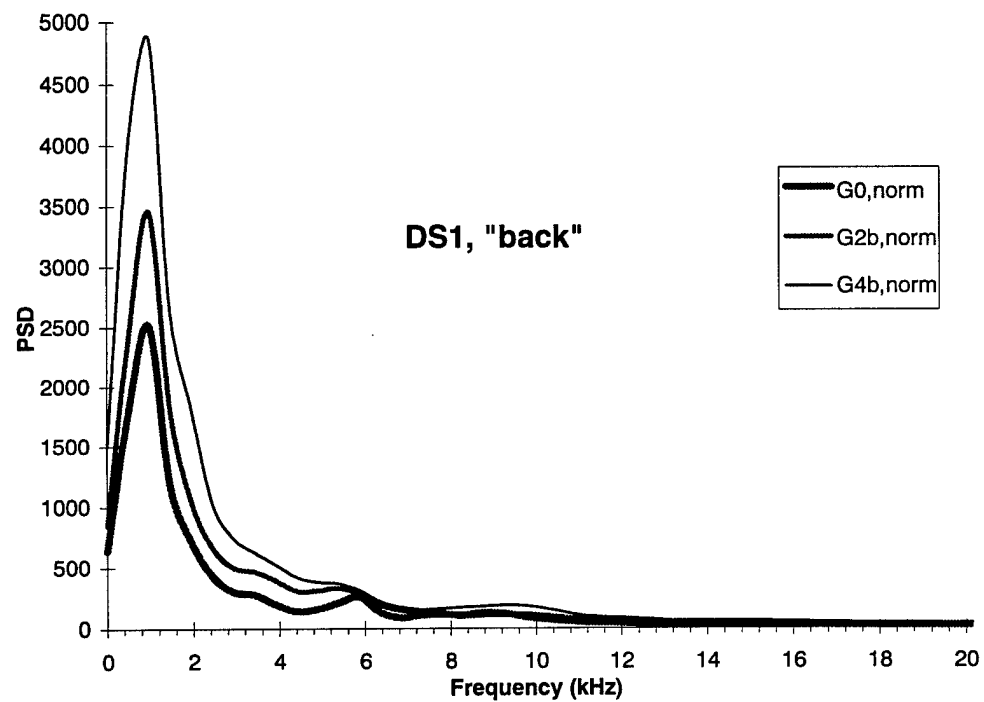
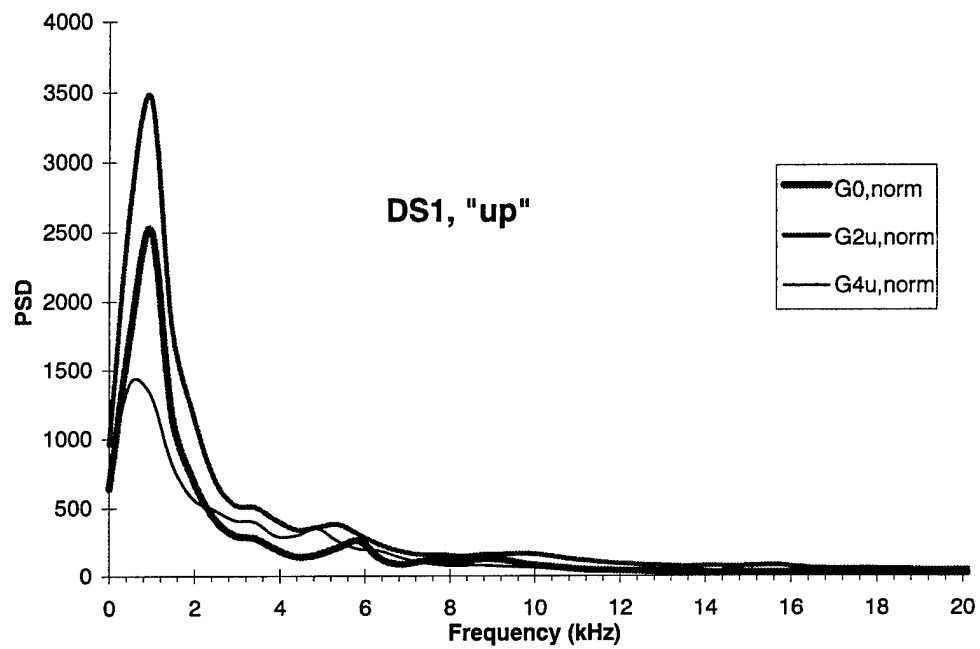


Figure 6.2.2 DS1 heat flux comparing "up" and "back" cases.

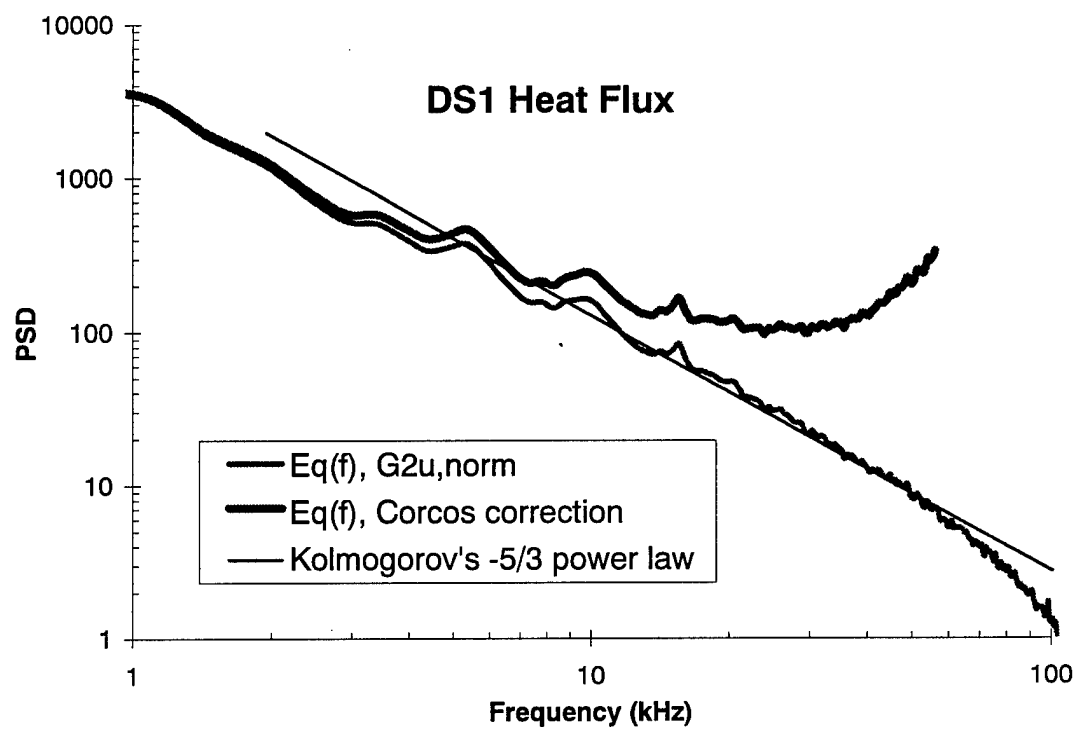


Figure 6.2.3 HFM heat flux attenuation at DS1 based on Corcos estimation.

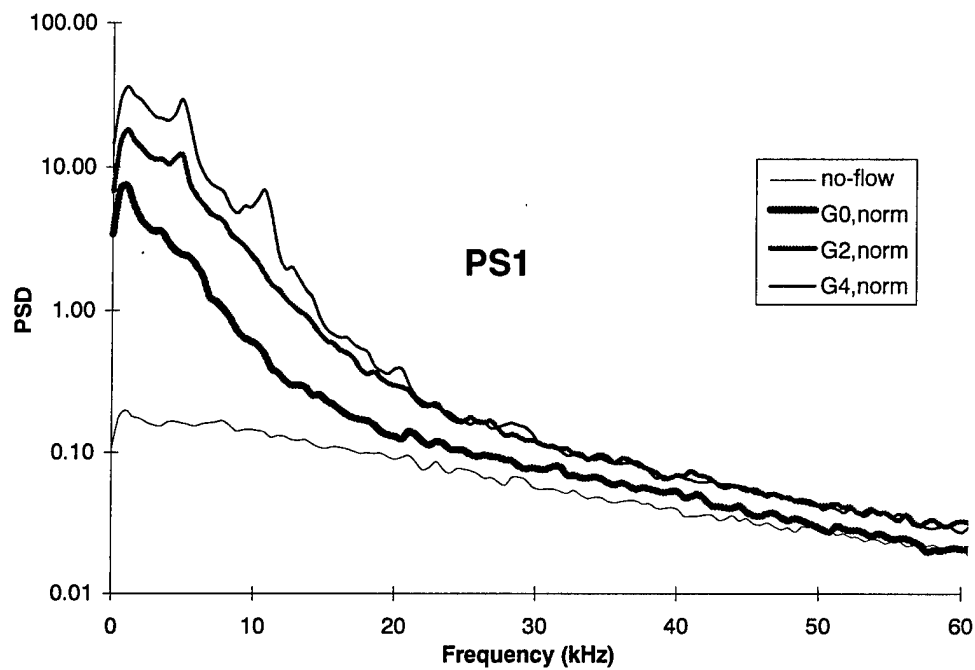


Figure 6.2.4 Heat flux spectra at PS1 comparing grids.

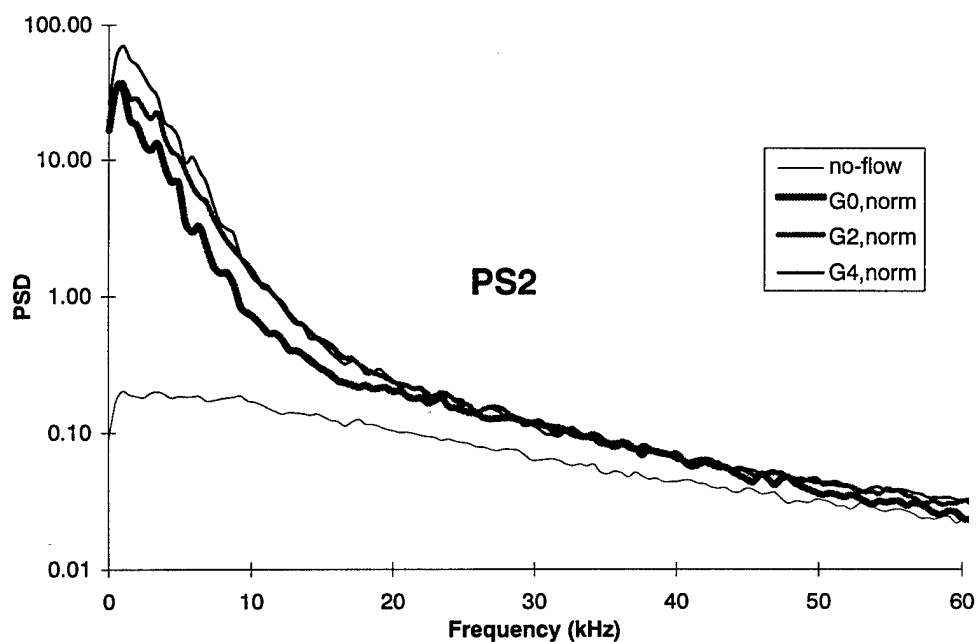


Figure 6.2.5 Heat flux spectra at PS2 comparing grids.

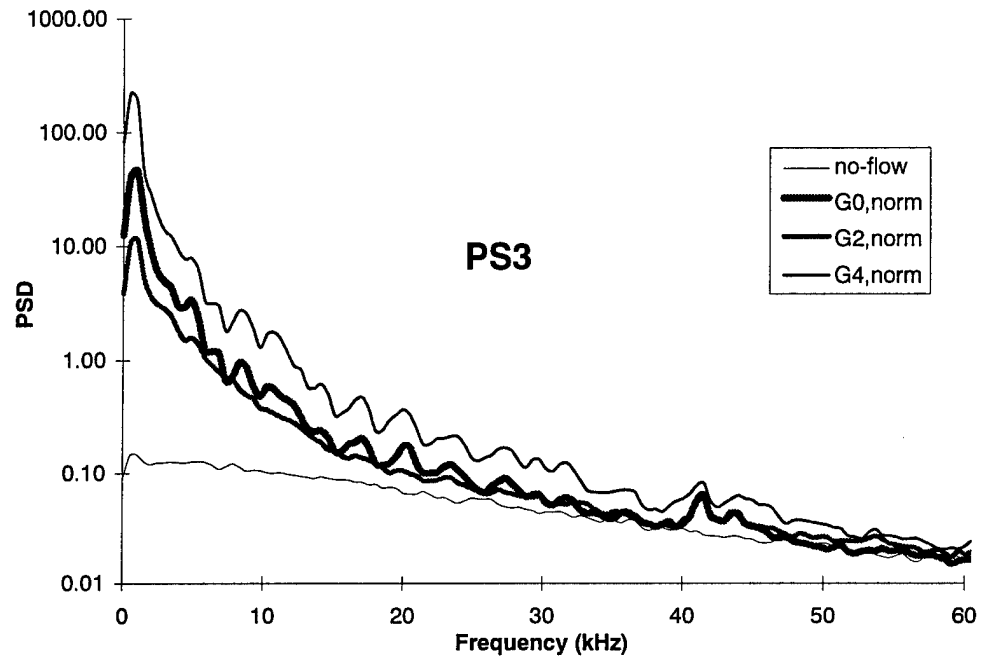


Figure 6.2.6 Heat flux spectra at PS3 comparing grids.

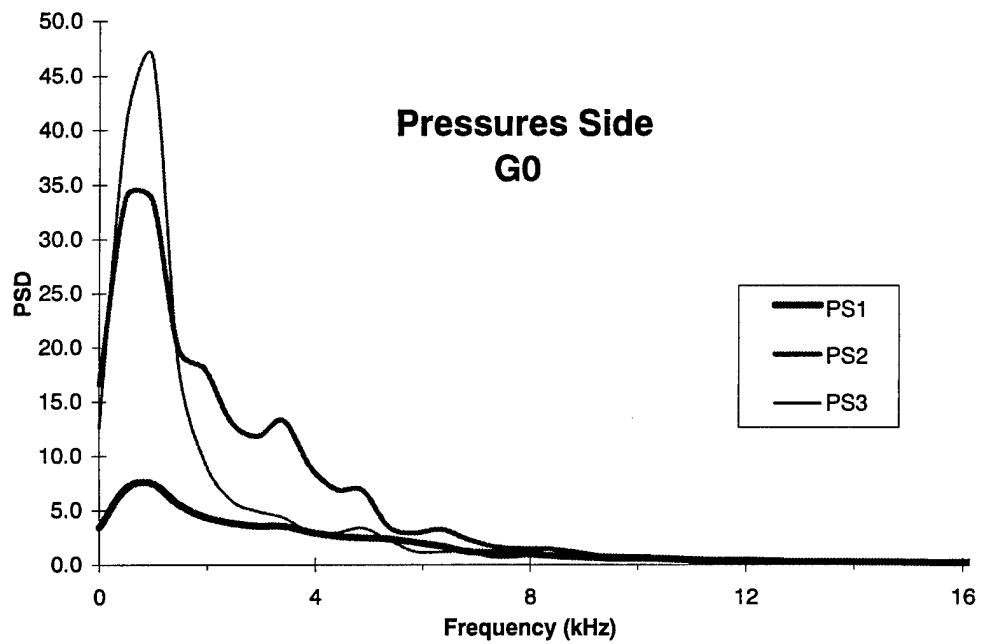


Figure 6.2.7 Pressure side heat flux spectra, G0 comparison.

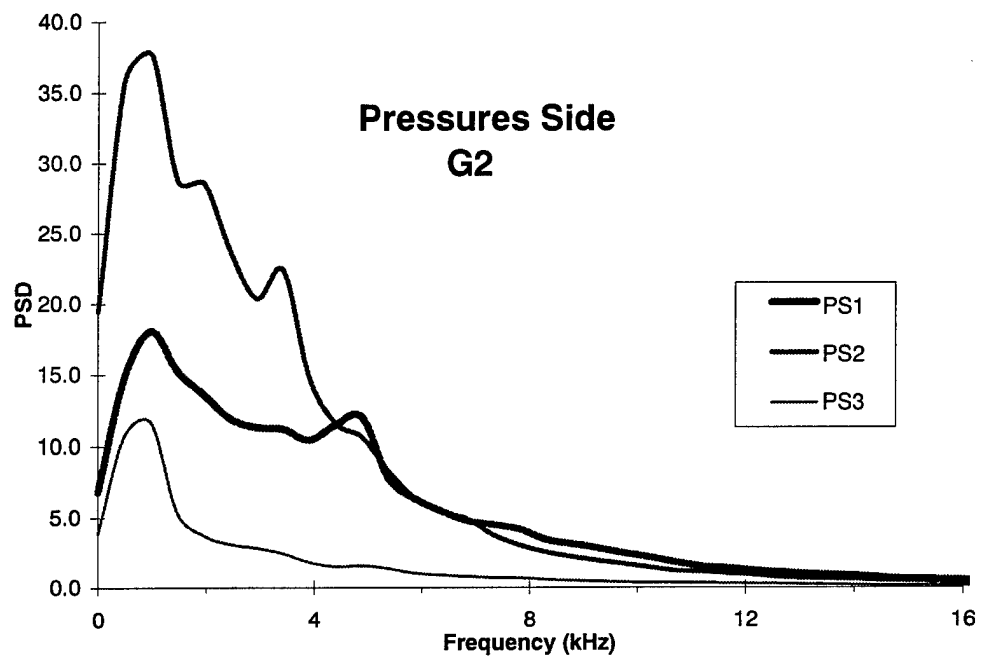


Figure 6.2.8 Pressure side heat flux spectra, G2 comparison.

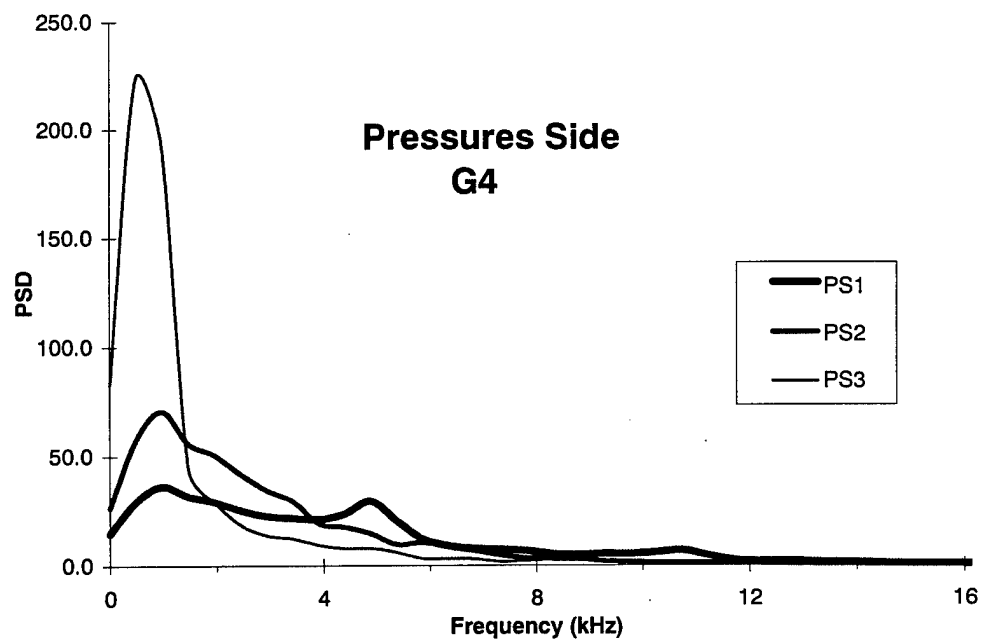


Figure 6.2.9 Pressure side heat flux spectra, G4 comparison.

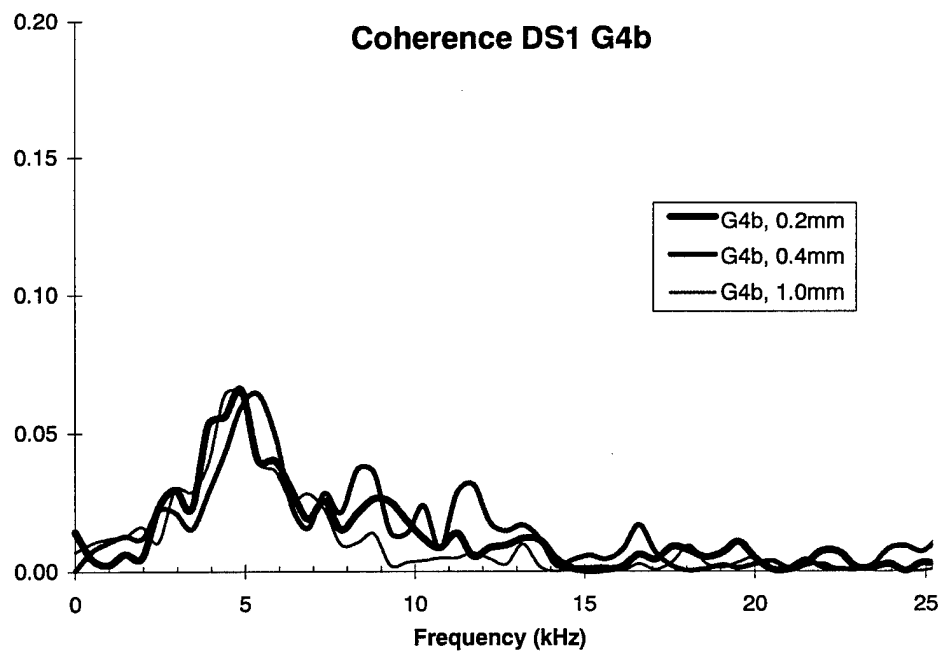
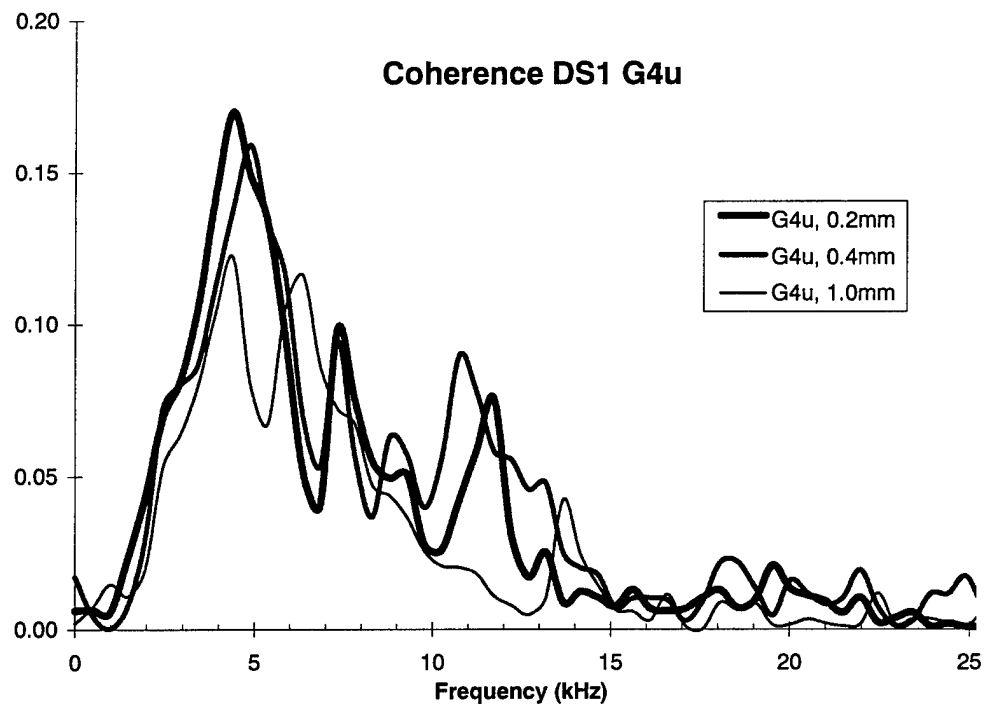


Figure 6.3.1 DS1 Coherence, G4u and G4b.

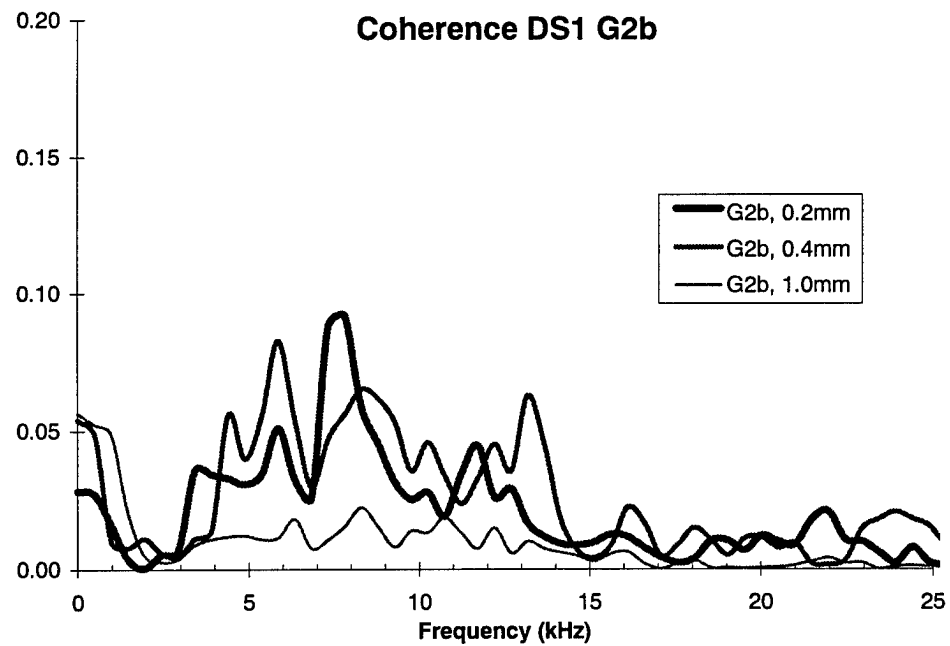
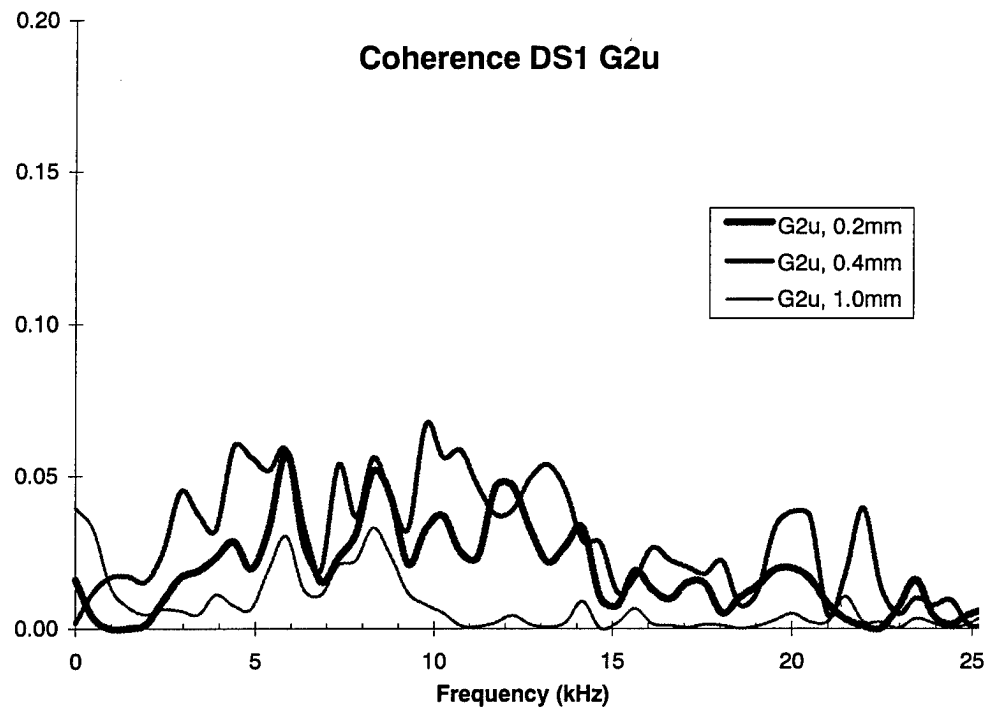


Figure 6.3.2 DS1 Coherence, G2u and G2b.

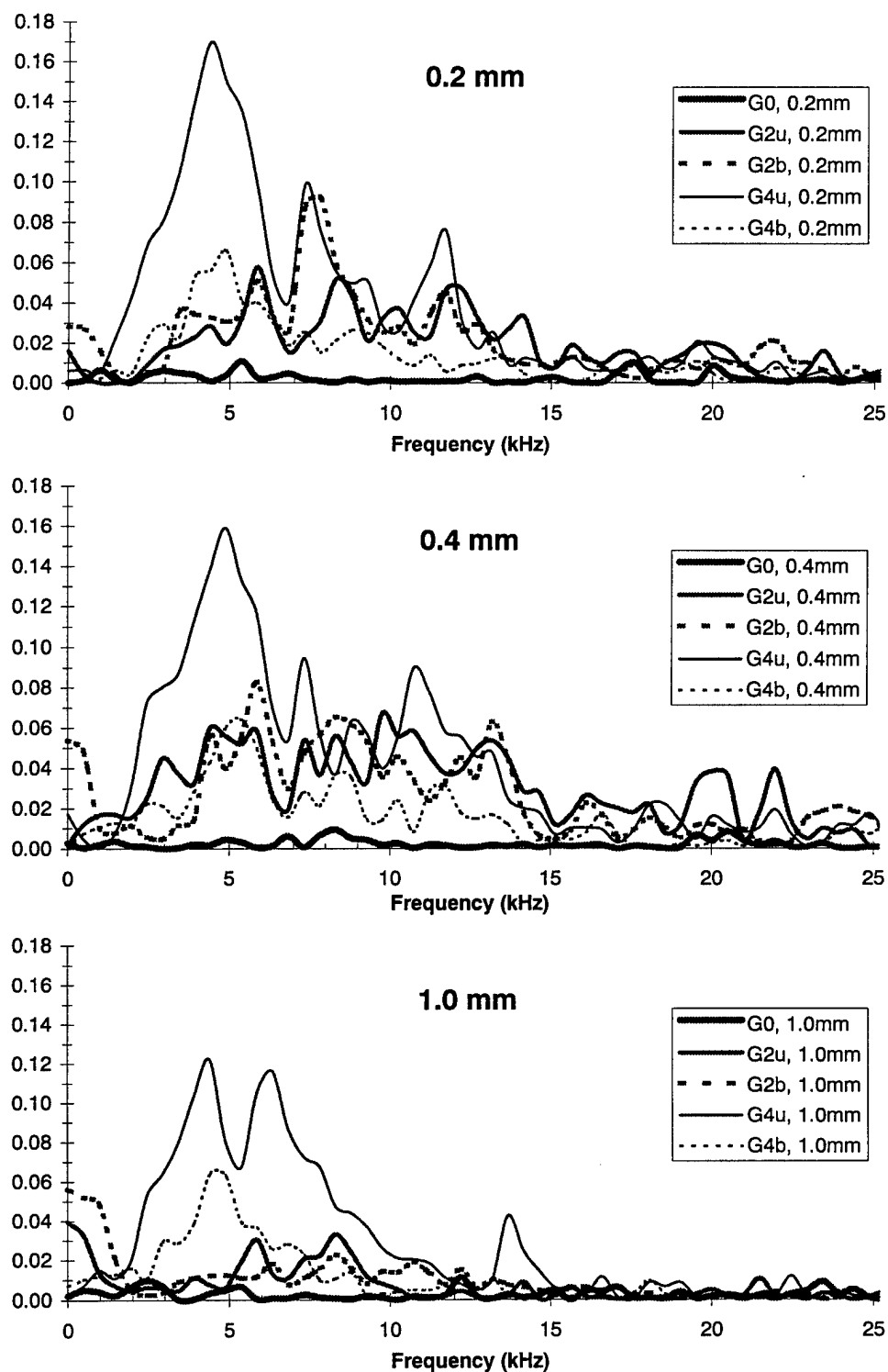


Figure 6.3.3 DS1 Coherence, all data.

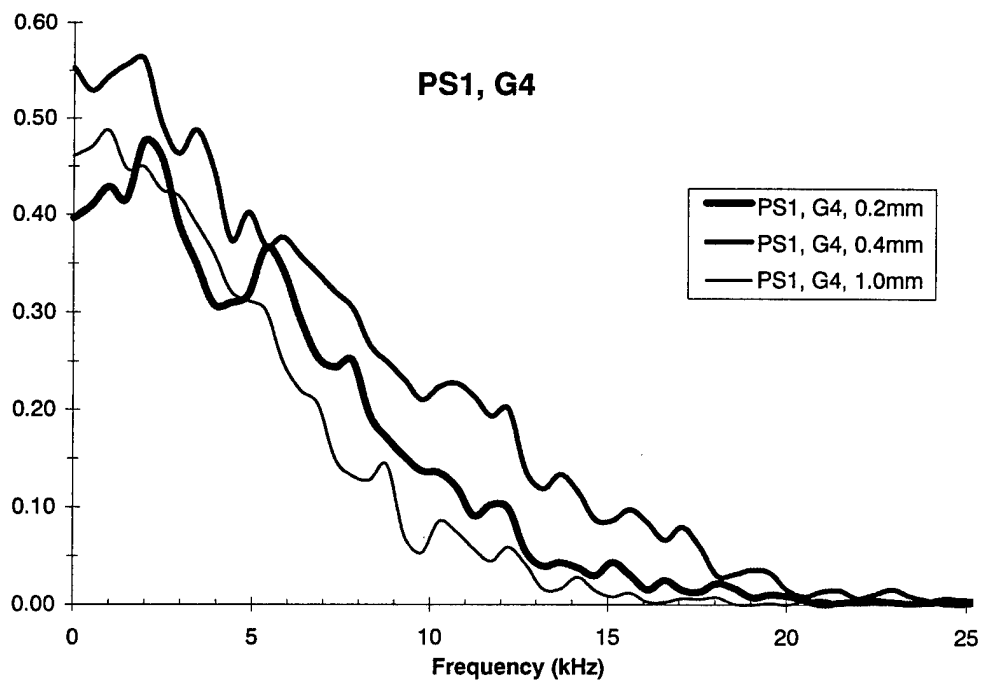
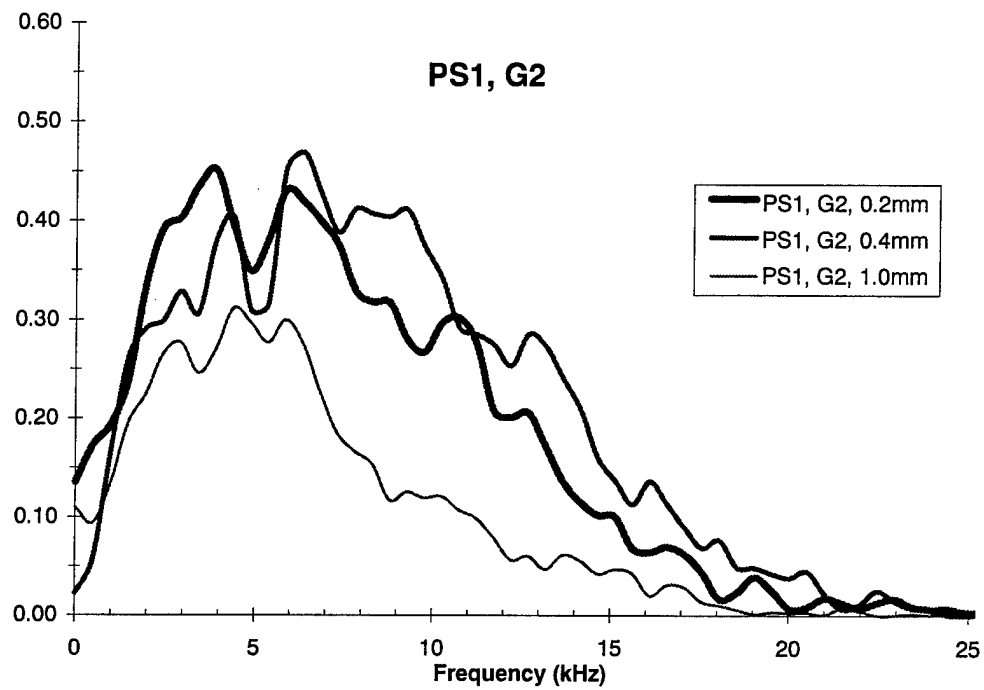


Figure 6.3.4 PS1 Coherence, G2 and G4.

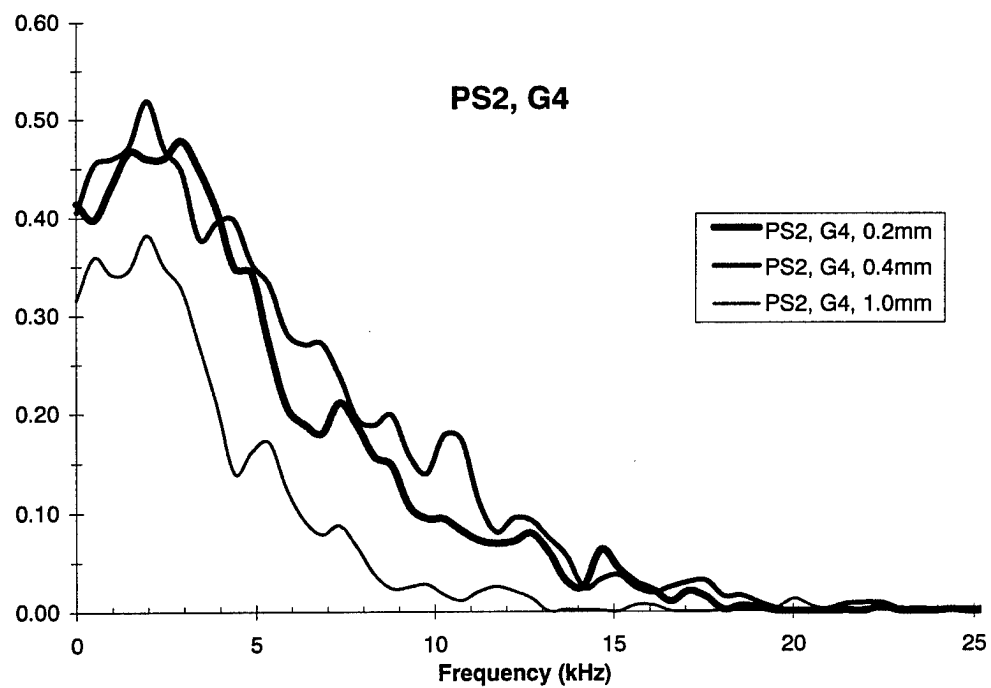
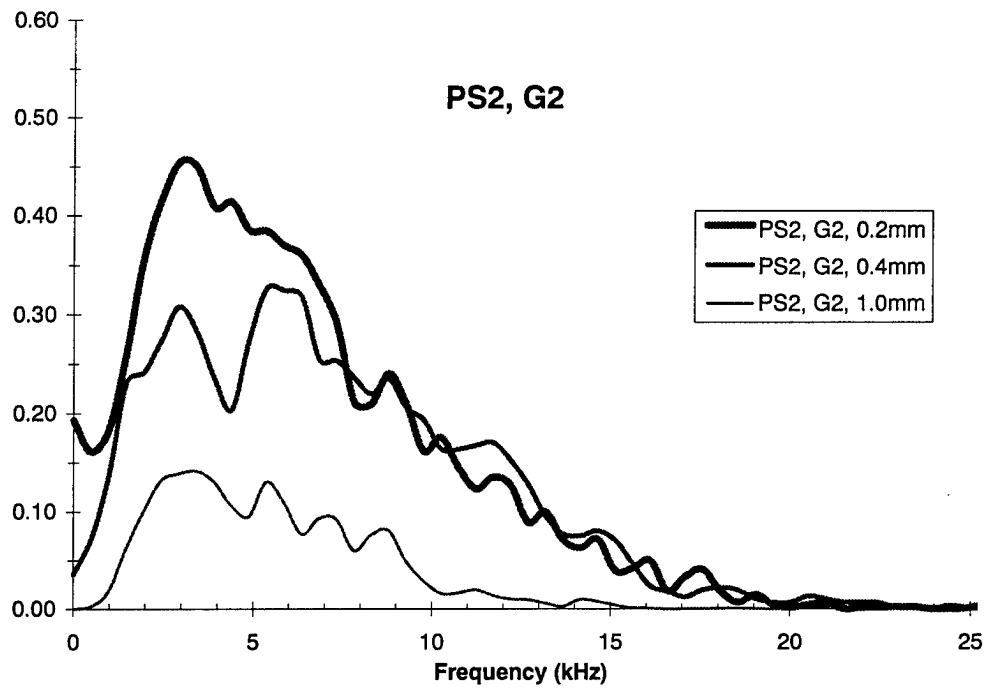


Figure 6.3.5 PS2 Coherence, G2 and G4.

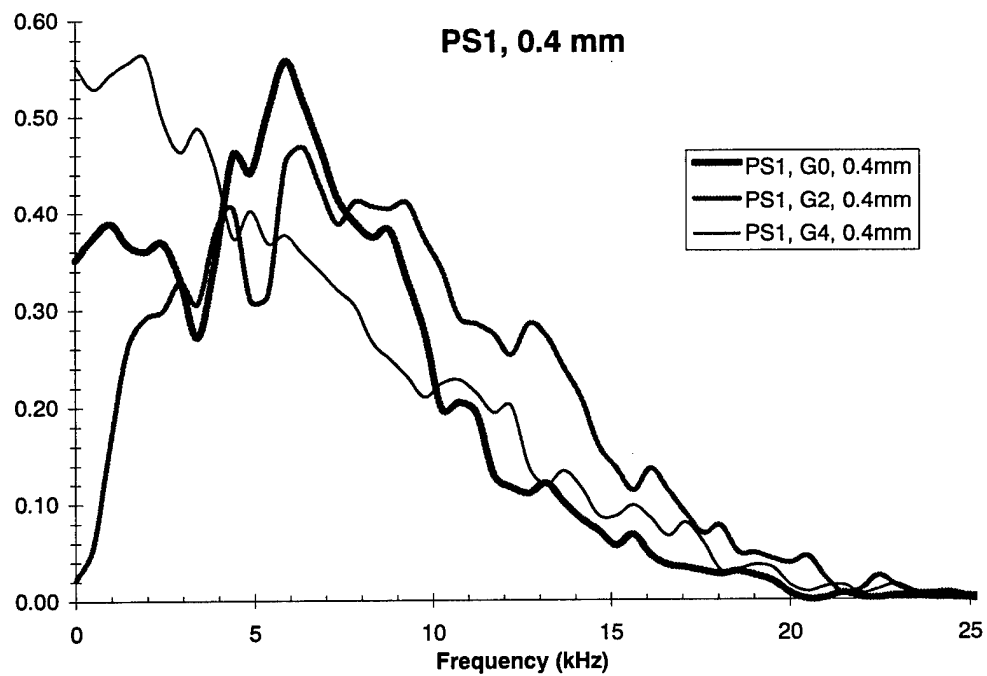
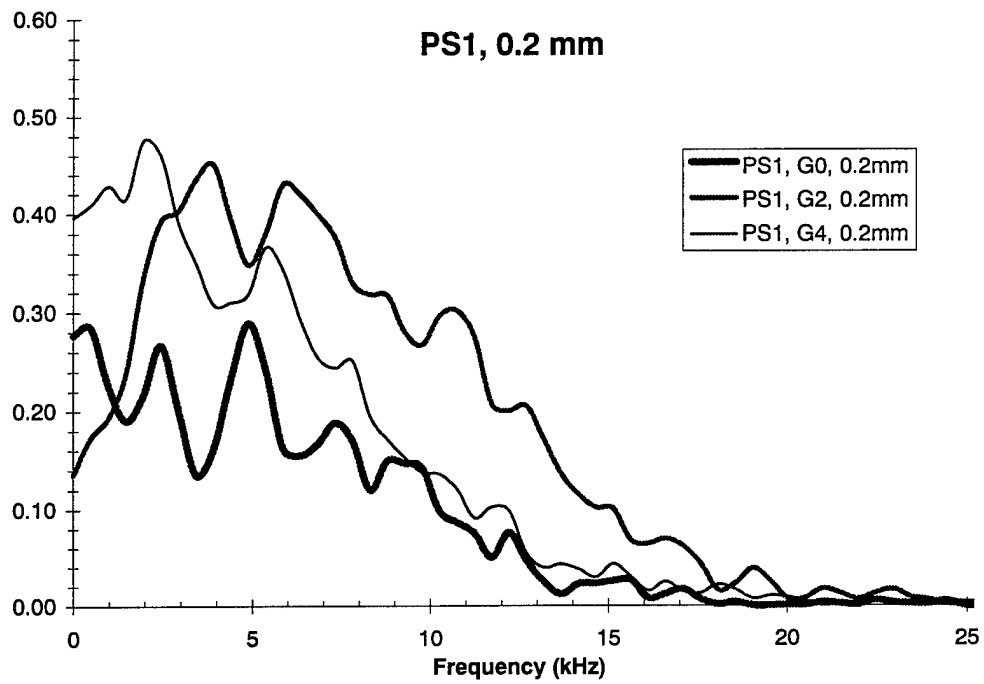


Figure 6.3.6 Coherence at PS1, 0.2 mm and 0.4 mm comparing grids.

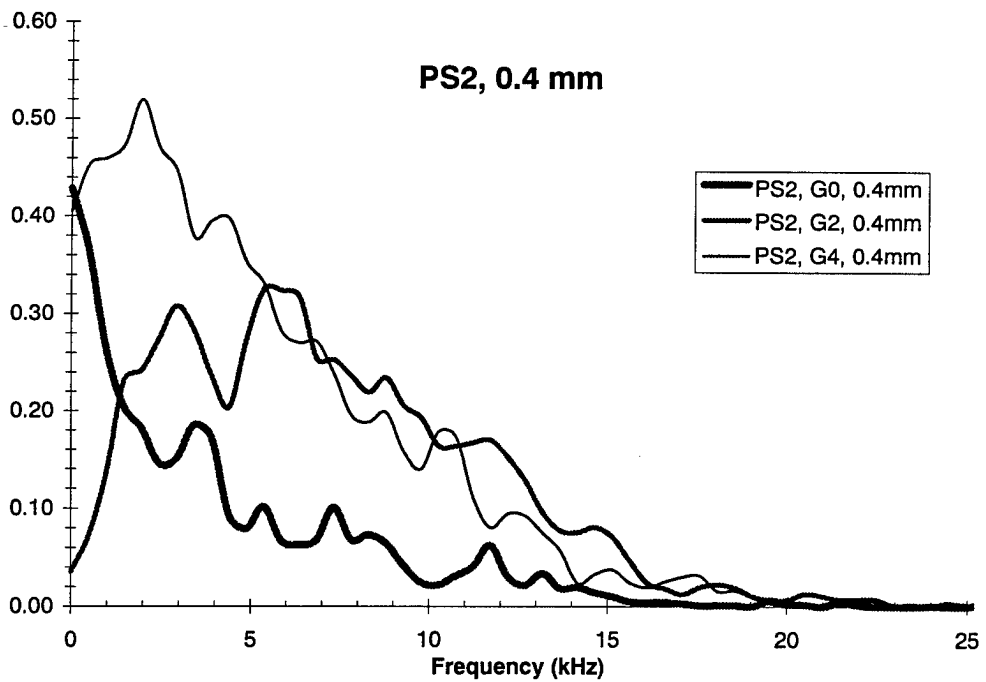
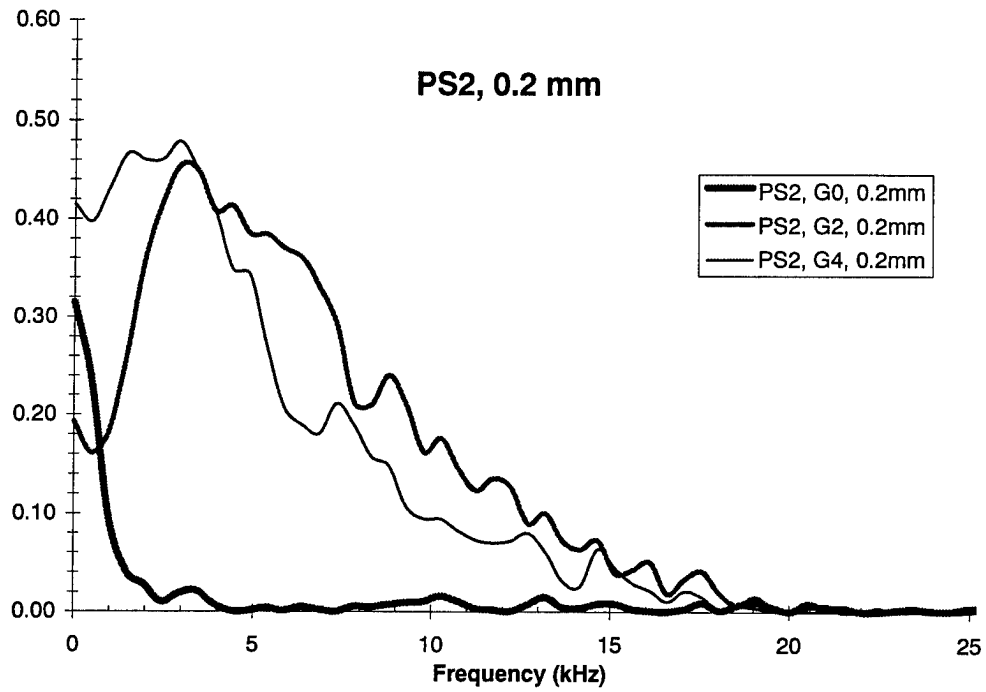


Figure 6.3.7 Coherence at PS2, 0.2 mm and 0.4 mm comparing grids.

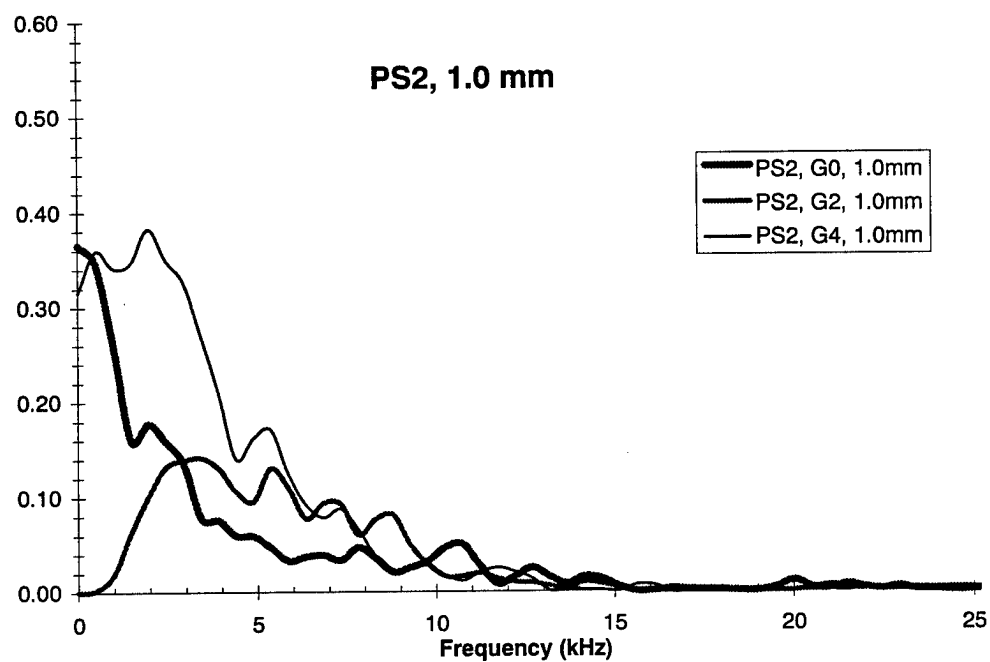
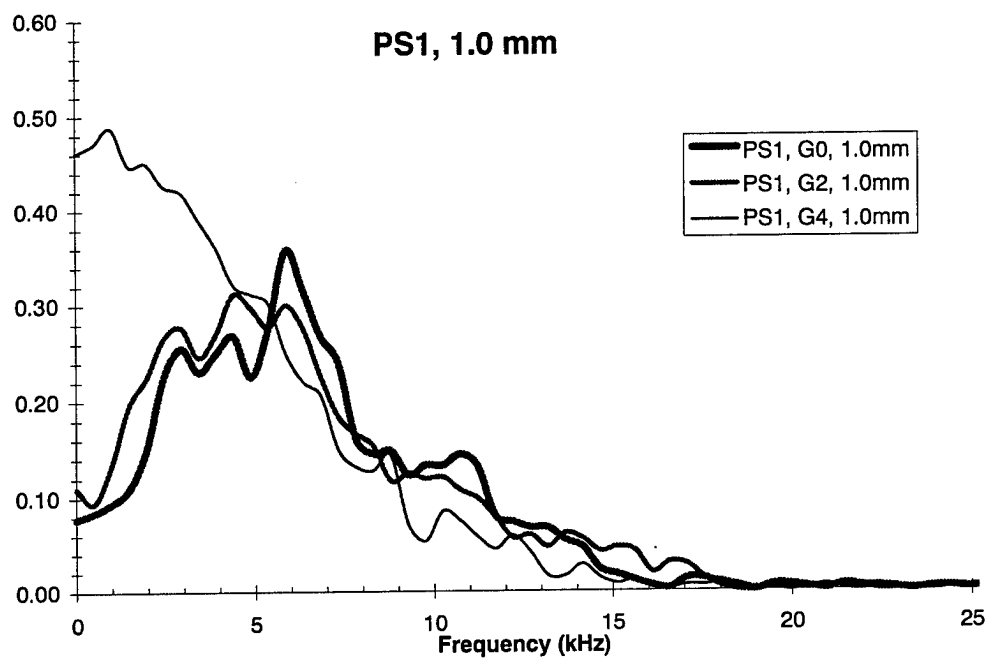


Figure 6.3.8 Coherence at 1.0 mm, PS1 and PS2, comparing grids.

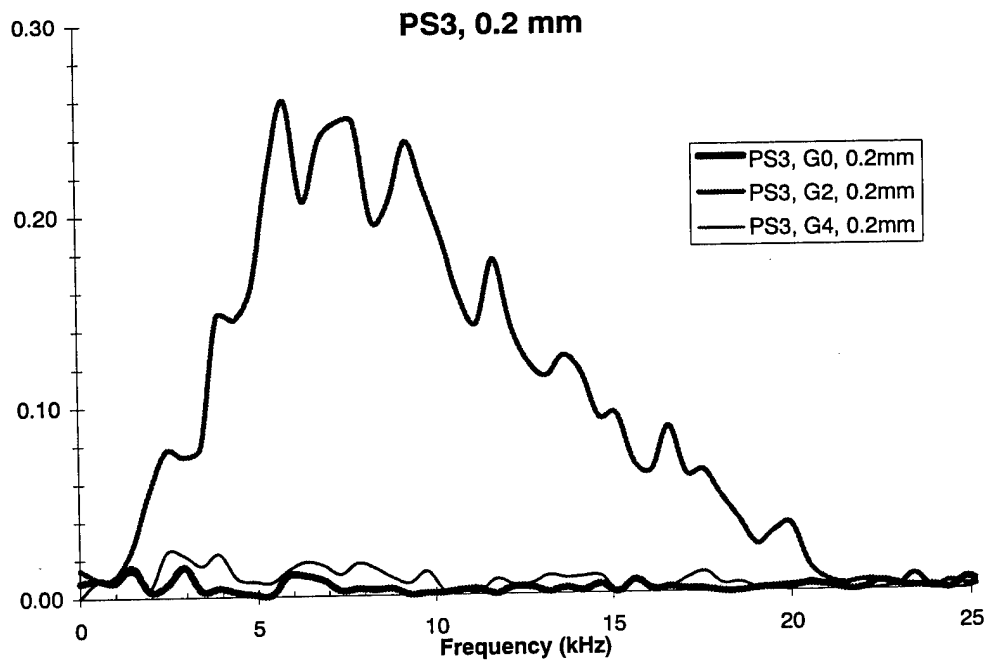
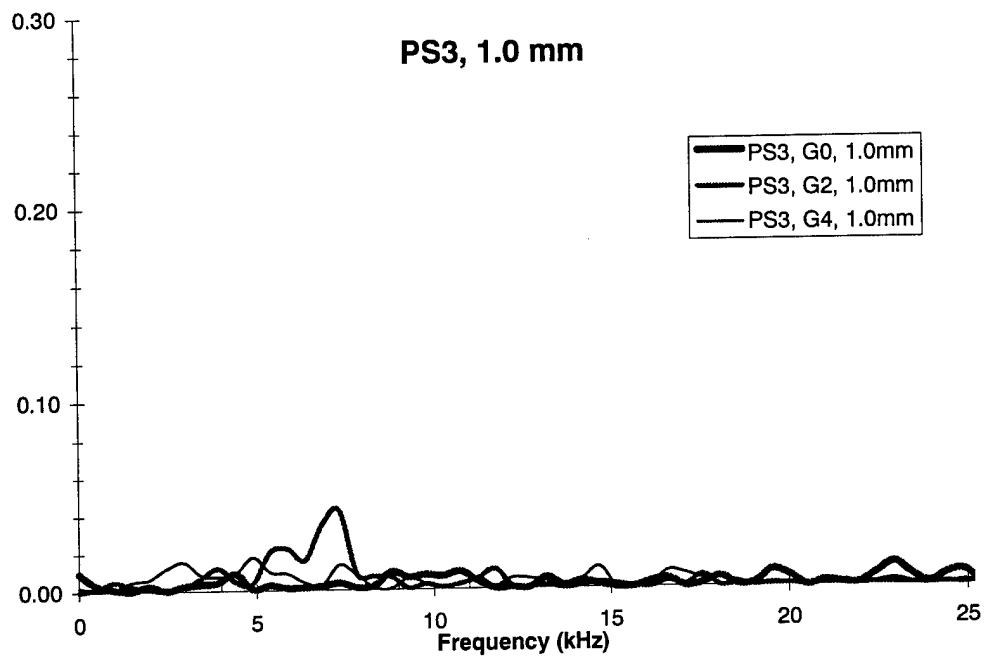


Figure 6.3.9 PS3 Coherence comparing grids.

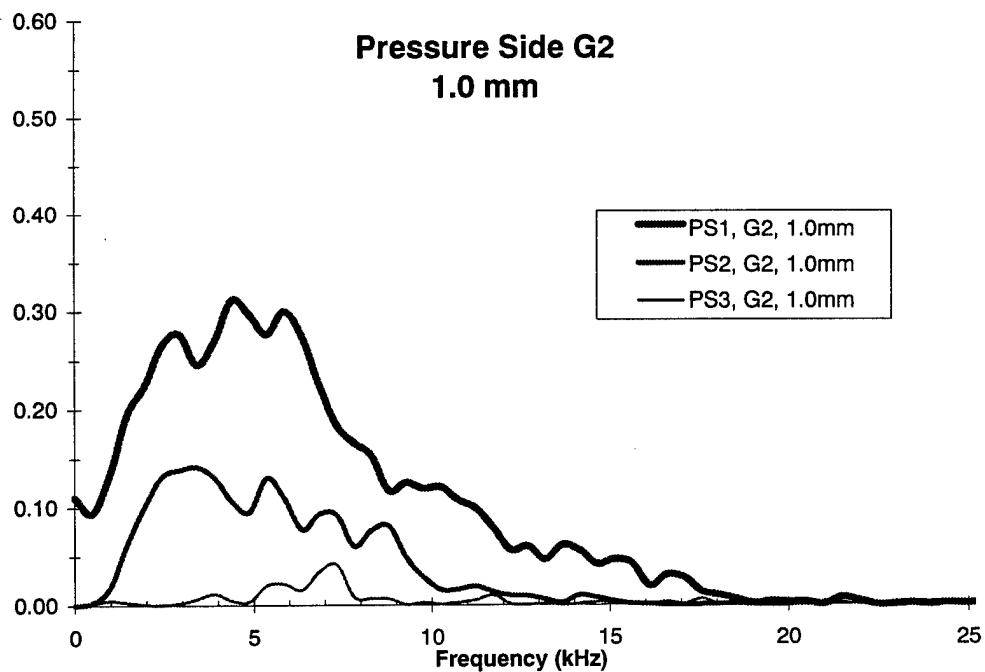
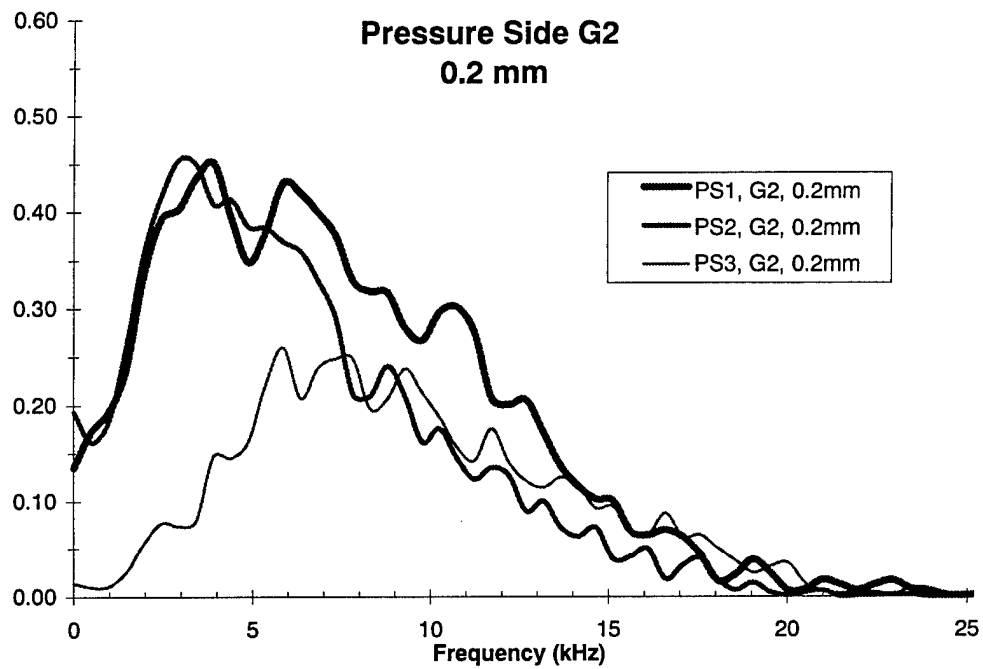


Figure 6.3.10 G2 Coherence along pressure side, 0.2 mm vs. 1.0 mm.

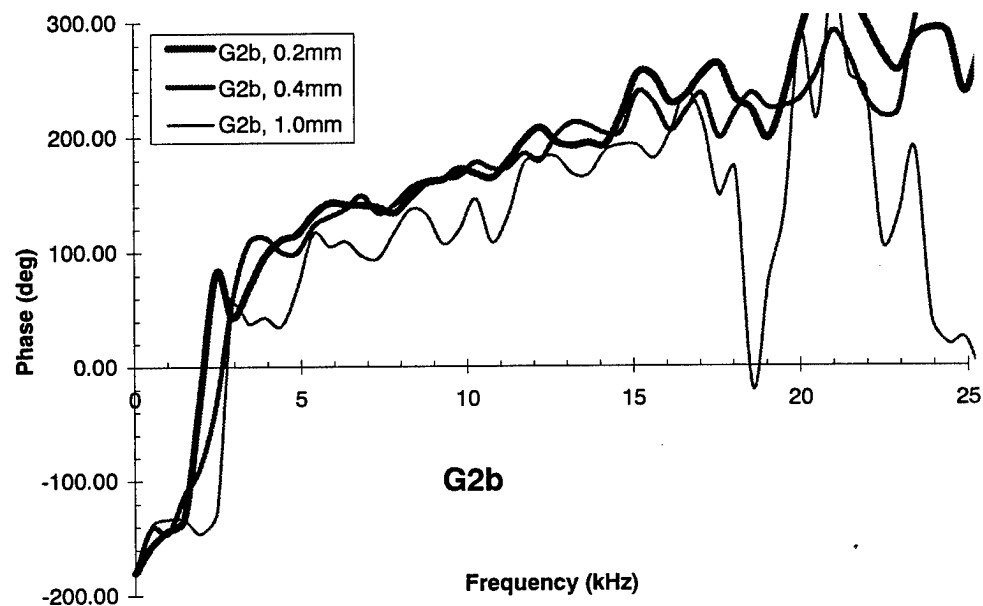
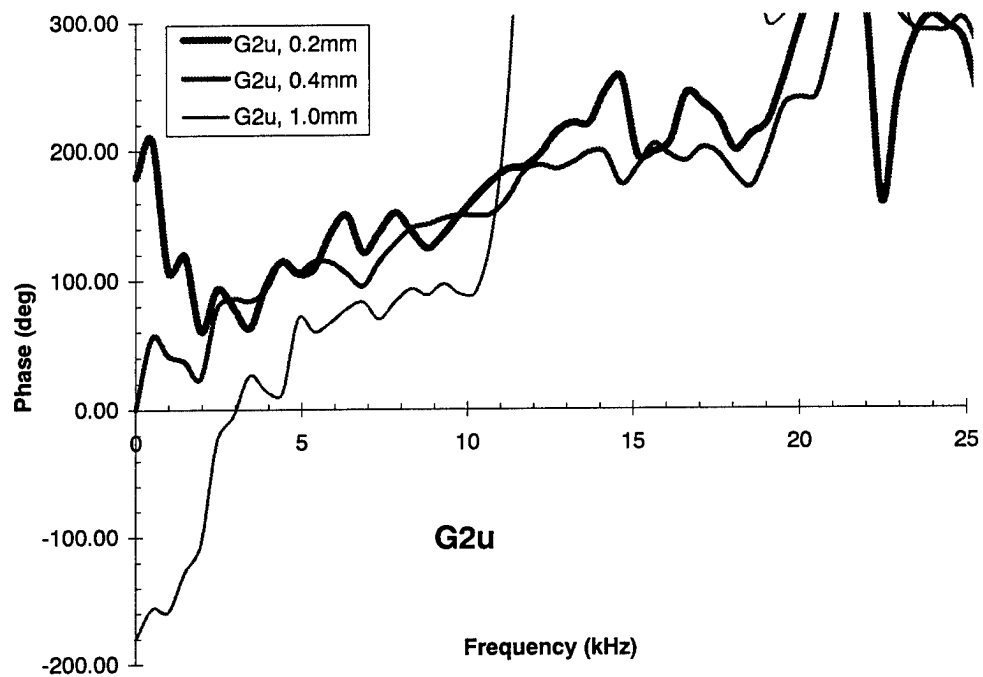


Figure 6.4.1 DS1 phase, G2u and G2b.

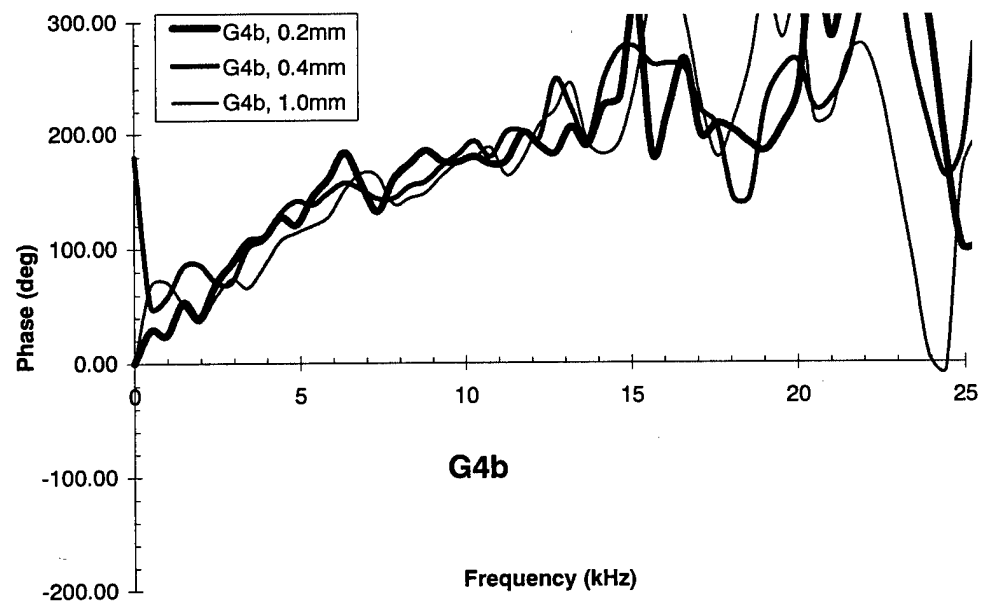
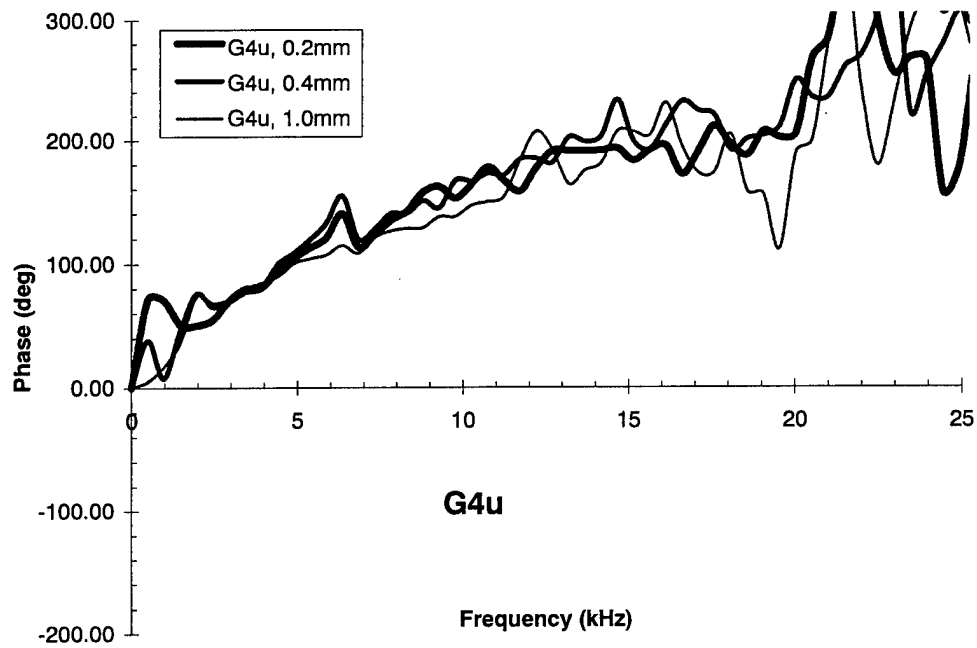


Figure 6.4.2 DS1 phase, G4u and G4b.

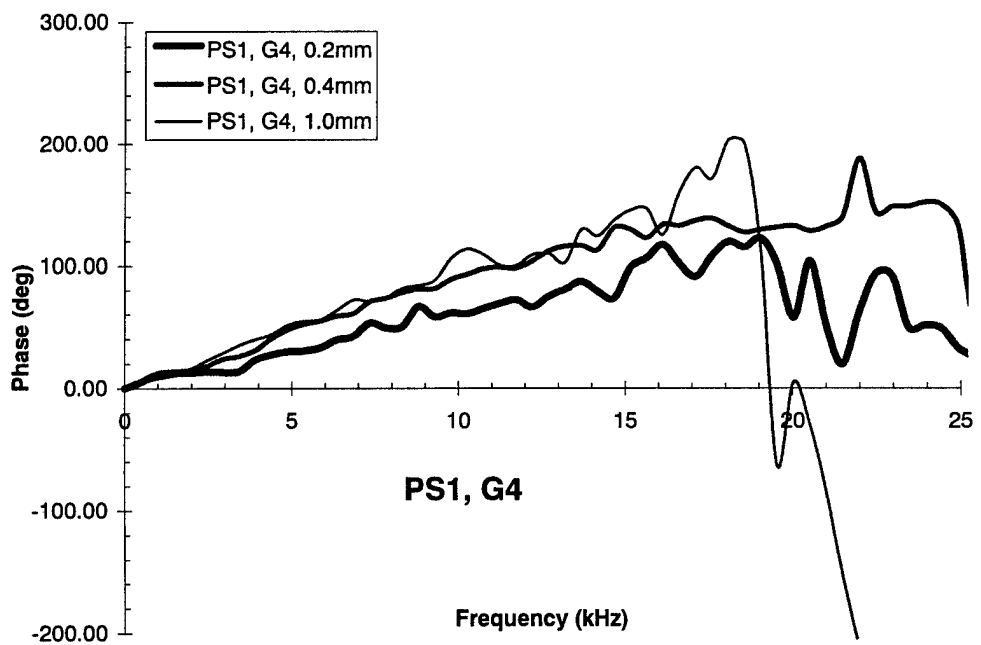
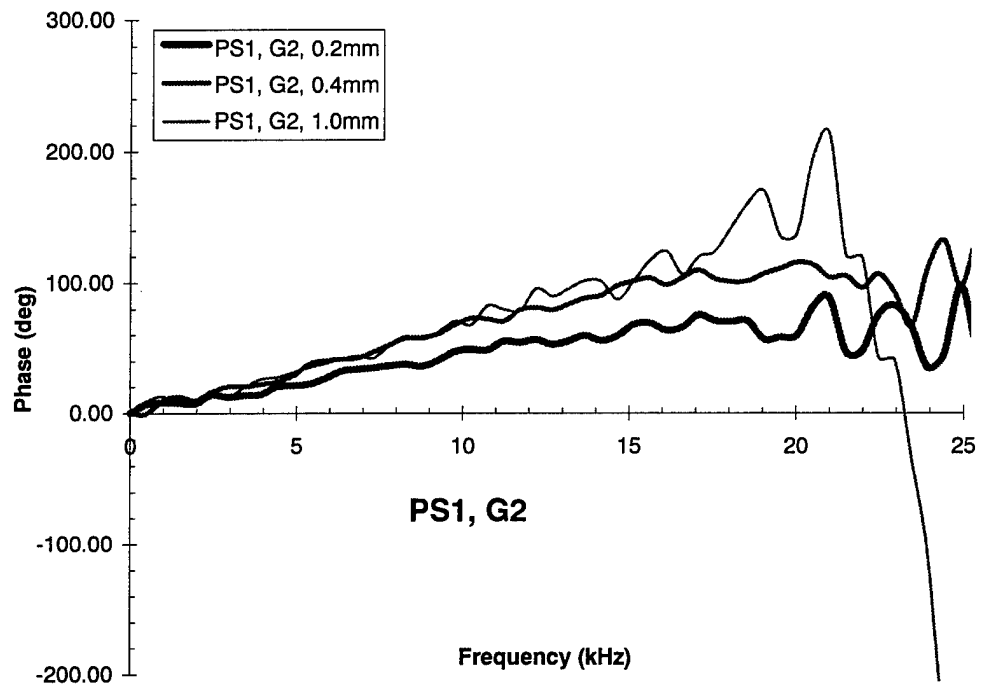


Figure 6.4.3 PS1 phase, G2 and G4.

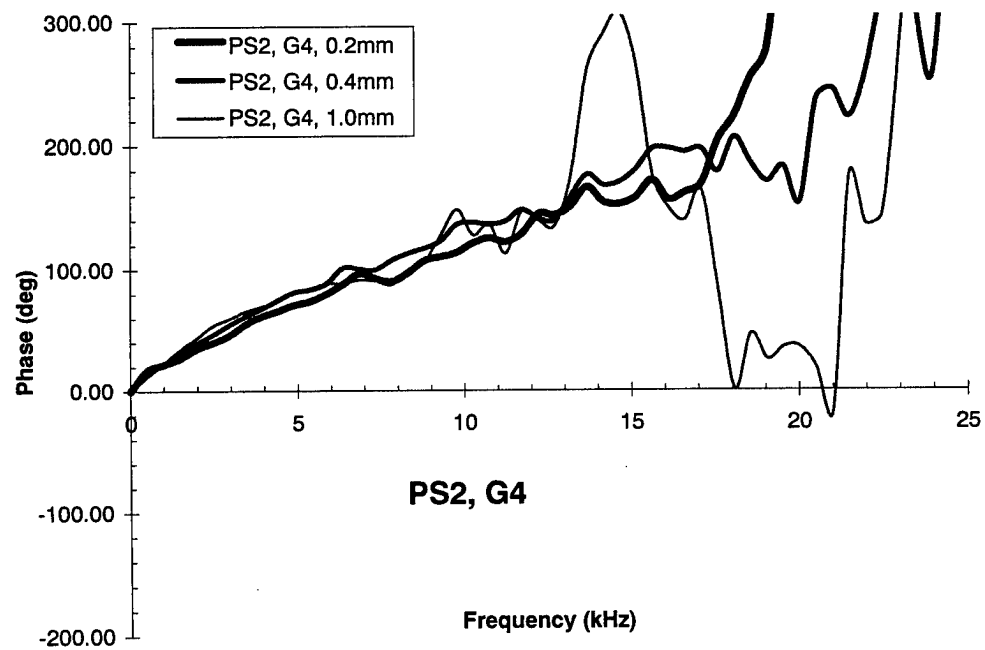
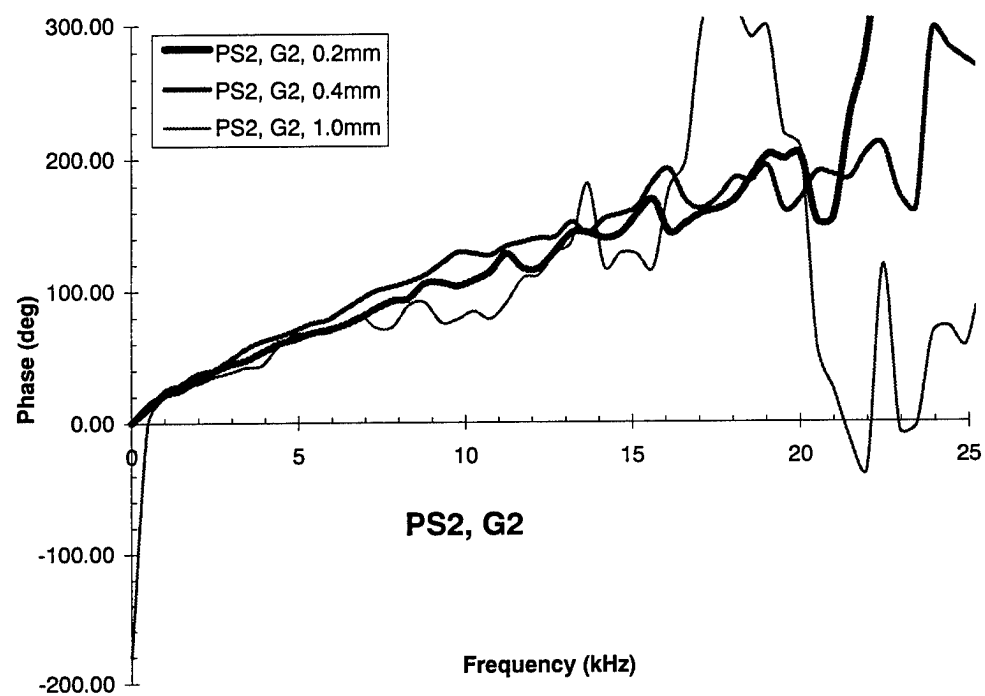


Figure 6.4.4 PS2 phase, G2 and G4.

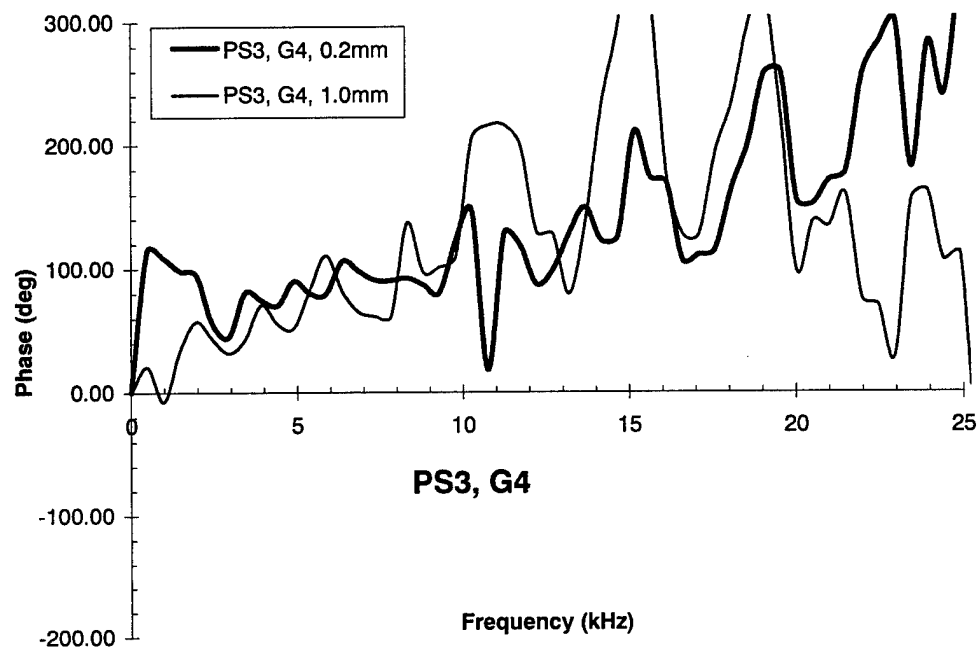
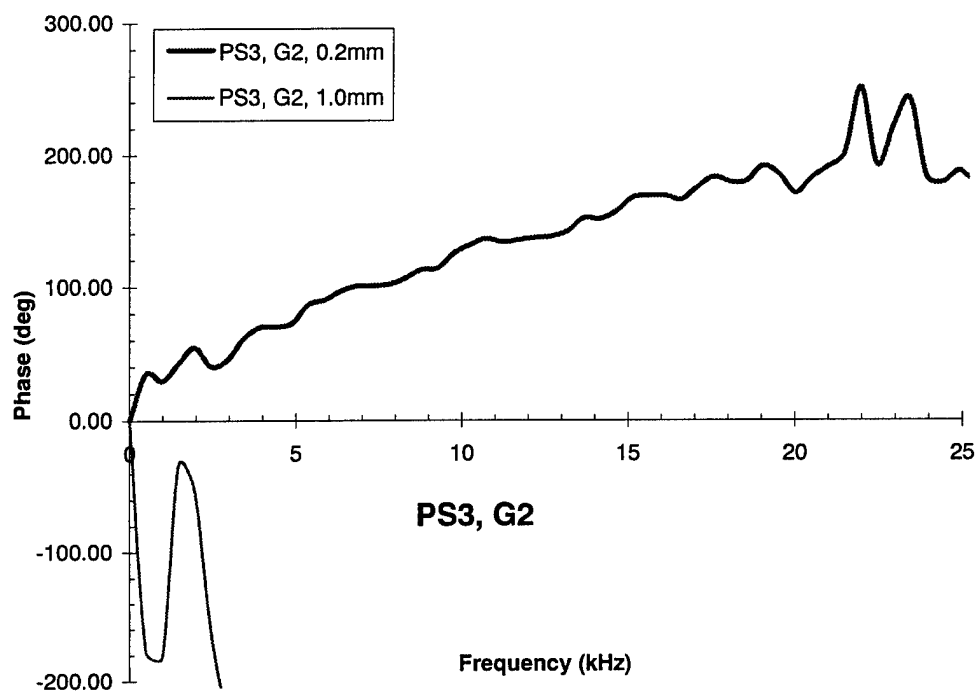


Figure 6.4.5 PS3 phase, G2 and G4.

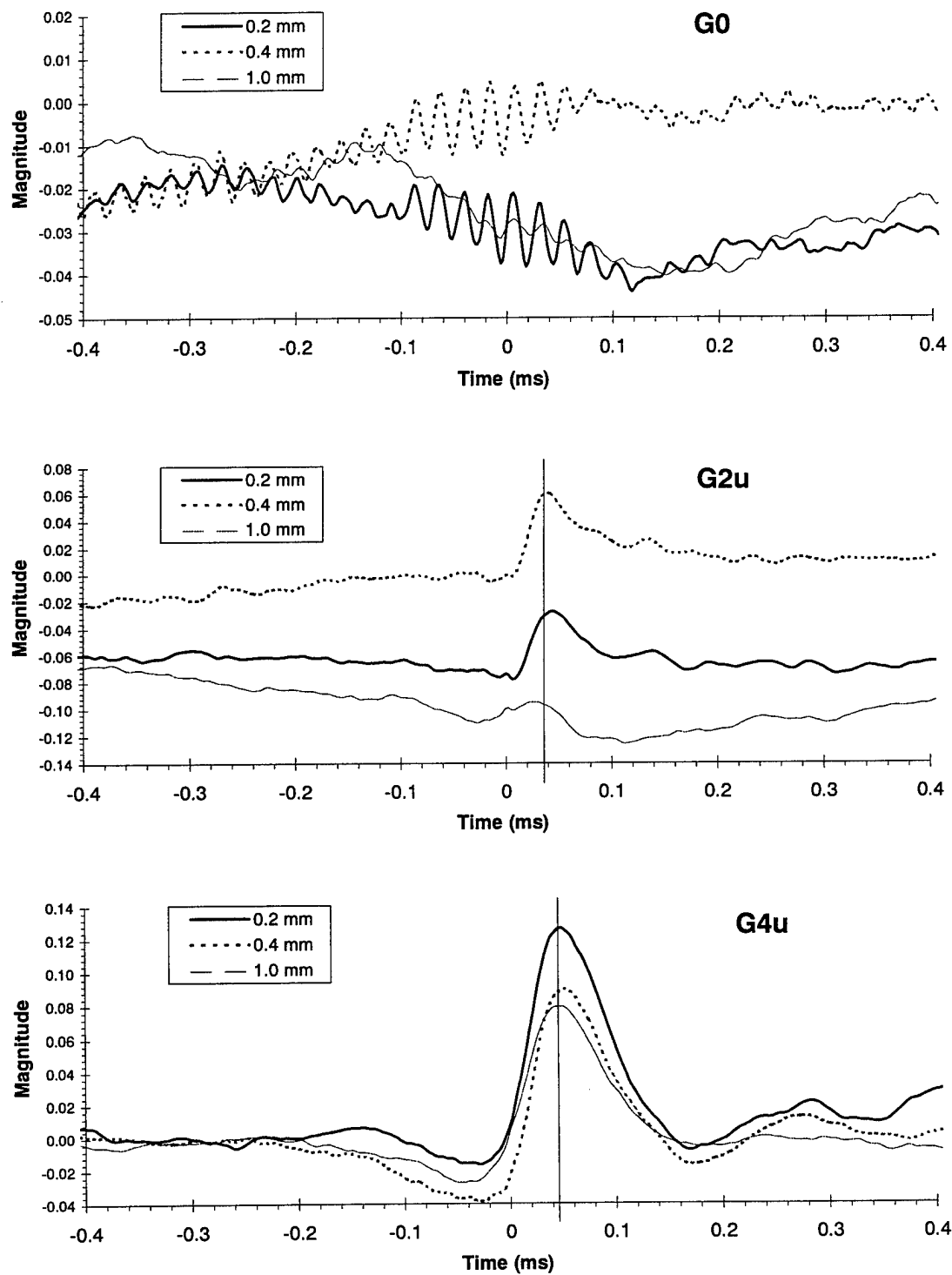


Figure 6.5.1 DS1 cross-correlation vs. y_{wire} for G0, G2u, and G4u.

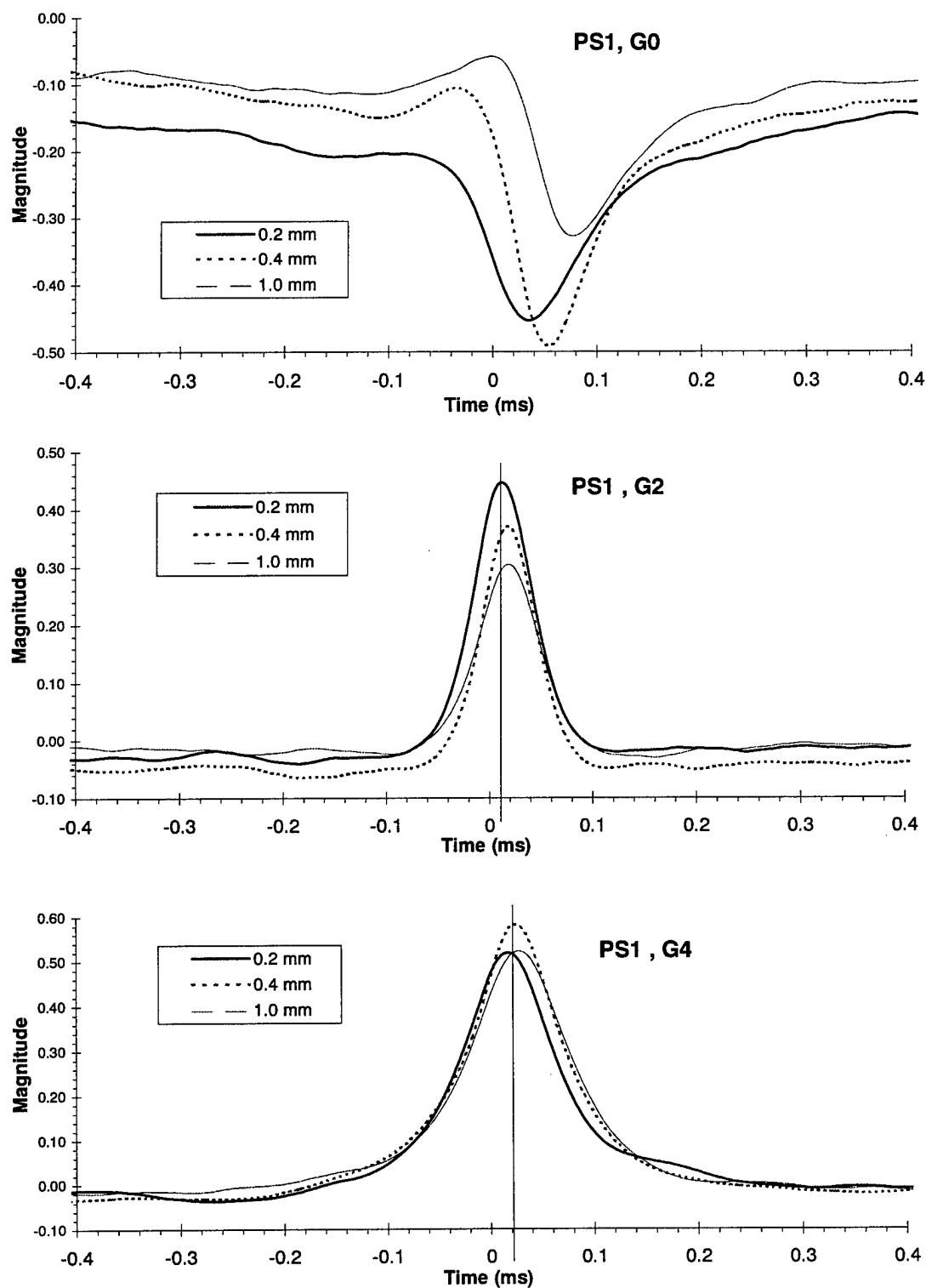


Figure 6.5.2 PS1 HF/PHW cross-correlation vs. y_{wire} for G0, G2, and G4.

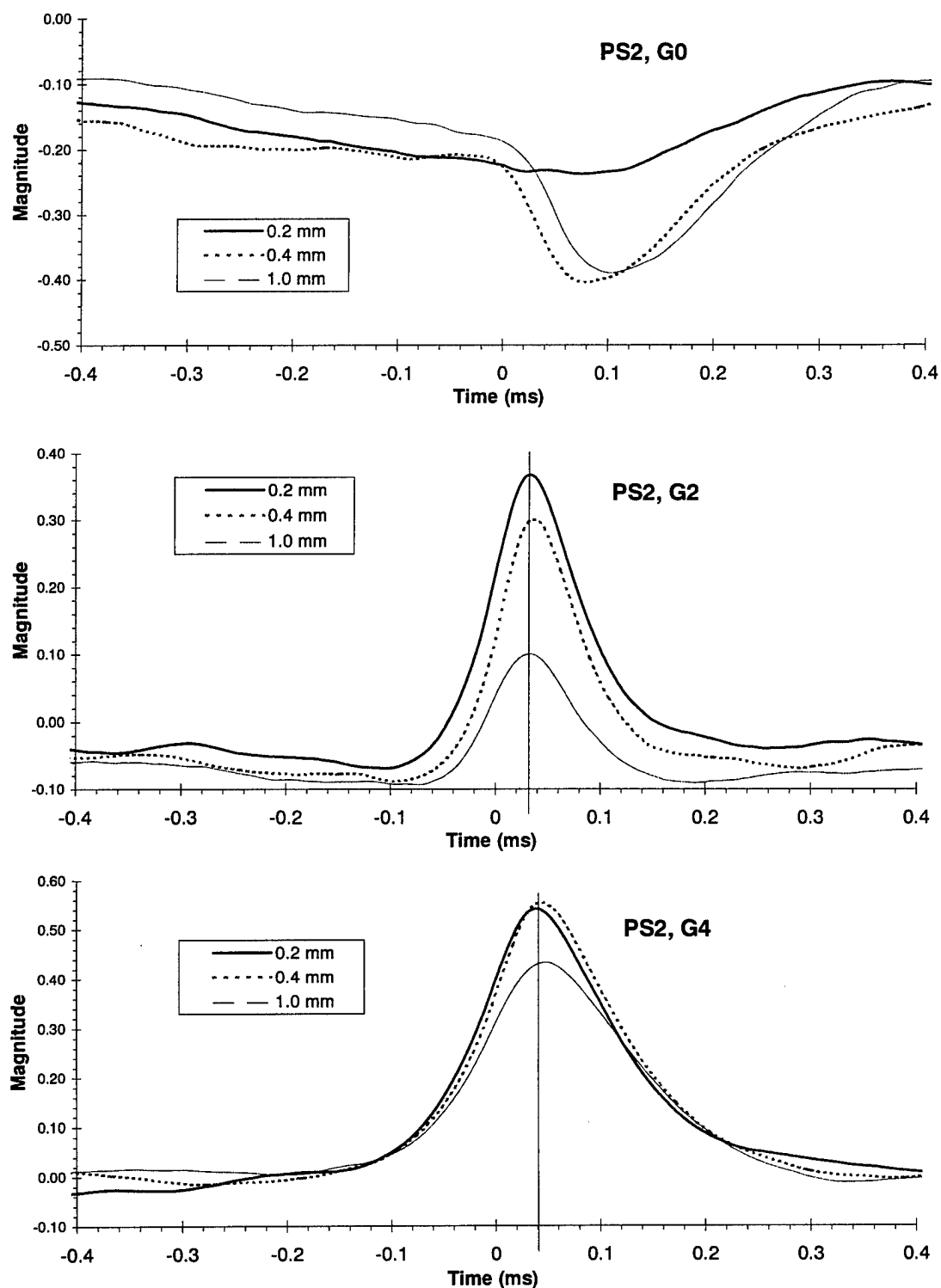


Figure 6.5.3 PS2 HF/PHW cross-correlation vs. y_{wire} for G0, G2, and G4.

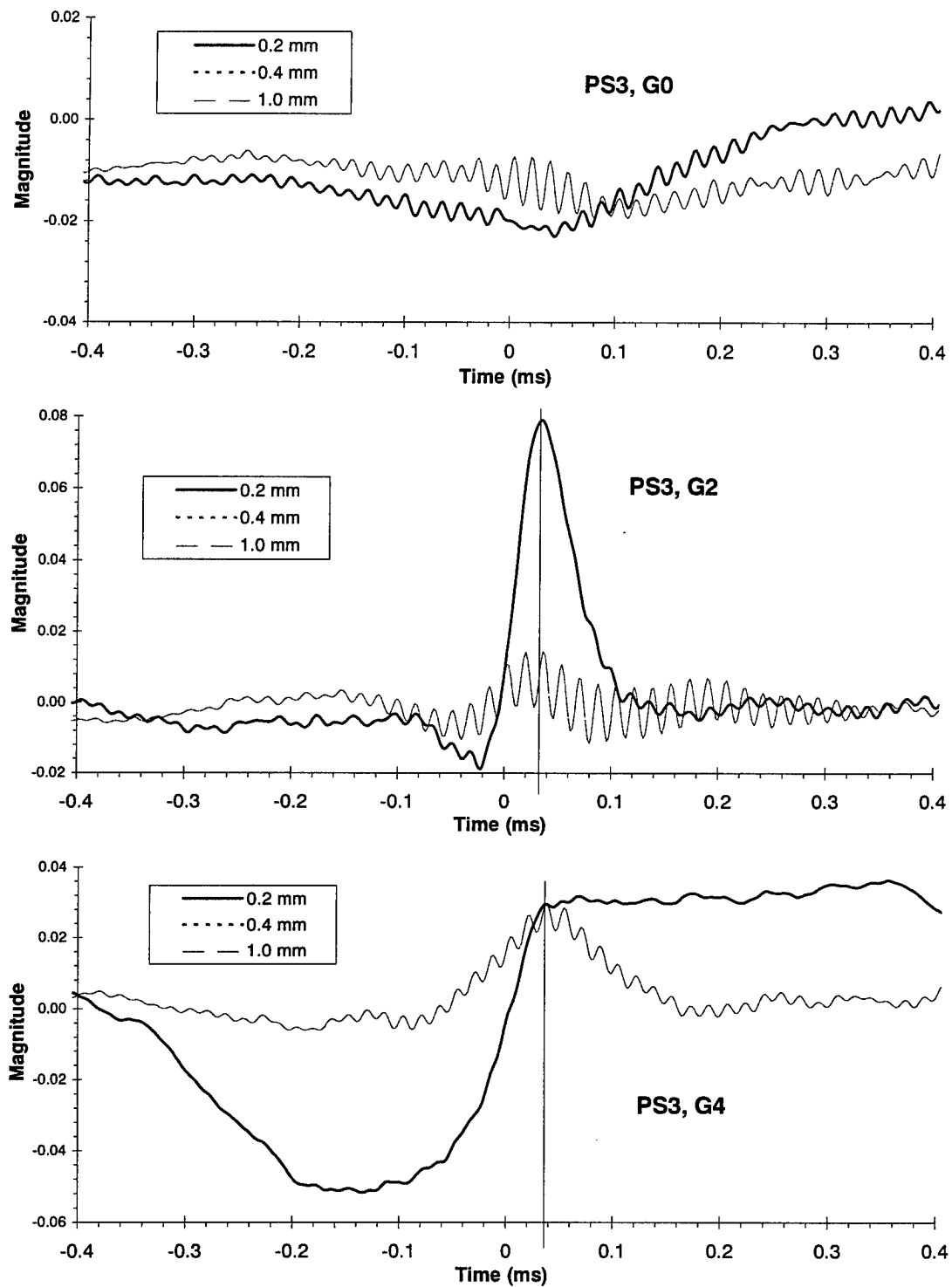


Figure 6.5.4 PS3 HF/PHW cross-correlation vs. y_{wire} for G0, G2, and G4.

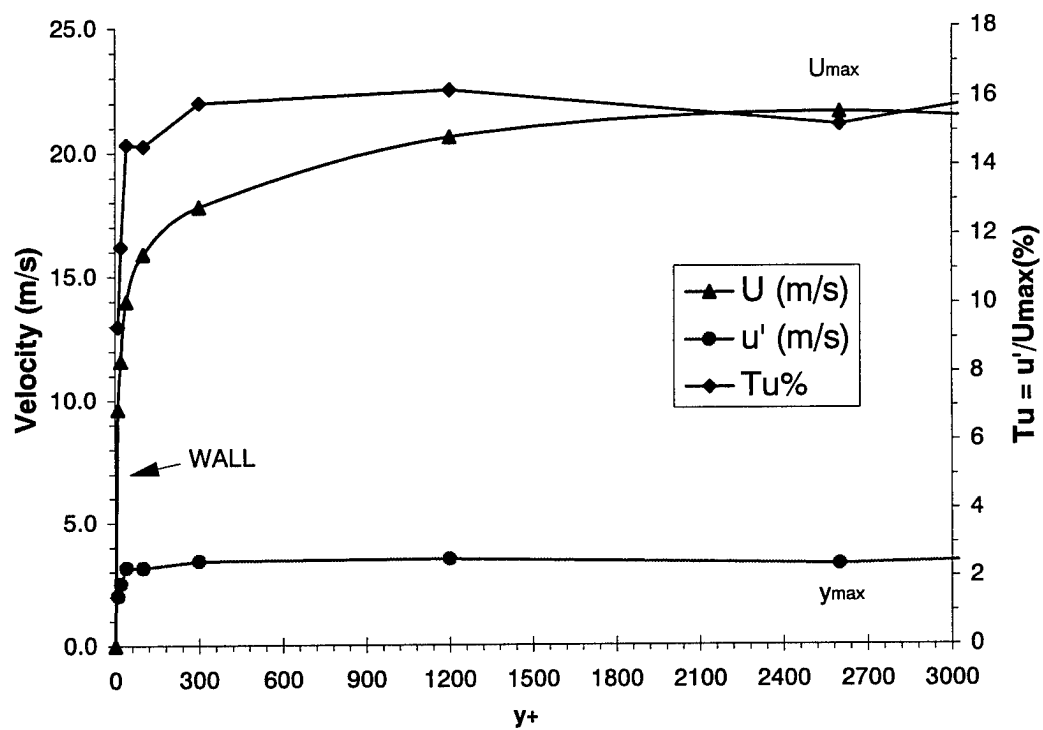


Figure 6.6.1 Mean and fluctuating velocity across WPAFB wall-jet boundary layer.

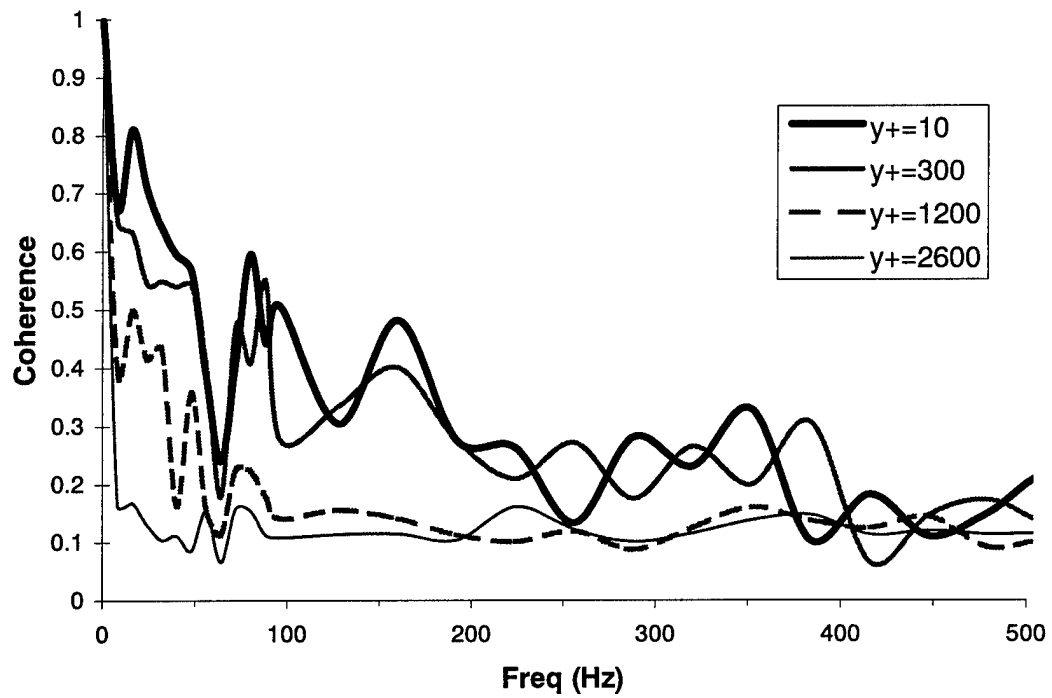


Figure 6.6.2 Coherence vs. y^+ in wall-jet boundary layer.

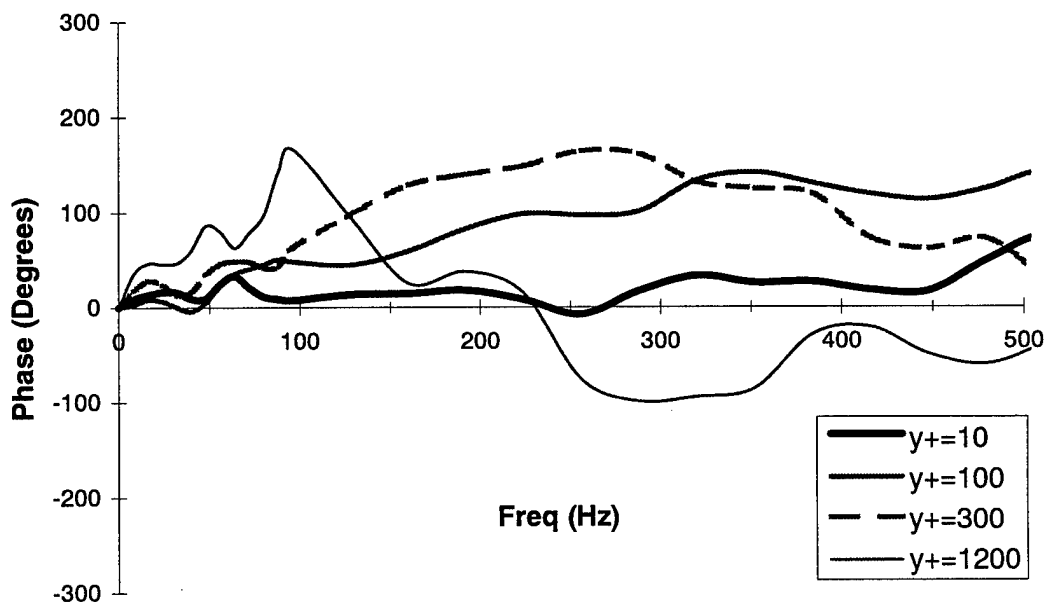


Figure 6.6.3 Phase vs. y^+ in wall-jet boundary layer.

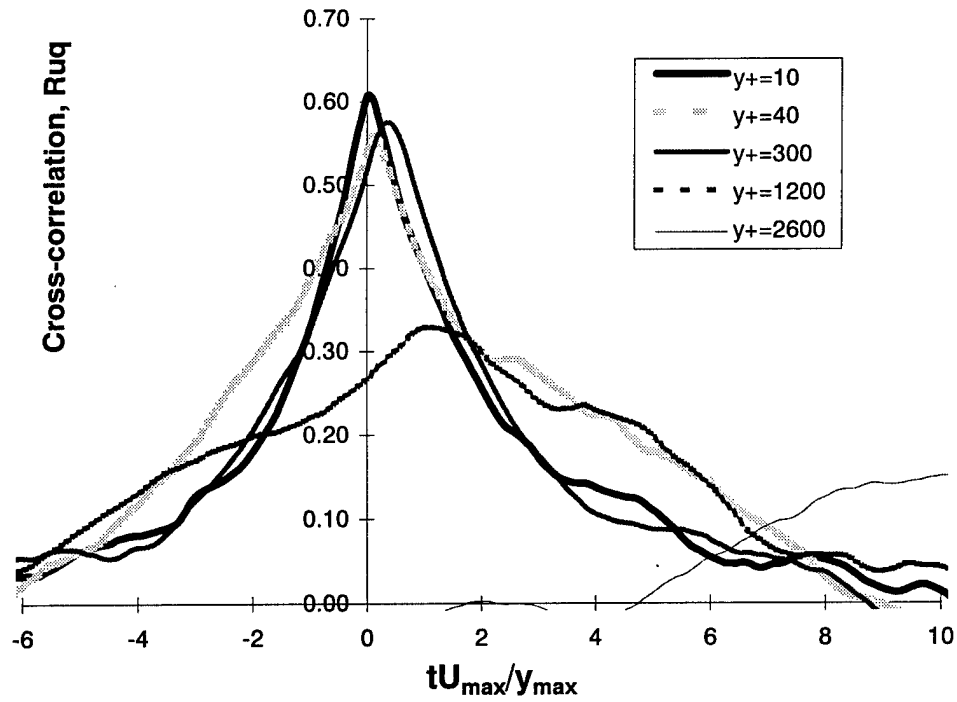


Figure 6.6.4 Cross-correlation time shift vs. y^+ in wall-jet boundary layer.

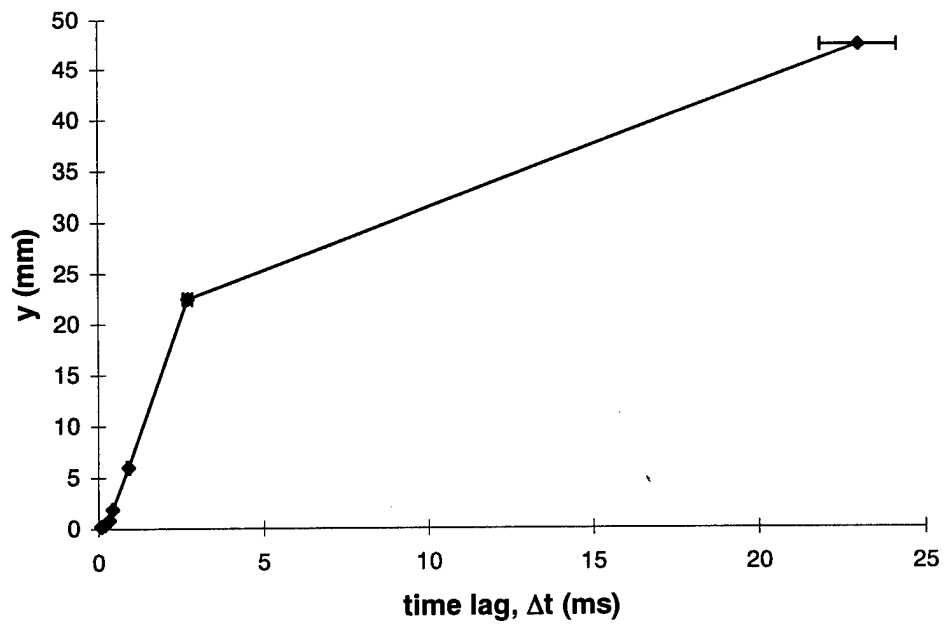


Figure 6.6.5 Time lag vs. y in wall-jet boundary layer

7. Analysis and Discussion

7.1 Introduction

Turbine blade heat transfer has traditionally been correlated in terms of normalized parameters (Nu , Re) and integral parameters (Tu , Λ_x). The leading edge laminar region of the blade has been modeled using cylinders in cross-flow, and other regions have been modeled with flat plate turbulent boundary layers. Correlations developed from these studies have tended to be facility dependent.

Facility dependence is tied both to the nature of the turbulence field as well as to the nature of the facility (e.g. flat-plate or cylinder). As noted by Van Fossen and Ching (1994), the data for stagnation region heat transfer shows widely varying correlations tied to differences in the nature of the turbulent flow. Ames (1994) notes that heat transfer is highly dependent on the large-scale, anisotropic region of the turbulent spectrum, which varies significantly from facility to facility. Ames suggests the need to better understand the actual anisotropy present in a real engine so as to better model its effect. The work of Maciejewski and Anderson (1996, discussed further below) is significant in that they attempt to bypass this uncertainty due to turbulence characteristics by correlating heat transfer to measurements in the boundary layer for turbulent heat transfer.

The present data, taken in a realistic engine scaled turbine passage, can shed some light on the usefulness of these recent ideas and correlations. What, for instance, does the present data tell us about the relationship of the free-stream to the surface heat flux? And, how useful is the construct of a length scale, given the strong influence of anisotropy? In addition, we hope to determine the usefulness of the fluctuating component of heat transfer, q' , as well as the import and potential use of frequency based analysis of time-resolved heat flux and velocity.

This chapter begins with a review of applicable correlations and their results with the present data, followed by some additional observations concerning fluctuating quantities of velocity and heat flux, and conclusions. Following this is a section giving an interpretation of possible flow phenomena leading to the observed frequency domain data seen in chapter 6. Finally, a number of topics are discussed by way of conclusions.

7.2 Application of existing correlations

Some correlations exist for heat transfer in a laminar boundary layer beneath a turbulent free-stream based primarily on cylinder stagnation point studies. In addition, there are several correlations in the literature relating mean heat transfer to flow variables for a surface beneath a

turbulent flow. Five of these correlations will be applied to the present data, beginning with two laminar boundary layer correlations, and followed by three for turbulent boundary layers.

7.2.1 Laminar boundary layers

7.2.1.1 Dullenkopf and Mayle's effective turbulence

Dullenkopf and Mayle (1994a) note that an accelerating laminar boundary layer is more sensitive to frequency than a turbulent boundary layer, while a non-accelerating laminar boundary layer is insensitive to length scale. They note that the typical fore-loaded turbine vane has roughly constant acceleration on the pressure surface, while the suction surface has roughly constant velocity after a strong initial acceleration indicating that one should expect FST length scale variations to have more effect on the PS, and near the leading edge of the SS only.

Dullenkopf and Mayle (1994b) present a correlation for laminar regions downstream of the stagnation point assuming constant acceleration of the flow at that point, applicable to cylinder stagnation region and the pressure side of some airfoils as mentioned above.

$$Nu_a = f(Pr, Tu_\lambda)$$

where the Nusselt number and turbulence intensity are based on free-stream strain rate and integral length scale.

$$a = strain = \frac{dU_e}{dx}$$

$$Nu_a = \frac{h\sqrt{\nu/a}}{k}$$

$$L_a = \Lambda / \sqrt{\nu/a}$$

$$u'_{eff} = \frac{u' \sqrt{L_a}}{(1 + 0.004 L_a^2)^{5/12}}$$

$$Tu_\lambda = \frac{u'_{eff}}{\sqrt{a\nu}}$$

$$Nu_a Pr^{-0.37} = 0.571 + 0.01 Tu_\lambda$$

The strain is used to form both a non-dimensional length scale, L_a , and to form Tu_λ . The u'_{eff} represents an "effective" turbulence level considering strain and length scale.

Based on Fig. 5.1.5 the strain at sensor DS1 is at a level point, although it has just completed a rapid drop from the stagnation point region. Application of the above formulation to the present data is given in Fig 7.1. The data appears to lie on a straight line, but as seen in the

lower part of the figure, the data is well above Dullenkopf and Mayle's correlation. This means that for this measured free-stream fluctuation level, strain, and scales, a much lower mean heat transfer is expected. For comparison purposes, the same data at DS1 is presented in Fig. 7.2 as heat transfer coefficient versus u' , rather than non-dimensionally as Nu vs. Tu (Nu_a vs. Tu_λ). This serves as a reference and shows a small improvement in the grouping of the data due to Dullenkopf and Mayle's formulation which allows for strain and length scale effects. Uncertainties shown on these plots, as well as all the plots in this chapter, have been estimated based on perturbations of individual components (e.g. Tu , u'), and total uncertainty taken as the square root of the sum of the squares of these individual contributions.

The strain on the present airfoil is not constant along the pressure side (Fig 5.1.6) as it was for the airfoils considered by Dullenkopf and Mayle. The criteria for acceptably "constant" is not given in Dullenkopf and Mayle's paper, but perhaps this would qualify as marginally constant. The data does not correlate against this formulation, however, except for a grid to grid dependence. Each grid could be fit with a reasonably straight line of slope similar to those seen in Fig. 7.1, however these lines were spread out between the two correlations given on Fig. 7.1.

7.2.1.2 Van Fossen's Frossling number correlation

Van Fossen and Ching (1994) conducted a study with a cylinder in cross-flow using grid generated turbulence. They developed a Frossling number correlation that includes effects of turbulence intensity and length scale for mean heat transfer in the stagnation point region. Their correlation grouped some data from other researchers reasonably well. Van Fossen and Simoneau (1995) conducted further work using the same facility and grids, however, heat transfer was measured on models with elliptical leading edges in order to judge the influence of velocity gradient on heat transfer. They found that, in contrast to the work of Dullenkopf and Mayle (1994a,b) presented above, heat transfer augmentation was independent of body shape (i.e. independent of strain). They found that the previous correlation of Van Fossen and Ching (1994) predicted the laminar heat transfer distribution downstream of the stagnation point. Their correlation, in terms of augmented heat transfer above a low FST baseline is

$$\frac{Fr(0)_{turb}}{Fr(0)_{lam}} = 0.00851 \sqrt{Tu Re_d^{0.800} \left(\frac{\Lambda_x}{d} \right)^{-0.574}} + 1$$

where d is the leading edge diameter, Re and Nu (in $Fr = Nu / \sqrt{Re}$) are based on leading edge diameter, inlet (upstream) velocity, and properties calculated at the total temperature, and Tu and Λ_x are based on grid correlation values at the leading edge "model removed."

For the present blade, the leading edge diameter is $d = 4.8$ mm (0.188 in.), inlet Tu is 5% and Λ_x is 0.9 mm for Grid 2 and 2.7 mm for Grid 4 at blade inlet based on grid correlations with

the blade removed. The results of applying this correlation to the present data are shown in Fig. 7.3, with the term under the square root presently defined as X_{Fr} . The heavy dashed line is the correlation of Van Fossen while the lighter dashed line is a fit to the DS1 data. Note that the correlation predicts the heat transfer for G4 at PS1 within the uncertainty of the data. The PS1 G2 data point is above the correlation. Note that the correlation groups the DS1 data nicely along a straight line, although not on the Van Fossen correlation. The data at PS2 and PS3 fall below the correlation.

It is noteworthy that this correlation performs better than that of Dullenkopf and Mayle, especially on the pressure side, supporting Van Fossen and Simoneau's contention that velocity gradient is not a significant factor in predicting mean heat transfer. For both correlations, however, the suction side DS1 data is grouped reasonably well but well above the respective correlations. Finally, the Van Fossen correlation in terms of Frossling number accounts for the slight variation in inlet Re seen in the present experiments due to grid differences and run-to-run variations in temperature.

7.2.2 Turbulent boundary layers

Consider now the correlations developed based on turbulent boundary layer work. In using these correlations, it should be understood that the present blade's pressure side boundary layer is believed to be transitional and is not likely fully turbulent for any of the measurements of the present work. However, because the pressure side of the present blade is believed to be representative of an actual high-pressure turbine blade, and because there is no region of the blade with a more turbulent boundary layer (except near the trailing edge of the suction side) these correlations will be tested and perhaps shown to be useful.

7.2.2.1 Moss and Oldfield's X_{lr}

A significant body of work, primarily in the past decade, deals with flat-plate turbulent heat transfer. The original correlation of Hancock and Bradshaw (1983) has been followed by similar ones from: Blair (1983), Castro (1984), and Moss and Oldfield (1992). These all take the form

$$\frac{Nu}{Nu_0} = f(X), \quad \text{where } X = \frac{Tu}{\left(\frac{A * L}{\delta} + B\right) * f(Re_{\odot})}$$

where L is some length scale, δ is a boundary layer thickness, and the Re correction was added due to the work of Blair. Moss and Oldfield give a good review of the use and application of this equation, and in their final form use an integral length scale to correlate their own and other's data to a reasonable degree. The specific form given by Moss and Oldfield (1992) is

$$\frac{Nu}{Nu_0} = 1.185(X_{ir})^{0.222}, \quad \text{where } X_{ir} = \frac{Tu}{\left(\frac{1.5\Lambda_x}{\delta_{995}} + 2\right)\left(1 + 3e^{-\frac{Re_\theta}{400}}\right)}$$

where for their work, Tu (in percent = $Tu \cdot 100$) and Λ_x were local free-stream values based on grid correlations, and the boundary layer thicknesses δ_{995} and θ were based on turbulent boundary layer correlations from Schlichting (1968).

Application of this correlation to the present pressure side data requires using KEP code ($Tu_{inlet} = 5\%$) boundary layer calculations for δ_{995} and θ . KEP predicts a laminar boundary layer at PS1 with $\delta_{995} = 0.10$ mm and $Re_\theta = 100$. The code predicts a rapid transitioning of the boundary layer so that boundary layer thickens to a maximum near PS2 where $\delta_{995} = 0.66$ mm and $Re_\theta = 310$. At PS3, $\delta_{995} = 0.56$ mm and $Re_\theta = 530$ are predicted. Due to the believed transitional nature of the boundary layer, the predicted turbulent values for δ_{995} at PS2 and PS3 may be regarded as maximum values, while the laminar value at PS1 may be regarded as a minimum value along the pressure side. The values of Tu and Λ_x were taken as those values measured at 1.0 mm above each gage location.

The results of applying this correlation to the present data are shown in Fig. 7.4. Despite the high uncertainties of the boundary layer parameters, the data shows conclusively that this correlation does not predict the measured heat transfer. An order of magnitude increase in δ_{995} would be required to move the PS2 data points over to the correlation, even though the turbulent boundary layer thickness used is already believed to be larger than the actual value. PS1 is even farther from the correlation as may be expected for this laminar region. It is notable that the present blade measurements have a large Λ_x relative to δ_{995} , and are probably at lower Re_θ than typical values used to formulate the X_{ir} correlation.

7.2.2.2 Ames' TLR

Work with very high levels of FST and the theoretical development of Ames and Moffat (1990) led to a new correlation, called TLR

$$TLR = Tu \left(\frac{\Delta}{Lu} \right)^{0.333} \left(\frac{Re_\Delta}{1000} \right)^{0.25}$$

where Δ is the enthalpy thickness of the boundary layer, and Lu is a dissipation based "energy scale". A similar cylinder stagnation point correlation was developed with a $Re_D^{5/12}$ power relationship with D as the leading edge diameter. Thole (1991) used this same flat-plate TLR correlation for similar high intensity ($Tu > 20\%$) data, however correlating her data with better success using the integral scale, L_x , rather than Lu . Ames (1994) went on to apply these relationships to low-speed turbine data, showing good application to his data. He found that the

laminar boundary layer on the pressure side of his test vane had heat transfer augmentation that scaled on $Tu_\infty Lu_\infty^{-1/3}$, with a Re dependence near a 1/3 power. The inlet turbulence in these tests was large scale relative to the thin boundary layer and of high intensity.

An attempt to apply this scaling to the pressure side data showed limited success. According to Ames' method, dissipation is found from the inertial subrange by fitting the following equation to the -5/3 power law region of the energy spectra

$$E(f) = \frac{18A}{55} \varepsilon^{2/3} f^{-5/3}$$

$$Lu = 15 |u|^3 / \varepsilon$$

where $A = 1.62$. Using this Lu and the free-stream turbulence intensity, two points can be calculated at each pressure side sensor for the G2 and G4 cases relative to the baseline G0.

$$\frac{Nu}{Nu_0} = \frac{h_{G2,G4}}{h_{G0}} \propto Tu_\infty Lu_\infty^{-1/3}$$

This correlation for the pressure side is presented in Fig. 7.5. The data does not appear to correlate well with any line drawn through the origin which would indicate the increase of heat transfer scaling on $Tu_\infty Lu_\infty^{-1/3}$. In support of the correlation, the baseline value is higher than a true $Tu = 0\%$ free-stream baseline due to the presence of some G0 inlet turbulence which would tend to reduce the value of h/h_0 . In addition, the TLR correlation was developed for high-FST of large scale relative to the boundary layer whereas the state of the boundary layer is likely transitional at PS3. The weakness of this correlation here can be seen as a general problem with all the correlations -- they do not account for transition and therefore are generally restricted to fully laminar or fully turbulent regions.

7.2.2.3 Maciejewski and Anderson's general correlation

Later work by Maciejewski and Moffat (1992) showed that for the collection of high-intensity flat plate data, heat transfer could be directly correlated to the fluctuating component of the free-stream velocity

$$\frac{h}{\rho c u'} = \text{constant}$$

However, it is likely that the free-stream velocity based u' relates to the heat transfer differently for different boundary layers and flow situations. Flat-plate turbulent boundary layer data can be correlated well based on a correlation as that given above, but it may not be generally applicable. Evidence of this can be seen in Fig 7.2 for u' vs. h around the present blade. For DS1 there seems to be a trend for u' increasing with h , while on the pressure side it is difficult to argue

for a correlation. The lack of direct correlation can be seen in the mean heat transfer data where $h_{PS3} > h_{PS2}$, even while $u'_{PS3} < u'_{PS2}$, which can be attributed to transition activity.

Recognizing this indirect connection, some very recent work (Maciejewski and Anderson, 1996) has sought to bring together the body of all turbulent boundary layer heat transfer based on the principle that mean heat transfer can be related directly to the maximum value of the u' fluctuating velocity *in the boundary layer* above the surface, u'_{max} . They looked at data sets from widely varying facilities to build a more generally applicable turbulent heat transfer correlation. They non-dimensionalize their correlating parameters with u'_{max} as the velocity scale and a fluid property based length scale, $L^* = (\rho c_p / k_B)^{-1/3}$, where k_B is Boltzmann's constant $k_B = 1.38 \times 10^{-23}$ J/K. In their notation

$$\pi_0 = 0.0092 \pi_1^{-1/6} \pi_2^{-17/30}$$

which is equivalent to

$$St = 0.0092 Re^{-1/6} Pr^{-17/30}$$

with the understanding that St and Re are based on u'_{max} and L^* .

For the present data, u' distributions across the boundary layer is not known. However, data from Zhou and Wang (1993) includes u' information in a flat plate boundary layer from the laminar state through transition to fully turbulent. This data set includes low FST, high FST, and variation in acceleration. The results show that whether a boundary layer is laminar or transitional, accelerating or not, high and low FST, the maximum u' in the boundary layer does not vary much, and is near $u'/U_e = 15\%$, and slightly lower for an accelerating laminar boundary layer.

Based on these results, a value of $u'_{max} = 0.15 U_e$ was chosen for all sensor locations, and the correlation applied to the present data. The results for this are shown in Fig. 7.6. Clearly there is a wide spread in the data, where error bars represent min and max values of u'_{max} based on Zhou's work where, for all boundary layer conditions, $0.12 < u'_{max}/U_e < 0.18$. This shows that the correlation fits the present data within allowable assumptions for u'_{max} . This is not insignificant in that the correlation was built based on several data sets all at Re numbers an order of magnitude lower or more. Also, consider that for some of the present data the boundary layer is laminar with a turbulent free-stream indicating that this correlation may apply to such data in general. However, uncertainties are high due to the lack of boundary layer information for the present blade set-up.

Note also that the data at PS3 is below the correlation, corresponding to lower u'_{max}/U_e near 0.12 (if the correlation is taken as correct) when Zhou's measurements indicate generally

higher u'_{\max} fluctuations in a transitional boundary layer. Finally, G0 points are well below the correlation as should be expected, and not included in the plot.

In conclusion, the correlations available in the literature often rely on information that is difficult to obtain in a *full-scale* (i.e. small blades) facility, e.g. boundary layer information for the present blade. The correlations applied here are difficult to judge due to the few measurement points along the blade surface in the present study. Van Fossen's correlation shows the most promise for the leading edge region of the blade while Maciejewski's general heat transfer correlation shows the most promise for correlating heat transfer at different points on a blade with the fluctuating velocity field. However, this correlation also requires detailed boundary layer measurements. It seems that simple correlations will continue to be very limited in their application. With this in mind, an understanding of the flow mechanisms at work driving heat transfer can aid in our efforts to relate the free-stream turbulence to the surface heat transfer.

7.3 An interpretation of the flow-field/ surface interactions

The present data allows one to "see", in a limited way, the interactions between the surface and the flow. Based on the work of others, and the evidence from the present data, one can form a picture of the flow over the laminar suction side at DS1 and over the curved PS. The intent of this interpretation is to develop our understanding of the complex flow-field that drives the unsteady heat transfer. With better understanding there can be better control.

The initial step in analyzing the effects of FST is a proper understanding of turbulent flow. Consider that the inlet flow is close to isotropic. It is customary to speak of turbulent "eddies", which are typically drawn as something like a circle in a 2-D drawing with the implication that all turbulent motion is due to fluid rotating with spanwise vorticity. However, eddies are actually coherent fluid motions, smaller ones inside larger ones, with randomly aligned vorticity for truly isotropic turbulence. These coherent motions are short lived with time scales that are proportional to the velocity and dimensions of a facility. A large "eddy" with vorticity angled in some manner to the flow is born through the influences of upstream eddies and surrounding forces. This large eddy in turn interacts continuously with fluid motions surrounding it so that it is dissipated or broken up. Generally the large scale motion persists (Townsend, 1976) while smaller motions are shorter lived. The demise of a large eddy spawns smaller eddies or contributes to the birth of other large eddies, while the work of viscosity steadily dissipates the energy in the flow.

Considering the turbulence from this 3-D perspective, let us consider three mechanisms that appear to be at work in the present flow. The first is that of vortices wrapped about the leading edge increasing turbulence in the stagnation region and in the near-field downstream. The second is the influence of large scale eddies near the pressure side leading edge, and the third is the mechanism of streamwise vorticity induced along the pressure side due to curvature effects.

First is a discussion of the mechanism of each in more detail, followed by an analysis of the present data in support of these.

7.3.1 Mechanisms of flow/ surface interactions

7.3.1.1 *The leading edge vortex*

The work of many researchers with cylinders in a turbulent free-stream has shown a strong sensitivity in the stagnation point region to turbulent eddies of the scale of the leading edge diameter and with y -vorticity -- aligned normal to the leading edge and normal to the flow. When such a vortical element meets the leading edge of the cylinder or blade, the eddy can become caught and stretched about the leading edge. The action of acceleration about the cylinder or leading edge draws out the vortical filament, tightening it so that the diameter is reduced with resulting increased vorticity. Good flow-visualization and review of this phenomena can be seen in the paper of Van Fossen and Simoneau, (1987). In their work, the leading edge vortices were stable due to a steady wake from upstream wires. The result of this action is increased heat transfer due to the scouring action of the vortical filament on the boundary layer. For the present unsteady flow, the vortical filament will break free of the leading edge and migrate down the surface of the blade, all the while diffusing and breaking up due to interactions with the strong turbulent eddies in the surrounding free-stream.

The effects of these vortical filaments downstream at the suction side gage location will be very complex. Consider the influence of this vortical filament as it develops at the leading edge, prior to breaking free. The "head" of this vortex is migrating downstream in the accelerating suction side flow, while the tail is pinned to the leading edge. The head is relatively low-energy and acted upon by the strong turbulent motions about it that tend to break it up. Nonetheless, the body of the vortex is maintained by the stretching effect that increases rotational speed. The very forces that cause this "stretching" imply drag on the vortex by the free-stream flow, which in turn implies that the vortex itself has lower streamwise momentum than the surrounding flow. This should produce a wake downstream of the vortex that may register as a drop in velocity at the hot-wire prior to the passing of the vortex. The heat flux, however, is likely to see increased heat transfer due to the upstream disruption of the boundary layer. As the vortex breaks free from the leading edge, the head and body sweep by the hot-wire with increased v' energy in the downwash or upwash regions at the side of the vortex, combined with a climbing U velocity due to the acceleration of the vortex now that it has broken free. The heat flux sensor should register a steadily increasing heat flux followed by a peak as the very-near-wall tail of the vortex sweeps by, followed by a drop in heat transfer. The time shift between the peak in the hot-wire and the later

peak in heat-flux should be relatively greater than the shift seen due to other flow-surface interactions assuming the vortex is highly stretched and thus steeply inclined in the flow.

7.3.1.2 Swirling flow

On the pressure side there are several significant regions of flow. Near the leading edge, the boundary layer is rapidly accelerating (Fig. 5.1.6) while the free-stream above is decelerating. Following this initial region of free-stream deceleration is a region of strong curvature and continued mild deceleration. Near PS2 the curvature is maximum, and the flow is accelerating. At PS3 the flow is strongly accelerating with less curvature as the flow moves on to the trailing edge.

PS1 is in the initial region of slowing free-stream flow. The large inlet turbulence scales have not yet been attenuated by the contraction of the passage or the acceleration beyond PS2. And unlike the flow on the suction side where high acceleration has distorted and attenuated the large eddies, here the opposite effect occurs. The effect of deceleration is to relax the vorticity, but also to generate the “inactive swirl” mentioned by Townsend (1976). The large eddies and smaller within have additive velocity vectors near the wall that lead to increased fluctuation levels near the wall, as seen in the previous chapters. The large eddies also produce high coherence at low frequencies with a short time lag between velocity and heat flux response.

The high coherence at PS1, and the growth of low-frequency disturbances in the boundary layer downstream of PS1 seem to indicate that the large eddies are effective in disturbing the boundary layer. The high heat flux intensity downstream of PS1 may be due to this low-frequency flow energy at PS1 causing unsteady transition. The implications of this in relation to fluctuating heat flux will be discussed further in section 7.4.

7.3.1.3 Streamwise vorticity due to curvature

Consider the effects of curvature beyond gage PS1. Fundamental to the flow in a curved channel is the influence of centrifugal force. At the same time, potential flow theory shows that the velocity gradient across a curved channel is such that $U_r = \text{constant}$. Therefore, the fluid at the smaller radius is moving at a higher velocity than the fluid at the larger radius. In the present blade passage, this means that the flow over the suction side will be higher velocity than the flow over the pressure side, as required to produce lift on the blade. However, this is a naturally unstable flow in that the higher momentum fluid is at the smaller radius. This instability is demonstrated by the well-known secondary flows where lower momentum near-wall fluid migrates along the endwalls toward the suction side due to the centrifugal force acting on the flow.

The action of this force is seen also in the formation of “Görtler” vortices on curved channel walls with low free-stream turbulence (Kim, Simon, and Russ, 1992, give a good review). These streamwise vortices grow in the laminar region of the boundary layer and are stable into the

turbulent boundary layer region, fixed spatially in counter-rotating pairs along the surface with corresponding regions of "downwash" and "upwash." Heat transfer is higher and lower corresponding with the downwash and upwash. The presence of small instabilities and some surface discontinuity allows the formation of these vortical structures and spatial fixation. In essence, these vortices offer a flow path for higher momentum fluid away from the surface to move toward the wall -- the direction that centrifugal forces are driving it. The lower momentum fluid near the wall is in turn lifted away from the wall. The preference for this streamwise vorticity can be explained by noting that streamwise momentum is maintained at the same time that momentum transfer occurs normal to the surface.

However, under a turbulent free-stream these Görtler vortices are not seen (Kestoras, and Simon, 1994). This implies that streamwise vorticity is no longer born and fixed spatially due to surface instabilities, but rather that streamwise vorticity is now produced by a more dominant source -- that of the instabilities in the free-stream. FST offers another means by which to move higher momentum fluid toward the pressure side. The unstable free-stream as the source of disturbance leading to streamwise vorticity explains the difficulty of observing it relative to the stable Görtler vortices. Kestoras reports that the flow far from the wall evidences the growth of scales and increased mixing and no longer obeys the potential flow profile of $U_r = \text{constant}$. In essence, the turbulence in the free-stream is acting like a cascade where the "heavier" balls go to the bottom.

An example of the relationship between low FST curved channel with Görtler vortices and the high FST without can be seen by comparison of a laminar versus turbulent flat plate boundary layer. For a laminar boundary layer the shear layer is stable. However, in the presence of turbulence, the boundary layer profile changes due to the transfer of momentum from the free-stream toward the wall allowed by the turbulent cascade. The mechanism of this momentum transfer is very similar. Correlation measurements in plane shear flow indicate large eddy motion in the form of inclined "double-roller" eddies (Townsend, 1976). Rapid distortion theory, "suggests prolonged strain of any simple eddy converts it to an elongated double roller," where this double roller is similar in form and action to the Görtler vortices.

Outside the boundary layer of a curved channel, it is centrifugal force that drives the turbulent momentum transport process, but the effect is the growth of a boundary layer profile out into the free-stream, as reported by Kestoras (1994). The mechanism responsible for cross-stream momentum transport is the same with curvature and in the flat-plate shear layer: streamwise vorticity.

Centrifugal force works to move higher momentum fluid toward the wall, and instabilities of the free-stream turbulence allow this v' momentum transfer to occur. As noted above, the only

fluid motion that effectively transfers momentum normal to the wall while maintaining streamwise momentum is that of streamwise vorticity -- the corkscrew pattern of the Görtler vortex. With free-stream turbulence, this corkscrew action is unattached to the surface. Instead it is as short lived as the free-stream motions. What does it look like? It is an unstable phenomena. Not a persistent vortex, but rather a rapid action due to the convergence of forces in a web of instabilities that forms a body of momentarily congruent high-momentum fluid. This high-momentum fluid then dives to the surface, with a sudden overturning of the near-wall flow, something like the action of a hand, initially palm-down, reaching into a pool of water to drink. This "diving" motion simultaneously brings up lower momentum fluid and also causes secondary disruption of the boundary layer in an amount proportional to the momentum and scale of the downrush. This secondary disruption would appear as nearer wall instabilities that grow and form smaller scale streamwise vorticity.

The effect on velocity and heat flux measurement through this process is complex. Prior to the initial downrush the heat flux may register a decrease due to the stagnation of near-wall lower momentum flow. This is followed by a peak as the downrush brings high momentum and high temperature fluid down. Finally, there is a post-peak increase in heat flux due to the secondary effects of the downrush promoting increased near-wall mixing. Fluctuations seen by the hot-wire will depend on its location. Assuming the wire is above any near-wall stagnation of the flow, the wire may see increased U velocity followed by the strong v' energy of the downrush, followed either by a general increase in U velocity due to the flow following the downrush, or a stagnation due to the lower momentum upwash.

The goal of the next section is to look for evidence of these interactions as the prime movers of heat transfer on the present blade. While this is somewhat speculative, it is nonetheless useful for building insight into the mechanisms at work.

7.3.2 Analysis of present data

What evidence should we look for in the data to "see" these vortical interactions at work? Beginning with the suction side, is there evidence for the work of streamwise vortical filaments as expected? If these vortices are formed at the leading edge and broken free, then swept over the sensor at DS1, we should expect to see their effect in the coherence, phase, time correlation, and individual spectra.

If these eddies are formed at the leading edge and break free, there may be some characteristic "shedding" frequency that would be indicated by a peak in the hot-wire spectra. This shedding frequency would most likely be related to anisotropy in the inlet flow, although not due to Karman vortex shedding in the present case due to the very high wire Re at the grid. In the hot-wire spectra above DS1 there is a peak in the G4 velocity spectra near 4 or 5 kHz at all wire

positions (e.g. Fig. 6.1.2). The same is perhaps seen in the G2 spectra at a slightly higher frequency. Also note that the "back" cases tend to have the same peak as the "up" cases, but shifted to lower frequencies. The heat flux spectra (Fig. 6.2.1) also show evidence of 5 kHz as well as 10 kHz disturbances, where the 10 kHz peak can be seen as a harmonic. Note that the same 5 and 10 kHz peaks are seen even more strongly in the PS1 heat flux, Fig. 6.2.4. The inlet spectra measured by the upstream hot-wire (see Fig. 4.2.3) evidences some 5 kHz energy in the G4 spectra, which now appears amplified above DS1. So, there appears to be some preferential amplification of some dominant frequencies evident in the individual spectra, but the real evidence for existence of leading-edge shed vortical filaments must come from the measured interactions of the heat flux and velocity.

The coherence at DS1 shows maxima at 5 and 10 kHz for both G4u and G4b (Fig. 6.3.1), while these are weak if present in G2. Corresponding phase shows a large phase shift, increasing with frequency. This phase indicates the degree that heat flux lags a coherent pulse at the hot-wire. A constant slope through zero in the phase plot would indicate that the time shift with which a velocity event leads heat flux is constant for all frequencies.

We would expect a vortical filament tied to the leading edge to consist of lower streamwise momentum fluid, even though it has higher vorticity. In addition, the "tail" of this filament is anchored close to the surface, and the filament has been stretched by the action of acceleration. Therefore, the time shift between the increased velocity registered at the hot-wire (primarily due to the v' energy at the sides of the filament) and the footprint of this vortex acting on the surface below (dragging behind) should be greater than the time shift based on a fluid motion acting directly from above. The effect of an increased time shift relative to a specific event frequency should be seen as an increase in phase shift at that frequency, and this is what we clearly see.

For G4u, Fig. 6.4.2, there is a distinctly higher slope in the 3-6 kHz region of the phase plot corresponding to the peak region of coherence. In this case, the less frequent larger vortices are seen near 3 kHz, and because they are larger they are seen at all wire positions at the same time relative to the heat flux giving the agreement in phase seen at 0.2, 0.4, and 1.0 mm. Smaller shed vortices are seen at a higher frequency nearer 6 kHz, but because of their smaller scale are not seen at 1 mm compared to 0.2 mm leading to the difference in phase near 6 kHz. The peak at 6 kHz occurs because the slope of the phase is dropping to a lower time shift for frequency activity above 6 kHz, where this higher frequency activity is presumably only due to the work of free-stream eddies.

What should we expect in the cross-correlation from such an event as this passing vortex? The increased time shift in phase at 5 kHz is lost due to the integral nature of this

correlation. One interesting thing to note though is the presence of an increased "post-peak" tail to the correlation plot, Fig. 6.5.1. This can be due to several effects. First, the action of some hot, high-momentum fluid impacting the boundary layer would register first as a strong correlation peak. The after-effects of this action would be increased heat transfer as the primary downward motion leads to boundary layer thinning and increased mixing. In addition, this tail can also be attributed to the passing of a vortical filament where the head of the filament registers as the peak followed by the drawn-out scouring of the tail following behind and raising heat transfer. Given that coherence is strong mainly at the frequencies where these shed vortices seem to exist leads to the conclusion that the peak in the time correlation is primarily due to the passing of these vortices, and that the post-peak increase in heat transfer is due to the disruption to the boundary layer caused by these vortices.

On the pressure side, similar evidence can be examined. As noted earlier, the presence of the leading edge shed vortices appears in the heat flux at PS1. as strong 5 and 10 kHz peaks. However, with the PHW probe present this 5 and 10 kHz energy is not seen in the heat flux and no coherence peaks are measured. Perhaps the probe is causing these vortices to be lifted off the surface, flowing over the probe. Note also that the flow above PS1 is very different than above DS1, where the deceleration above PS1 would be expected to diffuse the vortex rather than continue to stretch it as occurs above DS1.

What evidence of the curvature induced streamwise vorticity should we expect? We should not expect to see dominant frequencies, and the peak in coherence should scale on the relative scale of the flow, i.e. G2 coherence should peak at a higher frequency than G4. But, nothing very notable should be expected if this streamwise vorticity is the fundamental fluid motion governing v' motion at all frequencies.

The individual G2 and G4 hot-wire spectra along the pressure side show strong peaks below 2 kHz (e.g. Fig. 6.1.6 and 6.1.7), although less so for G2, and less so moving along the pressure side. The heat flux-spectra also have maxima near 2 kHz for both G2 and G4 along the PS. However, there is no coherence at these low frequencies except at PS1, indicative of the influence of "swirl" discussed earlier. This lack of coherence implies that the largest turbulent motions leading to cross-transport of momentum are not responsible for the peaks at or below 2 kHz. The low frequency energy seen in heat flux, at least at DS1, PS2 and PS3, seems to be boundary layer unsteadiness not related to the low frequency energy of the free-stream. The low-frequency energy seen in the free-stream appears to be only unsteadiness caused by the effect of large eddies disturbing the mean flow upstream.

The coherence does show clearly the growth and persistence of the higher frequency energy, Fig. 6.3.10. A clear growth in the higher frequencies can be seen between PS2 and PS3,

evidence of the work of acceleration in stretching the streamwise vortices. The phase information, Fig. 6.4.3 and 6.4.4 shows only a general increase from PS1 to PS2. This increase in time shift (also seen in cross-correlations) is evidence of the growth of this streamwise vorticity, and perhaps of the secondary vorticity generated after the initial downrush of fluid discussed earlier. Acceleration maintains this increased time shift at PS3.

The expected post-peak correlation, due to secondary effects after the initial downrush disrupts the boundary layer, is seen in the PS2 G2 cross-correlation, Fig. 6.4.3. It is not seen in G4, evidence indicating the increased influence of the smaller scale G2 turbulence on heat transfer. And it is not seen at PS1, evidence of the effects of curvature beginning after PS1 and seen at PS2.

It may be that this smaller scale envisioned "secondary vorticity" serves a very important role in the heat transfer on the PS. They do not have the momentum of the initial downrush, but their smaller scale (nearer the boundary layer thickness) and high vorticity due to stretching make them ideal for scouring the boundary layer and moving thermal energy near the wall. Larger scale motions, seen more clearly in the present data, could then move energy farther out from the wall. The apparently greater effectiveness of G2 sized turbulent scales in transporting momentum normal to the surface could partially explain the higher mean heat transfer seen by G2 relative to G4.

7.3.3 Conclusions

The conclusions based on the above discussion can be summarized as follows. Measurements at DS1 and less so at PS1 show clear evidence of the presence of vortical filaments shed from the leading edge at a 5 kHz frequency. The vorticity originates from the grid upstream, and is amplified through the stretching action of acceleration about the leading edge. This effect is seen primarily in G4, while only very weakly, if at all, in G2. This seems to evidence that the G2 scales are too small to generate much of this effect, while the G4 scales are more effective. Based on the strong peak in coherence at 5 kHz, it seems that these vortical filaments are the primary movers of heat flux on the suction side at DS1, although other mechanisms are certainly at work.

The pressure side shows different mechanisms at work, with no sharp peaks in the spectra except at PS1 where the same 5 kHz peak seen at DS1 is evident in G2 and G4 heat flux. G4 shows stronger coherence at lower frequencies while G2 coherence is stronger above 5 kHz. It appears that there is a different source of coherence at lower frequencies corresponding to mean flow unsteadiness, while coherence above 5 kHz corresponds to turbulent eddies actually transporting fluid normal to the surface. In addition, an increase in phase lag along the pressure side may be explained by the influences of secondary streamwise vortices formed near the

surface. The presence of this secondary vorticity is also seen in the “post-peak” correlation level in the G2 near-wall cross-correlations at PS2. It appears that the combination of the primary downrush of momentum from the free-stream combined with these secondary vortices work to significantly raise mean heat transfer for G2 above G4, indicating a greater effectiveness for heat transfer for the smaller scales of G2.

7.4 Pressure side q' increase and the significance of q'

The growth in fluctuating heat flux along the PS does not correspond directly to a growth in the mean heat transfer. The source of this is possibly due to unsteady transition activity, in which case the observed q' could be due to unsteady pulsating transition or even unsteady re-laminarization given the strong acceleration at PS3. It is clear from the coherence measurements (section 6.3) that the low frequency unsteadiness in $Eq(f)$ is not due to turbulent eddies; the velocity spectra show this energy dying out (section 6.1) even as it grows in the heat flux spectra. This evidence implies that the observed low frequency heat flux energy is confined to the boundary layer. This unsteadiness cannot be seen as laminar u' fluctuations due to the thinness of the boundary layer (< 0.1 mm), leaving transitional activity (turbulent spots) as the only probable source.

Representative time series of the measured heat flux at PS3 for the three grid cases is given in Fig. 7.7 (normalized on G0 mean). The grid to grid difference in low-frequency unsteadiness is clear, while the higher frequency turbulence that would be associated with turbulent activity ($f > 3$ kHz) is nearly the same for the three traces. Notice the character of the low frequency energy in G0 where a sharp rise is followed by a slow decay. This seems to agree with the idea of a passing zone of turbulent energy followed by a resting period where the boundary layer returns to laminar. G2 seems to stay at the higher turbulent level. The G4 low-frequency energy appears different than that seen in G0, evidently due to the interaction of transitional regions with the turbulence in the free-stream.

It is possible that the large eddies impacting near the leading edge are doing significant work on the boundary layer, or perhaps due to their presence changing the instantaneous pressure gradient enough to disrupt the boundary layer or cause unsteady boundary layer transition or separation that is then convected down the pressure side. This agrees with the lack of coherence seen at corresponding low frequencies downstream of the leading edge. If G2 is not transitional, then the lower observed q' for G2 is due solely to FST effects. The transitioning G0 and G4 boundary layers would see an increasing effect due to the growth of these convected disturbances. It may be that there is also a stronger interaction of the small intense streamwise vortices with the turbulent boundary layer relative to a laminar boundary layer.

The most significant conclusion of this phenomena is that fluctuating heat transfer energy, in terms of an rms quantity, does not necessarily relate to mean heat transfer. The transition process, while itself raising the mean heat transfer, occurs through a process that is characterized by low-frequency unsteadiness. Conversely, if the measured heat flux fluctuations do not relate directly to turbulent flow fluctuations, then the mean heat transfer will not relate directly either. The import of these thoughts is that q' is giving us information about the state of the boundary layer (as noted by others making high-frequency measurements, e.g. Moss and Oldfield, 1994). In addition, for a post-transition boundary layer, fluctuating heat transfer should correspond very closely to the level of fluctuation in the flow such that $q' \propto u'$, and then since $u' \propto h$ (e.g. Maciejewski and Anderson, 1996), q' will correlate directly with mean heat transfer.

Plots of q' ($q'_{\text{norm}} = q' / (T_{\text{aw}} - T_s)$) in relation to u' and the heat transfer coefficient are shown in Figs 7.8 and 7.9, where q'_{norm} is the value discussed in section 5.1.2 and shown in Table 5.1 (although the value of q'_{norm} used here is an average value for the different no-PHW runs while the values in Table 5.1 are run-specific). For reference, u' vs. h was given earlier in Fig. 7.2. From the q' vs. h plot, it is clear that no correlation exists, although the slope indicated for the DS1 data (laminar) seems to shift to a zero correlation flat line for the transitional PS3 data points. This agrees with the analyses presented so far. If q' is driven by boundary layer fluctuations of u' (say beneath a laminar or turbulent boundary layer), then since h scales on the same (i.e. assuming Maciejewski's u'_{max} relationship), q' should also scale on h as seen for DS1. If the boundary layer is transitional and q' is driven not by turbulent eddies but instead by low-frequency energy due to passing turbulent spots, then q' does not relate to u' or to h .

7.5 Length scale effects in the present data

There are some length scale effects evident in the present data. The mean heat transfer data in Ch. 5 showed that the smaller length scale Grid 2 had the highest measured values of heat transfer coefficient at all measurement locations, in agreement with laminar stability calculations for the blade (section 5.1.3). The spectral data has also shown what can be termed "length scale effects."

First, vortices shed from the leading edge appear to form at a preferred 5 kHz frequency, independent of grid, as evidenced by the heat flux spectra at DS1 and PS1. However, the presence of this activity is much stronger for G4, and at DS1 the intensity of G4 is lower than for G2. This seems to indicate that the larger scales present in G4 are preferentially formed into these 5 kHz passing structures seen at DS1.

Secondly, the boundary layer on the pressure side seems to be significantly disturbed leading to unsteady transition by the presence of large eddies near the leading edge. The

correlation of these large eddies with low-frequency fluctuations in the boundary layer at PS1, but not later on the pressure side seems to indicate that the large fluctuations in the heat transfer at PS3 are due to the work of these large eddies near the leading edge. This theory agrees with the lower q' seen at PS3 for G2 compared with the smaller scale of the G2 inlet turbulence. The interpretation is not clear, however, due to the unknown influence of the shifted G2 pressure gradient.

Thirdly, the coherence data shows the growth of higher frequency coherent structures which develop along the pressure surface in the curved accelerating boundary layer. This preference for certain frequencies can be seen as a length scale effect. The fact that much of the G4 energy spectrum is at lower frequencies that are quickly attenuated entering the passage shows that the smaller scales of G2 are more suited to doing work on the boundary layer. At PS3 only G2 shows coherence at 1.0 mm. The preference for frequency along the pressure side is not as narrow as that seen for the leading edge shed vortex, however. The average scale of G4 streamwise vortices along the pressure side is larger than for G2 based on coherence measurements at 1.0 mm at PS2 indicating larger motions corresponding to larger scale inlet turbulence.

Finally, and in conclusion, the preference for certain frequencies evidenced at different points on the blade shows clearly the weakness of the concept of inlet turbulence length scale. Can one number, not even capable of accurately defining anisotropy of the inlet flow, predict how the turbulence will react with the boundary layer through the passage? Nonetheless, the assumption of isotropy at the inlet can lead us to correlate a length scale with heat transfer based on preferred frequencies at different parts of the blade. The resulting correlations remain useful only at certain regions of the blade, just as the existing correlations reviewed earlier, and we cannot expect a way to simply tie together this complex flow-field.

7.6 The significance of coherence

Coherence gives time correlation with an added dimension. Instead of seeing simply an integrated time shift of a cross-correlation, coherence shows what frequency of energy is contributing to the observed correlation. This information is supported by the phase which gives time shift as a function of frequency. As seen in section 7.3, coherence provides a useful tool for interpreting the flow/ surface interactions leading to a clearer picture of flow dynamics responsible for heat transfer.

Does coherence equal mean heat transfer? If coherence is measured, is that indicative of a higher heat transfer coefficient? The relationship of coherence to h is similar to the relationship of Tu to h -- in general an increase in Tu or coherence will lead to increased heat transfer. Coherence between two probes means that some fluid motion of a scale larger than the

separation of the probes is correlating in time. In the present case, coherence means that some motion at the hot-wire is correlating with a fluctuation in heat flux indicating fluid motion of a scale larger than y_{wire} . Now, if the observed correlation is due to a structure that effectively transports fluid normal to the surface, or effectively brings up boundary layer fluid, then the measured coherence implies heat transfer at the frequency of that structure.

So coherence equals mean heat transfer only to the degree that the structure causing coherence also causes heat transfer. Generally, for coherence due to a turbulent structure, thermal energy is being transported away from the wall to some degree that should be proportional to the coherence. However, two things are clear: there could be coherence due entirely to mean flow unsteadiness so that no increase in heat transfer is seen despite good coherence. Alternatively, small scale ($<y_{wire}$) near-surface turbulence could be raising local heat transfer, but not be seen in the coherence due to the large separation distance. And, all of these issues are complicated by the resolution limits of the probes.

Similarly, Tu (i.e. free-stream u') correlates with surface activity only to the degree that the measured velocity fluctuations are tied to structures that are effectively transferring heat. However, coherence is much more useful in that we can see spatial correlation, and we can see it as a function of frequency.

7.7 Practical application to turbine design

Measuring surface fluctuating heat transfer is by itself useful. This is not a new concept, however, as many have used thin films to watch transition (e.g. Moss and Oldfield, 1994). In addition to simply watching turbulent spots pass by and calculating intermittency, this work shows the work of scales at different frequencies giving evidence of turbulence activity in the free-stream. Fluctuating heat transfer based on this higher frequency activity is useful for determining mean heat transfer apart from transition activity.

There are some useful applications resulting from this work. The observed phenomena of strong vortices apparently shed from the leading edge and driving coherence near the leading edge has implications for design. These vortices seem to exist in a narrow frequency band, indicating that they may be controlled by some means. This strong streamwise vorticity and that believed to be responsible for cross-stream transport on the pressure side has implications for film cooling as streamwise vorticity easily overturns the fluid and removes the protective film. In the strong unsteadiness of the engine, the film cooling air can become a jet detached from the surface. At this point the mechanism of streamwise vorticity erases its effectiveness.

Finally, the observed influence of large scale eddies near the leading edge on downstream boundary layer activity is significant. Many have looked at the effect of wake passing on unsteady boundary layer transition (e.g. Mayle and Schulz, 1996). However, the effect of large

eddy disruption may need serious consideration. If these large eddies are causing local pressure gradient fluctuations that induce unsteady boundary layer transition, then perhaps the pressure side profile should be designed with less of an adverse pressure gradient. The effect of the G2 pressure distribution shift (due to flow angle of attack) leads to similar conclusions where an angle of attack, as may be induced by a passing wake, has apparently led to early transition.

7.8 Conclusions and recommendations

This work makes a contribution both in the nature of the measured data, and in the analysis of that data. Data taken on and above the surface of an engine scaled turbine blade has been analyzed in the frequency domain and has provided some mean and fluctuating heat flux data points with simultaneous velocity information. These data have been used to examine recent correlations of mean heat transfer in relation to flow variables. The frequency domain data has been used to develop an interpretation of the flow mechanisms at work around the blade, and the value of frequency domain analysis has been discussed. The value of the fluctuating and integral parameters has been discussed, along with the issues of pressure side heat transfer, measurement of the integral scales, spatial averaging, and probe disturbance.

What we have learned:

- 1) *Mean heat transfer was higher for the grid of smaller inlet length scale.* This higher heat transfer was seen at all measurement locations despite lower pressure side intensity, T_u , and lower measured coherence as compared to the larger scale grid. This indicates the strong influence of small scale turbulence not easily seen by the present large sensors.
- 2) *Existing correlations for mean heat flux show some success.* The correlation of Van Fossen and Simoneau (1995) for laminar stagnation point heat transfer beneath a turbulent free-stream correctly predicted the heat transfer at the first pressure side location and showed the best correlation for the suction side data. The generally poor performance of these correlations along the pressure side is likely due to the transitional state of the boundary layer and high uncertainties of boundary layer parameters (δ , u'_{max}).
- 3) *Higher coherence was measured on the pressure side than on the suction side* indicating larger scale structures interacting with the pressure side surface. Not only levels of coherence but the regions of the frequency spectrum where coherence was highest was seen to vary with location on the blade. The higher coherence seen near the leading edge on the pressure side is strongest at low frequencies and apparently broadband, while coherence near the leading edge on the suction side (DS1) is at a

preferred frequency range tied to coherent structures passing by at frequencies between 3 and 6 kHz. Strong low frequency energy is seen in the heat flux and velocity spectra at DS1 but without corresponding coherence.

- 4) Coherence measurements show *the growth and propagation of high-frequency energy along the pressure side*. This energy is associated with coherent structures of a scale less than one millimeter for the smaller grid turbulence and greater for the larger grid, scaling on measured length scales (Λ_x) in the passage. Low frequency energy (larger eddies) decays in the passage while higher frequency energy does not decay and coherence actually grows corresponding to the growth of structures at these higher frequencies.
- 5) *The value of q' in predicting h is limited*, based on the present data. In general, q' and u' showed some correlation with heat transfer coefficient, h , for the suction side laminar region, but not for the pressure side measurements. Along the pressure side, no such correlation is seen. Instead, u' decreases along the pressure side while low frequency transitional activity causes q' to increase for all inlet conditions. Therefore, q' gives boundary layer information and may correlate with u' and mean heat transfer in specific regions of the blade (e.g. stagnation region, forward laminar pressure side). However, the behavior of the fluctuating heat transfer in a transitional boundary layer is characterized by low-frequency energy which does not correlate with u' or h .
- 6) *The value of u' and Λ_x (integral length scale) for predicting h on a turbine blade is limited*, but most useful for the nearly isotropic inlet turbulence in that truly isotropic turbulence can be characterized completely by intensity and scale. In the flow passage, non-isotropic flow structures dominate as seen in the coherence that is strong in limited regions of the frequency spectrum.
- 7) *Coherence did not correlate with mean heat transfer in the present data*. Instead, coherence is one more tool for relating flow energy to surface heat transfer. Mean heat transfer correlates with coherence at a certain frequency to the degree that this coherence is caused by a turbulent structure of efficient scale and sufficient energy.
- 8) *Coherence is a useful tool* for gauging flow scales and discriminating the source of frequency content present in heat flux and velocity. By moving the hot-wire relative to the heat flux sensor, the size of turbulent structures can be found. If no coherence is measured, this means that no free-stream unsteadiness is present and no turbulent flow structures of a scale larger than the wire distance above the surface are influencing heat transfer. This provides a means for discriminating low-frequency transitional boundary layer activity and small-scale low-frequency passing coherent

structures from large-scale mean flow unsteadiness. Comparison of coherence at different distances allows identifying the scales of structures at specific frequencies. The distance at which coherence is maximum gives insight into the flow mechanism where a single wire hot-wire is sensitive to flow velocity in certain directions only. The phase component of coherence can be used to find differences in time lag across the boundary layer of structures at specific frequencies relative to structures at other frequencies, and is seen to correlate with free-stream acceleration.

- 9) *Frequency domain analysis gives evidence useful for interpreting what structures are at work in moving heat flux away from the wall.* The higher frequency energy seen active on the pressure side is believed to be streamwise vorticity induced by the concave curvature and intensified in the accelerating flow. The suction side data shows the influence of streamwise vortices coming from the leading edge and acting on the near leading edge region. The leading edge pressure side shows the influence of large low-frequency energy which may be influencing transition along the pressure side.

What was not learned:

- 1) Length scale influence on heat transfer in terms of the effectiveness of specific kinds of structures acting at specific frequencies. However, coherent structures in limited frequency ranges with measured scale were seen acting in different regions of the blade. Their effect on mean heat transfer is not clear.
- 2) Any kind of general relationship for q' or free-stream u' relative to h . There is hope that with more data points the value of q' can be better understood.

Recommendations:

Additional data with fluctuating heat transfer in specific regions of flow (e.g. in the laminar region on the pressure side) would be helpful in determining useful relationships between q' and mean heat transfer, and between q' and flow fluctuations (through the boundary layer into the free-stream). A smaller heat flux sensor with better spatial resolution would allow more accurate measurements of q' and of the higher end of the heat flux energy spectrum.

Studies of specific structures to see interactions of the boundary layer with these structures and boundary layer sensitivity to specific frequencies. This would require a heat flux sensor able to resolve boundary layer details.

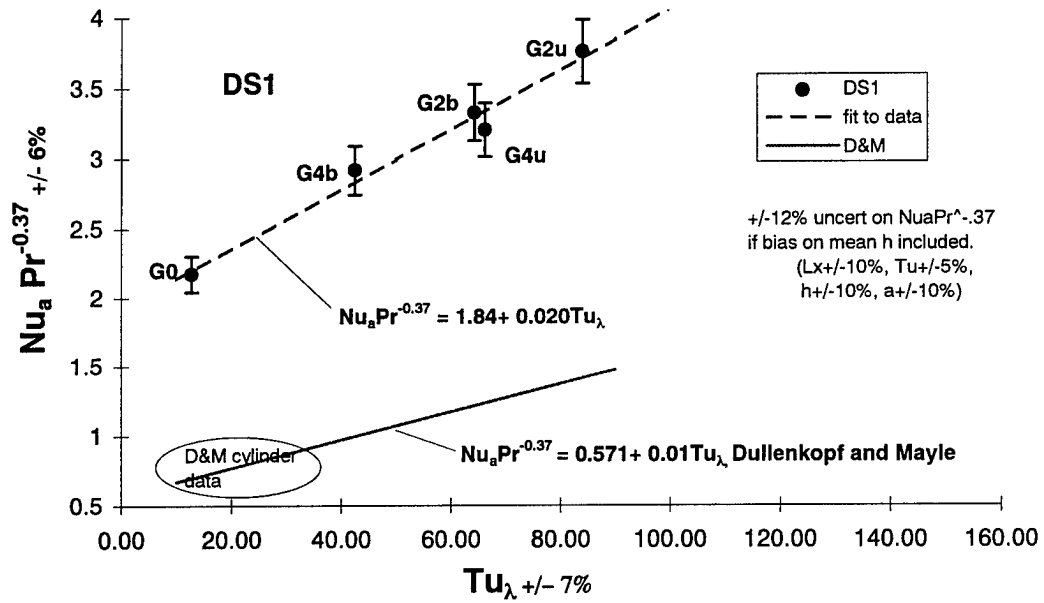


Figure 7.1 Dullenkopf and Mayle's correlation based on strain and length scale effective turbulence intensity.

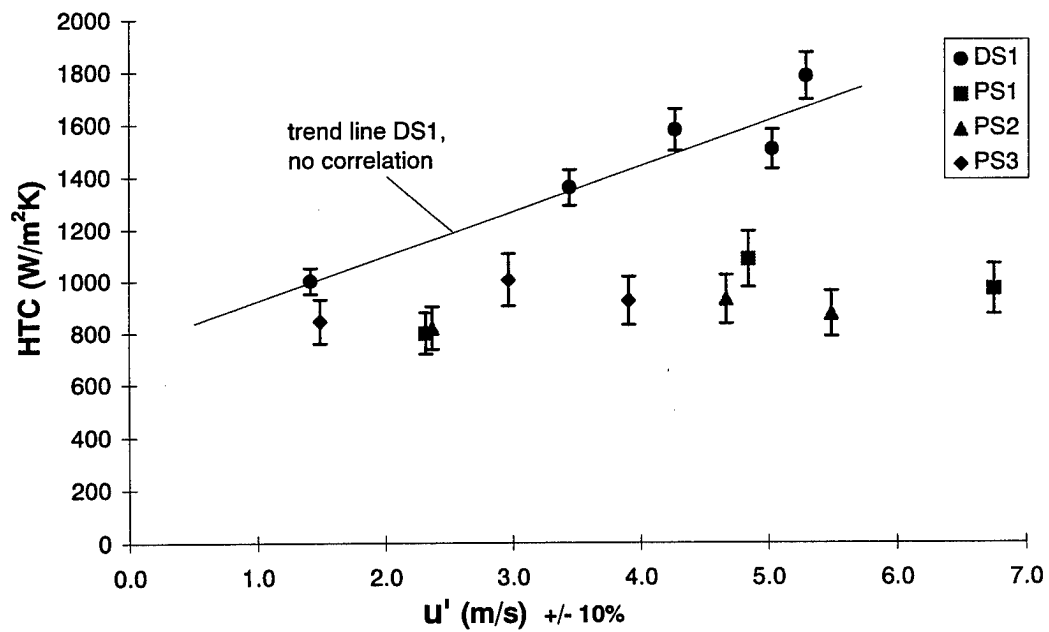


Figure 7.2 Heat transfer coefficient vs. u' .

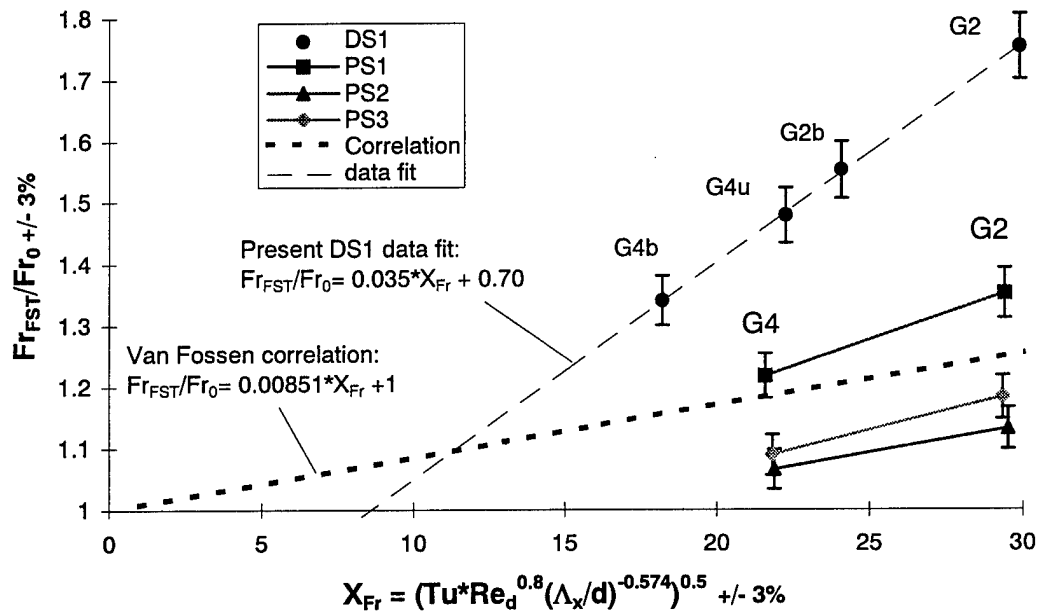


Figure 7.3 Van Fossen's heat transfer augmentation for FST above a low-FST baseline for laminar region downstream of the stagnation point.

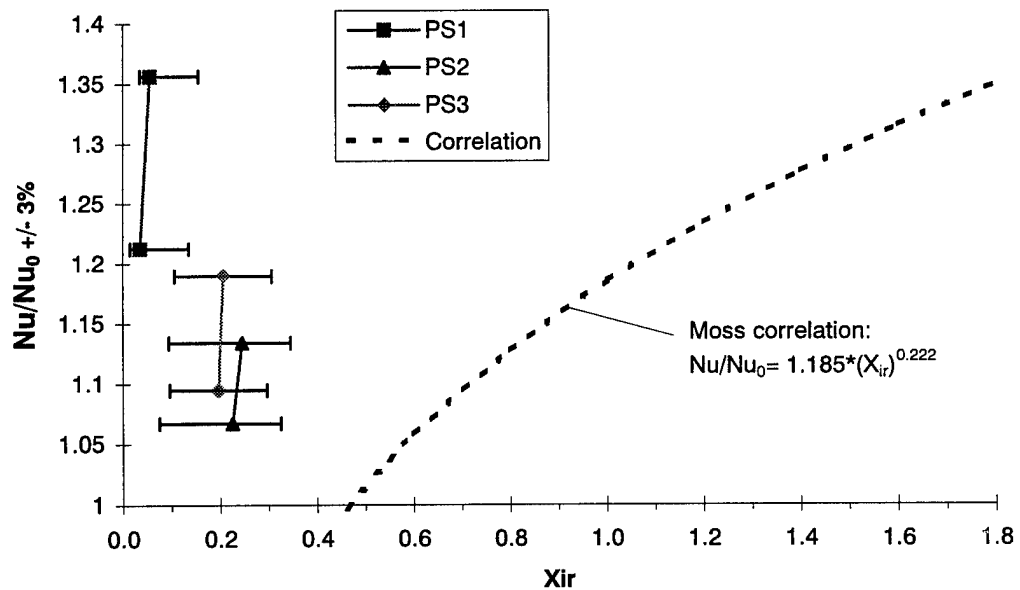


Figure 7.4 Moss and Oldfield's turbulent boundary layer heat transfer augmentation for FST above a low FST baseline against their X_{ir} parameter.

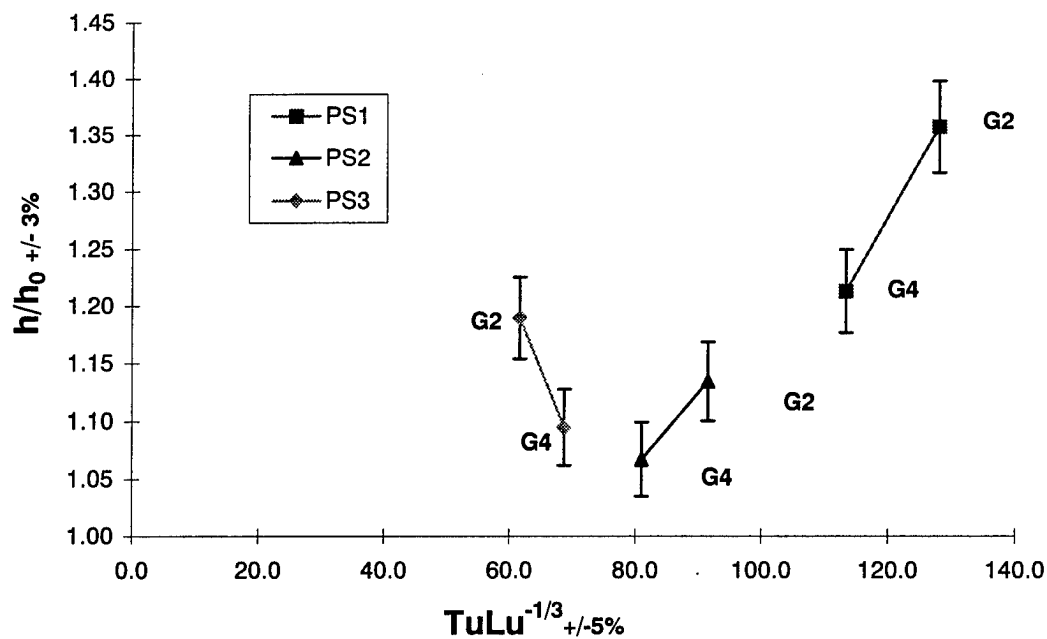


Figure 7.5 Ames' correlation of mean heat transfer increase and $TuLu^{-1/3}$.

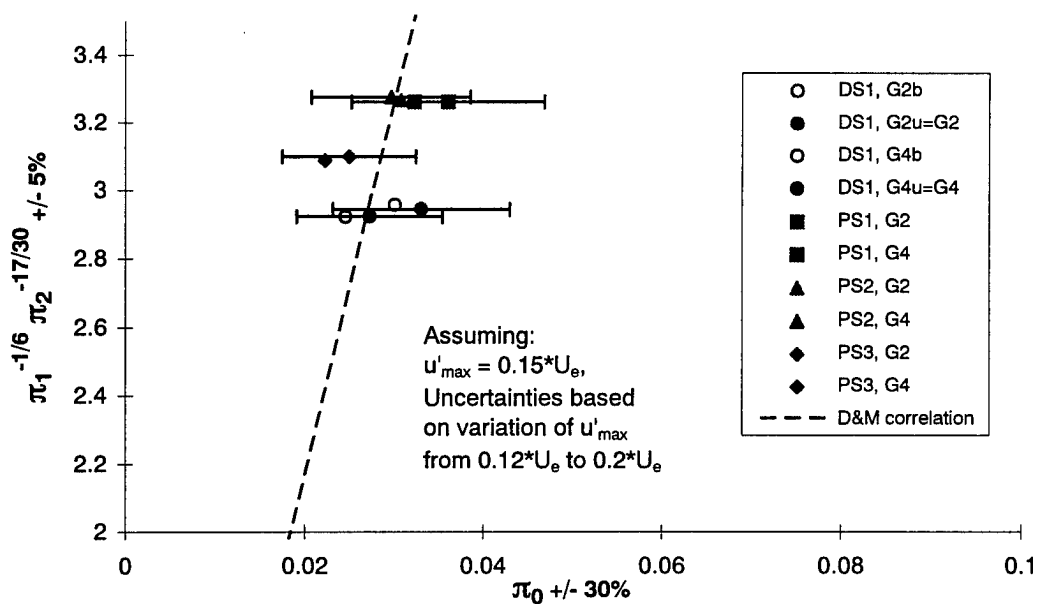


Figure 7.6 Maciejewski and Anderson's general turbulent heat transfer correlation.

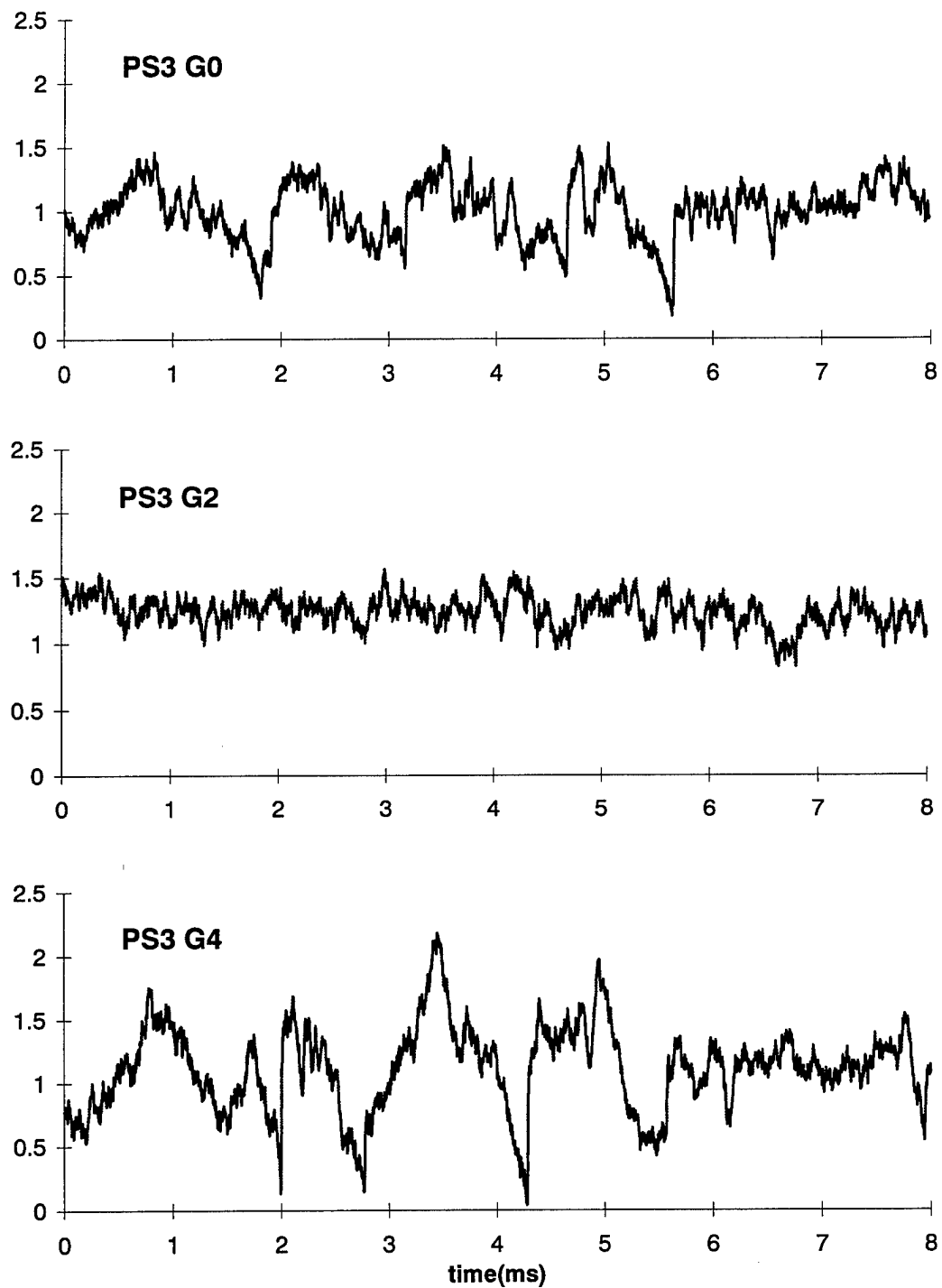


Figure 7.7 Comparison of PS3 heat flux time series, G0, G2, G4.

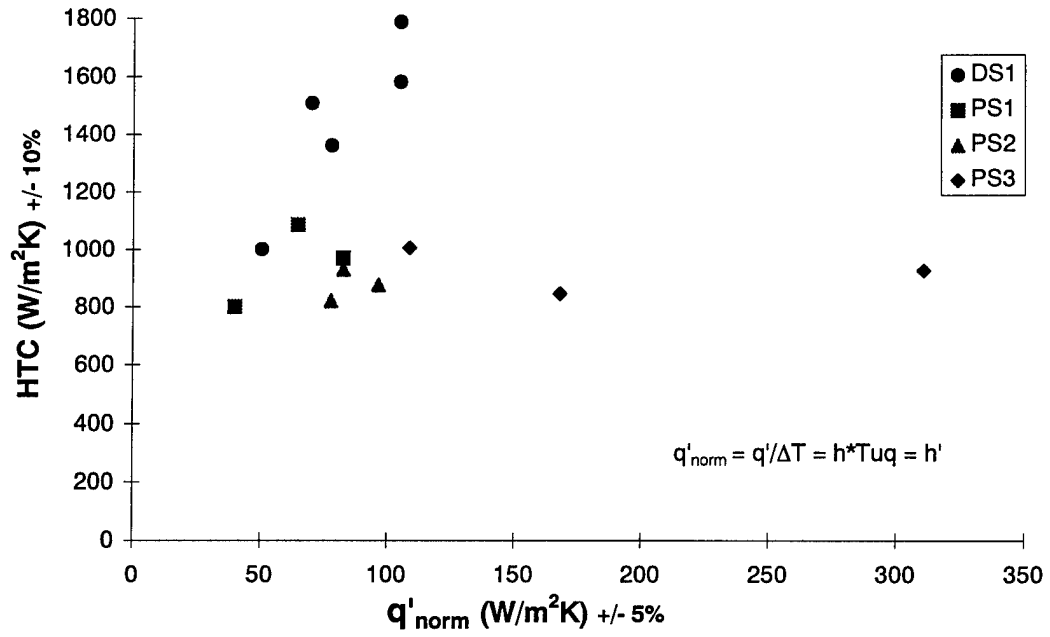


Figure 7.8 Heat transfer coefficient vs. q' .

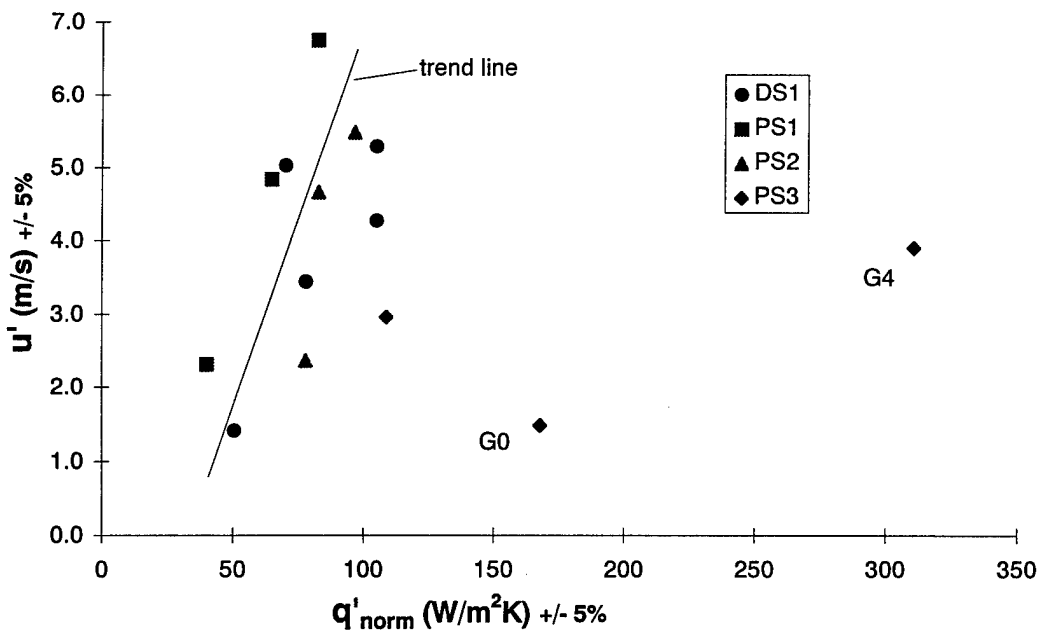


Figure 7.9 u' vs. q' .

References

- Abhari, R.S., Guenette, G.R., Epstein, A.H., Giles, M.B., 1992, "Comparison of Time-Resolved Turbine Rotor Blade Heat Transfer Measurements and Numerical Calculations," ASME J. Turbomachinery, Vol.114, p.818.
- Abu-Ghannam, B.J., Shaw, R., 1980, "Natural Transition of Boundary Layers --The Effects of Turbulence, Pressure Gradient, and Flow History," J. Mech. Engr. Sci., Vol. 22, No. 5.
- Ames, F.E., and Moffat, R.J., 1990, "Heat Transfer with High Intensity, Large Scale Turbulence: The Flat Plate Turbulent Boundary Layer and the Cylindrical Stagnation Point," Report No. HMT-44, Thermosciences Division of Mechanical Engineering, Stanford University.
- Ames, F.E., 1994, "Experimental Study of Vane Heat Transfer and Aerodynamics at Elevated Levels of Turbulence," NASA CR-4633.
- Ames, F.E., Plesniak, M.W., 1995, "The Influence of Large Scale, High Intensity Turbulence on Vane Aerodynamic Losses, Wake Growth, and the Exit Turbulence Parameters," ASME Paper 95-GT-290.
- Arts, T., Lambert de Rouvroit, M., 1992, "Aero-Thermal Performance of a Two-Dimensional Highly Loaded Transonic Turbine Nozzle Guide Vane: A Test Case for Inviscid and Viscous Flow Computations," ASME J. Turbomachinery, Vol.114, p.147.
- Ashworth, D.A., LaGraff, J.E., Schultz, D.L., 1989, "Unsteady Interaction Effects on a Transitional Turbine Blade Boundary Layer," ASME J. Turbomachinery, Vol.111, p.162.
- Blair, M.F., 1983, "Influence of FST on the Zero Pressure Gradient Fully Turbulent Boundary Layer, Part I -- Experimental Data, and Part II -- Analysis of Results," J. Heat Transfer, Vol.105, p.33.
- Bradshaw, P., 1976, Turbulence, Vol. 12 of Topics in Applied Physics series, Springer-Verlag, NY.
- Brown, G.L., and Thomas, S.W., 1977, "Large Structure in a Turbulent Boundary Layer," The Physics of Fluids, Vol.20, No.10, ppS243-S252.
- Camp, T.R., Shin, H.W., 1995, "Turbulence Intensity and Length Scale Measurements in Multistage Compressors," ASME J. Turbomachinery, Vol.117, p.38.
- Carlson, A.B., Reynolds, W.C., 1991, "An Experimental Technique for Investigation of Instantaneous Wall Heat Flux to a Turbulent Boundary Layer in Water," Report TF-51, Thermosciences Div., ME Dept., Stanford.
- Castro, I.P., 1984, "Effects of Free-Stream Turbulence on Low Reynolds Number Boundary Layers," J. Fluids Engr., Vol.106, p.298.
- Ching, C.Y. and LaGraff, J.E., 1995, "Measurements of Turbulent Spot Convection Rates in a Transitional Boundary Layer," Experimental and Thermal Fluid Science, 11:52-60, Elsevier Science, Inc.
- Corcos, G.M., 1963, "Resolution of Pressure in Turbulence," J. of the Acoustical Society of America, V.35, No.2, pp192-199.

Corcos, G.M., 1967, "The Resolution of Turbulent Pressures at the Wall of a Boundary Layer," J. Sound and Vibration, V.6, No.1, pp59-70.

Derkson, R.W., Azad, R.S., 1983, "An Examination of Hot-Wire Length Corrections," Phys. Fluids 26 (7), p.1751.

Diller, T.E., 1993, "Advances in Heat Flux Measurements," Advances in Heat Transfer, Academic Press, Inc., Vol.23, p.279.

Doorly, J.E., Oldfield, M.L.G., 1986, "New Heat Transfer Gages for Use on Multilayered Substrates," ASME Journal Turbomachinery, Vol. 108, p.153-160.

Doorly, J.E., Oldfield, M.L.G., 1987, "The Theory of Advanced Multi-layer Thin Film Heat Transfer Gauges," Intl. J. Heat Mass Transfer, Vol. 30, p.1159-1168.

Dring, R.P., Blair, M.F., Joslyn, H.D., Power, G.D., Verdon, J.M., 1988, "The Effects of Inlet Turbulence and Rotor/Stator Interactions on the Aerodynamics and Heat Transfer of a Large-Scale Rotating Turbine Model I--Final Report," UTRC, NASA CR-4079, Microfiche N89-13756.

Dullenkopf, K., Mayle, R.E., 1994a, "The Effects of Incident Turbulence and Moving Wakes on Laminar Heat Transfer in Gas Turbines," ASME J. Turbomachinery, Vol.116, p.23.

Dullenkopf, K., Mayle, R.E., 1994b, "An Account of Free-Stream Turbulence Length Scale on Laminar Heat Transfer," ASME Paper 94-GT-174.

Dunn, M.G., Martin, H.L., Stanek, M.J., 1986, "Heat Flux and Pressure Measurements and Comparison with Prediction for a Low-Aspect-Ratio Turbine Stage," ASME J. Turbomachinery, Vol.108, p.108.

Dunn, M.G., Seymour, P.J., Woodward, S.H., George, W.K., Chupp, R.E., 1989, "Phase-Resolved Heat-Flux Measurements on the Blade of a Full-Scale Rotating Turbine," ASME J. Turbomachinery, Vol.111, p.8.

Freymuth, P., and Fingerson, L.M., 1980, IFA Intelligent Flow Analyzer Instruction Manual, Apdx 1, "Electronic Testing of Frequency Response For Thermal Anemometers," TSI Inc.

Garside, T., Moss, R.W., Ainsworth, R.W., Dancer, S.N., Rose, M.G., 1994, "Heat Transfer to Rotating Turbine Blades in a Flow Undisturbed by Wakes," IGTI Aeroengine Congress and Expo, The Hague, Netherlands, ASME 94-GT-94.

Greenblatt, D., 1994, "The Effect of Wake-Passing and FST on Laminar Gas Turbine Blade Boundary Layers," ASME J. Turbomachinery, Vol.116, p.384.

Guenette, G.R., Epstein, A.H., Giles, M.B., Haimes, R., Norton, R.J.G., 1989, "Fully Scaled Transonic Turbine Rotor Heat Transfer Measurements," ASME J. Turbomachinery, Vol.111, p.1.

Hager, J.M., Simmons, S., Smith, D., Onishi, S., Langley, L.W., Diller, T.E., 1991, "Experimental Performance of a Heat Flux Microsensor," JEGTP, Vol.113, p.246.

Hancock, P.E. and Bradshaw, P., 1983, "The Effect of FST on TBL," J. Fluids Engr., Vol.105, p.284.

Hancock, P.E. and Bradshaw, P., 1989, "Turbulence Structure of a Boundary Layer Beneath a Turbulent Free-Stream," J. Fluid Mech., Vol.205, p.45.

Hinze, J., 1975, Turbulence, 2nd Ed., McGraw-Hill, New York.

Holder, D.W., North, R.J., and Wood, G.P., 1956, "Optical Methods for Examining the Flow in High-Speed Wind Tunnels", Part I, "Schlieren Methods", NATO Advisory Group for Aeronautical Research, November.

Hollingsworth, D.K., Moffat, R.J., Kays, W.M., 1992, "The Effect of Concave Surface Curvature on the Turbulent Prandtl Number and the Thermal Law of the Wall," Exp. Thermal and Fluid Sci., Vol.5, p.299-306.

Iyer, V., 1995, "Computer Program BL2D for Solving Two-Dimensional and Axisymmetric Boundary Layers," NASA CR-4668, maintained at NASA Langley RC, Hampton, VA.

Johnson, L.P., and Diller, T.E., 1995, "Measurements with a Heat Flux Microsensor Deposited on a Transonic Turbine Blade," 16th Intl. Congress on Instrumentation in Aerospace Simulation Facilities, June 18-21, Wright-Patterson AFB.

Johnson, L.P., 1995, "Effects of Freestream Turbulence on Turbine Blade Heat Transfer in Transonic Flow", masters thesis, Virginia Tech Dept. Mech. Engr.

Keller, F.J., Wang, T., 1994, "Flow and Heat Transfer Behavior in Transitional Boundary Layers with Streamwise Acceleration," ASME Paper 94-GT-24.

Kestoras, M.D., Simon, T.W., 1994, "Turbulence Measurements in a Heated, Concave Boundary Layer Under High Free-Stream Turbulence Conditions," ASME Paper 94-GT-37.

Kim, J., Simon, T.W., Russ, S.G., 1992, "Free-Stream Turbulence and Concave Curvature Effects on Heated Transitional Boundary Layers," ASME J. Heat Transfer, Vol.114, p.339.

Lewis, D.J., Simpson, R.L., 1996, "An Experimental Investigation of Heat Transfer in Three-dimensional and Separating Turbulent Boundary Layers," VPI&SU Dept. of Aerospace and Ocean Engr. dissertation, April.

Lighthill, M.J., 1954, "The Response of Laminar Skin Friction and Heat Transfer to Fluctuations in the Stream Velocity," Proc. Roy. Soc., Vol. A224, pp 1-23.

Maciejewski, P.K., and Moffat, R.J., 1992, "Heat Transfer with Very High Free-Stream Turbulence: Part I -- Experimental Data, and Part II -- Analysis of Results," ASME J. Heat Transfer, Vol.114, p.827.

Maciejewski, P.K., 1995, "Limitations to the Employment of Conventional Boundary Layer Parameters and Predictive Models to Heat Transfer in Complex Turbulent Flows," HTD Vol. 318, Heat Transfer in Turbulent Flows, ASME, p.37.

Maciejewski, P.K., and Anderson, A.M., 1996, "Elements of a General Correlation for Turbulent Heat Transfer," ASME J. Heat Transfer, Vol.118, p.287.

Magari, P.J., LaGraff, L.E., 1994, "Wake-Induced Unsteady Stagnation-Region Heat Transfer Measurements," ASME J. Turbomachinery, Vol.116, p.29.

Malik, M.R., 1990, J. Computational Physics, 86:376.

Mayle, R.E., 1991, "The Role of Laminar - Turbulent Transition in Gas Turbine Engines," ASME J. Turbomachinery, Vol.113, p.509.

Mayle, R.E., Schulz, A., 1996, "The Path to Predicting Bypass Transition," ASME paper, 96-GT-199.

Moore, J., and Moore, J.G., 1994, "Osborne Reynolds: Energy Methods in Transition and Loss Production: A Centennial Perspective," ASME Paper 94-GT-225.

Moss, R.W., and Oldfield, M.L.G., 1991, "Measurements of Hot Cumbustor Turbulence Spectra," ASME Paper 91-GT-351.

Moss, R.W., and Oldfield, M.L.G., 1992, "Measurements of the Effect of Free-Stream Turbulence Length Scale on Heat Transfer," ASME Paper 92-GT-244.

Moss, R.W., and Oldfield, M.L.G., 1996, "Effect of Free-Stream Turbulence on Flat-Plate Heat Flux Signals: Spectra & Eddy Transport Velocities," ASME J. Turbomachinery, Vol.118, pp.461-467.

Rigby, D.L., Van Fossen, G.J., 1991, "Increased Heat Transfer to a Cylindrical Leading Edge Due to Spanwise Variations in the Freestream Velocity," AIAA-91-1739.

Rivir, R.B., Troha, W.T., Eckerle, W.A., Schmoll, W.J., 1992, "Heat Transfer in High Turbulence Flows - A 2D Planar Wall Jet," AGARD 80th PEP Symposium on Heat Transfer and Cooling in Gas Turbines, Antalya, Turkey, October 12-16, 1992.

Roach, P.E., 1987, "The Generation of Nearly Isotropic Turbulence by Means of Grids," Int. J. Heat and Fluid Flow, Vol.8, No.2, p.82.

Rued, K., Wittig, S., 1986, "Laminar and Transitional Boundary Layer Structures in Accelerating Flow With Heat Transfer," ASME J. Turbomachinery, Vol.108, p.116.

Schetz, J.A, 1993, Boundary Layer Analysis, Prentice Hall.

Schlichting, H., 1968, Boundary-Layer Theory, McGraw-Hill Book Co., New York.

Simoneau, R.J., Simon, F.F., 1993, "Progress Towards Understanding and Predicting Heat Transfer in the Turbine Gas Path," Int. J. Heat and Fluid Flow.

Smol'yakov, A.V., and Tkachenko, V.M., 1983, The Measurement of Turbulent Fluctuations, subtitled, "An introduction to Hot-Wire Anemometry and Related Transducers," Springer-Verlag, New York.

Stearns, S.D., and Hush, D.R., 1990, Digital Signal Analysis, 2nd ed., Prentice Hall, Englewood Cliffs, NJ.

Thole, K.A., Whan-Tong, J., Bogard, D.G., 1991, "Generation of High Freestream Turbulence Levels and the Effects on Heat Transfer," 8th Symposium on Turbulent Shear Flows, Tech. Univ. Munich, Germany, September 9-11.

Townsend, A.A., 1976, The Structure of Turbulent Shear Flow, 2nd ed., Cambridge Univ. Press, New York.

Van Fossen, Jr., G.J., Simoneau, R.J., 1987, "A Study of the Relationship Between Free-Stream Turbulence and Stagnation Region Heat Transfer," JHT, Vol.109, p.10.

Van Fossen, G.J., and Ching, C.Y., 1994, "Measurements of the Influence of Integral Length Scale on Stagnation Region Heat Transfer," Fifth Intl. Sym. on Transport Phenomena and Dynamics of Rotating Machinery (ISROMAC-5), Kaanapali, Maui, Hawaii, Paper No. TP-16, and NASA Technical Memorandum 106503.

Van Fossen, Jr., G.J., Simoneau, R.J., 1994, "Stagnation Region Heat Transfer: The Influence of Turbulence Parameters, Reynolds Number and Body Shape," Sixth AIAA/ASME Thermophysics Conference, CO Springs, June 20-23, 1994, and NASA Tech Memorandum 106504.

Walraevens, R.E., Gallus, H.E., 1995, "Stator-Rotor-Stator Interaction in an Axial Flow Turbine and Its Influence on Loss Mechanisms," AGARD 85th Propulsion and Energetics Symposium on Loss Mechanisms and Unsteady Flows in Turbomachines, Derby, England.

Wesner, A., 1996, "A single-plate Interferometric Study of the Unsteady Density Field in a Transonic Cascade," Dissertation, Dept. AOE, Virginia Polytechnical Institute and State University.

Wittig, S., Dullenkopf, K., Schulz, A., Hestermann., 1988, "Laser-Doppler Studies of the Wake-Effected Flow Field in a Turbine Cascade," ASME Paper 88-GT-160.

Wittig, S., Schulz, A., Dullenkopf, K., Fairbank, J., 1988, "Effects of Free-Stream Turbulence and Wake Characteristics on the Heat Transfer Along a Cooled Gas Turbine Blade," ASME Paper 88-GT-179.

Wyngaard, J.C., 1968, "Measurement of small-scale turbulence structure with hot wires," J. Scientific Instruments (J. of Physics E.), Series 2, Vol.1.

Zerkle, R.D., and Lounsbury, R.J., 1988, "Freestream Turbulence Effect on Turbine Airfoil Heat Transfer," JP, Vol.5, p.82.

Zhou, D., Wang, T., 1993, "Combined Effects of Elevated FST and Streamwise Acceleration on Flow and Thermal Structures in Transitional Boundary Layers," HTD, Vol.242, Gas Turbine Heat Transfer, ASME, p.41.

Appendix A

Author's published research

A-1 Holmberg and Pestian, 1996

Wall-Jet Turbulent Boundary Layer Heat Flux, Velocity, and Temperature
Spectra and Time Scales

Holmberg, D.G.
Pestian, D.J.

ASME Paper 96-GT-529

A-2 Holmberg and Diller, 1995

High-Frequency Heat Flux Sensor Calibration and Modeling

Holmberg, D.G.
Diller, T.E.

Journal of Fluids Engineering

Vol.117, pp. 659-664



THE AMERICAN SOCIETY OF MECHANICAL ENGINEERS
345 E. 47th St., New York, N.Y. 10017

96-GT-529

The Society shall not be responsible for statements or opinions advanced in papers or discussion at meetings of the Society or of its Divisions or Sections, or printed in its publications. Discussion is printed only if the paper is published in an ASME Journal. Authorization to photocopy material for internal or personal use under circumstance not falling within the fair use provisions of the Copyright Act is granted by ASME to libraries and other users registered with the Copyright Clearance Center (CCC) Transactional Reporting Service provided that the base fee of \$0.30 per page is paid directly to the CCC, 27 Congress Street, Salem MA 01970. Requests for special permission or bulk reproduction should be addressed to the ASME Technical Publishing Department.

Copyright © 1996 by ASME

All Rights Reserved

Printed in U.S.A.

WALL-JET TURBULENT BOUNDARY LAYER HEAT FLUX, VELOCITY, AND TEMPERATURE SPECTRA AND TIME SCALES

David G. Holmberg
Department of Mechanical Engineering
VA Tech, Blacksburg, VA

David J. Pestian
Aerospace Mechanics Division
UDRI, Dayton, OH

ABSTRACT

The interactions of boundary layer flow temperature fluctuations (t') and velocity fluctuations (u' , v') together with surface heat flux fluctuations (q') have been investigated experimentally in a flat plate turbulent boundary layer in order to better understand time-resolved interactions between flow unsteadiness and surface heat flux. A Heat Flux Microsensor (HFM) was placed on a heated flat plate beneath a turbulent wall jet, and a split-film boundary layer probe was traversed above it together with a cold-wire temperature probe. The recorded simultaneous time-resolved $u'v't'q'$ data can be correlated across the boundary layer. Results indicate that wall heat transfer (both mean and fluctuating components) is controlled by the u' fluctuating velocity field. In the presence of high free-stream turbulence (FST), the heat flux is largely controlled by free stream eddies of large size and energy reaching deep into the boundary layer, such that heat flux spectra can be determined from the free-stream velocity field. This is evidenced by uq coherence present across the boundary layer, as well as by similarity in heat flux and u velocity spectra, and by the presence of large velocity scales down to the nearest wall measuring location just above the laminar sublayer.

NOMENCLATURE

Nu/Nu_0	Ratio of experimental to theoretical Nusselt number, $Nu = hx/k$
Re_x	x Reynolds number, $U_{\infty}x/\nu$
Re_{Δ}	Enthalpy thickness Reynolds number.
Re_{θ}	Momentum thickness Reynolds number.
St/St_0	Ratio of experimental to theoretical Stanton number for low FST turbulent boundary layer, $St = h/\rho u c_p$.
Tu_q	Heat flux turbulence intensity, q'/q
Tu_u	U velocity turbulence intensity, u'/u
Tu_t	Temperature turbulence intensity, $t'/(t_{wall} - t_{max})$
q, q'	Surface heat flux, and fluctuating component. (W/cm^2)

t, t'	Temperature in boundary layer, and fluctuating component.
t^*	Near-wall dimensionless temperature $(t_{wall} - t)u_{\tau} \rho c_p / q$, where $u_{\tau} = (\tau_{wall}/\rho)^{1/2} = (c_f/2)^{1/2}$
t_m	Property reference temperature $= (t_{wall} + t_{max})/2$
u, u'	Streamwise velocity, and fluctuating component. (m/s)
u^+	Near-wall dimensionless velocity $(u/u_{max}) / (c_f/2)^{1/2}$
v, v'	Normal velocity, and fluctuating component. (m/s)
y^+	Near-wall dimensionless distance $(yu_{max}/\nu) / (c_f/2)^{1/2}$
δ_{995}	Boundary layer thickness.
Λ	Integral length scale. (mm)
τ	Integral time scale. (ms)
Δt	Temperature change across boundary layer, $t_{wall} - t_{max}$

subscript

max Property taken at wall-jet maximum velocity point

INTRODUCTION

In the continuing effort to better understand heat transfer to turbine blading, much work has been done in recent years to elucidate heat transfer mechanisms and develop correlations to account for the effects of wake passing (due to upstream blade rows), transition (from laminar to turbulent boundary layer), free-stream turbulence (outside the boundary layer), acceleration (of the flow in the narrowing blade passages), length scales (some measure of turbulent eddy size), Reynolds number, etc. The work has generally fallen into three areas: transition, wake effects, and freestream turbulence (FST). Heat transfer is known to be highly sensitive to transition, and the variables that control transition are under continued study. The line between the effects of wakes and of FST is hazy, because FST after the first blade row exists only within a wake or between wakes. Except for the inlet flow to the first blade row, FST is primarily composed of lower frequency unsteadiness at the blade passing frequency, and higher frequencies due to the turbulent energy

Presented at the International Gas Turbine and Aeroengine Congress & Exhibition
Birmingham, UK — June 10-13, 1996

contained within the wake. The interaction of transition, wakes, and FST is complicated. Thus, the study of FST effects on heat transfer often addresses the more isotropic flow with larger scales exiting the combustor, while the study of wake influence attempts to quantify turbulence within and between wakes and the influence of wakes on transition and boundary layer disruption of other forms. The work has included flat-plate studies (e.g. Zhou and Wang, 1993, Keller and Wang, 1994, Rivir et al., 1992, Kim et al., 1990), cylinder stagnation point studies at NASA (Van Fossen and Ching, 1994) and Stanford (Ames and Moffat, 1990), low speed turbine cascades (Ames, 1994), transonic turbine cascades (Arts, 1992, Wittig, 1988), and full rotating rigs at Oxford (Ashworth, 1989; Garside, 1994), at MIT (Guenette, 1989), and CALSPAN (Dunn, 1989).

Freestream turbulence need not be confined, as it often has been, to the domain of an isotropic flowfield, but can be viewed instantaneously as the turbulence present outside of the boundary layer. This is dominated by wake passing effects, but also includes other flow structures, secondary flows, and shock disturbance effects. Viewing FST as simply that turbulence present at the boundary layer edge, whatever its source, allows the effects of FST to be separated out. By setting aside the issue of the source of turbulence, then, the issue of FST effects on heat transfer can be viewed independently of the complicated flowfield within an engine, and examined in a controlled environment.

Several correlations have been developed that account for FST and Reynolds Number (Re) effects for relating actual heat transfer to a baseline theoretical flow. The TLR parameter (T =turbulence intensity, L =length scale, R = Re correction) of Ames and Moffat (1990) is a parameter applied to flat plate high turbulence data, and has been related to airfoil data by Ames (1994). Ames (1990) also presents a similar parameter for the stagnation region for cases of large Lu/D , where Lu is a dissipation based "energy scale." Thole (1991) gives further data in support of TLR, but uses an integral length scale (Λ_x) rather than Ames' Lu . Other correlations include that of Moss and Oldfield (1992) at Oxford who give a parameter similar to that originally proposed by Hancock and Bradshaw and modified by Blair for flat-plate heat transfer. These two correlations indicate heat transfer increasing with turbulence intensity (Tu) and with decreasing length scale, but with no minimum length scale for optimum heat transfer. Van Fossen and Ching (1994) at NASA give a correlation for stagnation heat transfer similar to Ames' with different exponents on the various terms, and claim that Ames' correlation was unsatisfactory. The sensitivity of these correlations to particular data sets indicates their limited nature.

In contrast to this, Maciejewski (1995) gives reason to dismiss correlations based on Re and St entirely. This line of thought will be shown to have merit with the present data. Dullenkopf and Mayle (1994) present a promising correlation of cylinder and airfoil data that describes a linear relation between laminar stagnation heat transfer and an effective turbulence parameter. Their analysis presents an optimum length scale, as well as an optimum frequency for exciting a laminar boundary layer. While this correlation is not directly applicable to the present data, it highlights the need to go beyond some integral or energy length scale and intensity and look at the energy spectrum of data in the frequency domain.

Presently, there is limited time-resolved heat transfer data. Direct heat transfer measurements have been made at MIT in a rotating rig (Guenette, 1989), and thin film gages have been used at CALSPAN (Dunn, 1989) and Oxford (Ashworth, 1989) in rotating rigs, and also at VKI in a transonic cascade (Arts, 1992). There are many studies of mean heat flux with mean and time resolved boundary layer information. The work of Wang, Simon, and Ames stand out as recent examples. Of the work done with time-resolved heat flux, very few measurements include simultaneous velocity information. The work at Oxford is one notable exception (Moss and Oldfield, 1992, 1994). Oxford has shown that it is the largest length scales reaching through the boundary layer that drive fluctuations in heat flux. Oxford used a single wire probe traversed above thin-film temperature gages on a flat plate in a short duration flow to back out heat flux (q) and velocity (u) correlations, as well as spatial correlations between heat flux gages. They concluded that eddies in the boundary layer mimicked those in the free-stream, convecting at the free-stream velocity rather than at the characteristic boundary layer velocity $\approx 0.8U_\infty$ (turbulent spot propagation velocity of a transitional boundary layer, Mayle, 1991), and that free-stream eddies reach into the boundary layer rather than enhancing existing boundary layer turbulence.

The present data complements the work at Oxford by presenting a more complete picture of the boundary layer. It adds to their data by presenting u and v components of velocity as well as time resolved temperature across the boundary layer giving complete time-resolved $uvTq$. The data is limited to a single boundary layer axial position and flow condition so that correlations based on length scale, Tu , and Re can only be checked at one location. In addition, probe spatial resolution limits cross-correlation of signals to the larger scales present.

FACILITY AND INSTRUMENTATION

Tests were performed in a wall-jet channel facility, Fig.1, at Wright Labs, WPAFB. A blower feeds room air through a section of ducting to a settling chamber with soda straw flow straighteners, and then through a contracting nozzle with its lower lip flush with the test section floor. The nozzle height is 10.2 cm, and width 30.5 cm. The inlet flow velocity at the nozzle exit was 25 m/s with less than 10% non-uniformity across the nozzle face. A 30.5 cm long heated plate was set into the plexiglass floor with its leading edge 122 cm (4 ft.) from the nozzle exit, in a region with a fully developed turbulent boundary layer.

The heated plate consisted of 6 aluminum bars each instrumented with thermocouples and with an independently controlled strip heater to provide a constant temperature surface. A Heat Flux Microsensor (HFM) was located 28cm (11 in.) from the leading edge of the plate, at $x/h = 14.7$. At this location $Re_x = 1.7 \times 10^6$, $Re_\delta = 1130$, and $Re_\delta = 3500$. The surface temperature of the bars (monitored by a thermocouple array) was maintained at 101.0 ± 1.5 °C with $\Delta T = 72$ °C across the boundary layer. Radiation was therefore significant, but only in calculating the mean heat transfer. The HFM directly outputs heat flux and is believed to be largely transparent to radiative heat flux. Therefore the mean heat flux values presented here will be less than the actual mean heat flux with an error

estimated to be near 10%. Fluctuating heat flux, q' , will not be affected as surface temperature is not changing.

Four channels with heat flux, u and v velocity, and cold-wire temperature were sampled by a National Instruments NB-A2150 board with data collected using LabVIEW software. The NB-A2150 samples simultaneously and filters data to remove aliasing. Data were post processed to convert from volts to calibrated units of heat flux, temperature and velocity. 8KB at 4kHz were sampled for each channel at 33 points across the boundary layer. Frequency data presented here are averaged 128 times.

Heat flux measurements were made using a Heat Flux Microsensor (HFM), Fig.2. The HFM consists of two sensors: a surface resistance temperature sensor (RTS) in a serpentine pattern (0.64cm in length), and a heat flux sensor (HFS, 1.85cm in length) stretching across the gage face. The HFM used in these tests (model HFM-2B-AIN-B from Thermotec Division of Vatec Inc.) was sputtered on an aluminum nitride ceramic disk with approximately the same thermal properties as the aluminum bar surrounding it, so that there is no thermal disruption due to the sensor's presence. The HFS consists of a thermopile with 100 pairs of Ni-Nichrome thermocouple junctions arranged above and below a thin (0.8 μ m) resistive layer so that heat flux is directly output (Holmberg, 1995). The RTS is a sputtered platinum wire driven by a 0.1mA current. Frequency response of both sensors is better than 100kHz (Holmberg, 1995). Calibration of the HFS was provided by the manufacturer ($\pm 10\%$ uncertainty on the mean), while the RTS calibration was done in-situ.

Velocity measurements were made using a TSI model 1287 split-film seen in Fig.2. The sensor active length is 2.0mm, thus allowing resolution 10X that of the HFS, and the ability to see "mixing-length" scale ($\sim 0.1d$) boundary layer turbulence. The cold-wire was a "home-made" wire (on a standard TSI Inc. U-wire probe body) with a wire etched down to a 0.5 μ m diameter, and driven in constant current mode to measure fluctuating temperature in the boundary layer. The active length is less than 0.2mm giving resolution 10X that of the split-film. The cold-wire was calibrated in-situ immediately after the completion of the test.

The cold-wire and split-film were displaced spanwise, Fig.2, to

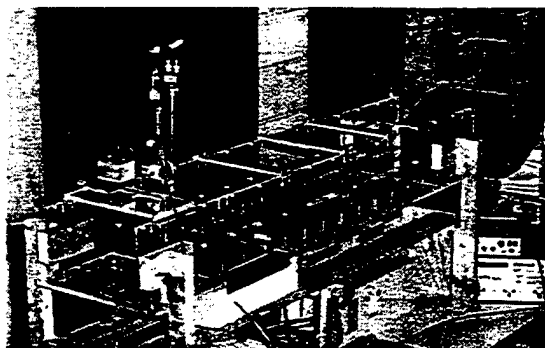


Fig.1 Wall-jet facility

avoid interference of one in front of the other, but this led to reduced coherence due to this spatial separation, as will be seen. The probes were shown to significantly disturb wall heat flux values when near the wall. Heat flux measurements increased significantly at probe locations below 1mm due to flow distortion, with a 20% increase at the nearest location to the wall (0.2mm). Velocity measurements showed 2° of angular distortion at the wall, but it is not clear how much of this is due to potential flow distortion and how much to split film imbalance due to wall proximity to the lower film.

The HFS stretches across the face of the disk in a line to maximize axial resolution, and passes beneath both the split-film and cold-wire probes. As a result, coherence between velocity and heat flux (uq , vq) and between heat flux and cold-wire temperature (qt) is diminished at higher frequencies due to spanwise averaging across the HFS, and across the boundary layer probes as well. As mentioned above, coherence between velocity and temperature (ut , vt) is seriously affected by the probe separation, and this is especially evident near the wall where length scales are reduced.

TIME MEAN RESULTS

Mean velocity, and temperature profiles in dimensionless wall coordinates are shown in Figs. 3 and 4. The characteristic drop-off in the wake of a wall jet is seen in the u^+ vs. y^+ plot at large y^+ . Temperature and velocity profiles are compared in Fig. 5 showing the less developed temperature profile. At the nearest probe location ($y^+=10$), the velocity is 7 m/s and temperature 56°C (where $t_{wall}=101^\circ\text{C}$, $t_{max}=28^\circ\text{C}$, and $u_{max}=21.8$ m/s) indicating the large temperature and velocity gradients across the laminar sublayer below $y^+=10$ ($y=0.2\text{mm}$). The enthalpy thickness (based on a variable property numerical integration) is only 1.0mm, where enthalpy thickness is an integral measure of the energy containing thickness of the boundary layer. Using air properties across the boundary layer based on the cold-wire temperature, and matching the log-layer to the Kays and Crawford (1980) correlation for a turbulent boundary layer ($u^+ = 5.6 \log_{10} y^+ + 4.9$), a skin friction value of $c_f=0.0035$ was found.

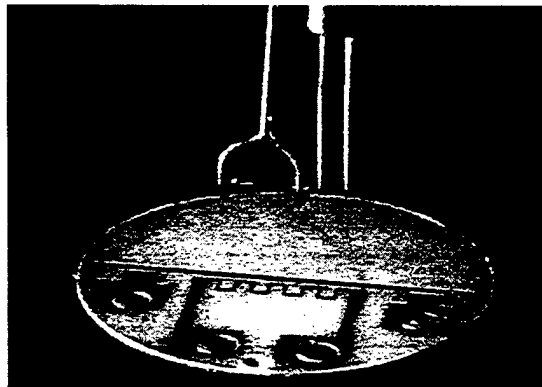


Fig.2 Probe arrangement above HFM

This is 7% above the theoretical value $c_D = 2 \cdot 0.0287 \text{ Re}_x^{-0.2}$, and indicates an increase in heat transfer above a conventional low FST turbulent boundary layer. All properties have been taken at Eckert's reference temperature which for low-speed flows is equivalent to the mean temperature, $t_m = (t_{wall} - t_{max})/2$.

Taking properties at t_m results in an experimental heat transfer increase $St/St_0 = 1.08$, where St_0 is the Stanton number ($h/\rho u c_p$) for a theoretical low FST flat plate turbulent boundary layer with an unheated starting length, $St_0 = 0.0287 \text{ Pr}^{-0.4} \text{ Re}_x^{-0.2} [1 - (\xi/x)^{1/3}]^{-1/3}$. Accounting for radiation would raise this to $St/St_0 \approx 1.2 \pm 10\%$. Ames' TLR, which is based on enthalpy thickness Δ , predicts for this flow $St/St_0 = 1.18$, and Thole's $TA_{\Delta}R$ (also based on Δ) predicts $St/St_0 \approx 1.1$. The TLR parameter requires knowledge of the dissipation which was determined here from the u autospectrum according to the method outlined by Ames (1990). Oxford's X_s parameter, which does not base length scale effect on Δ , but instead on δ_{995} (here substituting y_{max}), gives $Nu/Nu_0 = 1.4$. Dullenkopf (1994) states that the most effective length scales for heat transfer are $4 < L/\delta < 12$, and for this flow $\Lambda_{u, rms}/y_{max} = 2.5$, indicating what should be heat transfer near that effective range. However, it is likely that enthalpy

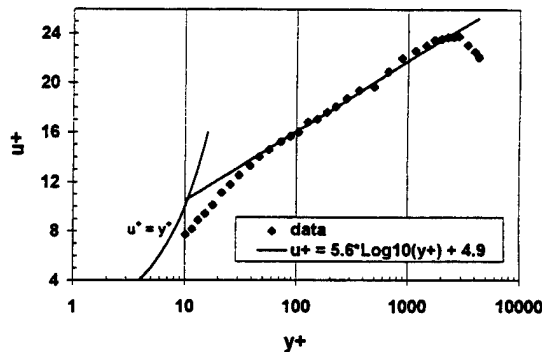


Fig.3 Mean velocity profile across boundary layer

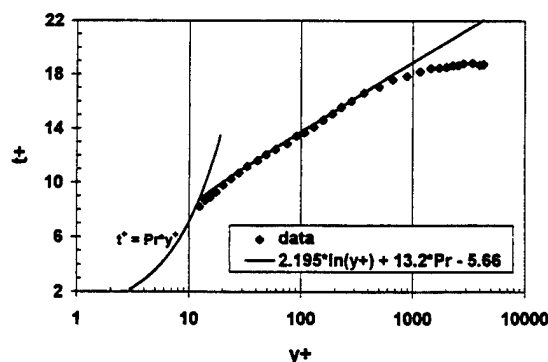


Fig.4 Mean temperature profile across boundary layer

thickness Δ must be accounted for in determining an optimum length scale.

Figure 6 shows $u'v'/U_{max}^2$ and Tu_{Δ} across the boundary layer. These data agree closely with that taken by Rivir (1992) on a different 2-D wall-jet facility at a similar x/h . Rivir shows $u'v'$ initially going negative and then states that it crosses the axis to positive at $\sim 60\%$ of y_{max} , and then continues to increase into the wake shear layer. The values reported for Tu_{Δ} show similar values in the wake region dipping to 13% at y_{max} , and increasing above 15% near the wall (the exact value is obscured by other data and plot scaling). The agreement of these data and that of other mean data above lend strength to the validity of the data despite potential problems of large Δt across the boundary layer, radiation effects, and probe flow interference.

It is very interesting however that Rivir measured a $St/St_0 \approx 2.0$ or a 100% heat transfer increase. This is a tremendous difference considering the similarities in the facilities. Rivir did not have the TLR parameter available, but did compare his data to a parameter similar to Oxford's X_s and found no agreement. This large disagreement can be resolved by viewing the data in the terms of Maciejewski (1995) where heat flux scales on the RMS value of u' (not Tu_{Δ} which scales on the mean velocity). He offers a simple

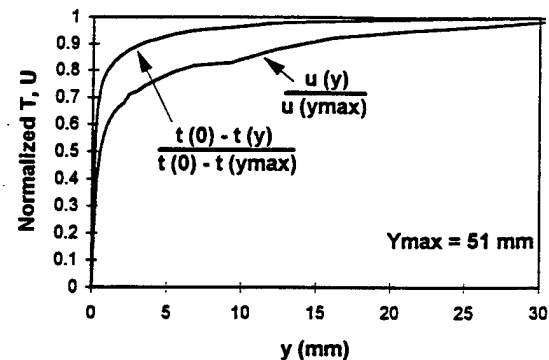


Fig.5 Normalized velocity and temperature profiles

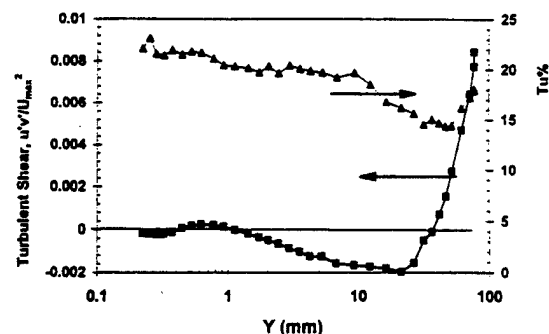


Fig.6 $Tu_{\Delta} \%$ and $u'v'$ across boundary layer

correlation for the heat transfer coefficient, h ($\text{W/m}^2\text{K}$) = $22.7 u'$ (m/s). Applying this to Rivir's data (to the accuracy allowed from his figures) as well as to the present data results in agreement between the two data sets, with the heat transfer coefficients based on respective u' both falling approximately 10% below Maciejewski's correlation.

TIME DOMAIN RESULTS

Some useful information can be gathered by looking at the time series across the boundary layer. Figure 7 shows simultaneous $uvtq$

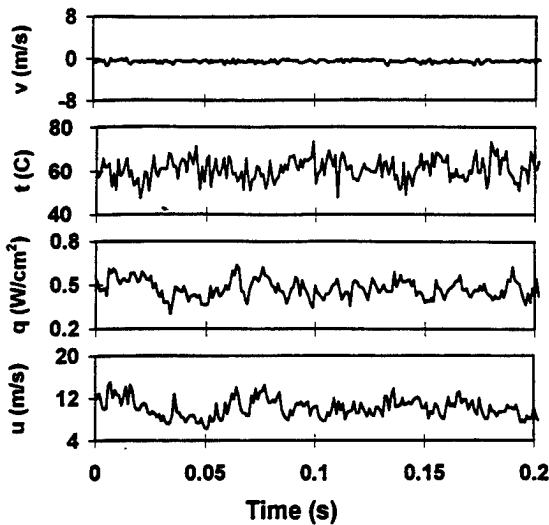


Fig.7 Comparisons of $uvtq$ time series at $y^+=10$

time traces near wall at $y^+=10$. Note the similarity in the u and q traces, with good coherence, and similar time scales, while q and t show limited coherence, which may be due to the much poorer resolution of the HFS. The v trace is near the noise floor (also seen in Fig.12), whereas t shows strong higher-frequency fluctuations. The development of u , v , and t are shown at three points across the boundary layer in Figs. 8, 9, and 10. Note that u does not change much in character above $y^+=100$, while v changes dramatically. Temperature fluctuations are strong near the wall, but die out away from the wall.

Table 1 gives integral time scales, length scales, and turbulence intensities across the boundary layer for u , v , t , and q . The classic turbulent boundary layer (low FST) has an eddy size equal to $0.41y$ out to 0.09δ . It is clear that this is not the case here by examining the Λ_u (integral length scale) column. Λ_u equals y_{\max} (51mm) already at $y^+=10$, or just above the laminar sub-layer, but does peak near $0.4y_{\max}$

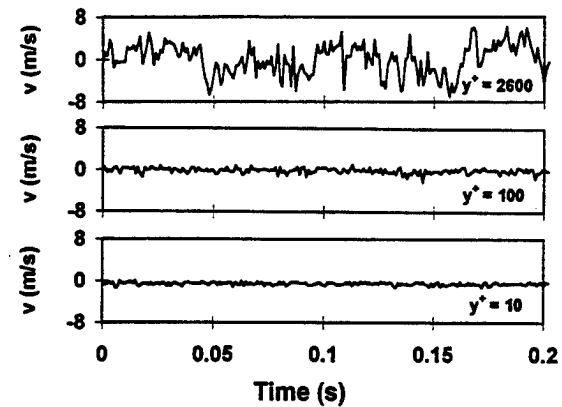


Fig.9 V velocity signal at $y^+=10, 100$, and 2600 .

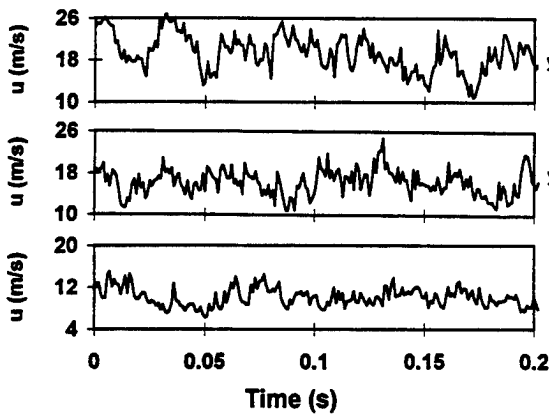


Fig.8 U velocity signal at $y^+=10, 100$, and 2600 .

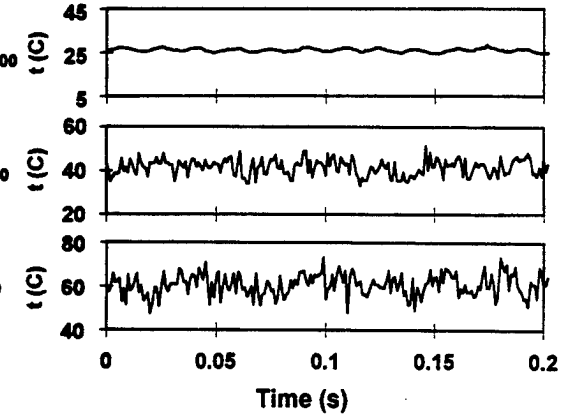


Fig.10 Temperature signal at $y^+=10, 100$, and 2600 .

($y^+=1200$). This data agrees with that of Rivir (1992).

For v , t , and q , it is only reasonable to talk in terms of integral time scale, not a length scale, since Λ_u itself is based on Taylor's hypothesis that $\Lambda_u = u\tau_u$, and the length scale comes from the length dimension of a velocity. The autocorrelation function actually gives integral time scale τ_u , where τ has been calculated by integrating the area under the autocorrelation curve to the first zero crossing. From Table 1, the τ_u column reveals that the integral time scale of the u fluctuations is almost constant across the boundary layer, decreasing only slightly near the wall. This evidences the penetration of free-stream eddies, as noted by Moss and Oldfield (1994). The variability in τ_v near the wall indicates the inability of the split-film probe to resolve the small scales of v' fluctuations. The cold-wire is able to resolve the small scales, and at $y^+=10$, near wall higher-frequency activity results in a smaller integral time scale, τ_v . 60Hz noise in t and q was post-process filtered out so as to not bias integral time scales.

The large size of $\Lambda_u = y_{max}$ at $y^+=10$ appears to be due to large low frequency structures in the free stream that are affecting the u velocity spectrum deep into the boundary layer. Based on this evidence, one can envision something like an ocean wave passing in shallow water where the underlying water is disturbed both in a "sloshing" motion and a "splat" motion. The sloshing motion would cause large u fluctuations of low frequency without v fluctuations, while the effect of a large eddy "splat" would be to translate low frequency v fluctuations away from the wall into u fluctuations near the wall, as well as to generate intense mixing of the boundary layer fluid. This implies that large structures near and beyond the maximum velocity point are causing the large values of the length scale near the wall. Based on the similarity in u and q , the q fluctuations also appear to be controlled by these large structures. This agrees with the analysis of Maciejewski (1995).

It may be helpful to point out that what others (e.g. Keller, 1990) have called heat flux in reference to time-resolved boundary layer information is not wall heat flux, but $v't'$, which gives a picture of how energy is transferred through the boundary layer, but is not the surface flux. In this work, time-resolved surface heat flux has been measured directly. This then allows an investigation of how the boundary layer fluctuations of v and t are translated to the surface; at what frequencies, and at what length scales that produce the measured mean heat transfer.

FREQUENCY DOMAIN RESULTS

The need to view boundary layer fluctuating quantities in the frequency domain can be seen in the discussion of Time Mean Results above where the correlations of heat transfer augmentation largely ignore the distribution of turbulent energy in the frequency domain because they are based on integral scales (which by definition integrate the whole spectrum into a single value). Instead, isotropic turbulence is assumed, which has a known frequency spectrum. As noted in the Introduction, isotropic turbulence is not likely present in an actual gas turbine engine. Some use of velocity autospectrum is seen in the literature (e.g. Ames, 1990, and Oldfield, 1994). In the following discussion, autospectra as well as coherence and phase information will be presented.

The autospectrum, $S_{xx}(f)$ of a quantity is basically a squared FFT, and here it is the average of autospectra of 128 individual data blocks, presented in dB versus frequency. Coherence is a measure of the correlation between two signals in the frequency domain, equaling 1 at a frequency where correlation is exact, and 0 where there is none. It is defined as the averaged cross-spectrum of two signals squared divided by the averaged autospectrum of each signal, $S_{xy}(f)^2 / (S_{xx}(f) S_{yy}(f))$. Phase information presented here is the phase shift between two signals as a function of frequency.

First examine the auto-spectral data of u , v , t and q across the boundary layer, Figs. 11-14. S_{uu} shows an increasing energy at all frequencies with distance from the wall as eddy sizes increase, with larger eddies carrying more energy. A noticeable 15 Hz peak is evident in the data, but this seems to be due to disturbance from the probe body. Notice that the 15 Hz peak is not present at $y^+=100$, but is present near-wall, and further out. This same pattern appears in the surface heat flux spectrum which ideally would remain constant irrespective of probe position, suggesting that the 15 Hz peak is related to flow unsteadiness due to the probe body itself, and not due to an upstream source. According to Dullenkopf and Mayle (1994), the optimum frequency for FST to excite the boundary layer is at $f_k \approx 0.03 U_\infty/\delta$, which for this flow data is at 20Hz, suggesting that any probe disturbance may more effectively excite the boundary layer near this frequency.

S_{vv} , Fig. 12, evidences an even stronger increase in fluctuating energy moving away from the wall corresponding to wall damping. Near wall, the spectrum is flat out to 1kHz, while away from the wall, the spectrum matches that of u velocity for frequencies above 100Hz. In general, lower frequency energy increases, with the spectra merging off the plot beyond 1kHz.

Table 1 Mean quantities, fluctuating components, and integral scales across the boundary layer

y^+	y (mm)	u (m/s)	Tu_u (%)	τ_u (ms)	Λ_u (mm)	v (m/s)	τ_v (ms)	t (°C)	Tu_t (%)	τ_t (ms)	q (W/cm ²)	Tu_q (%)	τ_q (ms)
10	0.23	9.62	21.0	5.28	50.8	-51	0.92	60.2	9.2	1.48	0.47	14.6	3.2
20	0.40	11.6	21.7	5.21	60.4	-56	1.76	52.2	9.5	1.45	0.48	14.9	4.3
40	0.85	14.0	22.6	6.44	90.4	-10	0.54	44.3	8.4	2.2	0.48	15.1	4.4
100	1.9	15.9	19.8	5.85	92.8	-04	0.68	39.4	6.8	2.0	0.46	14.4	3.1
300	6.0	17.8	19.2	6.4	114	-11	1.16	33.3	4.6	2.2	0.44	14.3	3.2
1200	22.5	20.6	17.0	6.7	138	.08	2.10	29.0	1.7	2.2	0.41	15.7	3.8
2600	47.4	21.6	15.2	6.0	130	.17	2.8	28.6	1.0	2.5	0.41	16.2	3.7
4000	74.5	20.5	18.0	5.9	122	.41	3.2	27.9	1.0	2.5	0.41	15.5	3.9

So, Fig. 13, evidences the large decrease in temperature fluctuations across the log-region moving away from the heated wall. The high frequency fluctuations drop off more, indicating a decrease in smaller-scale temperature variations. This implies the diffusion of small high-energy eddies originating from near-wall activity (e.g. "bursting"), as well as the dominance of larger eddies (lower frequencies) that are responsible for moving the high enthalpy fluid away from the wall. 60Hz noise is buried in the strong near wall fluctuations, but evident away from the wall.

S_{eq} , Fig. 14, shows the change in the heat flux spectrum as the probe is traversed across the boundary layer. Without probe disturbance there would be no change in heat flux at the wall, but a small amount is evident. Note the drop off in the spectrum. The drop between 10 and 100 Hz of 10dB and between 100 and 1000Hz of 15 dB is equivalent to the drop in the u velocity spectrum despite the lower HFS resolution, again giving support to the scaling of q on u fluctuations. The 60Hz noise should be disregarded.

Second, examine the uq coherence and phase data in Figs. 15 and 16. The uq coherence across the boundary layer gives insight into the heat transfer mechanism. As expected, there is very good coherence near the wall and at lower frequencies, with coherence

dropping off with distance from the wall and with frequency. Of note is that coherence is nearly zero at the maximum velocity point $y^+=2600$, but then increases slightly at $y^+=4000$. This may be an effect of large scale structures with spanwise vorticity rotating about the maximum velocity point. From the plot of uq phase, one can see that near the wall at $y^+=10$, and $y^+=40$ the u velocity and heat flux signals are in phase out to 200Hz (and could be expected to go out farther if not for probe spatial resolution issues), while at $y^+=1200$ the two signals are in phase only at the DC level, and then as frequency increases, heat flux lags velocity until they are 180 degrees out of phase at 150Hz. But at this point coherence is zero, and the phase fluctuations have become completely erratic. The phase lag grows even faster for points farther from the wall. Based on these plots we can see that q and u show high coherence across the entire log layer, with phase lag slowly increasing with distance from the wall. Only in the wake region is coherence lost.

The vq coherence, Fig. 17, shows a complementary profile. The coherence in the lower part of the log layer is zero, while out at $y^+=1200$ and beyond the coherence is significant. The vq phase, Fig. 18, reveals that at $y^+=1200$ there is some phase agreement. This appears to support a "splat" phenomena where v energy is

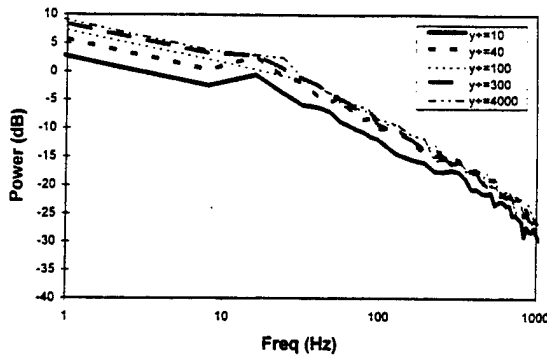


Fig.11 U autospectrum across boundary layer

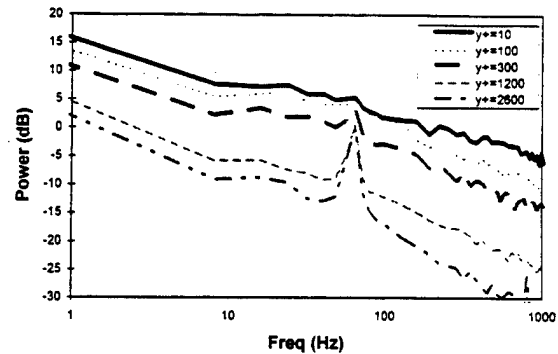


Fig.13 Temperature autospectrum across boundary layer

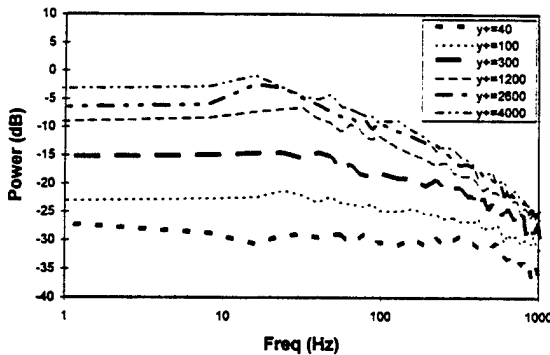


Fig.12 V autospectrum across boundary layer

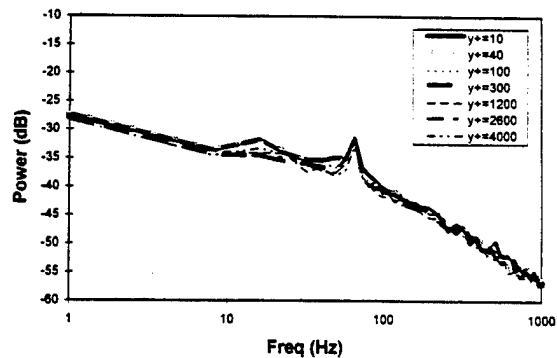


Fig.14 Heat flux autospectrum across boundary layer

transferred to u energy within the log-layer such that vq coherence is strong only high in the log layer, while uq coherence is strongest at the wall and drops off within the log layer. There is no agreement at points in the lower log region and these are not shown. It is important to note the lack of vq coherence which would be expected from any small-scale wall activity that may be present may be lost due to sensor resolution limits.

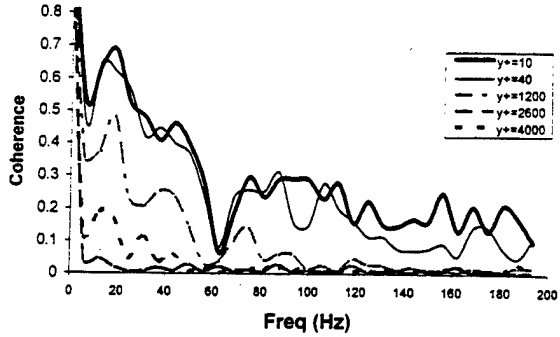


Fig. 15 uq coherence across boundary layer

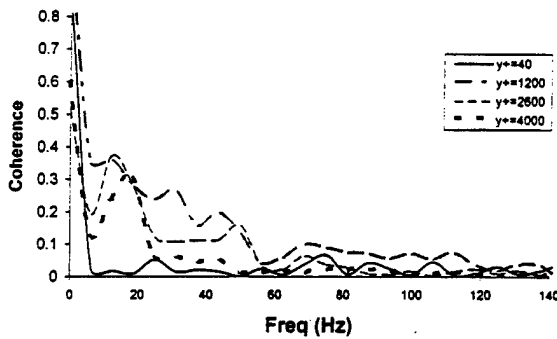


Fig. 17 vq coherence across boundary layer

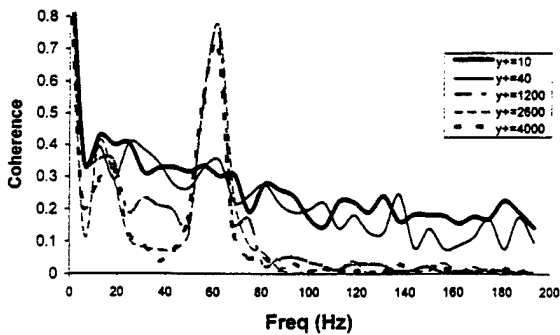


Fig. 19 qt coherence across boundary layer

Finally consider the qt coherence and phase, Figs. 19 and 20. Here we can see that despite what appears to be little coherence in the time series data of Fig. 7, there is nonetheless significant coherence at the wall which remains significant across the log layer. As with uq phase, qt fluctuations are in phase at the wall out to beyond 200Hz, with increasing lag away from the wall. The coherence and phase agreement evidence the cold-wire's responding

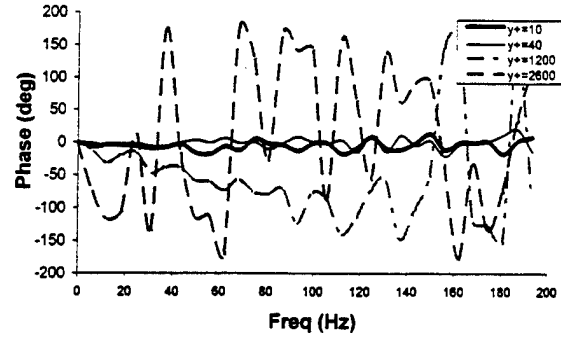


Fig. 16 uq phase across boundary layer

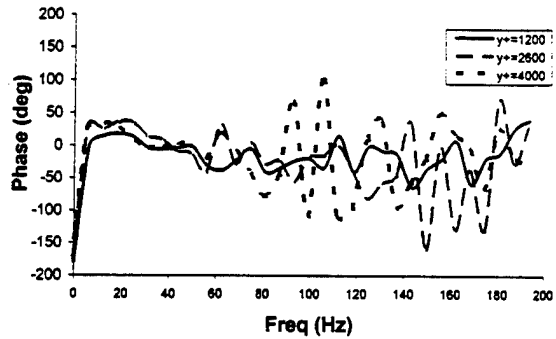


Fig. 18 vq phase across boundary layer

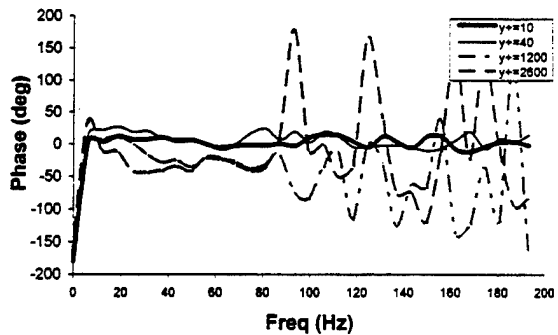


Fig. 20 qt phase across boundary layer

to convected temperature variations primarily in the u direction. It seems likely that the coherence between q and t is a combination of large eddies from outside the boundary layer (seen here) and higher frequency bursts from the wall region (not seen here).

Based on the above discussion it is clear that whatever near-wall small-scale activity may be present and responsible for heat transfer across the lower 4% of the boundary layer ($y^+ < 100$), outside of this inner region heat transfer is dominated by large freestream turbulence reaching deep into the boundary layer and controlling the observed heat flux. It is also evident that the large increases in heat transfer over low-FST due to the presence of high-FST are due to these large freestream eddies reaching into the boundary layer, adding energy and enhancing the mixing of wall fluid into the freestream. This also explains the observed scaling of heat transfer on velocity fluctuations.

CONCLUSION

The interactions of cold-wire temperature (t') and split-film velocity fluctuations (u' , v') together with surface heat flux fluctuations (q') from a Heat Flux Microsensor have been investigated experimentally in a wall-jet facility. Mean results give $St/St_0 \approx 1.2$ which is near the enhancement due to the presence of FST that is predicted by existing correlations which base length scale effects on the enthalpy thickness. However, similar data from another 2-D wall-jet facility gives $St/St_0 \approx 2.0$. This disagreement is resolved by dismissing St correlations, based on mean velocity, and instead basing the heat transfer coefficient strictly on the fluctuating velocity component, u' .

This scaling of heat flux on velocity fluctuations is seen not only in the mean heat transfer, but also in time-resolved measurements. In the presence of high FST, the heat flux is largely controlled by free stream eddies of large size and energy reaching deep into the boundary layer. This is evidenced by the uq coherence present across the boundary layer, as well as by the similarity in heat flux and u velocity spectra, and by the integral time scale τ_u which remains nearly constant across the boundary layer even at the nearest wall measuring location just above the laminar sublayer. Whatever small-scale wall activity (e.g. "bursting") that may be present is not relevant in relating heat transfer to free-stream phenomena. Or in other words, knowledge of the fluctuating velocity field outside the boundary layer can be used to determine the frequency spectra of the heat flux, as well as mean heat flux levels.

In summary, wall heat transfer is controlled by the u velocity field. Large freestream eddies reaching down into the boundary layer cause near wall fluctuations in u , as well as mixing in the boundary layer. The heat flux spectrum matches the velocity spectrum in its distribution of energy, with similar time scales, and high coherence at the wall.

ACKNOWLEDGMENTS

The use of Dr. Richard Rivir's Turbine Aerothermal Research Laboratory of the Turbine Branch (WL/POTT) at Wright Lab at Wright Patterson AFB, and his support in modifying the wall-jet facility and subsequent guidance is greatly appreciated. The assistance of Mr. Greg Cala is also appreciated. The work was made

possible as part of the Air Force Laboratory Graduate Fellowship, with funding administered through the office of Prof. Peele of the Southeastern Center for Electrical Engineering Education.

REFERENCES

- Ames, F.E., and Moffat, R.J., 1990, "Heat Transfer with High Intensity, Large Scale Turbulence: The Flat Plate Turbulent Boundary Layer and the Cylindrical Stagnation Point," Report No. HMT-44, Thermosciences Division of Mechanical Engineering, Stanford University.
- Ames, F.E., 1994, "Experimental Study of Vane Heat Transfer and Aerodynamics at Elevated Levels of Turbulence," NASA CR-4633.
- Arts, T., Lambert de Rouvroit, M., 1992, "Aero-Thermal Performance of a Two-Dimensional Highly Loaded Transonic Turbine Nozzle Guide Vane: A Test Case for Inviscid and Viscous Flow Computations," JT, Vol.114, p.147.
- Ashworth, D.A., LaGraff, J.E., Schultz, D.L., 1989, "Unsteady Interaction Effects on a Transitional Turbine Blade Boundary Layer," JT, Vol.111, p.162.
- Dullenkopf, K., Mayle, R.E., 1994, "An Account of Free-Stream Turbulence Length Scale on Laminar Heat Transfer," ASME Paper 94-GT-174.
- Dunn, M.G., Seymour, P.J., Woodward, S.H., George, W.K., Chupp, R.E., 1989, "Phase-Resolved Heat-Flux Measurements on the Blade of a Full-Scale Rotating Turbine," JT, Vol.111, p.8.
- Garside, T., Moss, R.W., Ainsworth, R.W., Dancer, S.N., Rose, M.G., 1994, "Heat Transfer to Rotating Turbine Blades in a Flow Undisturbed by Wakes," IGTI Aeroengine Congress and Expo, The Hague, Netherlands, ASME 94-GT-94.
- Guenette, G.R., Epstein, A.H., Giles, M.B., Haines, R., Norton, R.J.G., 1989, "Fully Scaled Transonic Turbine Rotor Heat Transfer Measurements," JT, Vol.111, p.1.
- Holmberg, D.G., Diller, T.E., 1995, "High-Frequency Heat Flux Calibration and Modeling," J. Fluids Engineering, Vol.117.
- Kays, W.M., and Crawford, M.E., 1980, Convective Heat and Mass Transfer, 2nd Ed., McGraw-Hill, Inc., N.Y.
- Keller, F.J., Wang, T., 1994, "Flow and Heat Transfer Behavior in Transitional Boundary Layers with Streamwise Acceleration," ASME Paper 94-GT-24.
- Kim, J., Simon, T.W., Russ, S.G., 1992, "Free-Stream Turbulence and Concave Curvature Effects on Heated Transitional Boundary Layers," JHT, Vol.114, p.339.
- Maciejewski, P.K., 1995, "Limitations to the Employment of Conventional Boundary Layer Parameters and Predictive Models to Heat Transfer in Complex Flows," in Heat Transfer in Turbulent Flows, Eds. N.K. Anand et al., ASME, NY, pp.37-44.
- Mayle, R.E., 1991, "The Role of Laminar - Turbulent Transition in Gas Turbine Engines," JT, Vol.113, p.509.
- Moss, R.W., and Oldfield, M.L.G., 1992, "Measurements of the Effect of Free-Stream Turbulence Length Scale on Heat Transfer," ASME Paper 92-GT-244.
- Moss, R.W., and Oldfield, M.L.G., 1994, "Effect of Free-Stream Turbulence on Flat-Plate Heat Flux Signals: Spectra & Eddy Transport Velocities," ASME Paper 94-GT-205.

Rivir, R.B., Troha, W.T., Eckerle, W.A., Schmoll, W.J., 1992, "Heat Transfer in High Turbulence Flows - A 2D Planar Wall Jet," AGARD 80th PEP Symposium on Heat Transfer and Cooling in Gas Turbines, Antalya, Turkey, October 12-16, 1992.

Thole, K.A., Whan-Tong, J., Bogard, D.G., 1991, "Generation of High Freestream Turbulence Levels and the Effects on Heat Transfer," 8th Symposium on Turbulent Shear Flows, Tech. Univ. Munich, Germany, September 9-11.

Van Fossen, G.J., and Ching, C.Y., 1994, "Measurements of the Influence of Integral Length Scale on Stagnation Region Heat Transfer," Fifth Intl. Sym. on Transport Phenomena and Dynamics of Rotating Machinery (ISROMAC-5), Kaanapali, Maui, Hawaii, Paper No. TP-16, and NASA Technical Memorandum 106503.

Wittig, S., Schulz, A., Dullenkopf, K., Fairbank, J., 1988, "Effects of Free-Stream Turbulence and Wake Characteristics on the Heat Transfer Along a Cooled Gas Turbine Blade," ASME Paper 88-GT-179.

Zhou, D., Wang, T., 1993, "Combined Effects of Elevated FST and Streamwise Acceleration on Flow and Thermal Structures in Transitional Boundary Layers," HTD, Vol.242, Gas Turbine Heat Transfer, ASME, p.41.

High-Frequency Heat Flux Sensor Calibration and Modeling

D. G. Holmberg

T. E. Diller

Mechanical Engineering Department,
Virginia Polytechnic Institute
and State University,
Blacksburg, VA 24061-0238

A new method of in-situ heat flux gage calibration is evaluated for use in convective facilities with high heat transfer and fast time response. A Heat Flux Microsensor (HFM) was used in a shock tunnel to simultaneously measure time-resolved surface heat flux and temperature from two sensors fabricated on the same substrate. A method is demonstrated for estimating gage sensitivity and frequency response from the data generated during normal transient test runs. To verify heat flux sensitivity, shock tunnel data are processed according to a one-dimensional semi-infinite conduction model based on measured thermal properties for the gage substrate. Heat flux signals are converted to temperature, and vice versa. Comparing measured and calculated temperatures allows an independent calibration of sensitivity for each data set. The results match gage calibrations performed in convection at the stagnation point of a free jet and done by the manufacturer using radiation. In addition, a finite-difference model of the transient behavior of the heat flux sensor is presented to demonstrate the first-order response to a step input in heat flux. Results are compared with shock passing data from the shock tunnel. The Heat Flux Microsensor recorded the heat flux response with an estimated time constant of 6 μ s, which demonstrates a frequency response covering DC to above 100 kHz.

Introduction

One method of measuring heat flux to or from a surface is to measure the rate of change of temperature of the material. With appropriate transient conduction modeling and material properties, the heat flux that caused the measured temperature history can be determined. The most common method is to assume that the material responds as a one-dimensional, semi-infinite substrate (Scott, 1976; Jones, 1977; Diller, 1993). Because this assumption is only valid for sufficiently short times, its use in short-duration flow facilities is natural. The temperature response is proportional to the inverse of $\sqrt{(k\rho C)}$ of the substrate. The surface temperature measurements are usually made on a low conductivity ceramic substrate to maximize the sensor response for short time measurements. The temperature response on a high conductivity substrate is proportionately smaller.

The use of thin-film resistance gages to measure the required surface temperature history to calculate heat flux is detailed by Schultz and Jones (1973) and has been successfully used for many years. Analog electrical circuits are sometimes used for the conversion of the temperature signal to heat flux, but digital data processing or a combination of the two has also been effectively used (George et al., 1991; Dunn et al., 1986). For use in continuous flow facilities a pre-heated model can be injected into the flow to provide the required transient conditions (O'Brien, 1990). Several groups have used the transient temperature method to measure heat flux in transient flow facilities with applications from gas turbine engines to hypersonic flow (Dunn, 1990; Nicholson et al., 1987; Camci and Arts, 1991; Miller, 1985).

Roberts et al. (1990) used a shock tube to study the transient response of a hot-film sensor mounted in the tunnel wall. The time required for the incident shock to pass over the gage was estimated as 2 μ s for the pressure ratios used. Direct measurements of transient heat transfer were made by Hayashi et al. (1989) in a Mach 4 supersonic flow, and by Hager et al. (1993) during the starting transients of a Mach 2.4 flow.

Baker and Diller (1993) demonstrated a method of calculating surface temperature from time-resolved heat flux measurements. This has the advantage that the effects of electrical noise are diminished because the data processing technique is an integration type process. They used a Heat Flux Microsensor in a low frequency combustion flame to demonstrate the correspondence between the heat flux and temperature signals. The results were within the experimental uncertainties of the sensor calibrations and material property determinations. Holmberg et al. (1994a) demonstrated this method with heat flux and surface temperature measurements for Mach 3 flow in a shock tunnel.

When using heat flux sensors in a high-speed flow, there are two important gage parameters: the gage sensitivity (voltage output/heat flux) and the time response. Neither are easy to measure accurately, particularly in a convective flow environment. A shock tunnel using a supersonic nozzle provides an environment with fast transients, high speed flows, and moderately high heat fluxes. This is ideal for characterizing the transient response of sensors. The present paper documents a method for using shock tunnel data to determine both the heat flux sensitivity and the time response of the Heat Flux Microsensor. The experimental results are compared to a numerical model of the thermal response of the sensor and substrate. The potential for in-situ calibration of heat flux is also examined. Because the individual sensor measurements are not limited by length of time, the sensors once calibrated can be used in any type of flow facility.

Experimental Facilities and Instrumentation

Shock Tunnel Facility. The shock tunnel used for these tests has an 8 ft (2.44 m) driver section and a 20 ft (6.1 m) long driven section; both sections made of 3 in. inside diameter steel pipes. A Mach 3 two-dimensional supersonic nozzle is attached to the end of the driven section to obtain supersonic flow. The driver section of the shock tunnel is filled with compressed gas from a bottle, with the driven section, for the present research, left open to the atmosphere. A mylar diaphragm is sized to break at a specified driver gas pressure, which allows the high pressure gas to expand into the low pressure driven section, producing a traveling shock wave.

Contributed by the Fluids Engineering Division for publication in the JOURNAL OF FLUIDS ENGINEERING. Manuscript received by the Fluids Engineering Division April 20, 1994; revised manuscript received February 16, 1995. Associate Technical Editor: Wing-Fai Ng.

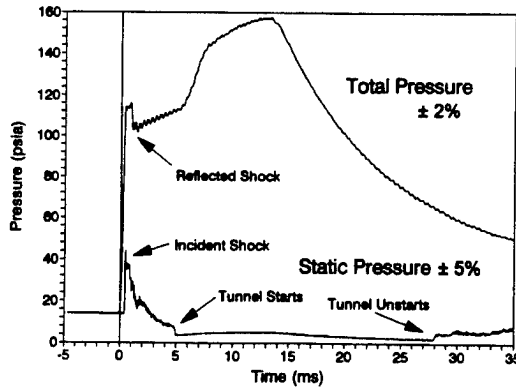


Fig. 1 Total and static pressures for shock tunnel test

Upstream total and exit static pressure measurements for a sample run with an air driver at 210 psig (1.45 MPa) and 300 K are given in Fig. 1. The incident shock wave is the initial spike in the pressure trace at 0 ms. Unsteady wave formation and transmission in the nozzle persist until about 5 ms at which time the nozzle starts. The region of low static pressure in the nozzle defines the time of supersonic flow. The nozzle unstarts at 28 ms and the remaining flow is subsonic. Calculations and measurements of the total temperature in the nozzle indicate an initial total temperature of approximately 600 K.

For the present tests, both air and helium were used as driving gases. For a fixed driver gas to driven gas pressure ratio a lighter driver gas with a larger specific heat yields a faster and stronger incident shock wave. Thus, helium was used both to produce a faster passing shock for time response estimation, as well as a stronger heat flux signal compared to an air driver.

Shock Tunnel Instrumentation and Data Acquisition. The heat transfer measurements were carried out with a Heat Flux Microsensor (HFM-3) manufactured by Vatel Corp. The HFM consists of two separate sensors in close proximity to independently measure the heat flux and surface temperature at one location. The heat flux sensor, as described by Hager et al. (1991), uses a differential thermopile across a thin thermal resistance layer and is made with microfabrication techniques. The sensor outputs a voltage directly proportional to the heat flux. A schematic of the sensor pattern is shown in Fig. 2. The heat flux is measured using the output of 280 copper-nickel thermocouple pairs arranged above and below a 0.8 μm layer of silicon monoxide. The size of the heat flux sensor on the surface is approximately 4 mm by 6 mm.

A radiation calibration was performed by the manufacturer according to the method outlined by Kidd (1992) using a 200 watt tungsten filament lamp with a highly polished ellipsoidal reflector. A circular foil heat flux gage that was calibrated at AEDC by the same method was used as the standard. The sensitivity was reported with an uncertainty of ± 10 percent as

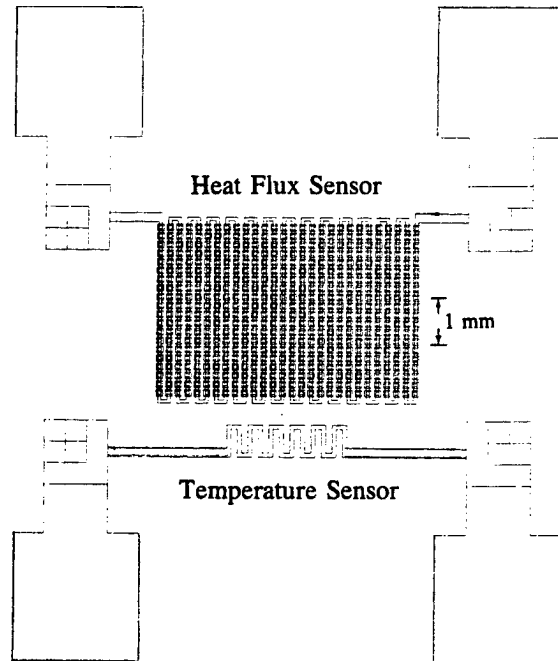


Fig. 2 Detail of HFM pattern

$$S = \frac{E_q}{q} = 50.0 \mu\text{V}/(\text{W}/\text{cm}^2) \quad (1)$$

where E_q is the output voltage from the sensor and q is the heat flux. A separate convection calibration was performed using an impinging air jet with the sensor placed at the stagnation point perpendicular to the jet as detailed by Holmberg et al. (1994a). Using a measured heat transfer coefficient for this configuration of 213 $\text{W}/\text{m}^2 \cdot \text{K}$ produced a sensitivity of 49.2 $\mu\text{V}/(\text{W}/\text{cm}^2)$ ± 5 percent.

The second HFM sensor, also shown on Fig. 2, is a platinum resistance element which provides an independent measure of the surface temperature. A 0.1 mA current is supplied to the sensor through an amplifier unit supplied with the sensor to provide the resistance measurement. The manufacturer's calibration to convert the voltage signal to temperature T_s is

$$T_s - T_i = (28.0^\circ\text{C}/\text{mV}) E_T \quad (2)$$

where E_T is the unamplified voltage, and T_i is an initial reference temperature. The estimated uncertainty in the calibration coefficient in Eq. (2) was reported as ± 4.0 percent. The corresponding error in the measurement of the temperature change, $T_s - T_i$, is ± 4.3 percent.

The sensor was fabricated on a 1.0 in. (2.5 cm) diameter, 0.625 cm thick aluminum nitride substrate by a sputtering pro-

Nomenclature

C = specific heat, $\text{J}/\text{kg} \cdot \text{K}$
 E_q = heat flux sensor output, V
 E_T = temperature sensor output, V
 k = thermal conductivity, $\text{W}/\text{m} \cdot \text{K}$
 n = number of thermocouple pairs in differential thermopile
 q = heat flux, W/cm^2
 q_{calc} = heat flux calculated from surface temperature, W/cm^2

q_{exp} = measured heat flux, W/cm^2
 q_{max} = maximum heat flux, W/cm^2
 S = sensitivity of Heat Flux Microsensor, $\mu\text{V}/(\text{W}/\text{cm}^2)$
 t = time, s
 T_i = reference for temperature sensor, $^\circ\text{C}$
 T_0 = initial substrate temperature, $^\circ\text{C}$
 T_s = surface temperature, $^\circ\text{C}$

T_{calc} = surface temperature calculated from heat flux, $^\circ\text{C}$
 T_{exp} = measured surface temperature, $^\circ\text{C}$
 T_{num} = surface temperature calculated from numerical model, $^\circ\text{C}$
 ρ = substrate density, kg/m^3
 σ = thermocouple sensitivity, $\mu\text{V}/^\circ\text{C}$
 τ = first-order time constant, μs

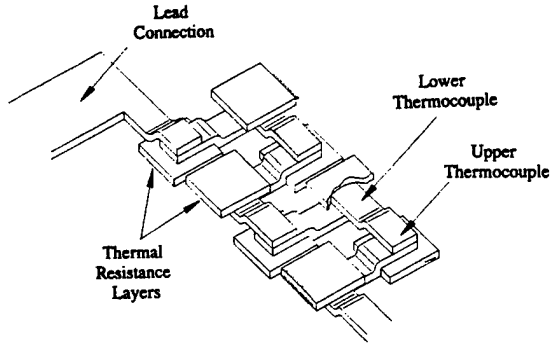


Fig. 3 Heat flux thermopile construction

cess. The thermal properties of the substrate were measured by independent laboratories (Holometrix and Anter Laboratories) as $k = 165 \text{ W/m} \cdot \text{K}$, $C = 713 \text{ J/kg} \cdot \text{K}$, and $\rho = 3290 \text{ kg/m}^3$. The corresponding value of $\sqrt{(k\rho C)}$ is 19,670 in SI units, with an uncertainty calculated from the reported individual measurements of ± 5 percent. All of these values are close to those of the aluminum nozzle where the gage is mounted. Four pins were countersunk into the substrate to bring the surface temperature and heat flux signals from the surface to the tunnel exterior without disturbing the flow. The HFM was mounted flush with the bottom surface of the shock tunnel, near the exit plane of the nozzle.

For the purpose of gage sensitivity analysis, two channels of data were sampled using an HP 3562A Dynamic Signal Analyzer. Heat flux and temperature signals from the HFM were sampled at different frequencies from 25 kHz for 80 ms up to 250 kHz for 8 ms. Simultaneously, a LeCroy 6810 Waveform Digitizer was used to sample the HFM at a $1 \mu\text{s}$ interval. The faster sample rate allowed better resolution of the incident shock for time response estimation.

Data Conversion, Digital Data Processing Routine. To convert measured heat flux to the corresponding calculated surface temperature a one-dimensional, semi-infinite model of the heat transfer in the substrate was used. The substrate was assumed to initially be at a uniform temperature, T_0 . Baker and Diller (1993) developed a method for calculating time-resolved surface temperature from the measured heat flux signal. Using a Green's function approach, individual heat flux impulse solutions were combined to include a series of heat flux data points.

$$T_s(t_n) - T_0 = \frac{2}{\sqrt{\pi k\rho C}} \sum_{j=0}^{n-1} q_j \left[\sqrt{t_n - t_j} - \sqrt{t_n - t_{j+1}} \right] \quad (3)$$

A computer code was written making use of this equation to process the E_q signal from the HFM. In addition to converting heat flux, the code calculates a heat flux sensitivity based on each data set by minimizing the sum of the errors between individual time values of the measured surface temperature, T_{exp} and the temperature calculated from the heat flux, T_{calc} . By this method, an independent measure of gage sensitivity can be obtained for each data sample (one test run of the shock tunnel). This is equivalent to obtaining an in-situ calibration of the heat flux sensor while tests are being performed.

Numerical Model of HFM

To provide an analytical basis for the heat flux sensor and substrate thermal response, a numerical model was developed. A close-up of the sputtered gage surface can be seen in Fig. 3. The gage consists of resistance layer (silicon monoxide) square pads interconnected with copper and nickel leads forming thermocouple junctions above and below alternating pads. The nu-

merical model is a one-dimensional implicit finite-difference code which has fifteen nodes across the $1.4 \mu\text{m}$ of sputtered gage thickness, shown as a cross-section of the pads in Fig. 4. There are ten nodes (not shown) across the $0.8 \mu\text{m}$ thick resistance layer. Below the gage are 50 nodes with increasing spacing across the quarter inch thick substrate of aluminum nitride. As can be seen in Fig. 4, the sputtering pattern for HFM-3 consists of two separate layering orders. Thermocouple junctions alternate from top to bottom of the resistance layer, rather than being present on the top and bottom of each resistance layer pad as in previous sensors (Hager et al., 1991).

The approximate dimensions (thicknesses of layers based on manufacturer given sputtering rates), are shown in Fig. 4, where the width to thickness ratio of an individual pad is $230 \mu\text{m} / 1.4 \mu\text{m} = 164$. Consequently, a one-dimensional model was considered justified. Because of the different layering orders for the alternating pads, two separate node networks were set up across the gage itself, but joined at the substrate surface to become one. The model assumed an adiabatic condition on the back surface of the substrate, which is valid for time less than 0.15 seconds for the substrates used (Baker and Diller, 1993).

The material properties used for the aluminum nitride substrate were as given earlier. Properties for all of the sputtered layers (except SiO) were taken as the same as the bulk properties. The model (and gage itself) is most sensitive to the SiO resistance layer properties, which were estimated based on the measured sensor response.

The program solves for the temperature profile across the sensor and through the substrate at each time step. The theoretical voltage output of the sensor can then be calculated from the temperature difference between the thermocouple junctions above and below the thermal resistance layer

$$E_q = n\sigma\Delta T \quad (4)$$

where n is the number of thermocouple pairs (280) and σ is the thermoelectric output, which was taken as $21.5 \mu\text{V}/^\circ\text{C}$ for copper and nickel. This allows comparison of input heat flux to heat flux output from the modeled sensor. In addition, three surface temperature versus time traces can be compared: the experimental temperature, T_{exp} , the temperature from the numerical model, T_{num} , and the temperature from the converted experimental heat flux signal, T_{calc} .

Results

As an example of the conversion method, the heat flux and temperature signals for one of the tests (air driver at a pressure of 1.65 MPa) are presented in Fig. 5 using the manufacturer's calibrations in Eqs. (1) and (2). Notice the initial passing shock and accompanying unsteadiness before the tunnel starts at 5 ms. The tunnel unstarts at 35 ms (refer back to Fig. 1 for pressure traces of a typical run at these conditions): While the heat flux is initially strong, it becomes negative by 40 ms. The corre-

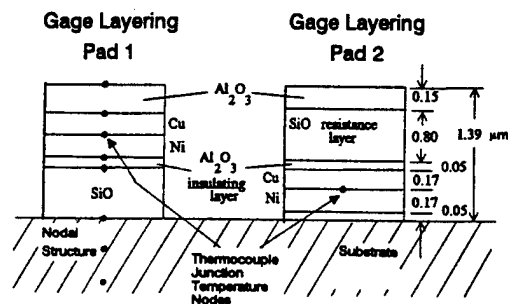


Fig. 4 Numerical model of heat flux sensor

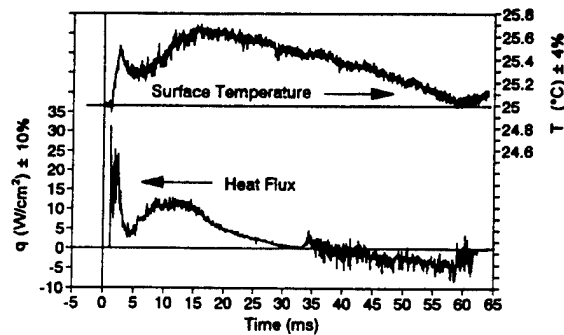


Fig. 5 Heat flux and surface temperature for shock tunnel

sponding temperature change is very small because of the high thermal conductivity of the substrate and the short duration of the flow. Consequently, the effects of electrical noise on the signal are noticeable, and the uncertainty due to it ($\pm 0.05^\circ\text{C}$) is in addition to the 4 percent bias error (from calibration) indicated on the Fig. 5 axis label. The high-frequency fluctuations seen on the heat flux trace are actual flow phenomena, with the signal to noise ratio being much higher than for the temperature signal.

The HFM heat flux signals were converted to the corresponding surface temperature values using equation (3). Comparison of the actual gage surface temperature (T_{exp}) with the calculated gage surface temperature (T_{calc}) is shown in Fig. 6. There is good agreement between T_{exp} and T_{calc} , demonstrating the accuracy of the data processing based on the one-dimensional model. The values of T_{calc} in the 5 to 15 ms range rising slightly above the values of T_{exp} was a common result, although not always present. The values of T_{calc} dropping below T_{exp} past 25 ms was also observed frequently. Although not seen in Fig. 6, longer data sets show that the disagreement between T_{calc} and T_{exp} shown in Fig. 6 does not continue to diverge, but in fact the agreement in the two curves is excellent at longer times. The agreement holds for approximately half a second. A reason for the disagreement at short times (first 50 ms) is possibly related to the radiation from the high temperature flow to the cold (room temperature) sensor. Neither the aluminum-nitride substrate nor the HFM absorb all of the radiation at the surface, which the conversion model assumes.

As evidence of the strength of the conversion methodology of going from heat flux to temperature, note that the temperature curve calculated from the heat flux is much smoother than the measured temperature curve because of the integration process represented by Eq. (3). Comparison of the actual heat flux (q_{act}) with the calculated heat flux (q_{calc}) can also be used to determine S , but q_{calc} is an extremely noisy curve. Because heat flux is proportional to the time rate of change of temperature, the effects of electrical noise are increased when converting from temperature to heat flux because the data processing is a differentiation type process (Baker and Diller, 1993).

Heat Flux Sensitivity Calibration. By comparing the temperature and heat flux signals from the Heat Flux Microsensor (HFM) processed according to the digital-data-processing routine presented above, an independent measure of gage sensitivity S , can be found. This measure of S is particularly valuable because it is determined in the actual high speed flow and high temperature environment of the test.

There are several conceptual issues that underlie the calibration method. Instead of relying on a known input heat flux as the standard for comparison, the change in temperature of the surface is used with the substrate properties as the standard. Because the two sensors are located close together physically

on the surface, it is assumed that they measure the same thermal phenomena, as demonstrated in Fig. 6. The advantages of this calibration method are that temperature is easier to calibrate than heat flux and calibration of the heat flux sensor can be checked during the start of every experiment. The uncertainty of the method is the combination of the uncertainties of the heat flux and temperature measurements plus the uncertainty of the substrate properties, which in this case is estimated as a total uncertainty in S of ± 8 percent.

Heat flux sensitivities were calculated for 12 separate shock tunnel runs. The driver pressures used were set between 1.21 and 2.07 MPa, using helium or air. Run time lengths varied from 8 to 64 milliseconds. All data sets were 2048 points in length. Raw voltages were input to the conversion program described earlier, and the sensitivity that minimized the error between the resulting T_{exp} and T_{calc} curves (such as shown in Fig. 6) was found for each run. An average value for the 12 runs of $S = 49.3 \mu\text{V}/(\text{W}/\text{cm}^2)$ was obtained with a 95 percent confidence interval of ± 12 percent. This value is in excellent agreement with the manufacturer supplied radiation calibration of $S = 50.0 \mu\text{V}/(\text{W}/\text{cm}^2)$ and the value obtained in convection calibration of $S = 49.2 (\mu\text{V}/\text{W}/\text{cm}^2)$. The confidence interval was higher than the expected uncertainty of the measurements, which was attributed to noise in the temperature signal. To minimize this effect, an average value of many data points prior to tunnel startup was used as the initial T_0 upon which the converted heat flux signal T_{calc} was built. In order to have accurate sensitivities calculated from the data, input signals with high signal to noise ratios (aided by high heat fluxes), and high sampling frequencies (to get more data points) are necessary. As this implies, the shorter shock tunnel data sets (8 ms) had higher uncertainties than the longer ones (64 ms).

It should be noted that the accuracy of the data conversion routine is limited to short run-times due to the semi-infinite conduction assumption. The resulting sensitivity and the individual measurements of temperature and heat flux, however, are valid for any length of time.

Numerical Model. The heat flux sensitivity, S , found from the shock tunnel results was used to calculate the appropriate thermal conductivity of the silicon monoxide layer in the sensor. The value obtained was $0.97 \text{ W}/\text{m} \cdot \text{K}$, which is lower than the assumed bulk value of $1.38 \text{ W}/\text{m} \cdot \text{K}$. It is much higher than the value reported by Hager et al. (1991) for sputtered silicon monoxide of $0.1 \text{ W}/\text{m} \cdot \text{K}$. Properties of sputtered materials are known to be highly dependent on the conditions used during the sputtering process.

Because of the flexibility of the numerical model, a wide range of input signals can be used. One important test is to

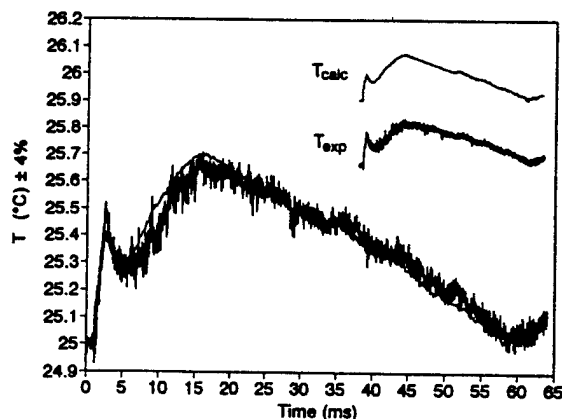


Fig. 6 Calculated and experimental surface temperature

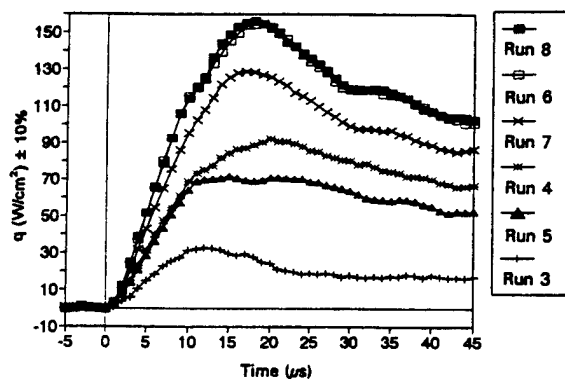


Fig. 7 HFM record of passing shocks in shock tunnel

determine if the sensor alters the measurement of heat flux. To model this situation, measured heat flux data (Fig. 5) were used as input to the numerical model. The heat flux sensor output from the numerical model, q_{num} , differed by less than 1 percent from the input as a result of high-frequency attenuation effects. Therefore, the sensor should not alter the measurement over these time scales. It also demonstrates that the HFM outputs a heat flux signal directly proportional to the actual surface heat flux.

Likewise, the resulting surface temperature, T_{num} , predicted by the model can be compared with the HFM temperature signal, T_{exp} shown in Fig. 5. The temperature at the surface of the substrate below the heat flux gage was found to agree nearly exactly with T_{calc} in Fig. 6 (less than 1 percent difference). This indicates that the one-dimensional numerical model of the substrate matches the analytical representation in Eq. (3) and can be used to convert heat flux to surface temperature.

The temperature at the top surface of the heat flux sensor was also compared with the temperature at the substrate surface. The difference in temperature was found to be a maximum of 0.1°C at the point of maximum heat flux ($q = 20 \text{ W/cm}^2$ on Fig. 5). This difference is negligible for most applications, and is a small fraction of a percent of the total temperature difference from the fluid to the surface. This illustrates the extremely small thermal disruption due to the sensor presence.

Frequency Response Estimation. Previously, a Bragg cell and laser were used to create a step change of heat flux for estimating the time response of a thin-film heat flux sensor (Hager et al., 1991). One problem with any radiation measurement, however, is that a coating of high absorptivity is required over the sensor to insure uniform absorption of the heat flux. Unfortunately, because the coating is typically thicker than the sensor itself, the time response is severely altered. One big advantage of the shock tunnel is that an absorption coating is not required because the heat transfer is based on convection. The incident shock provides a sharp change in the thermal and flow properties as the shock passes over the wall position of the gage in about 5 μs .

Figure 7 shows six different passing shock records. These traces are expansions of the incident shock passings of the same data used in sensitivity estimation. The scale has been expanded from milliseconds to microseconds and the individual data points are marked for the 1 MHz sampling rate. Note the magnitude of the heat flux pulses. Also, there is no initial dip in heat flux as observed by Roberts et al. (1990). This is confirmation that the dip was an artifact of using a hot-film sensor driven by an anemometer.

The response of the gage to a step input in heat flux was simulated using the numerical model. Results showed a nearly first-order exponential rise (within 10 percent), with no evi-

dence of overshoot in the gage response. Consequently, a first-order model was used to estimate a time constant for the sensor from the passing shock data.

$$\frac{q}{q_{max}} = 1 - e^{-t/\tau} \quad (5)$$

Results based on Fig. 7 show that the passing shocks ramp up in approximately 5 μs as the shock passes over the physical space of the gage, followed by a segment of roughly constant heat flux. To model the passing shock as a step in heat flux, average heat flux values were estimated for the first 10 μs for different runs. These values were used for q_{max} in Eq. (5) yielding an approximate thermal time constant of $\tau = 6 \mu\text{s}$ for the data in Fig. 7.

Based on this result, the values of the parameters in the numerical model were adjusted. Originally, the numerical model used the bulk properties of silicon dioxide because no properties of silicon monoxide were available. This resulted in a calculated time constant of $\tau = 2 \mu\text{s}$. To correspond to the experimentally estimated 6 μs time constant, the product of ρC was increased from $1.16 \text{ J/cm}^3 \cdot \text{K}$ (bulk value) to $18.0 \text{ J/cm}^3 \cdot \text{K}$. Such large differences between properties of sputtered and bulk materials are common (Goodson et al., 1994). It is important to note that this difference only affects the theoretical response of the sensor to high-frequency input ($>100 \text{ kHz}$).

The combined results of the numerical model and passing shock experiments demonstrate the first-order response characteristics of the HFM, as well as a method for estimating frequency response of a heat flux sensor in a convective environment.

Conclusions

A method has been developed for determining heat flux sensitivity for the Heat Flux Microsensor (HFM) from shock tunnel test data. Using a simple data processing code, it was demonstrated how measured heat flux can be converted to surface temperature and compared with the measured temperatures. By minimizing the difference between these two data sets, an independent measure of sensitivity can be determined for each test run. Values from 12 runs were compared with sensitivity calibrations performed by other means. The results were well within the calibration uncertainties.

A numerical model of the heat flux sensor and substrate was used to predict the heat flux response of the sensor to an actual heat flux signal. In addition, the transient surface temperature predicted by the model agrees with the experimental surface temperature. The model also shows first-order characteristics in response to a step input of heat flux. Analysis of heat flux resulting from passage of the incident shock gave an approximate first-order time constant for the heat flux sensor of 6 μs . The data and model, therefore, support a frequency response better than 100 kHz, with a flat response across the entire bandwidth.

Because the high speed and high temperature flow in a shock tunnel is similar to the environment often encountered in heat flux testing, the sensitivities and time response determined in the shock tunnel are particularly appropriate.

Acknowledgments

The authors gratefully acknowledge support for this research from the U. S. Air Force Office of Scientific Research under the supervision of Major Dan Fant, program manager.

References

- Baker, K. I., and Diller, T. E., 1993, "Unsteady Surface Heat Flux and Temperature Measurements," ASME Paper No. 93-HT-33.

- Camci, C., and Arts, T., 1991, "Effect of Incidence on Wall Heating Rates and Aerodynamics on a Film-Cooled Transonic Turbine Blade," *ASME Journal of Turbomachinery*, Vol. 113, pp. 493-501.
- Diller, T. E., 1993, "Advances in Heat Flux Measurements," *Advances in Heat Transfer*, Vol. 23, J. P. Hartnett et al., eds., Academic Press, Cambridge, pp. 279-368.
- Dunn, M. G., George, W. K., Rae, W. J., Woodward, S. H., Moller, J. C., and Seymour, P. J., 1986, "Heat-Flux Measurements for a Full-Stage Turbine: Part II-Description of Analysis technique and Typical Time-Resolved Measurements," *ASME Journal of Turbomachinery*, Vol. 108, pp. 98-107.
- Dunn, M. G., 1990, "Phase and Time-Resolved Measurements of Unsteady Heat Transfer and Pressure in a Full-Stage Rotating Turbine," *ASME Journal of Turbomachinery*, Vol. 112, pp. 531-538.
- George, W. K., Rae, W. J., Seymour, P. J., and Sonnenmeier, J. R., 1991, "An Evaluation of Analog and Numerical Techniques for Unsteady Heat Transfer Measurement with Thin Film Gauges in Transient Facilities," *Experimental Thermal and Fluid Science*, Vol. 4, pp. 333-342.
- Goodson, K. E., Flik, M. I., Su, L. T., and Antoniadis, D. A., 1994, "Prediction and Measurement of the Thermal Conductivity of Amorphous Dielectric Layers," *ASME Journal of Heat Transfer*, Vol. 116, pp. 317-324.
- Hager, J. M., Simmons, S., Smith, D., Onishi, S., Langley, L. W., and Diller, T. E., 1991, "Experimental Performance of a Heat Flux Microsensor," *ASME Journal of Engineering for Gas Turbines and Power*, Vol. 113, pp. 246-250.
- Hager, J. M., Onishi, S., Langley, L. W., and Diller, T. E., 1993, "High Temperature Heat Flux Measurements," *AIAA Journal of Thermophysics*, Vol. 7, pp. 531-534.
- Hayashi, H., Aso, S., and Tan, A., 1989, "Fluctuation of Heat Transfer in Shock Wave/Turbulent Boundary-Layer Interaction," *AIAA Journal*, Vol. 27, pp. 399-404.
- Holmberg, D. G., Mukkamala, Y. S., and Diller, T. E., 1994a, "Shock Tunnel Evaluation of Heat Flux Sensors," *AIAA Paper No. 94-0730*.
- Holmberg, D., Reid, T., Kiss, T., Moses, H. L., Ng, W. F., and Diller, T. E., 1994b, "Effects of Shock Wave Passage on Heat Transfer in a Transonic Turbine Cascade," *ASME Paper No. 94-GT-179*.
- Jones, T. V., 1977, "Heat Transfer, Skin Friction, Total Temperature, and Concentration Measurements," *Measurements of Unsteady Fluid Dynamic Phenomena*, B. E. Richards, ed., Hemisphere Publishing, Washington DC, pp. 63-102.
- Kidd, C. T., 1992, "High Heat Flux Measurements and Experimental Calibrations/Characterizations," *NASA CP 3161*.
- Miller, C. G., 1985, "Refinement of an 'Alternate' Method for Measuring Heating Rates in Hypersonic Wind Tunnels," *AIAA Journal*, Vol. 23, pp. 810-812.
- Nicholson, J. H., Forest, A. E., Oldfield, M. L. G., and Schultz, D. L., 1987, "Heat Transfer Optimized Turbine Rotor Blades-An Experimental Study Using Transient Techniques," *ASME Journal of Engineering for Gas Turbines and Power*, Vol. 106, pp. 173-182.
- O'Brien, J. E., 1990, "A Technique for Measurement of Instantaneous Heat Transfer in Steady-Flow Ambient-Temperature Facilities," *Experimental Thermal and Fluid Science*, Vol. 3, pp. 416-430.
- Roberts, A. S., Jr., Orties, K. R., Gartenberg, E., and Caraway, D. L., 1990, "Convective Response of a Wall-Mounted Hot-Film Sensor in a Shock Tube," *International Symposium on Nonsteady Fluid Dynamics*, J. A. Miller and D. P. Telonis, eds., ASME, N.Y., pp. 253-258.
- Schultz, D. L., and Jones, T. V., 1973, "Heat Transfer Measurements in Short Duration Hypersonic Facilities," *AGARDograph* 165.
- Scott, C. J., 1976, "Transient Experimental Techniques for Surface Heat Flux Rates," *Measurements in Heat Transfer*, E. R. G. Eckert and R. J. Goldstein, eds., McGraw-Hill, New York, pp. 375-396.

Appendix B

Computer programs

Calibration (HFS, HW)

QT.FOR

```
*****
*      QT96.FOR
*
*      Originally written by Karen Baker
*      Expanded by David Holmberg
*      Last modified      6/27/96
*
*      This program is designed to convert an HFM surface heat flux
*      signal to the corresponding surface temperature according to a
*      one dimensional semi-infinite model of heat conduction into a
*      substrate of known thermal properties and initially constant
*      temperature. This model is valid for short times where the 1-D,
*      semi-infinite assumptions are valid. Documentation of this method*
*      can be found in HFM related publications.
*      Data are input from a two column text file with the first
*      column temperature and the second heat flux with a space between
*      columns. The temperature and heat flux signals should be the same*
*      output by the HFM amplifier. Then this program converts the
*      voltages obtained from the heat flux microsensor to their corr-
*      esponding heat flux and temperature responses. The amplifier
*      gains, RTS calibration, and substrate properties are entered into*
*      the uncompiled code as constants. If you want any of these to be
*      entered as inputs, then the source code must be changed.
*      This program utilizes the Cook and Felderman method to
*      differentiate temperature with respect to time to obtain the
*      corresponding heat flux and Green's function method to integrate
*      the heat flux with respect to time to yield temperature.
*      While the RTS calibration is entered as a known constant, the
*      HFS sensitivity is only entered as a guess value and this program*
*      iterates to find the best value of gage sensitivity for each data
*      set such that the difference between experimental temperature and
*      the temperature converted from the experimental heat flux is
*      minimized. A secant method algorithm is used to close on the
*      best solution for S (the HFS sensitivity).
*      This program should not be used without looking at plotted
*      results to check PREPT and match in temperatures with increasing
*      time. PREPT is designed to take an initial segment of data points*
*      before anything changes in order to zero the heat flux and temp-
*      ature. And the results must be plotted to see that this is the
*      case, and also that the calculation has not been carried out too
*      far in time such that the 1-D assumption is invalid. If the
*      program crashes, try a different initial guess for S.
*
*      VaTell HFM calibrations are now given in the form:
*      HFS,  $Q = V * 1.0E6 / (G * S)$ , where  $S = Sslope * Temp + Soffset$ 
*      RTS,  $T = RTSslope * (V / G)$ 
*      V = amplified voltage (Volts)
*      T = temperature (C)
*      Q = heat flux (W/cm2)
```

```

*      G = gain on HFS and RTS: HFSGAIN, RTSGAIN below.      *
*      S = sensitivity (uV/(W/cm2))                          *
*
*      This program solves for sensitivity, S, without the    *
*      temperature effect. So the equation used here is:      *
*       $Q = V * 1.0E6 / (G * S)$ , S constant                *
*      Therefore, the value of S that results from this program will *
*      be sensitive to temperature, but in general the change in temp- *
*      erature during any given test is not significant, and the result- *
*      ing S is valid for that temperature range.             *
*      Also, Heat flux is assumed to be zero at the beginning of the *
*      data set, and so the average voltage over the first PREPT data *
*      points is subsequently subtracted from the heat flux Qin.    *
*      In practice, to get an absolute temperature (rather than *
*      differential temperature) from the RTS voltage signal, two values *
*      must be recorded. That is, a reference voltage (RTSVref) from the *
*      amplifier RTS out and a simultaneous measure of the RTS sensor *
*      resistance (RTSRref). The equation for temperature is then: *
*
*       $T = \text{RTSslope} * ((\text{TempIN} - \text{RTSVref}) / \text{RTSGAIN} * 1E4 + \text{RTSRref}) + \text{RTSintcp}$  *
*
*      In this equation, RTSVref corrects the voltage (TempIN) so *
*      that zero voltage is referenced to RTSRref. At that point, the *
*      CHANGE in voltage divided by the gain and current (1E-4 amps) *
*      gives the change in resistance. This is added to the reference *
*      resistance and the sum multiplied by RTSslope and added to the *
*      calibration y-intercept to give temperature (The only absolute *
*      calibration for the RTS is resistance vs. temperature).    *
*      The algorithm here requires only RTSslope in order to find *
*      sensitivity, S. If the temperature is known from elsewhere, or *
*      not an issue, then set RTSVref, RTSRref, and RTSintcp equal to 0. *
*      The program is presently set-up with constants for the HFM-192 *
*      on old blades with material constants as found by Loren, amp#1, *
*      and RTS HFS cal based on p128 and p133, LB4. Input Tvolts, Qvolts *
*      from LeC files and re-convert to temp and q".            *
*      Also, the found SENS must be entered back and the program *
*      rerun to get accurate comparison of Qexp and Qcalc.      *
*
*      Variables used are:
*
*      K.....Thermal conductivity of substrate (W/cmK)
*      RHO.....Density of substrate (kg/cm^3)
*      CP.....Specific heat of substrate (J/kgK)
*      ALPHA.....Thermal diffusivity of substrate (cm^2/s)
*      QEXP()....Heat flux calc from experimental voltage (W/cm2)
*      TEXP()....Temperature calc from experimental voltage (degC)
*      QCALC()....Heat flux calculated from temperature
*      TCALC()....Change in temp calc from heat flux based on SENS,
*                  not final sensitivity. TCALC is an offset from TAVG
*      TEMPIN.....Input temperature (Volts), with or without gain
*      QIN.....Input heat flux (Volts)
*      RTSLOPE....Slope of RTS calibration curve; sensitivity(degC/V)
*      RTSGAIN....Amplifier gain setting for RTS
*      RTSRref, RTSVref, RTSintcp See above discussion
*      HFSGAIN....Amplifier gain setting for HFS
*      SAMPFREQ...Sampling Frequency (kHz)
*      DT.....Time step (s), SAMPFREQ(Hz)^-1
*      TAVG.....Average temp of first PREPT points, substrate Tinit
*      TDIF.....Individual TCALC(J) - TEXP(J); individual errors
*      SUMTDIF....Sum of errors
*      SENS.....Input sensitivity of sensor (uV/W/cm^2)
*      S().....Sensitivity output from convergence routine
*      E().....Absolute error, equals ABS(SUMTDIF)

```

```

*   MAXERR.....Error level defining convergence on S
*   TIMEF.....Number of data points taken
*   STEPMAX.....Max number of iterations in convergence routine
*   SKIP.....Input file size reduction factor
*   LONGDATA...Length of unreduced input file
*   PREPT.....Initial number of pts where T ~ constant, and q" ~ 0
*   VARYS.....Yes/No to vary input sensitivity
*****

```

```

      REAL K, RHO, CP, ALPHA,
+ QEXP(3500), TEXP(3500), QCALC(3500), TCALC(3500),
+ TEMPIN, RTSRref, RTSVref, RTSintcp, RTSLOPE, RTSGAIN,
+ QIN, HFSGAIN, QOFF, SAMPFREQ,
+ DT, TAVG, TDIF, SUMTDIF(100), SENS, S(100), E(100), MAXERR
      INTEGER TIMEF, STEPMAX, SKIP, LONGDATA, PREPT, VARYS
      CHARACTER INFILE*50, OUTFILE*50
      PARAMETER (PI=3.141592654)

```

```

*****
*   Definition of thermal properties of substrate, and other
*   parameters related to temp and S iteration.
*   THESE MUST BE CHANGED FOR A GIVEN GAGE SUBSTRATE,
*   RTS CALIBRATION, AND GAIN SETTINGS
*   PREPT is sensitive to starting length of individual data sets.
*   STEPMAX and MAXERR should be fine for all cases.
*****

```

```

      K=1.29
      RHO=2.77E-3
      CP=921
      ALPHA=K/RHO/CP
      RTSslope= 3.148
      RTSVref = -0.006
      RTSGAIN = 496.
      RTSRref = 164.4
      RTSintcp= -491.2
      HFSGAIN = 5088.
      PREPT   = 30
      STEPMAX = 100
      MAXERR  = 0.0001

```

```

*****
*   Input filenames, open the ASCII input data file and create the
*   output file. Anything in the output file before running is erased
*   during each run.
*****

```

```

      PRINT*
      PRINT*
      PRINT*, '
      PRINT*
      PRINT*, '          The operation of this program is documented in the
+source'
      PRINT*, 'code. Substrate properties, calibration constants, and am
+plifier'
      PRINT*, 'gains must be entered there and the code recompiled.'
      PRINT*
      PRINT*
      PRINT*, 'Enter input filename:'
      READ(*, '(A)') INFILE
      PRINT*
      PRINT*, 'Enter output filename:'
      READ(*, '(A)') OUTFILE
      PRINT*

```

```

OPEN (9, FILE = INFILE)
OPEN (6, FILE = OUTFILE)

*****
*       To use this program successfully, the number of data points,
*       TIMEF = LONGDATA/SKIP must be less than 3500, or the arrays will
*       overflow. The ideal data set would have two seconds of data at
*       100Hz with the heat flux pulse beginning after a one second
*       period at constant temperature conditions.
*       By increasing the value of SKIP, higher frequency data files can
*       be processed as if they were sampled at a lower frequency, but
*       it may be better to reduce LONGDATA than to increase SKIP.
*       SENS as entered is a known value or initial guess, depending
*       on VARYS. The final output value of S(N) is the best sensitivity
*       for the particular data set being analyzed.
*****

PRINT*, 'Enter length of input file:'
READ*, LONGDATA
C   PRINT*, 'Enter sampling frequency of data (kHz):'
C   READ*, SAMPFREQ
SAMPFREQ=.05
c10 PRINT*, 'Enter input file size reduction factor (SKIP):'
C   READ*, SKIP
SKIP=1
TIMEF = INT(LONGDATA/SKIP)
C   IF (TIMEF.GT.3500) THEN
C       PRINT*, 'SKIP value too small.'
C       GOTO 10
C   ENDIF
DT = SKIP/SAMPFREQ/1000
PRINT*, 'Enter heat flux sensitivity (known or initial guess)'
PRINT*, 'used in converting V to W/cm2 (uV/W/cm2):'
READ*, SENS
PRINT*, 'Do you want to vary this sensitivity value? (1=yes,0=no):'
READ*, VARYS
PRINT*
*****
*       Do loop to read ASCII file and convert voltages to correspond-
*       ing temperature and heat flux according to given calibration
*       constants and gains.
*       DUM1,2 may be used to take up unwanted columns in the
*       input file. The IF stmt serves to remove all data pts where
*       (I-1)/SKIP is not an integer.
*****

J = 0
DO 110 II=1,PREPT
    READ (9,*) T,Q
    QOFF = QOFF + Q/PREPT
110 CONTINUE
REWIND (9)

DO 1 I = 1, LONGDATA
    READ (9, *) TEMPIN, QIN
    *
    IF (INT((I-1)/SKIP).EQ.((REAL(I)-1)/REAL(SKIP))) THEN
        J = J + 1
        TEXP(J)=RTSslope*((TempIN-RTSVref)/RTSGAIN*1E4+RTSRref)+RTSintcp
        QEXP(J)= (QIN-QOFF)*1000000./HFSGAIN/SENS
    ENDIF
    *
    as given, for HFM-192, S=10.836+.0331*T
1 CONTINUE

```

```

*****
*   Do loop to find average of the first PREPT points of TEXP(I).   *
*   PREPT is the initial number of data points where TEXP is approx- *
*   imately constant, and where QEXP is approximately 0, before the *
*   heat flux pulse arrives. PREPT should be as large as possible. *
*   This average serves as the starting temp (TCALC(1)) in "DO 4..." *
*   below, and minimizes error due to noise on the temp signal. *
*****

      DO 33 I = 1, PREPT
        TAVG = TAVG + TEXP(I)/PREPT
33      CONTINUE

*****
*   Do loop to perform numerical expression developed by Cook and *
*   Felderman to calculate heat flux from surface temperature *
*****
      DO 2 M = 1, TIMEF
        QCALC(M) = 0
        DO 3 L = 2, M
          QCALC(M) = QCALC(M) + (TEXP(L) - TEXP(L-1))/(SQRT((M-L)*DT)
+          +SQRT((M-L+1)*DT))
3        CONTINUE
        QCALC(M) = 2.*SQRT(K*RHO*CP)/SQRT(PI)*QCALC(M)
2      CONTINUE

*****
*   Do loop to perform method of Green's function to calculate *
*   temperature from heat flux *
*****
      DO 4 I = 1, TIMEF
        TCALC(I) = 0
        DO 5 J = I, 1, -1
          IF (J.EQ.1) THEN
            TCALC(I) = TCALC(I) - 2.*SQRT(ALPHA)/K/SQRT(PI)*QEXP(J)
+            *(SQRT((I-.5)-(J-.5))*DT)-SQRT((I-.5)*DT))
          ELSE
            TCALC(I) = TCALC(I) - 2.*SQRT(ALPHA)/K/SQRT(PI)*QEXP(J)
+            *(SQRT((I-.5)-(J-.5))*DT)-SQRT((I-.5)-(J-1.5))*DT))
          ENDIF
5        CONTINUE
4      CONTINUE

*****
*   Do loop where S is iteratively reduced to find the best least *
*   error fit between the actual temperature data, TEXP, and the *
*   temperature converted from the actual heat flux, QEXP. The loop *
*   also contains IF statements to govern the value and direction *
*   of the next step in determining a more accurate value of S. *
*****

      N = 0
      S(0) = SENS
      S(1) = SENS
      Smin = 0.
      Smax = 100*SENS
      IF (VARYS.EQ.0) GOTO 100
      WRITE (*, *) ' Sensitivity   Convergence Error'
      DO 77 N = 1, STEPMAX
        SUMTDIF(N) = 0
        DO 7 J = 1, TIMEF

```



```

      IF(N.EQ.1) THEN
        TDIF = TCALC(J) + TAVG - TEXP(J)
        SUMTDIF(N) = SUMTDIF(N) + TDIF
      ELSE
        SUMTDIF(N) = SUMTDIF(N) + (S(1)/S(N)-1)*TCALC(J)
      ENDIF
7    CONTINUE
      IF(N.GT.1) SUMTDIF(N) = SUMTDIF(N) + SUMTDIF(1)
      E(N) = ABS(SUMTDIF(N))

      IF (N.EQ.1) THEN
        S(2) = S(1) + SENS/1000
        GOTO 76
      ENDIF
      IF (E(N).GT.E(N-1)) THEN
        IF(S(N).GT.S(N-1)) Smax = S(N)
        IF(S(N).LT.S(N-1)) Smin = S(N)
      ENDIF
      IF (E(N).LT.E(N-1)) THEN
        IF(S(N).GT.S(N-1)) Smin = S(N-1)
        IF(S(N).LT.S(N-1)) Smax = S(N-1)
      ENDIF

      S(N+1) = S(N-1) - (S(N)-S(N-1))*E(N-1)/(E(N)-E(N-1))

      IF (S(N+1).GT.Smax.OR.S(N+1).LT.Smin) THEN
        IF ((Smax-S(N)).GT.(S(N)-Smin)) S(N+1) = (Smax+S(N))/2
        IF ((Smax-S(N)).LT.(S(N)-Smin)) S(N+1) = (Smin+S(N))/2
      ENDIF
      IF (ABS(S(N+1)-S(N)).LT.MAXERR) GOTO 100
76    WRITE (*, '(1X, F10.3, 8X, F10.6)') S(N), E(N)
77    CONTINUE

*****
*      Do loop to write final values to file opened above      *
*****

100  WRITE (6, '(1X, A14, F7.3)') 'Sensitivity = ', S(N+1)
      WRITE (*, '(1X, F10.3, 8X, F10.6)') S(N+1), E(N+1)
      WRITE (*, *) 'Total time (ms) =', TIMEF*DT*1000
      WRITE (*, *) 'Total # of points =', TIMEF
      WRITE (*, *) 'dt (ms) = ', DT*1000
      WRITE (*, *) 'Data infile = ', INFILE
      WRITE (*, *) 'Data saved to: ', OUTFILE
      WRITE (*, *) 'SKIP = ', SKIP
      WRITE (6, *) 'Total time (ms) =', TIMEF*DT*1000
      WRITE (6, *) 'Total # of points =', TIMEF
      WRITE (6, *) 'dt (ms) = ', DT*1000
      WRITE (6, *) 'Data infile = ', INFILE
      WRITE (6, *) 'SKIP = ', SKIP
      WRITE (6, *)
      WRITE (6, *) '   Time (msec)      q" exp      T exp      q"calc
+      T calc '
      DO 12 I = 1, TIMEF
20    FORMAT (1X, F12.7, 4(2X, F12.7))
      WRITE (6, 20) (I-1)*DT*1000, QEXP(I), TEXP(I), QCALC(I),
+      TCALC(I)*SENS/S(N+1)+TAVG
12    CONTINUE
      PRINT*
      STOP
      END

```

HFM2qt.for

PROGRAM HFM2QT

```
*      HFM2QT.FOR/ Jun version modifies HFM2QT.for/ Apr version (which was
*      set-up for 4 HFM's with HFS data taken on the four ch Lecroy, and the
*      RTS and tt, pt, and Lec trg to LV (to sync HFS to RTS)).
*      The June version is set up for 1 HFM with RTS and HFS and tt on one LeC
*      box so no need for a trig signal.
*      The purpose is still to convert signals to q" and T.
*      VRT1OF = ref voltage at Rref for RTS
*      G1 = gains, see p.38, LB4, amp 1 used 6/24, 6/25
*      Last Mod: 6/26/96
```

```
REAL HF1V,HF2V,HF3V,HF4V,RTS1V,RTS2V,RTS3V,RTS4V,TRIGV,TTV,TTC,
+Q1,Q2,Q3,Q4,TSUR1,TSUR2,TSUR3,TSUR4,SENS1,SENS2,SENS3,SENS4,
+HF1OFF,HF2OFF,HF3OFF,HF4OFF,VRT1OF,VRT2OF,VRT3OF,VRT4OF,
+RREF1,RREF2,RREF3,RREF4,TIME
```

```
VRT1OF= -0.006
RREF1=164.4
GRTS1=496.
GHF1 =5088.
```

```
OPEN (2, FILE='d:\dave\071196\htc\dsar2tt.asc')
OPEN (4, FILE='d:\dave\071196\htc\dsar2hf.asc')
OPEN (8, FILE='d:\dave\071196\htc\dsar2rt.asc')
OPEN (13,FILE='D:\dave\OUTPUT\DAT1.OUT')
```

```
K=0
HF1OFF=0.
DO 10 I=1,50
    READ (4,*) HF
    HF1OFF=HF1OFF+HF/50
10 CONTINUE
REWIND(4)
DO 15 J=1,4000
    TIME=K/50.
    K=K+1
    READ (2,*) TTV
    READ (8,*) RTS1V
    READ (4,*) HF1V
    TSURF1= 3.148*((RTS1V-VRT1OF)/(GRTS1/1E4))+RREF1)-491.2
    SENS1 = 0.0331 *TSURF1 + 10.836
    Q1    = (HF1V-HF1OFF)*1E6/(GHF1*SENS1)
    TTC   = TTV*245 + 6.15
    WRITE(13,35)TIME,TTC,Q1,TSURF1
35 FORMAT(1X,F6.3,3(1X,F8.5))
15 CONTINUE
STOP
END
```

HWcal.FOR

```

*****
*   The input to this program is low-speed Pt, Tt, and HW voltage.
*   A constant Mach No. is assumed and this value needs to be supplied.
*   This program then gives Re' and Nu' as output which then is plotted
*   in Excel. Plotting in Excel allows evaluation of how good the
*   calibration fit is through the data (Re' vs. Nu').
*   Only data taken where Pt>13 psig is used in the Re-Nu processing.
*   Mach number will be constant as long as the throat is choked, or
*   above some Pt/Pe that is not easily known because of the complex
*   turbine exit flow (non-isent or 1-D). 13psig was chosen simply
*   based on the knowledge of atmospheric back pressure (typically 13.7
*   psia), and a theoretical ratio of Pe/Pt = 0.528 to have choked flow.
*   The code assumes M=constant, only true if choked flow.
*   LeC low-speed 50Hz: HW, PT, TT, input here files 1,2,3.
*   Getting Pstat upstream would allow direct velocity measurements.
*   Use "FL filename.for" to compile.
*   Last mod 7/17/96 by David Holmberg
*****

      REAL HW,PT,TT,PTPSI,PATM,PTKPA,PSKPA,TTC,TSK,TMK,TMTS,U,Urev,
&  RHOM,CPAIR,KAIRm,VISCm,NUP,REP,NUPT,RED,TW,dw,G,R,M,Mach,Time
      INTEGER ILECFs,IFLAG,ICOUNT

**** Change the following filenames and values for the given data: ****
      OPEN (9, FILE='D:\dave\output\CAL.OUT',STATUS='OLD')
      OPEN (1, FILE='d:\dave\071196\cal\dsarl4hw.ASC')
      OPEN (2, FILE='d:\dave\071196\cal\dsarl4PT.ASC')
      OPEN (3, FILE='d:\dave\071196\cal\dsarl4TT.ASC')
      Mach = 0.356
      Patm = 94.91
      Tw = 233
      dPgrid = 0.
      ILECFs = 4
*****

      ILECFs = ILECFs*1024 -10
      G = 1.4
      R = 287.
      dw= 0.000005
      M = Mach
      IFLAG=0
      ICOUNT=0
      TIME=0
      WRITE(9,*) ' Time(s) ', 'PT(psig) ', 'TT(C) ',
&  'NuP ', 'ReP

      DO 10 J=1, ILECFs
      READ(1,*) HW
      READ(2,*) PT
      READ(3,*) TT
      PTPSI= (PT*25.128-25.11) - dPgrid
      IF(PTPSI.GT.13) THEN
        PTKPa= PTPSI*6.895+Patm
        TTC = TT*251.7 +2.0403
        TSK = (TTC + 273.15)/(1.+((G-1.)/2.)*(M**2.))
        CPair = 1037.8 -0.22371*(TSK) +2.8556E-4*(TSK**2)
&  +5.2694E-7*(TSK**3) -5.3327E-10*(TSK**4)
        G = (1-R/CPair)**(-1)
        PSKPA= PTKPA*(1.+((G-1.)/2.)*(M**2.))**(G/(1-G))

```

```

        Uinf = M*((G*R*TSK)**.5)
        TmK = ((TW+273.15) +TSK)/2.
        TmTs = TmK/TsK
        RHOM = (PsKPA*1000.)/(R*TmK)
        VISCm= 1.716E-5*((TmK/273.16)**1.5)*(383.716/(TmK+110.556))
        Kairm= 2.414E-2*((TmK/273.16)**(3./2.))*(473.16/(TmK+200.))
        ReD = RHOM*Uinf*dw/VISCm
        ReP = (RHOM*Uinf/VISCm)**0.51
        NuPT = HW**2/(Kairm*(TmK-TsK))
        NuP = NuPT*(TmTs)**(-.17)
        WRITE(9,99) TIME,PTPSI,TTC, NuP, ReP
        TIME = TIME+.02
    ENDIF
10    CONTINUE
99    FORMAT(1X,4(F8.3),F9.3)
56    STOP
END

```

High speed data processing

dghspec.m (Matlab)

```

% 8/15/96
% dghspec.m -- to look at PHW with linearization and filter
% Filter: Butterworth, low-passor high-pass, set with Fc and poles below
% Linearization is done using  $U^{.51} = C * V^2$ , or  $U=Clinear*V^{3.92}$ 
% Output Tu based on filtered data if filtering is used
% To look at high resolution (few avgs) of highspped data, vector "x" of 128K (131070 bytes)
% files: ITSx.m, Tux.m

Fs=500;           %sampling frequency (kHz)
Fc=30;           % Butterworth low-pass filter cutoff freq (kHz). IF Fc=0, NO LP filter is used.
Fchp=1.5;        % Butterworth high-pass filter cutoff freq (kHz). IF Fchp=0, NO HP filter is used.
polesLP=8;       % # of poles of LP filter
polesHP=4;       % # of poles of HP filter
linYN=1;         % Linearize vector x? no=0, yes>0, if yes,  $x=x^{3.92}$  for PHW
m=8192;          % #points for averaging, freq res= Fs/m (16384,8192,4096)
n=262142;        % # of points in data files 256KB=262142, 128KB=131070
ovlp=0;          % overlap length, %ovlp=ovlp/m*100
s=n;             % # of points to use in Tu calc
ts=5;           % time in ms to plot for corr data
cutoff=0.2;      % match exponential fit to Rxx curve above cutoff value
s2=10000;        % length used for multiple short ITS (Rxx) calcs
nitsavgs=12;     % # of ITS calculations of pieces of x of length s2

%load dsb18hw.asc;
x(1:n)=dsb18hw';

%linearize PHW signal x:
if linYN>0;
    x = x.^3.92; end;

% Calculate x power spectrum
[p,f]=psd(x(1:n),m,Fs,[],ovlp);
pow(1:m/2+1,1)=f; pow(1:m/2+1,2)=p;

```

```

subplot(3,1,1); semilogy(f,pow(1:m/2+1,2));...
                        title(['Pxx, kHz, dsb18hw.asc']);...
axis([0,50,min(pow(:,2)),max(pow(:,2))]); pause(3);
subplot(3,1,2); semilogy(f*1000,pow(1:m/2+1,2));...
axis([0,2000,min(pow(:,2)),max(pow(:,2))]);...
title(['dghspec.m, Pxx, Hz']);

% Unfiltered Tu
Xmean = mean(x(1:s)); Tu=100*std(x(1:s))/Xmean;
Xmean % answer
Tu % answer

% filters
if Fc>0;
    Wn=2*Fc/Fs; [b,a]=butter (polesLP,Wn); y=filter(b,a,x);
    [p,f]=psd(y(1:n),m,Fs,[],ovlp); pow(1:m/2+1,1)=f; pow(1:m/2+1,3)=p;
    subplot(3,1,1); hold on; semilogy(f,pow(1:m/2+1,3),'m--'); hold off;
    subplot(3,1,2); hold on; semilogy(f*1000,pow(1:m/2+1,3),'m--'); hold off;
    x=y; end;
% LP filtered Tu
Tuflp=100*std(x(1:s))/Xmean; Tuflp % answer
if Fchp>0;
    Wn=2*Fchp/Fs; [b,a]=butter (polesHP,Wn,'high'); y=filter (b,a,x);
    [p,f]=psd(y(1:n),m,Fs,[],ovlp); pow(1:m/2+1,1)=f;
    if Fc==0; pow(1:m/2+1,3)=p;
        subplot(3,1,1); hold on; semilogy(f,pow(1:m/2+1,3),'m--'); hold off;
        subplot(3,1,2); hold on; semilogy(f*1000,pow(1:m/2+1,3),'m--'); hold off;end;
    if Fc>0; pow(1:m/2+1,4)=p;
        subplot(3,1,1); hold on; semilogy(f,pow(1:m/2+1,4),'m--'); hold off;
        subplot(3,1,2); hold on; semilogy(f*1000,pow(1:m/2+1,4),'m--'); hold off;end;
    x=y; end;
pows=pow(1:m/4,:);
save dsb18p.asc pows -ascii;

% HP filtered Tu
Tufhp=100*std(x(1:s))/Xmean;
Tufhp % answer

Xmean % mean linearized V^3.92 of input file x
Tu % Tu answer in %
Tuflp % filtered Tu %
Tufhp % filtered Tu %
print;

```

hfmphw2.m (MATLAB)

```
% Do spectrum of two files, look at PSD, Coherence, and cross-correlation
% HFMPHW2.m last mod 8/15/96 for 256KB, and Rxx done in dghspec.m, not here

Fs=500000; %sampling frequency
m=1024; % #points for averaging, freq res= Fs/m
n=262142; % # of points in data files
ovlp=512; %overlap length, %ovlp=ovlp/m*100
s=10000; % # of points to use in auto and cross corr calcs
t=(1:n)/Fs; %time
ts=1; %time in ms to plot for corr data
Xcoravgs=20; % # of averages of Xcor vectors of length s.

load dsb23hf.asc; y(1:n)=dsb23hf; %%%%%change%%%%% heat flux sensor
load dsb23hw.asc; x(1:n)=dsb23hw; %%%%%change%%%%% passage hot-wire

% Spectral Analysis
[p,f]=spectrum(x(1:n),y(1:n),m,ovlp,[],Fs);
pow(1:m/2+1,1)=f;
Pxx=p(:,1); pow(1:m/2+1,2)=Pxx;
Pyy=p(:,2); pow(1:m/2+1,3)=Pyy;
Gxy=(abs(p(:,3)).^2).^0.5; pow(1:m/2+1,4)=Gxy;
Cxy=(abs(Gxy).^2)./(Pxx.*Pyy); pow(1:m/2+1,5)=Cxy;
Phxy=phase(p(:,3)).*(180/pi); pow(1:m/2+1,6)=Phxy;
plot(f/1000,Cxy);axis([0,50,0,max(Cxy)]);xlabel('frequency(kHz)');...
    title('DGH, hfmphw2.m, Coherence hf/ hw, dsb23, 8/13/96'); %%%%%change%%%%%
    print;
plot(f/1000,Phxy);axis([0,50,-500,500]);...
    xlabel('frequency(kHz)');ylabel('Phase (deg)');...
    title('DGH, Phase shift hf/ hw, dsb23, 8/13/96'); %%%%%change%%%%%
    print;
for i=(1:3);
    semilogy(f/1000,pow(1:m/2+1,i+1));...
    axis([0,50,min(pow(:,i+1)),max(pow(:,i+1))]);...
    title(['DGH, 1=Pxx, 2=Pyy, 3=Pxy, dsb23, 8/13/96, i=',int2str(i)]); %%%%%change%%%%%
    print; end;
pows=pow(1:m/4,:); save dsb23xy.asc pows -ascii; %%%%%change%%%%%
```

```
% Cross-correlation
a=Fs*ts/1000; Rxysum=zeros(size(t(s-a:s+a)));
for k=(1:Xcoravgs);
    xs=x(s*(k-1)+1:s*k); ys=y(s*(k-1)+1:s*k);
    Rxy=xcorr(xs-mean(xs), ys-mean(ys),'coeff'); Rxya=Rxy(s-a:s+a);
    plot(t(1:1+2*a).*1000-ts,Rxya);...
        axis([-ts,ts,min(Rxya),max(Rxya)]);xlabel('time(ms)');...
        title('DGH, HFS/PHW Cross-corr'); pause(2);
    Rxysum=Rxysum+Rxya; end;
Rxyavg=Rxysum/Xcoravgs;
plot(t(1:1+2*a).*1000-ts,Rxyavg);...
    axis([-ts,ts,min(Rxyavg),max(Rxyavg)]);xlabel('time(ms)');...
    title('DGH, HFS/PHW Cross-corr, dsb23, 8/13/96'); %%%%%change%%%%%
    print;
XCor=Rxyavg; save dsb23xor.asc XCor -ascii; %%%%%change%%%%%
```

PSD3Lx.FOR

```

PROGRAM psdlx
*****
*      To read in 4 col file with freq and PHW Eu(f) for G0 @ 0.2, 0.4,
*      and 1.0mm hw y locations. Calculates Rxx and ITS and Lx.
*      Last mod 9/3/96 by David Holmberg
*****
      REAL f(260),g(3,260),R(3,1000),err(1000),TS(3),LS(3),fit(3),
      &      x,sumx,t,df,cutoff,ITS,ITSold,ITSnew,samp,rxxtime,tcut
      INTEGER high,itest,mmax,nof

*  Change the following filenames and values for the given data: ****
      OPEN (1, FILE='d:\dave\082996\rxx\ps3g4psd.txt')
      OPEN (2, FILE='D:\dave\output\dat1.OUT',STATUS='OLD')
      IFileSz = 256      (Length of E(f) input vector)
      df      = 488.28   (frequency resolution in Hz)
      Ufs     = 118.     (FS Velocity m/s)
      cutoff  = 0.1      (Rxx calc fit exponential above this value)
      tcut    = .17      (Rxx calc fit exponential at time less than this)
      samp    = 500      (sample freq in kHz)
      rxxtime = 1.       (amount of Rxx to write to file in ms)
      nof     = 3        (No. of Files)

*** Read data
      DO 10 J=1, IFileSz
        READ(1,*) f(j),g(1,j),g(2,j),g(3,j)
10    CONTINUE

*** Rxx(t) calc
      mmax = int(rxxtime*samp)
      DO 12 k=1,mmax
        t=(k-1)/samp
        sumx1=0.
        sumx2=0.
        sumx3=0.
        DO 22 kk=1,IFileSz
          x = cos(2*3.14159*f(kk)*t)*df
          sumx1 = sumx1 + x*g(1,kk)
          sumx2 = sumx2 + x*g(2,kk)
          sumx3 = sumx3 + x*g(3,kk)
22    CONTINUE
        If (k.eq.1) then
          Rg01 = sumx1/Ufs**2
          Rg21 = sumx2/Ufs**2
          Rg41 = sumx3/Ufs**2
        Endif
        R(1,k) = sumx1/Ufs**2/ Rg01
        R(2,k) = sumx2/Ufs**2/ Rg21
        R(3,k) = sumx3/Ufs**2/ Rg41
12    CONTINUE

*** Find ITS to fit exponential curve to Rxx
      DO 21 mama = 1,nof
***** Truncate Rxx
        high=0
        DO 23 m=1,mmax
          t=(m-1)/samp
          IF(R(mama,m).lt.cutoff.and.t.gt.tcut.and.high.eq.0) THEN
            mR=m
            high=1

```

```

        ENDIF
        IF(m.eq.mmax.and.high.eq.0) mR=mmax
23    CONTINUE
****  Fit exponential
        itest=0
        ITS=0.001
        DO 24 mm=1,50
            sumerr=0
            DO 25 n=1,mR
                time = (n-1)/samp
                err(n)= exp(-time/ITS) - R(mama,n)
                sumerr = sumerr + err(n)
25    CONTINUE
            IF(mm.EQ.1) THEN
                sumrold=sumerr
                ITSold=ITS
                ITS=ITS*1.2
            ENDIF
            IF(mm.GT.1.AND.itest.EQ.0) THEN
                IF(abs(sumerr).LT.0.001) itest=1
                ITSnew=ITS-sumerr*((ITS-ITSold)/(sumerr-sumrold))
                ITSold=ITS
                ITS=ITSnew
                sumrold=sumerr
            ENDIF
c        write(*,*) mama, mR, mm, ITS, sumerr
24    CONTINUE
        TS(mama)=ITS
        LS(mama)=ITS*Ufs
21    CONTINUE

*** Calculate fit for Rxx and write data
        DO 30 i=1,300
            t = (i-1)/samp
            fit(1) = exp(-t/TS(1))
            fit(2) = exp(-t/TS(2))
            fit(3) = exp(-t/TS(3))
            IF(i.eq.1) THEN
                write(2,'(6X,3(F6.4))') TS(1),TS(2),TS(3)
                write(2,'(6X,3(F6.3))') LS(1),LS(2),LS(3)
                write(*,'(6X,3(F6.4))') TS(1),TS(2),TS(3)
                write(*,'(6X,3(F6.3))') LS(1),LS(2),LS(3)
            ENDIF
            write (2,99) t,R(1,i),R(2,i),R(3,i),fit(1),fit(2),fit(3)
30    CONTINUE
99    FORMAT(7(F6.3))
56    STOP
        END

```


Appendix C

HW Frequency response tests

PHW

3/25/96: These tests were performed using the PHW driven by the TSI, Inc. IFA-100 anemometer. A square wave test signal (with a range of 1 to 43kHz) from the IFA-100 was applied to the wire to allow viewing the frequency response and stability of the wire in different environments and at different anemometer control settings. Except for frequency response estimation, the test signal was set to 20kHz. The wire was run at an over-heat ratio ($OHR = R_{wire, Tope} / R_{wire, To} = 1.9$), with bridge voltage from the anemometer sent to an oscilloscope to view the triggered time series waveform. The wire bridge voltage was also sent to the HP 3562A Dynamic Signal Analyzer where the frequency spectrum could be observed from 0 to 100kHz. The wire was tested in no flow conditions as well as in the jet (laminar and turbulent regions) of a TSI HW calibrator, and in the tunnel upstream of the blades and in the passage.

The IFA-100 anemometer allows setting the OHR via an Operating Resistance knob on the front panel. In addition to this there are two other knobs used to tune the frequency response of a wire, namely the Bridge Compensation (BC) knob and the Cable knob. TSI provides recommended BC settings for their standard probes, and give procedures for setting Cable. In general, the settings of BC and Cable should be set while the wire is in the actual test conditions, i.e. in the tunnel at flow for the present tests. In simple terms, the Cable knob is largely responsible for the stability of the wire in that there is a narrow range, analogous to a plateau, around which the wire is unstable leading to frequency oscillations (OSC). These oscillations are evidenced by a lower output mean voltage, by wild fluctuations of the oscilloscope trace, and also by broad-band noise in the frequency spectrum. These tests were performed to examine the proper control settings for these two wires.

Initially, with the PHW in *no-flow*, the following was observed:

- BC = 90 and adjusting "Cable" allows for a textbook pulse (Freymuth and Fingerson, 1980) with a width of 20 μ s.
- By increasing the frequency of the test signal, the waves of the test signal began to merge on the oscilloscope (as the period approached 20 μ s). The amplitude of the wire response to the test signal started to decay at a frequency of 35kHz or so (5% decay at 40kHz). This

should be an estimate of wire frequency response at no flow. Thus the width of the test signal ($18\mu\text{s}$ should be close to $1/\text{frequency response}$ or $1/35\text{kHz} = 29\mu\text{s}$)

- Increasing "Cable" caused more noise (broadband and peaks) in the frequency response, while increasing BC did not, although increasing both would lead to OSC as seen on the oscilloscope

Using the TSI calibrator it was found :

- BC and Cable need to be decreased (turned CCW) to get a desired test signal response with flow.
- In the laminar portion of the jet there is no measurable energy in the frequency spectrum.
- BC seemed best at ~ 60 .
- At these settings there were no noise peaks in the frequency spectrum.
- In the turbulent region of the jet, the turbulent energy decayed out by 50kHz .
- As BC is increased, the amount of higher frequency noise grows, until the levels on the high end of the frequency spectrum are as high as the low-end. This is similar to noise seen in some of the passage measurements (e.g. data taken 1/30/96), but is very different from the desired decay to zero seen as noted above for a lower BC.

In the tunnel with PHW in inlet flow (upstream):

- With BC = 60, and cable adjusted below (CCW) OSC, the frequency spectrum is similar to the TSI calibrator jet with all energy dying out by 50kHz . Increasing BC leads to noise at high frequency as noted above.
- At the optimum settings for BC and cable, the test signal had a peak and double dip (i.e. a second lower peak to the right), as opposed to the single textbook dip (drop below the initial level and recovery to the original level). Several runs were done trying to adjust this, but this was the best possible.
- The difference between flow and no-flow settings on the IFA was large. The test signal with flow and the above double dip had a peak width of about $4\mu\text{s}$, while at no-flow the same signal had a double peak and peak width of more than $20\mu\text{s}$. In other words, at no-flow, the test signal has a double peak where the two peaks were close and of the same magnitude, but with-flow the second peak dropped to a lower magnitude.
- The $4\mu\text{s}$ peak width implies a frequency response better than 150kHz .

In the tunnel with PHW in the passage over the blade SS (where HFM2 was 1/30):

- With BC = 60 there was some high frequency noise present; had to reduce BC = 50.
- At no flow at these settings, cable is slightly more than $1/2$ turn back from complete OSC:

In the tunnel with PHW in the passage above PS2, 5/4/96 tests:

A persistent 70kHz peak was successfully eliminated by adjusting BC. A value of BC = 60 removed the 70kHz , with the "cable" knob $1/2$ turn back from OSC.

PHW concluded optimum settings in passage:

BC = 60 (SS higher velocity maybe BC = 50)
"cable" knob slightly more than $1/2$ turn back from complete OSC.

UHW

The UHW is a HW probe similar to the standard TSI U-wire, but custom made by Auspex Fig. 3.2.1, having the wire at 90° to the support. Tests were run on 3/27/96 to take measurements downstream of grids, upstream of the blades. The frequency response of this probe is significantly different from the PHW. The HP Spectrum Analyzer was not used to look at frequency response, only the oscilloscope. The wire was run at OHR = 2.0. During runs, the frequency response became more unstable, requiring the "cable" knob to be re-adjusted. The number of turns CCW from OSC did not change, instead, the OSC point shifted on the Cable knob.

NO-flow results:

- The wire showed a strong 350kHz wave on top of the test signal response. This could be removed by the filtered output. To remove it without the filter, Cable and BC had to be decreased significantly.
- The test signal peak width = 50μs.
- The range where the test signal was clean (textbook) without the 350 kHz noise was very narrow--reducing "cable" much further led to OSC the other direction (falling off the non-OSC "plateau").
- BC = 78 seemed best, with "cable" decreased enough to not see significant 350kHz noise, which was far back from complete OSC.

In tunnel:

- The narrow non-OSC plateau remained for BC = 78
- Found this situation could be improved by decreasing BC and increasing "cable"
- At the best setting of BC = 30 the test signal at no-flow was about 50μs wide, but with no 350kHz noise. At flow, these same settings led to a peak width of 10μs, or a frequency response of about 70kHz before roll-off begins.

Final best settings for UHW:

BC = 30

"cable" 1/4 turn from complete OSC, 1/8 turn from beginning of OSC

Appendix D

KEP overview

KEP is a $k-\epsilon$ code written by engineers at GE in the late 80's, Zerkle and Lounsbury (1988). It is a modified version of the well known STAN5 code of Crawford and Kays (Crawford, M.E., and Kays, W.M., "STAN5 --A Program for Numerical Computation of Two-Dimensional Internal and External Boundary Layer Flows," NASA CR-2742, 1976.) allowing the use of the Lam-Bremhorst low-Reynolds-number $k-\epsilon$ turbulence model as modified by Rodi and Scheuerer. KEP was run with different inlet turbulence levels (Tu_0) for our GE blade design to give reference heat transfer levels and transition predictions for different inlet conditions. We have generally judged our blade heat transfer results by how well they match the KEP predictions. The purpose here is to summarize what is known about KEP and then give a balanced judgment of its accuracy.

Published performance of KEP:

Zerkle's paper documents performance of the KEP code versus: Blair's flat plate data with different grids upstream, earlier GE cascade data, and earlier GE data from a rotor test. The results are quite good, with mean heat-transfer levels generally matching experiment, and transition predicted fairly well. Specific points noted:

- 1) KEP was run with different inlet Tu_0 to find what inlet turbulence level created a numerical result that most closely matched mean heat transfer levels and transition location as measured experimentally. Generally a one or two percent change in Tu_0 resulted in a small (<10%) change in mean heat transfer and was in the scatter of the experimental data points.

- 2) Transition location was significantly affected by adjusting Tu_0 , such that transition location can be off significantly from KEP predictions. Comparing KEP to the flat-plate data, KEP predicted a transition distance from start to finish that was too short). It predicted the start of transition late for the low $Tu_0 = 1.3\%$ case, and early for the $Tu_0 = 2.6\%$ case, resulting in full transition at $Re_x < 0.4Re_{\text{transition actual}}$.

- 3) For the cascade blade at design (similar to our transonic blade) KEP did very well on the PS, but had trouble matching mean heat transfer on the SS. The experimental data showed no distinct shock location, but instead a peak in heat transfer at mid-chord and large scatter behind that. KEP over-predicted HT ahead of this SS peak, and under-predicted at the peak and

behind it. A 2% change in Tu_0 did not affect the calculation significantly except to raise the mean level by 10% upstream of the SS peak and across the PS.

4) For the air-turbine rig test, KEP did reasonably well matching the data on both PS and SS. For the $Tu_0 = 8\%$ level that best matched the SS however, PS heat transfer was over-predicted somewhat, but the scatter in the experimental data makes it hard to judge.

Based on these results, we can assume that KEP predictions are good on the PS within 10%, and that the SS prediction probably gives transition near where it should be, but that mean heat transfer levels may be off significantly, but within 25%

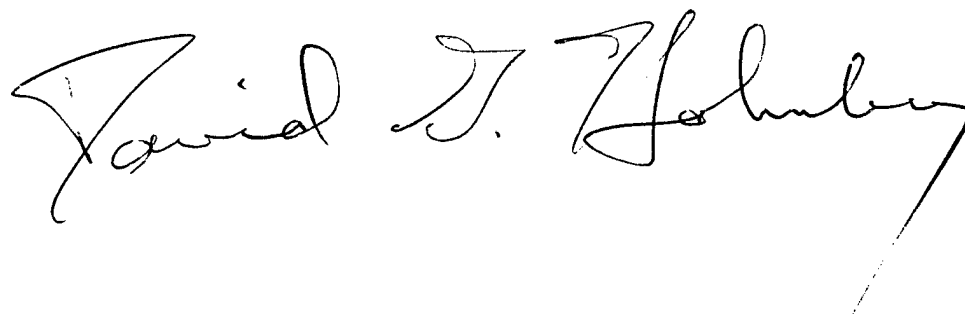
Constant Tu_0 and varied Δ_x in KEP:

KEP allows setting inlet turbulent kinetic energy, but the length scale is not addressed. KEP allows setting Tu_0 , but the dissipation value (ϵ_0), is determined from fixed constants. These constants are the familiar constants present in $k-\epsilon$ models and are necessary to limit the number of unknowns in the equation set. The values of these constants have been determined based on data sets available in the literature and are dependent on the turbulence fields from which they were estimated. The constants used are therefore typical of some general turbulence field, but do not allow for predicting changes in heat transfer based on constant Tu_0 with different length scales.

Vita

David Holmberg was born in Cleveland to a young graduate student and his wife and he was raised in the Washington, DC area. His family includes two sisters, and presently nephews, a niece and in-laws. High school years were filled with music and study before coming to Virginia Tech and Mechanical Engineering. After getting his BS, David spent two years in China teaching English and expanding his world. He came back to graduate school, and through his involvement with a local Chinese Bible study group came to marry a young lady from Taiwan. He is blessed with a loving wife, family, and friends.

"Of making many books there is no end, and much study wearies the body." Ecclesiastes 12:12.

A handwritten signature in black ink that reads "David T. Holmberg". The signature is written in a cursive style with a large, sweeping initial 'D' and a long, trailing flourish at the end of the name.